Alkali activated materials as a sustainable material solution for waste remediation, smart construction, and energy storage applications

by

Michael DI MARE

MANUSCRIPT-BASED THESIS PRESENTED TO ÉCOLE DE TECHNOLOGIE SUPÉRIEURE IN PARTIAL FULFILLEMENT FOR THE DEGREE OF DOCTOR OF PHILOSOPHY
Ph.D.

MONTREAL, FEBRUARY 1, 2023

ÉCOLE DE TECHNOLOGIE SUPÉRIEURE
UNIVERSITÉ DU QUÉBEC

BOARD OF EXAMINERS

THIS THESIS HAS BEEN EVALUATED

BY THE FOLLOWING BOARD OF EXAMINERS

Dre. Claudiane Ouellet-Plamondon, Thesis Director
Département de génie de la construction, École de technologie supérieure

Dr. Éric David, President of the Board of Examiners
Département de génie mécanique, École de technologie supérieure

Dr. Lucas Hof, Member of the jury
Département de génie mécanique, École de technologie supérieure

Dr. Waltraud Kriven, External Evaluator
Department of Materials Science and Engineering, University of Illinois at Urbana-Champaign

THIS THESIS WAS PRENSENTED AND DEFENDED

IN THE PRESENCE OF A BOARD OF EXAMINERS AND PUBLIC

DECEMBER 5, 2022

AT ÉCOLE DE TECHNOLOGIE SUPÉRIEURE

ACKNOWLEDGMENT

In hindsight, many events in my life seem preordained. However, I know that it is but a series of benevolent accidents that led me to pursue a Ph.D. in Montréal. I am endlessly grateful for the chance to experience the unexpected twists and turns and I would like to take a moment to thank some of the people who have made it possible.

First, I would like the jury of my thesis for their time and patience, particularly my supervisor, Claudiane Ouellet-Plamondon, without whom I would never have had this truly unique opportunity to come to Montréal. I am grateful to the technicians of ÉTS, especially Michaël Dubois and Marielle Jacques, for their assistance and endless patience. This work would not have been possible without the support of the Mitacs Acceleration program, which facilitated the collaboration to study bauxite residue (Chapters 3-4) and the Natural Sciences and Engineering Research Council of Canada, which supported the study of the dielectric and electromechanical phenomena (Chapters 5-8).

I would like to thank my collaborators at Rio Tinto who made much of the research described in this thesis possible. I would like to give special thanks to Julie Guerin who made time to listen to my wild theories and even gave me the resources to turn some of them into realities.

I cannot begin to give enough thanks to the many mentors who have helped me get this far. In particular, I would like to thank my mentor at the University of Illinois, Waltraud Kriven, who recognized my potential and challenged me to expand my comfort zone. I would also like to thank my prior supervisor, Wojciech Suchanek, for giving me the opportunity to grow and encouraging me to pursue my passion for research.

I would like to thank my father for encouraging my curiosity and teaching me how to build my own tools to parse the overwhelming unknown. I would like to thank my mother for teaching me to act with patience and awareness. She taught me to look for inspiration and creativity in both the unusual and the mundane. I would also like to thank my sisters who have always been my oldest, closest, and best friends. I hope someday to create a family as nurturing and loving as the one that we have shared.

Méthodes et matériaux pour les matériaux à activation alcaline dans des applications structurelles, d'auto-détections et diélectriques

Michael DI MARE

RÉSUMÉ

Les matériaux à activation alcaline (AAM) sont une catégorie de solides aluminosilicates amorphes qui ont suscité l'intérêt de la communauté scientifique en raison de leur production facile et de leurs propriétés inhabituelles. Ils durcissent à température ambiante sans traitement à forte intensité énergétique et peuvent être produits à partir de sous-produits industriels, ce qui en fait une alternative écologique aux produits en céramique et en ciment. AAM a fait l'objet d'études approfondies en tant que solution de rechange écologique au ciment Portland mais, à ce jour, il a été peu commercialisé en Amérique du Nord. Deux obstacles clés à l'augmentation de la production sont (1) la concurrence pour les matières premières avec l'industrie du ciment et (2) le manque d'applications à forte valeur ajoutée pour faciliter le passage à l'échelle de la production d'AAM. Cette thèse relève ces défis en proposant une nouvelle méthodologie pour utiliser les résidus de bauxite comme matière première pour l'AAM à haute résistance et en identifiant de nouvelles applications qui servent de tremplin pour la production à grande échelle d'AAM.

Le résidu de bauxite est un sous-produit de l'industrie de l'aluminium qui revêt une importance particulière pour la province de Québec. Dans cette thèse, le premier obstacle à la production d'AAM est abordé en développant une nouvelle méthodologie pour utiliser les résidus de bauxite comme matière première pour l'AAM à haute résistance. Bien que l'utilisation de résidus de bauxite comme matière première ne soit pas nouvelle, la méthodologie proposée permet de tripler la teneur en résidus de bauxite dans l'AAM (jusqu'à 77%), de valoriser les résidus de bauxite à l'état brut sans modification supplémentaire et d'atteindre une résistance à la compression supérieure à 32 MPa, dépassant les normes ASTM pour les matériaux structurels porteurs.

Le deuxième obstacle à la production d'AAM est abordé par l'identification de nouvelles applications à haute valeur ajoutée pour l'AAM à partir d'une étude de leurs propriétés électriques et électromécaniques uniques. Il a été démontré que les AAM possèdent une

propriété unique d'auto-détection qui peut être exploitée pour produire des matériaux de construction intelligents. Contrairement au ciment, les AAM possèdent l'auto-détection comme propriété intrinsèque du matériau, sans qu'il soit nécessaire d'ajouter de coûteux additifs. Cela fait des AAM une solution inégalée dans le domaine des matériaux de construction intelligents. L'AAM testé a été produit avec une piézorésistivité supérieure à 50 % et une résistance à la compression supérieure à 50 MPa, ce qui démontre la possibilité d'ajuster la composition de l'AAM pour obtenir des performances mécaniques et d'auto-détection élevées. Une étude des propriétés électriques de l'AAM a révélé un comportement diélectrique sans précédent. Les AAM n'ont pas été considéré auparavant comme une alternative aux céramiques diélectriques, mais les résultats démontrent qu'ils sont parmi les matériaux les plus polarisables jamais rapporté avec des constantes diélectriques aussi élevées que 10^9. Cela présente une nouvelle opportunité d'utiliser les AAM comme une alternative puissante et peu coûteuse pour les supercondensateurs. Ces deux applications offrent une nouvelle possibilité d'augmenter la production d'AAM et de tirer parti de cette catégorie de matériaux respectueux de l'environnement.

Mots-clés: Alkali activated materials, one-part geopolymer, bauxite residue, red mud, leaching behavior, self-sensing, piezoresistivity, structural health monitoring, dielectric constant

Methods and materials for alkali activated materials in structural, self-sensing, and dielectric applications

Michael DI MARE

ABSTRACT

Alkali activated materials (AAM) are a class of amorphous aluminosilicate solids that have attracted interest because of their facile production and unusual properties. They cure at room temperature without energy-intensive processing and can be produced from industrial by-products, making them an environmentally friendly alternative to ceramics and cement products. AAM have been heavily studied as a green alternative to Portland cement but, to date, have seen little commercialization in North America. Two key obstacles to their industrial production are (1) the competition for raw materials with cement production and (2) the lack of high-value applications to facilitate the scale up of AAM production. This thesis addresses these challenges by proposing a new methodology to utilize bauxite residue as a raw material for high-strength AAM and identifying new applications that serve as a stepping stone to scale up AAM production.

Bauxite residue is a large volume by-product of the aluminum industry that is particularly significant to the province of Quebec. In this thesis, the first obstacle to AAM production is addressed by developing a new methodology to utilize bauxite residue as a raw material for high-strength AAM. While the use of bauxite residue as a raw material is not new, the proposed methodology triples the content of bauxite residue in the AAM, up to 77%, can valorize bauxite residue in its raw state without additional modification, and achieve compressive strength over 32 MPa, exceeding the ASTM standards for load-bearing structural materials.

The second obstacle to AAM production is addressed through the identification of new high-value applications for AAM from an investigation of their unique electrical and electromechanical properties. AAM were discovered to possess a unique self-sensing property that can be leveraged to produce smart construction materials. Unlike cement, AAM exhibit self-sensing as an intrinsic material property without the need for costly self-sensing additives. This makes AAM an unparalleled solution for the field of smart construction materials. AAM with self-sensing piezoresistivity above 50% and compressive strength above 50 MPa were

produced, demonstrating the possibility to tune the composition of AAM to achieve both high self-sensing and mechanical performance. An investigation of the electrical properties of AAM revealed an unprecedented dielectric behavior. AAM have not been previously considered as an alternative to dielectric ceramics, but the results demonstrate that they are among the most polarizable materials ever reported with dielectric constants as high as 10^9. This presents a novel opportunity to utilize AAM as a powerful low-cost alternative for supercapacitors. These two applications provide a new avenue to scale up AAM production and take advantage of this environmentally friendly class of materials.

Keywords: Alkali activated materials, one-part geopolymer, bauxite residue, red mud, leaching behavior, self-sensing, piezoresistivity, structural health monitoring, dielectric constant

TABLE OF CONTENTS

LIST OF TABLES

LIST OF FIGURES

LIST OF ABBREVIATIONS

AAM	Alkali activated materials
BR	Bauxite residue
FCR	Fractional change in the electrical resistance of the specimen
KASH	Potassium-alumina-silica-hydrate gel
K-AAM	Alkali activated materials from a potassium activator
K/Al ratio	Potassium / Aluminum molar ratio
NASH	Sodium-alumina-silica-hydrate gel
Na-AAM	Alkali activated materials from a sodium activator
Na/Al ratio	Sodium / Aluminum molar ratio
N/CASH	Sodium/Calcium-alumina-silica-hydrate gel
Si/Al ratio	Silicon / Aluminum molar ratio
W/B	Water / binder ratio

LIST OF SYMBOLS

δ	Dirac delta function
ε	Corresponding eigenvalue
σ	Electrical conductivity
ω	Perturbation frequency
D_s	Skeletal density
e	Euler's constant
f	Fermi-Dirac occupation number
$\hbar$	Reduced Planck constant
Hz	Hertz, unit of frequency
i	Unit imaginary number
mdarcy	millidarcy, unit of permittivity
m_e	Mass of an electron
m, m'	A pair of atoms
MPa	Megapascals, unit of compressive strength
$R_{1,2,3}$	Electrical resistance of Wheatstone bridge resistors 1, 2, or 3
$R_{samples}$	Electrical resistance of specimen
V	Unit cell volume
$V_{applied}$	Voltage applied to Wheatstone bridge
$V_{measured}$	Voltage measured across specimen
W_a	Water absorption

INTRODUCTION

This thesis addresses alkali activated material (AAM) technology, their electrical behavior, and how they can be leveraged to create greener, smarter structural materials. AAM are a category of aluminosilicate compounds that can be shaped in a liquid state before curing through a recrystallization reaction to form an amorphous solid. They are a versatile category of materials that have been proposed for various applications from catalysts to precursors for valuable high-tech ceramics, but they have been most heavily studied as construction materials. AAM are an alternative to Portland cement with similar physical and mechanical properties but a substantially lower environmental impact. Since their discovery, researchers of AAM have promised a more sustainable future for construction using AAM as a low-carbon alternative to cement. However, these low-carbon alternatives have not materialized due to commercialization problems. The commercial production of AAM has been stymied by two obstacles and the purpose of this thesis is to address both obstacles through a two-pronged research investigation to support AAM as a sustainable material technology.

The origins of the commercial difficulties of AAM production lie in the low availability of raw materials and the lack of small high-value applications to allow the gradual scale-up of production. The competition for raw materials with cement production has created a bottleneck for AAM production and diminished the economic viability of AAM as a cement replacement. While many new raw materials have been suggested for AAM, including high-availability by-products such as bauxite residue, researchers in the field have grappled with the question of how to effectively transform these materials into high-strength AAM without compromising the sustainability advantages of AAM over cement. Simultaneously, the massive production scale required for construction applications has created a first-mover obstacle for the growth of the AAM industry. The absence of small-volume, high-value applications to facilitate the development of the necessary supply chains and production infrastructure has reinforced this impediment. While the chemical properties of AAM have been investigated as catalyst materials, no application has yet been found to be economically viable. This has caused researchers to turn to other unique properties of AAM, such as the electronic and electromechanical properties, in search of new high-value applications that are

commercializable. This thesis addresses both of the principal obstacles facing the AAM industry through a two-pronged effort to develop new techniques to utilize high-availability raw materials and identify new high-value electromechanical applications to accelerate the growth of the AAM industry. Together, these efforts improve the commercializability of AAM and support the development of AAM as a sustainable material industry for construction applications and beyond.

Despite decades of scientific study, AAM are underutilized in the construction sector due to the competition for raw materials with cement production. The development of supplemental cementitious materials for cement production has created fierce competition for certain industrial by-products that has undercut efforts to commercialize AAM. This has led many researchers to search for new alternative raw materials that are widely available and compatible with AAM, but not suitable for use in cement. Bauxite residue is a highly available by-product that has favorable chemistry for AAM and has limited compatibility with cement, making it an ideal candidate for further study. The first prong of this thesis will improve upon the methods to utilize bauxite residue in AAM and create a new means for using this by-product as a raw material for AAM production.

AAM have been long recognized as a means for addressing the circularity gap that exists in metallurgical industries by utilizing by-products and waste products as raw materials for construction materials. The circularity gap is a quantification of the quantity of non-renewable raw materials extracted globally to maintain an industry or national economy. Each year, a multinational sustainability advocacy group known as Circle Economy quantifies the circularity gap for nations and industrial sectors in the global economy and challenges the world to develop solutions to improve sustainability (CGRi, 2022). Reducing the circularity gap is key to achieving a so-called circular economy that minimizes the long-term impact on the environment and ensures sustainable industrial practices. In the aluminum industry, bauxite residue is a large volume by-product whose global accumulation and lack of viable valorization options is a circularity gap recognized by the Aluminum Stewardship Institute, a global non-profit that advocates for sustainability in the aluminum industry (ASI, 2022). Bauxite residue is particularly significant in Quebec because of the presence of the aluminum industry in the province. The valorization of bauxite residue will reduce the environmental impact of the

aluminum industry in Quebec and create an opportunity to export this technology globally. The first prong of this thesis is to develop a new method for transforming bauxite residue into a high-strength AAM through a collaboration with Rio Tinto and the Mitacs Accelerate program. This research proposes a new methodology for maximizing the content of bauxite residue that can be valorized and the scalability of the process by minimizing the complexity, cost, and environmental impact of the transformation process.

The second prong of this thesis addresses the development of high-value applications to support the commercialization of AAM. A major obstacle to the realization of AAM technology in construction is the pre-eminence of cement and the associated economy-of-scale efficiency. The development of smaller high-value applications for AAM will provide stepping stones to bridge the gap between pilot production and the massive production scale required to effectively compete with cement. To accomplish this, this section of the thesis investigates unique properties of AAM that have not been previously studied in the literature and proposes applications to leverage them.

Though the mechanical and chemical properties of AAM have been heavily studied, the electrical properties of AAM have been neglected from significant scientific scrutiny. The growing interest in smart multifunctional materials has highlighted the importance of the electrical properties of construction materials and their potential value to the Industry 4.0 technological revolution. In this investigation, two unique electrical properties have been discovered that present the opportunity to create new high-value applications for AAM. AAM were found to exhibit an unusual electromechanical behavior that makes them a superior smart material for self-sensing structural applications. In addition, AAM were discovered to exhibit exceptionally high dielectric polarization, achieving the highest polarizability reported so-far for an inorganic material. This could revolutionize energy storage technology and lead to high capacity, low-cost energy storage based on AAM technology. The identification of these high-value applications will support the commercialization of AAM and the growth of an AAM industry.

This thesis leverages the unique compositional flexibility of AAM as a category of materials to expand their range of raw materials and optimize their properties for applications in construction and beyond. The specific objectives of this thesis can be defined as follows:

1) Develop a new methodology to valorize bauxite residue as a high-strength AAM.
    a) Explore techniques that can valorize large volumes of bauxite residue without expensive, energy-intensive, or low scalability technologies.
    b) Conduct a compositional optimization to maximize the bauxite residue content in AAM while maintaining sufficient strength to meet construction standards.
2) Identify new applications to serve as a stepping stone to scale up AAM production.
    a) Examine the self-sensing behavior of AAM, investigate its prevalence across a range of compositions, and optimize its performance.
    b) Computationally model the piezoresistivity in AAM to mechanistically explain the origin of its self-sensing properties.
    c) Determine the effect of compositional parameters on the dielectric properties of AAM and optimize the properties for dielectric applications.

The throughline of this thesis is taking advantage of the versatility of AAM to optimize the composition and production processes for different applications. This thesis is, fundamentally, a study of the materials science of AAM, investigating new process-property relationships which are the quintessential backbone of all materials science. The work draws inspiration and methodologies from electrical engineering, civil engineering, and ceramic science to address the challenges facing current AAM technology and propose creative solutions. This thesis is structured into nine chapters. Chapter 1 is a literature review of the current understanding of process-property relationships in AAM, the state-of-the-art in AAM applications, and the challenges currently facing the field. Chapter 2 consists of a summary of the experimental and computational methodologies used to conduct the research for this thesis. Chapter 3-7 address Objectives 1 and 2 in the manner visualized in Figure 0.1.

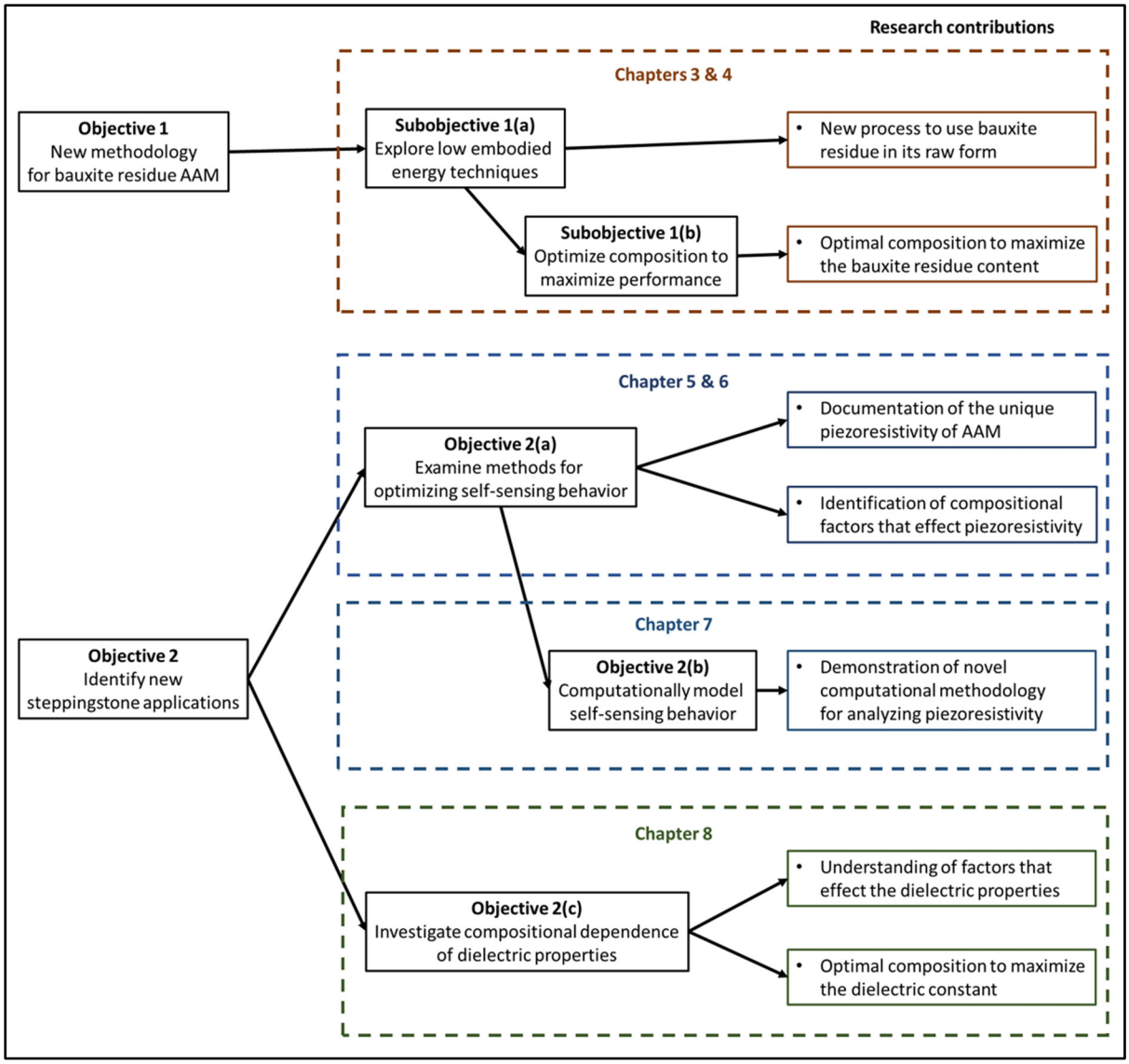

Figure 0.1 Organization of the thesis objectives, research contributions, and chapters.

Chapter 3, Chapter 4, and Appendix I address the remediation of BR as a waste product and describe the research to accomplish Objective 1 of the thesis. Chapter 3 is a published article in the *Journal of Cleaner Production* which describes the development of the novel mixing methodology to transform BR into AAM more effectively and with lower embodied energy than conventional methods. The new technique neutralizes the ecotoxic leaching of transition metals from bauxite residue, making it a suitable alternative to traditional disposal. Chapter 4 continues this research in a communication published in the *Journal of Sustainable Metallurgy*. This publication details the optimum composition discovered for maximizing the content of

BR in high-strength AAM using the new mixing technique. The result of this work describes how to maximize the potential of AAM as a means of mitigating BR waste accumulation while creating a new amply available raw material for AAM production. An additional article on the topic of other methods for valorizing BR in the construction industry was published in *Cleaner Materials*. This publication has been included in the Annex I but excluded from the primary text because it is focused only on cement production, which is outside the scope of this thesis. Interested readers will find this article's quantitative assessment of viability of BR use in cement supplemental to contextualize the advantages of valorizing BR in high proportions in AAM.

The complete citations for the articles in these chapters are listed below:

Di Mare, M., & Ouellet-Plamondon, C. M. (2022). Valorization of unmodified, filter-pressed bauxite residue as a precursor for alkali activated inorganic polymers in a one-part mixing process. *Journal of Cleaner Production,* 135658.

Di Mare, M., & Ouellet-Plamondon, C. M. (2022). High-Strength Construction Material from Raw Bauxite Residue by One-Step Alkali Activation. *Journal of Sustainable Metallurgy, 1-6.*

Di Mare, M., Nattrodt Monteiro, V., Brial, V., Ouellet-Plamondon, C. M., Fortin, S., Tsesmelis, K., & Rosani, D. (2021). A calculator for valorizing bauxite residue in the cement industry. *Cleaner Materials*, *1*, 100009.

Chapter 3 and 4 detail my independent conceptualization of an improved mixing methodology and my investigation of the compositional optimization of BR AAM using this method to maximize its viability and performance. Together, these chapters resolve Objective 1 of the thesis through the invention of an improved process to transform BR into high-strength AAM more effectively and with less energy consumption than traditional methods. The contributions of these works to the scientific literature can be summarized as follows:

- Demonstration of a new process to valorize bauxite residue in its raw form without the need for cost-prohibitive pre-processing techniques;
- Compositional optimization of bauxite residue AAM using the new methodology to maximize the bauxite residue content while exceeding mechanical strength requirements for precast structural members and ensuring neutralization of ecotoxic metal leaching.

Chapters 5-8 address the need to develop new small-volume, high-value applications for AAM and Objective 2 of this thesis. The chapters explore the electromechanical and dielectric behavior of AAM to propose new applications where AAM should be considered as viable alternatives to conventional technology. Chapter 5 is an article that has been published in *Materials Today Sustainability* detailing the discovery of this unique self-sensing property in potassium-based AAM. This article describes how this previously undiscovered property of AAM can be leveraged to create new high-value applications for AAM. Chapter 6 expands upon this topic with the optimization of sodium-based AAM to produce smart, self-sensing construction materials with properties that exceed those of traditional self-sensing materials. These results bring a low-cost and environmentally friendly material solution to the new field of smart construction. This chapter is a journal article currently in peer review with *Construction and Building Materials*. Chapter 7 continues this investigation with the development of a novel computational methodology to quantitatively model self-sensing behavior of AAM and offers a first-look at the underlying mechanisms that cause this uncommon phenomenon. This chapter was published in the *Journal of Physical Chemistry C*. Finally, Chapter 8 concludes Objective 2 with another new application of AAM discovered through an investigation of their dielectric behavior. This article, published in *Materials Today Communications*, details how AAM can be optimized to revolutionize the field of dielectric ceramics and provide a new high-value energy storage application for AAM materials. The complete citations for the published articles of Chapters 5-8 are listed below:

Di Mare, M & Ouellet-Plamondon, C. M. (2022). Highly piezoresistive, self-sensing, one-part potassium activated inorganic polymers for structural health monitoring. *Materials Today Sustainability, 20,* 100261.

Di Mare, M., Inumerable, N., Brisebois, P. P., & Ouellet-Plamondon, C. M. (2022). Combined Experimental and Computational Prediction of the Piezoresistivity of Alkali-Activated Inorganic Polymers. *The Journal of Physical Chemistry C*.

Di Mare, M., & Ouellet-Plamondon, C. (2022). The effect of composition on the dielectric properties of alkali activated materials: A next generation dielectric ceramic. *Materials Today Communications*, *32*, 104087.

Chapter 5-8 present the results of my conceptualization of new high-value applications for AAM and my independent investigation of their electromechanical and dielectric properties. The research demonstrated that with careful compositional optimization, the chemistry and structure can be controlled to give the AAM unusual and valuable properties for a variety of specialized applications. The research contributions of these publications to the scientific literature can be summarized as follows:

- Thorough documentation of the piezoresistivity of AAM and the means for utilizing it self-sensing mechanism for smart construction applications;
- Identification of the compositional factors which effect the self-sensing properties of AAM;
- Demonstration of a novel computational methodology for studying the theoretical self-sensing behavior of materials.
- New understanding of the impact of compositional factors on the dielectric properties of AAM;
- Optimization of an AAM to achieve dielectric constant in excess of 10^9, the highest reported dielectric polarization in the literature.

Additional publications, listed below, that were completed during my doctoral studies on topics outside of the development of AAM have been excluded from this text because their focuses are outside of the scope of this thesis.

Bhojaraju, C., Di Mare, M., & Ouellet-Plamondon, C. M. (2021). The impact of carbon-based nanomaterial additions on the hydration reactions and kinetics of GGBS-modified cements. *Construction and Building Materials*, *303*, 124366.

Bhojaraju, C., Mousavi, S. S., Brial, V., Di Mare, M., & Ouellet-Plamondon, C. M. (2021). Fresh and hardened properties of GGBS-contained cementitious composites using graphene and graphene oxide. *Construction and Building Materials*, *300*, 123902.

Thibaut Nkeumaleu, A., Benetti, D., Haddadou, I., Di Mare, M., M. Ouellet-Plamondon, C., & Rosei, F. (2022). Brewery spent grain derived carbon dots for metal sensing. *RSC Advances*, *12*(19), 11621-11627.

Brisebois, P. P., Di Mare, M., & Ouellet-Plamondon, C. M. (2022, October). Dielectric properties of fly ash geopolymers with two types of potassium activators. In *2022 IEEE Conference on Electrical Insulation and Dielectric Phenomena (CEIDP)* (pp. 491-494). IEEE

This thesis addresses Objectives 1 and 2 to answer the fundamental research question and improve the prospects of commercializing AAM. The results demonstrate a means for circumventing the competition for raw materials which currently limits the growth of AAM production. This is accomplished through a new technique for valorizing a highly available raw material, bauxite residue, as a high-strength AAM. The thesis continues by discovering new means to create green material alternatives for smart construction and energy storage applications from AAM. The work accomplishes this through the discovery of a latent self-sensing property in AAM and the optimization of AAM to maximize their piezoresistivity and polarizability. The study was limited in the characterization of AAM to understand the nature of these properties in AAM. There is an absence of suitable techniques in the field capable of analyzing the mechanistic origins of the electrical, dielectric, and electromechanical behavior of AAM. Conventional nuclear magnetic resonance-based analysis to correlate AAM compositions with bonding coordination was not possible due to the high content of iron in both the bauxite residue and fly ash used to produce AAM. Future studies may be capable of building upon the results of this thesis once improved characterization methods have been developed. Readers who wish to focus on the highlights and critical results of this research are encouraged to start with the literature review in Sections 1.2.5, 1.3.2, 1.3.3, and 1.4 of Chapter 1 and the discussion of the results of the thesis presented in Chapter 9.

CHAPTER 1

LITERATURE REVIEW

This literature review is structured in four parts to provide a background on alkali activated materials (AAM) and a context for the improvements presented in Chapters 3-8. AAM are a sustainable binder technology discovered only a few decades ago and the intricacies of their chemistry remains a topic of continued study. Section 1.1 presents a brief history of AAM and the evolution of both the terminology used to describe them and the present understanding of their chemical structure. Early on, AAM were recognized as means to create a more circular economy for metallurgical wastes and other industrial by-products. Section 1.2 summarizes the state-of-the-art in terms of raw materials and conventional methods for producing AAM. The section concludes with a review of the current methods for producing AAM from bauxite residue the limitations therein which this thesis seeks to improve upon in Chapter 3 and 4. With the production methods established, Section 1.3 continues by the state-of-the-art for the applications under investigation in this thesis. Sections 1.3.2 discusses the conventional materials used for self-sensing and dielectric applications and the very limited research that has been done to apply AAM in these applications. Chapter 5-8 address these research gaps and demonstrate how AAM can combine superior properties and sustainability to improve upon the state-of-the-art. Section 1.4 concludes the literature review with a discussion of the current shortcomings of AAM technology and how this thesis intends to address them.

1.1 The fundamentals of alkali activated materials

1.1.1 Definition and history

Alkali activated materials (AAM) are amorphous aluminosilicate solids. They are formed when the dissolution of an aluminosilicate raw material in an alkali solution causes a recrystallization reaction to precipitate a polymer containing an aluminum oxide (alumina) and silicon oxide (silica) backbone. AAM represent a broad category of materials that are defined

not by crystallography or physical properties, but instead by the raw materials used to make them and the chemical reaction that causes them to harden into a solid. In the literature, the terms “alkali activated materials,” “inorganic polymer,” and “geopolymer” are, by some authors, used interchangeably. However, they refer to overlapping categories of materials with similar characteristics but produced from different raw materials and, consequently, have slightly different chemistry. Geopolymer is the narrowest category, defined to contain only pure aluminosilicate polymers. The term geopolymer is typically used when the material is derived from chemosynthetic sources or high-purity calcined clay, particularly metakaolin. Due to their purity, geopolymers are modeled as pure sodium – aluminum – silicon – hydrate (NASH) gels, though the sodium can be substituted for other alkali metals.

The term “inorganic polymers” is used for similar materials from lower purity raw materials that contain considerable amounts of calcium and other transition metals. Most commonly, inorganic polymers are formed from industrial by-products that are rich in reactive alumina and silica phases. The calcium, and to a lesser extent other metals, substitute with the sodium in the polymer creating so-called N/CASH gels. The difference in coordination between calcium and sodium causes N/C-A-S-H gels to have greater disorder and degree of crosslinking than NASH gels. This has been observed to cause some differences in the chemistry and properties of inorganic polymers compared to geopolymers. Since inorganic polymers can be synthesized from by-product sources, these materials are the most relevant to applications with low environmental impact and circular economy valorization of waste materials.

“Alkali activated materials” (AAM) is a superset encompassing geopolymers, inorganic polymers, and some hybrid cements. By this definition, AAM refers to any material which is formed through an alkali activated recrystallization reaction, whether the product is composed primarily of NASH, N/CASH, or a blend of N/CASH and CSH (calcium – silicon – hydrate) gels. For the purposes of this thesis, the preferred terminology will be alkali activated materials or, where appropriate, alkali activated inorganic polymers. The definitions of these terms has evolved over time and the convention adopted in this thesis is in accordance with the publication by van Deventer (2007) which is generally accepted in the community (van Deventer, Provis, Duxson, & Lukey, 2007).

At the time of their inception, all AAM were first known as “mineral polymers.” Joseph Davidovits is widely considered to be the modern father of AAM. His discovery of them in the late 1970s (Joseph Davidovits, 1991) and his early patent (Joseph Davidovits, 1982) on their methods created a new field of room temperature curing materials. They were developed in an investigation of fire-resistant wood laminates but grew rapidly into an emerging field for various applications (Joseph Davidovits, 1994). To this day, much of the academic literature on AAM is based on Davidovits’ work. In the earliest works, Davidovits reported that kaolin clay which had been thermally treated above its decomposition temperature will react with caustic aqueous solutions to form a high-strength solid. From these observations, he proposed a conceptual model for a polycondensation reaction into a hydroxysodalite ceramic. Calcined kaolin clay, now more commonly called metakaolin, continues to be the most studied precursor material for geopolymers and hydroxysodalite structures remain the backbone of many modeling approaches.

AAM are most commonly compared to Portland cement because of their physical properties and the methods used to produce them. Like cement, AAM have a liquid-like intermediate state where they can be easily cast into various shapes. Their recrystallization reaction causes them to harden at room temperature without the need for sintering or pressing, and their final mechanical properties typically meet or exceed that of cement. AAM have been heavily investigated as an alternative for use in conjunction with, in so-called blended cements, or complete replacement of Portland cement. Early commercial installations headed by Davidovits demonstrated a significant advantage of AAM over Portland cements in the form of their rapid strength development (Joseph Davidovits, 2002b). This commercial AAM was known to reach a compressive strength of 20 MPa in as little as four hours, significantly faster than Portland cement. In addition, the AAM exhibited superior thermal stability, improved fire retardance, and substantially reduced environmental impact. These early studies and successes by Davidovits inspired an entire field of materials science focused on the development and application of AAM.

1.1.2 The chemistry and modeling of alkali activated materials

AAM are defined by the raw materials that they are produced from and the recrystallization reaction which causes them to harden from a liquid paste into a high-strength solid. The recrystallization reaction is composed of a series of dissolution, condensation, and polymerization reactions which consume the reactive alumina and silica sources in the raw material to yield the final AAM product. Much like the chemical reactions involved with Portland cement, the chemistry of alkali activation is complicated and not completely understood. In contrast to the hypotheses of early authors, it is now known that AAM undergo multiple reactions during synthesis as the paste transforms to an amorphous material with a variable degree of nanocrystallinity (Joseph Davidovits, 1994 ; Provis, Palomo, & Shi, 2015). The sequencing of the reactions is shown in Figure 1.1. Many studies have been conducted in an effort to quantify the different stages of these reactions and attribute the effects to the properties of the resulting AAM. Understanding the governing mechanisms of the chemistry may help to inform the compositional and process optimization required to synthesize high-quality AAM from a wider range of raw material sources. However, it was not until recently with the development of magic angle spinning nuclear magnetic resonance, time-resolved infrared spectroscopy, and pair distribution theory x-ray diffraction that accurate characterization could be conducted on the transient AAM paste as it evolves (Provis et al., 2015 ; Shi, Qu, & Provis, 2019).

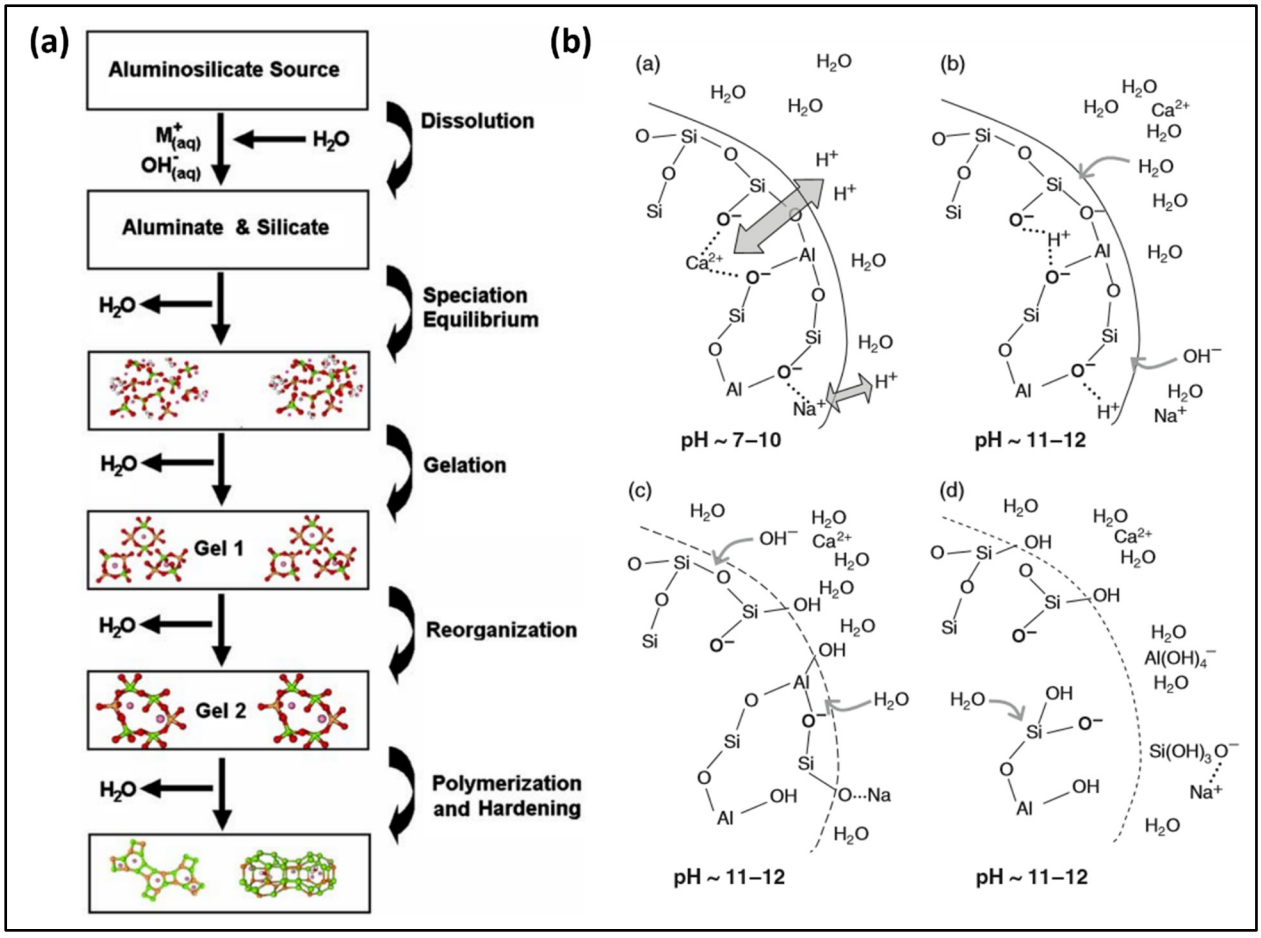

Figure 1.1 (a) A process flow diagram of the alkali activation reactions to highlight the sequencing of the reactions through different stages, adapted from Duxson et al., 2007. (b) A visualization of how the alkaline activator solution interacts with the surfaces of precursor particles through the series of alkali activation reactions, adapted from Duxson & Provis (2008)

The first stage of the alkali activation reaction is the dissolution of aluminum and silicon into the alkaline solution of the paste. High paste pH is essential for the dissolution of aluminum and silicon as the solubility of these species at neutral pH is very low (Duxson & Provis, 2008). In principle, the dissolution of aluminum and silicon occurs simultaneously. However, in most cases the rate of aluminum dissolution is sufficiently higher, causing the paste in the early stages of reaction to be dominated by aluminate compounds. The dissolved silicon content gradually increases until the paste becomes dominantly silicate in composition (Dyson, Richardson, & Brough, 2007 ; Provis et al., 2015). The relative rates of the aluminum and

silicon increase in the paste effect the rate of strength development in the paste. If silicon dissolution is sufficiently slow, the alkali activation reactions will consume the paste water before all of the silicon has been dissolved (Duxson et al., 2007). This will result in an AAM with inhomogeneities of unreacted silicon oxide phases. This is especially relevant in cases where supplemental silicon oxides are added as an additional additive to modify the geopolymer composition.

Many physical and chemical parameters influence the dissolution rate of aluminum and silicon. The easiest controlled is the alkalinity of the reacting solution, which can be increased to accelerate both reactions. More subtly, the phases present in the aluminosilicate raw material play an important role in controlling the dissolution kinetics. Highly crystalline materials are slow to dissolve compared to amorphous counterparts of equal elemental composition. To control the dissolution, thermal pretreatments of raw materials can be used to reduce crystallinity. This is particularly important with AAM derived from clays, as discussed in Section 1.1.3. Reducing the crystallinity requires oxide decomposition typically above 600ºC, in a process commonly called calcination. Excessive heating, above 1000ºC, can cause recrystallization into stable phases which reduces the dissolution kinetics (Badogiannis, Kakali, & Tsivilis, 2005 ; Granizo & Blanco, 1998). For AAM derived from industrial by-products, the crystallinity is a function of the processing temperatures in the production facility which cannot be controlled. Differences in crystallinity are a significant contributor to the differences between AAM from different raw material sources. Other factors include physical parameters such as the particle size distribution and morphology which can affect the accessibility of the phases to the alkaline solution, retarding their dissolution.

Since the early studies by *Davidovits*, AAM have been known to be composed of NASH and N/C-A-S-H gels, but the exact structure of these compounds is not rigorously defined. Once the content of aluminate and silicate monomers within the paste has reached a critical level, interactions between them drive the formation of aluminosilicate complexes. Recent developments in nuclear magnetic resonance and infrared spectroscopy now enable time-resolved characterization of the change in coordination of these oligomers as the short chains of monomers polymerize and cross-link depending on the composition of the paste (Fernández-Jiménez & Palomo, 2005, p. ; W. K. W. Lee & van Deventer, 2003 ; Rees, Provis, Lukey, &

van Deventer, 2007). In a process analogous to Portland cement, a silicon hydrate gel forms as the oligomers react. However, unlike Portland, where calcium silicon hydrates (C-S-H) form, AAM include aluminum and sodium in the polymer chemistry.

Sodium/calcium aluminum silicate hydrate chains (N/C-A-S-H) can be observed by pair distribution function assisted X-ray and neutron diffraction (Meral, Benmore, & Monteiro, 2011 ; White, Provis, Bloomer, Henson, & Page, 2013 ; White, Provis, Llobet, Proffen, & Deventer, 2011). This N/C-A-S-H gel is modeled to have greater stability than C-S-H gels, which may explain AAM's enhanced chemical resistance compared to Portland cements (Duxson et al., 2007 ; Garcia-Lodeiro, Palomo, Fernández-Jiménez, & Macphee, 2011). The type of gel which forms is a function of the elemental composition of the raw material used to produce the AAM. Figure 1.2 illustrates, on a ternary phase diagram, the composition of the most common types of AAM derived from fly ash (FA) and blast furnace slag (GGBS), compared to Portland cement (OPC). Fly ash AAM are typically categorized as having either high or low calcium, which can be seen in Figure 1.2 to influence the position of the phase diagram significantly.

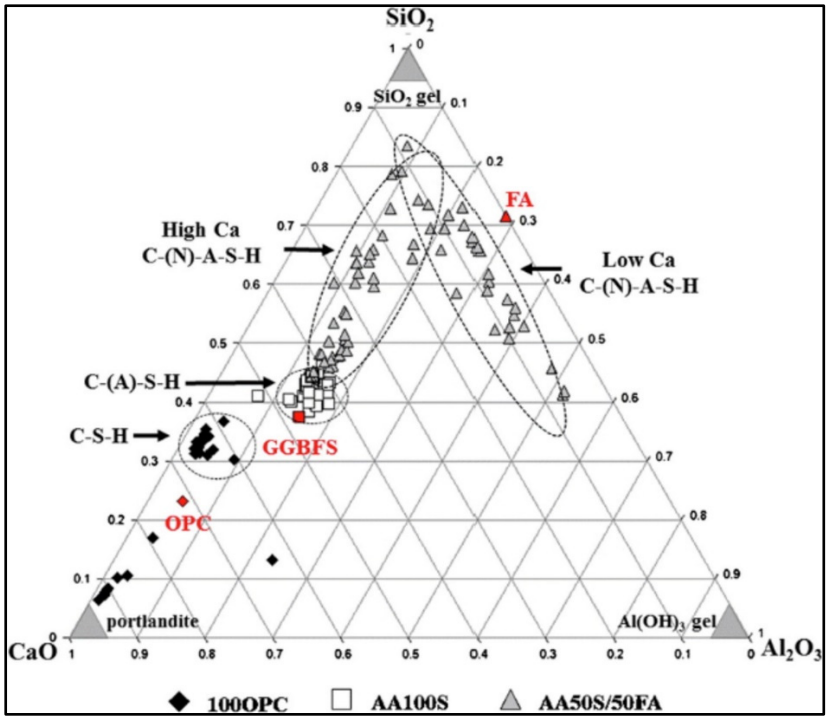

Figure 1.2 Ternary phase diagram of aluminum, silicon, and calcium oxides with approximate compositional regions of different gel phases circled, adapted from Puertas et al. (2011)

The presence of impurities is also known to have a significant effect on the chain structure of the gels which evolve in the AAM paste. Alkali earth metals, typically impurities of calcium and magnesium, have a network modifying effect on the polymer. The divalent cations prefer to coordinate with bridging oxygens, which limits the crosslinking of the polymer chains (Susan A. Bernal et al., 2014 ; Susan Andrea Bernal, 2016). Iron, another common impurity in precursors, has been observed to act as a network former, creating crosslink sites (Daux, Guy, Advocat, Crovisier, & Stille, 1997). As with the considerations for aluminum and silicon within the precursor, the presence of alkali earth and iron impurities are subject to the same variations caused by the chemical and physical attributes of the phases and particles in which the impurities are present. As such, strictly elemental analysis is insufficient for predicting the behavior of these impurities. In some cases, the impurities may be in the form of unreactive phases or precipitate out of the paste into discrete oxide phases and have little effect on the AAM (Keyte, Lukey, & van Deventer, 2005).

The development of new understanding of the structure of AAM will lead to better prediction of how to manipulate the properties of AAM. This understanding is limited by the difficulty to model the form of the N/C-A-S-H gel that develops in an AAM and how the structure of this gel is influenced by different compositional factors. Different models for the evolution of the N/C-A-S-H gel have been proposed with varying degrees of success. Some models build on early works using hydroxysodalite structures similar to the initial models proposed by Davidovits shown in Figure 1.3(a). In this type of model, the ratio of silica to alumina tetrahedra and the type of alkali activator can be seen to have a dramatic impact on the structure of the AAM. Other models are based upon clays or other minerals that have been modified to match the elemental composition of an AAM. An example is shown in Figure 1.3(b) of a AAM structure based on a modified version of the hydrated tobermorite unit cell (Myers, Bernal, San Nicolas, & Provis, 2013). These mineral-based models have been used to predict the stability of different forms of NASH and N/CASH gels hypothesized to form during the alkali activation reactions (Garcia-Lodeiro et al., 2011 ; Puertas et al., 2011).

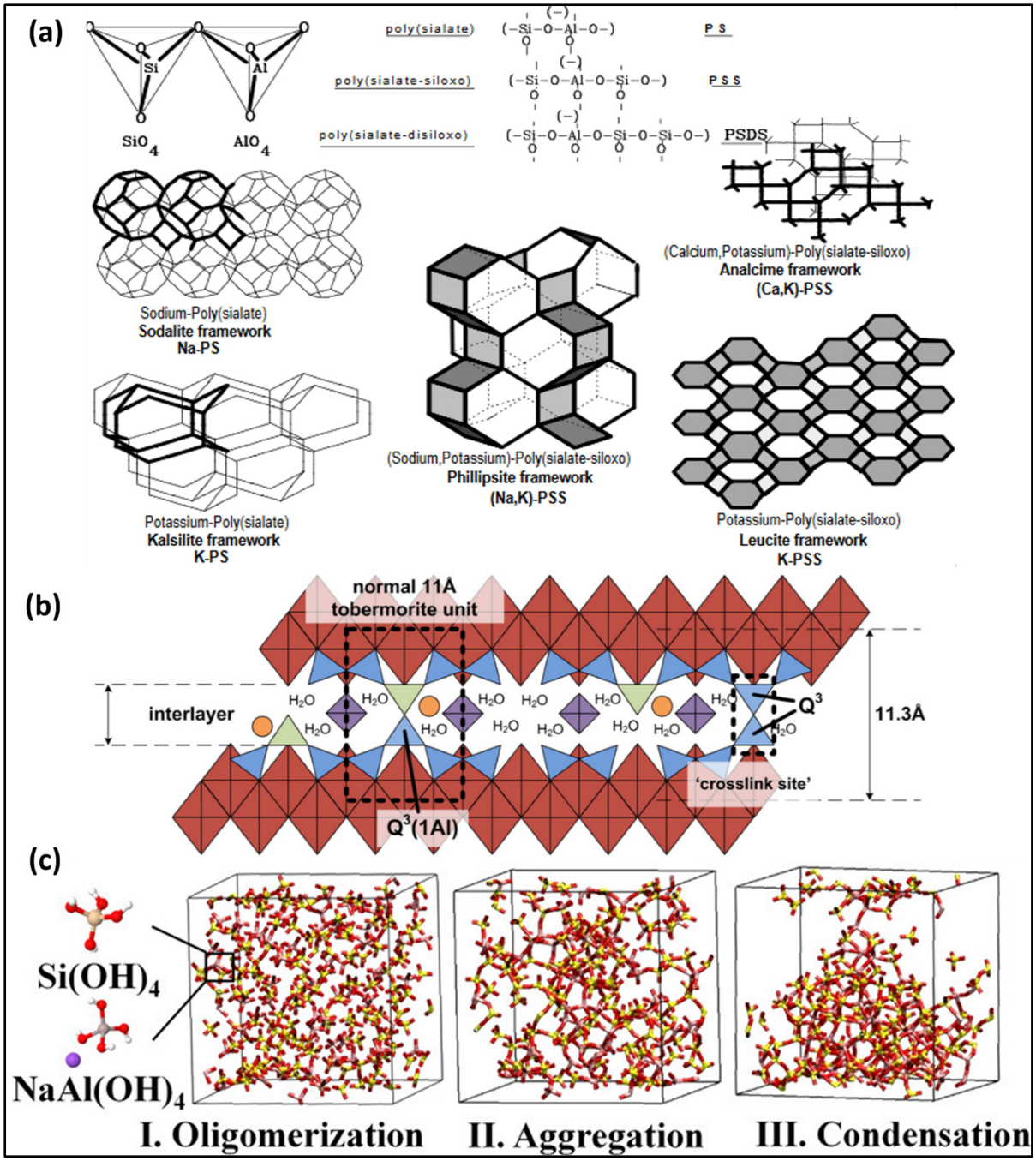

Figure 1.3 The evolution of modelling of the amorphous structure of AAM: (a) an early model based on ceramics with the same elemental composition, adapted from Joseph Davidovits (1994*)*, (b) a model based on a modified clay (tobermorite) unit cell, adapted from Myers et al. (2013), and (c) a modern molecular dynamics simulation of an AAM structure from M. Zhang, Deskins, Zhang, Cygan, & Tao (2018)

Recent advancements in computational processing capabilities have made it possible to improve the models of AAM structures. The interactions between alumina and silica tetrahedra in the presence of water and alkali cations can be modeled using molecular dynamics software. In principle, this technique can provide a significant improvement in the accuracy of AAM structural models and enhance the understanding of the connection between the composition and structure of an AAM an its macroscopic properties. This is an area of ongoing study in the field and, to date, only a handful of publications have reported molecular dynamics simulations of AAM structures. The example of one such study is shown in Figure 1(c). Molecular dynamics simulations of AAM require the modeling of thousands of atoms through multiple stages of oligomer formation and crystallization reactions to form a final amorphous gel. The number of atoms required to accurately simulate N/C-A-S-H gel formation continues to create a computational bottleneck. Only a few studies have investigated the effect of compositional factors (e.g. silicon to aluminum ratio) on the AAM structure using molecular dynamics (Sadat, Bringuier, Asaduzzaman, Muralidharan, & Zhang, 2016). No study has yet used a computational AAM model to successfully predict a macroscopic property of the AAM. This thesis will address this topic by using an AAM model generated with molecular dynamics that was published in a recent publication by Zhang et al. (2018), to predict the electromechanical behavior of AAM and confirm this property experimentally.

1.2 Production methods for alkali activated materials

1.2.1 Precursors

Fundamentally, an AAM is composed of three components, an aluminosilicate-rich raw material, known as the "precursor," an "activator" to create an alkaline solution, typically a sodium salt, and water. The choice of precursor has a great effect on the resulting AAM. Many precursor parameters are influential on the material's final properties. This includes chemical properties, such as elemental composition and the presence of impurities, as well as physical chemistry considerations, such as precursor particle size, phases of different constituents, and degree of crystallinity of key phases (Duxson et al., 2007 ; Duxson & Provis, 2008 ; Luukkonen, Abdollahnejad, Yliniemi, Kinnunen, & Illikainen, 2018). However, due to the

variability in supplies of both relevant natural and by-product raw materials used for AAM, precursors are generally grouped into a discrete number of categories. This simplifies the discussion of suitable precursors but introduces a range of performances for each type of precursor. The impact of these variations in the context of the physical phenomena will be discussed in detail in Section 1.2.2.

AAM can be synthesized from virgin raw materials or industrial by-products. Metakaolin is the most common virgin raw material studied (Kriven, Bell, & Gordon, 2003 ; Yunsheng, Wei, & Zongjin, 2007). Metakaolin is derived from natural kaolin clay which is heated to 700ºC and then cooled quickly, sometimes with quenching, to preserve the glass-like phase composition achieved at high temperatures. Kaolin, like all clay materials, consists of alternating atomic planes of aluminum in silicon. For natural kaolin, the silicon is tetrahedrally coordinated, and the aluminum is octahedrally coordinated at an elemental ratio of 1. The calcination treatment to 700ºC causes a change in the oxygen coordination of aluminum to change to 5-fold (Badogiannis et al., 2005 ; Granizo & Blanco, 1998). This reduces the crystallinity of the kaolin clay, increasing the solubility of the metal and the kinetics of the alkali activation reaction.

Metakaolin has been heavily studied in the field of AAM since its inception. Original work by Davidovits used metakaolin and many researchers have demonstrated techniques for improving its performance in AAM. In the field of AAM, metakaolin is often taken as a reference precursor. Alkali activated metakaolin is often referred to as a geopolymer to indicate that it is free of impurities found in other precursors and thus forms nearly perfect NASH polymer chains. Only a few geopolymer studies have been conducted on purely synthetic aluminosilicate precursors, synthesized from chemically pure aluminum and silicon sources (Catauro, Bollino, Cattaneo, & Mustarelli, 2017). In theory, purely synthetic precursors would enable a more fundamental characterization of the impact of different precursor parameters on AAM properties. However, kaolin is highly available worldwide and the closest naturally occurring high purity, high reactivity precursor, which has standardized it as a reference precursor. The performance of metakaolin-based geopolymers is among the best reported in the literature (Duxson & Provis, 2008 ; Provis et al., 2019). AAM from different precursors are compared to metakaolin equivalents as a metric of their performance.

The vast majority of research on AAM is derived from clay using a calcination process to create amorphous phases in the clay and improve the reactivity of the precursor. However, the calcination process has been identified as a limitation to the economic viability of AAM due to the high energy cost and environmental impact. A small number of studies have attempted to produce AAM from un-calcined clay, but the results have yielded low mechanical results (Marsh, Heath, Patureau, Evernden, & Walker, 2018). The more common solution is to utilize industrial by-products which have already undergone some degree of calcination during their production as precursors for AAM. Many waste materials or by-products of manufacturing and energy generation contain elemental composition which is close to or suitable for AAM synthesis (Duxson et al., 2007 ; Duxson & Provis, 2008). The most prominent industrial by-products which meet these criteria are coal fly ash and blast furnace slag. Fly ash is a waste product of bituminous coal combustion which is captured in the gaseous effluent of the combustion process. It is called fly ash because it is composed of very fine particles that are captured in the particulate filtration system of exhaust gases. The source of these un-combusted particles is, primarily, clay impurities in the coal which have been exposed to extreme temperatures in the combustion process. This results in amorphous aluminosilicate particles of low particle size and low crystallinity, but varied chemical composition, as they mix with the concentrated alkali and heavy metal impurities from large volumes of coal.

As with all industrial by-products, the precursors are subject to great variation based on the operating conditions of the producing facility. This is especially true for fly ash which can exhibit extreme compositional changes based on the geographical sourcing of the coal. Among fly ashes, two subcategories exist labeled Class C and Class F (Luukkonen et al., 2018). Class C fly ashes are high calcium minerals, up to 10wt%, whereas Class F is low in calcium. Class F is more commonly studied in the literature, but the few studies conducted on Class C fly ashes yield greater performance (Keyte et al., 2005 ; Perera, Nicholson, Blackford, Fletcher, & Trautman, 2004). This has been attributed to the impact of the free calcium, the impact of which on precursor performance will be discussed in Section 1.2.2.

The other common by-product precursor is blast furnace slag. This is a metallurgical slag produced as float-waste from the blast furnace of iron refinement. It is separate from the metallic melt and represents a coalescence of the clay and mineral impurities in the iron ore.

Though, like fly ash, the properties of the blast furnace slag vary due to the source of the ore and the operational conditions of the blast furnace, this slag is known to have a relatively good consistency and produce AAM of good reproducibility across different geographical sources (Duxson & Provis, 2008). Blast furnace slag-based AAM generally outperform fly ash and other industrial by-product equivalents. Their mechanical strength development is more similar to, though lesser than, metakaolin-based geopolymers. A comparison was presented in a recent publication, summarized here in Figure 1.5. The data shows that the strength, performance homogeneity, and rate of strength development are greater for metakaolin and slag AAM compared to those of fly ash.

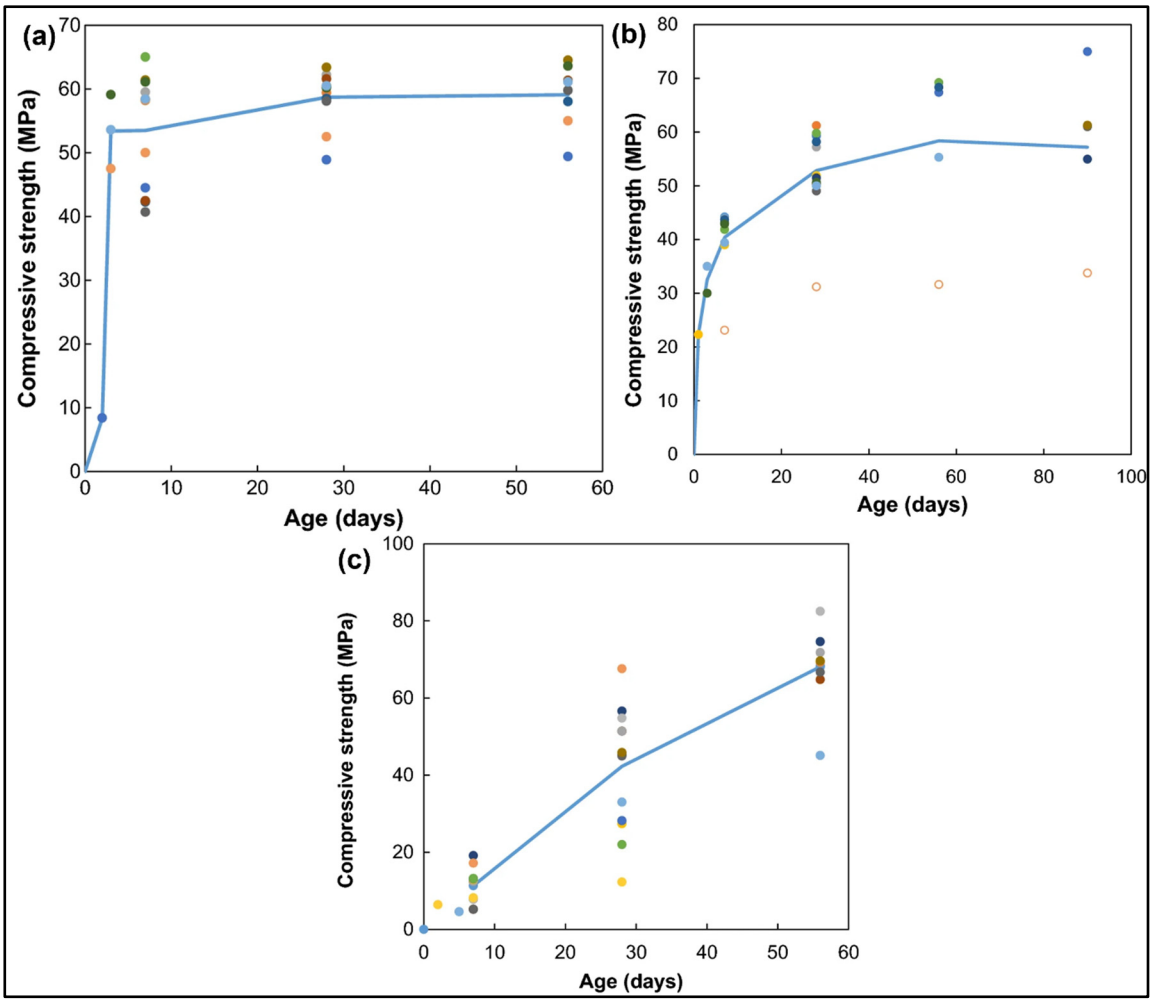

Figure 1.4 Literature example comparison of the compressive strength and rate of strength development of AAM from different precursors: (a) metakaolin, (b) blast furnace slag, and (c) fly ash, adapted from Provis et al. (2019)

In recent decades, a growing scarcity of high-quality fly ash and blast furnace slag has led to an increased focus on developing methods to utilize other industrial by-products as precursors for AAM. Many new by-products, referred to as emerging precursors, have been studied to use AAM production as a waste mediation technique to valorize by-products that are unsuitable for reuse in other applications (Provis et al., 2015). Many studies have focused on by-products that are similar to traditional precursors, such as bottom ash from coal power plants, and other metallurgical slags (S. Kumar, García-Triñanes, Teixeira-Pinto, & Bao, 2013 ; Sarkar, Basu, & Samanta, 2017 ; Sathonsaowaphak, Chindaprasirt, & Pimraksa, 2009 ; Topçu & Toprak, 2011). Other researchers have turned to agricultural by-products, such as ash from the incineration of rice and corn husks (Barbosa, Foletto, Dotto, & Jahn, 2018 ; Hajimohammadi & van Deventer, 2017). AAM have even been studied as a means to valorize unrecyclable glass waste from municipal recycling plants (Pascual, Tognonvi, & Tagnit-Hamou, 2014 ; Walther, Feichtenschlager, & Zhou, 2017). The use of emerging precursors presents new opportunities to reduce the disposal of waste products and create greener AAM materials.

The ideal emerging precursors balance high availability, high aluminum and silicon contents for the AAM chemistry, and high reactivity of these aluminosilicate phases. Many researchers have identified mineralogical wastes as containing two of these three qualities: high availability and ideal elemental composition. Mine tailings are a large volume mining waste with no suitable application for reuse. Various types of mine tailings have been demonstrated to be potential AAM precursors (Duan, Yan, Zhou, & Ren, 2016 ; Jiao, Zhang, & Chen, 2013 ; L. Zhang, Ahmari, & Zhang, 2011). Bauxite residue has drawn similar attention as a large volume waste and has shown promise as a potential precursor (X. Chen et al., 2019 ; Hajjaji et al., 2013 ; Ye et al., 2014). The state-of-the-art for producing AAM from bauxite residue is discussed in detail in Section 1.2.4. The principal obstacle for both mine tailings and bauxite residue as precursors is that these wastes have not undergone a high temperature process during their production and, thus, their aluminosilicate phases have not been decomposed into amorphous phases. These uncalcined emerging precursors are plentiful but have low reactivity during alkali activation because their aluminum and silicon bearing phases are unable to fully dissolve.

1.2.2 Alkali activators

The alkali activation reactions require the mixing of a suitable precursor in a highly alkaline solution. This solution is made by dissolving a soluble alkali metal salt, called the activator, in water. Since the original work by Davidovits, sodium silicate, also known as waterglass, has been the most studied activator (J. Davidovits, 1991). The activator raises the pH of the paste, which increases the solubility of aluminum and silicon from the precursor, and supplies alkali metal ions which charge balance the N/C-A-S-H gel. Sodium salts are by far the most common activators used because of the lower cost and higher availability compared to other alkali metals. However, AAM have also been created using potassium and cesium activators, which achieves different chemistry and physical properties (Bell, Driemeyer, & Kriven, 2009a ; Hosan, Haque, & Shaikh, 2016). The quantity and type of activator influence the structure of the gel network and ultimately the amount of crosslinking in the AAM (Duxson et al., 2007 ; van Deventer et al., 2007). The activator is a controlled parameter in AAM design that is optimized in type and quantity to achieve the desired properties.

Table 1.1 Examples of alkali activators and a comparison of their advantages

Activator	Physical form	Advantages	Disadvantages
Sodium silicate	Aqueous solution	Most common activator. Facile modification of Sodium / Silicon ratio.	Environmental impact.
Sodium hydroxide	Aqueous solution or anhydrous powder	Can be used in conjunction with sodium silicate. Compatible with one-part mixing processes.	Low commercial availability. Highly caustic.
Sodium carbonate	Anhydrous powder	Environmental impact. Compatible with one-part mixing processes.	Lower solubility. Slower strength development of AAM.
Sodium sulfate	Anhydrous powder	Environmental impact.	Limited compatibility with alkali activation. Low strength AAM.
Sodium aluminate	Anhydrous powder	Facile modification of Silicon / Aluminum ratio.	Only compatible with high-silica content precursors.
Potassium silicate	Aqueous solution	Facile modification of Potassium / Silicon ratio.	Environmental impact.
Potassium hydroxide	Aqueous solution or anhydrous powder	Rapid curing and strength development of AAM.	Lower strength than sodium equivalents.
Potassium carbonate	Anhydrous powder	Advantages not established.	Low strength AAM. Environmental impact.

The anion in the activator salt is critical in controlling the physical properties of the resulting AAM. Sodium silicate can be prepared with a range of sodium to silicon ratios by mixing and dissolving silicate sources in sodium hydroxide solutions. This provides an avenue for bolstering the reactive silica content within the AAM. Added silica generally improves the AAM's density and mechanical properties and it is particularly important in the use of lower-quality emerging precursors (Joseph Davidovits, 2002b ; Duxson et al., 2007 ; Tchakouté, Rüscher, Kong, Kamseu, & Leonelli, 2016). The most common activator is a blend of sodium silicate and sodium hydroxide to achieve a targeted pH and silicon content in the activating solution. Alternative activators can be used for different effects. Sodium aluminate has been

used as an activator with some emerging activators that are high in silica but low in alumina, such as rice husk ash, to achieve a comparable effect as sodium silicate (Hajimohammadi & van Deventer, 2017 ; Sturm, Greiser, Gluth, Jäger, & Brouwers, 2015 ; Ye et al., 2016). The use of other sodium salts that are naturally occurring, such as sodium carbonate and sodium sulfate, have been identified as alternatives to reduce the environmental impact of AAM (Susan Andrea Bernal, 2016 ; Ouellet-Plamondon & Habert, 2015). While some studies have shown good results with these activators, their lower solubility has been found to retard alkali activation reactions and necessitate a re-optimization of the curing conditions to achieve high-strength materials (Susan A. Bernal, Provis, Myers, San Nicolas, & van Deventer, 2015 ; Susan Andrea Bernal, 2016 ; Ke, Bernal, & Provis, 2016 ; N. Li, Shi, & Zhang, 2019).

1.2.3 Compositional dependence of properties

The properties and microstructural qualities of AAM can be influenced by the composition of the AAM. AAM represent a broad range of materials from different raw materials sources and compositions. Their properties are dependent on its microstructure which is strongly influenced by the compositional design of the AAM and the processing techniques used to produce them. As previously mentioned, the elemental composition of a precursor is not always a good indicator as the crystallinity and dissolution kinetics can dramatically influence the reactivity during alkali activation. This has led to a similar variation in best practices for designing the composition of an AAM depending on the precursor and activator used. The properties of an AAM are largely subject to the synergy between the precursor, activator, and composition.

Many studies have been conducted to characterize the microstructure of AAMs after curing to understand the influence of different composition and processing parameters on the material's properties and predict the long-term properties. The microstructure can vary significantly for different precursors (Myers et al., 2013). Clay-based AAM, particularly metakaolin, exhibit a significantly different microstructure than by-product-based equivalents. Metakaolin AAM have a higher content of mesopores, which can be observed by scanning electron microscopy and mercury intrusion porosimetry (Collins & Sanjayan, 2000). This results in a higher

permeability for these AAM which lowers their chemical resistance and durability (Hassan, Arif, & Shariq, 2019). Despite the greater porosity, metakaolin-based AAM exhibit exceptionally high mechanical properties (Provis et al., 2019). An example comparison of metakaolin and by-product-based AAM is shown in Figure 1.6. Metakaolin AAM, shown in Figure 1.6(b,d), exhibit a more platelet-like structure compared to the spherical fly ash AAM in Figure 1.6(a,c). This difference in microstructure from the precursor has been attributed to the plate-like crystal structure of metakaolin as a calcined clay which is partially preserved after the precursor transforms into an amorphous AAM (Duxson & Provis, 2008 ; Hassan et al., 2019).

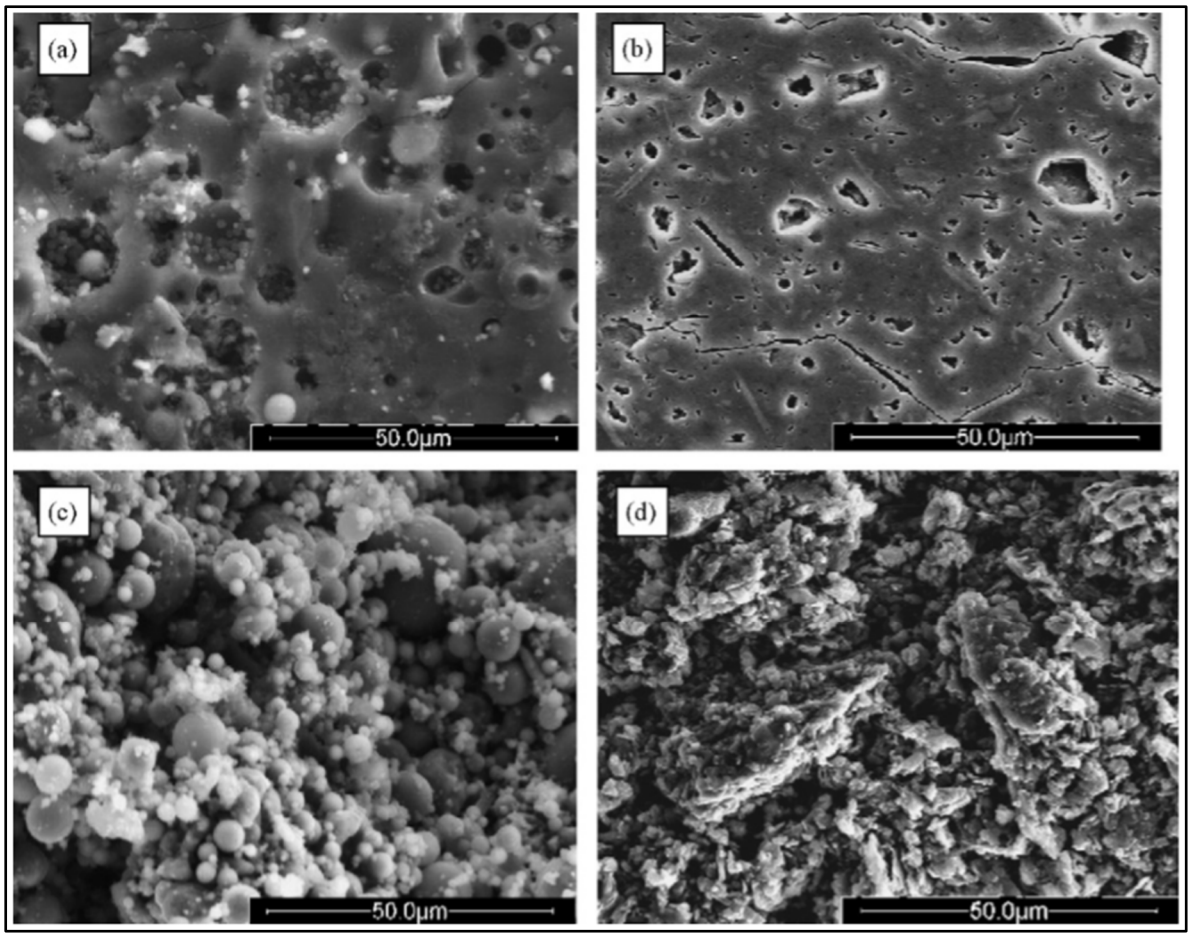

Figure 1.5 Scanning electron micrographs of fly ash (a,c) and metakaolin (b,d) AAM, active with (a,b) sodium silicate or (c,d) sodium hydroxide. Adapted from van Deventer et al. (2007)

Among industrial by-product precursors, the principal drivers for microstructural differences are crystallinity and impurities. Depending on the degree of crystallinity, the physical and chemical nature of precursors can lead to different rates of solubility of the phases present which can affect the transient gel chemistry and, consequently, the final microstructure. In some cases, incomplete dissolution or rapid curing leaves some phases of the precursor unreacted. This can lead to unintended discrepancies between the targeted elemental composition and the achieved composition of the AAM. High quality precursors, such as fly ash, dissolve and decompose uniformly to form a homogenous paste (Fernández-Jiménez, Palomo, & Criado, 2005). There has been a concerted effort to develop methods to improve the reactivity of lower quality precursors to expand the availability of precursors through calcination to reduce crystallinity. This is discussed in detail in Section 1.2.3.

Alkali earth metals, namely calcium and magnesium, are the most common impurities which vary between precursors and influence the microstructure. This is most commonly studied in the context of fly ashes which are categorized as Class C or Class F based on their calcium content. Class C, called high-calcium fly ashes, can contain up to 10% calcium oxides and have been observed to rapidly solidify and cure during alkali activation. This phenomenon has been attributed to the early precipitation of calcium hydroxide within the paste which gives it its early strength development (W. K. W. Lee & van Deventer, 2002). The content of alkali earth ions in the AAM paste modifies this gel network structure. Compared to Portland cement, where C-S-H gels form, the N/C-A-S-H gels in AAM have been observed to have longer chain lengths. This corresponds to a denser microstructure than is typically achieved in Portland cement (Puertas et al., 2011). This characterization correlates well with mercury intrusion porosimetry which measures a shift in the mesopore size between 10-100 nm in Portland cement to below 20 nm in AAM (Collins & Sanjayan, 2000).

Another mechanism by which the microstructure can be modified is through the addition of inorganic additives. Supplemental sources of reactive silica or alumina can be added through the activator to change the chemical composition of the AAM and change the gel structure. This aspect of the composition is often discussed as a proportion of silica to alumina or silicon to aluminum (Si/Al ratio). Many authors have concluded that a Si/ Al ratio of approximately 2 is preferred for synthesizing high-strength AAM (Luukkonen et al., 2018). This ratio is

typically achieved by adding sodium hydroxide and/or silicon oxides into a solution of sodium silicate to achieve certain sodium-to-silicon ratios. The effect of supplemental silica addition can be seen on the microstructure of the AAMs in Figure 1.6. This figure shows the micrographs of fly ash and metakaolin AAM activated with sodium hydroxide (no added silica) in Figure 1.6(a,c) and sodium silicate (added silica) in Figure 1.6(b,d). With both precursors, the addition of silicon results in a denser and more homogenous microstructure. The addition of supplemental aluminum, such as from the use of sodium aluminate, has received some attention but the current understanding of the impact of this additive is incomplete (Hajimohammadi & van Deventer, 2017 ; Sturm et al., 2015). The change in microstructure has a significant impact on the mechanical properties of the AAM. The mechanical properties are known to be significantly influenced by the Si/Al ratio and the activator content, which is often quantified by the Na/Al ratio, or K/Al ratio for potassium activators. The mechanical properties, such as the compressive strength, can be optimized by varying these two parameters in an array to yield a compositional optimization such as the one shown in Figure 1.7.

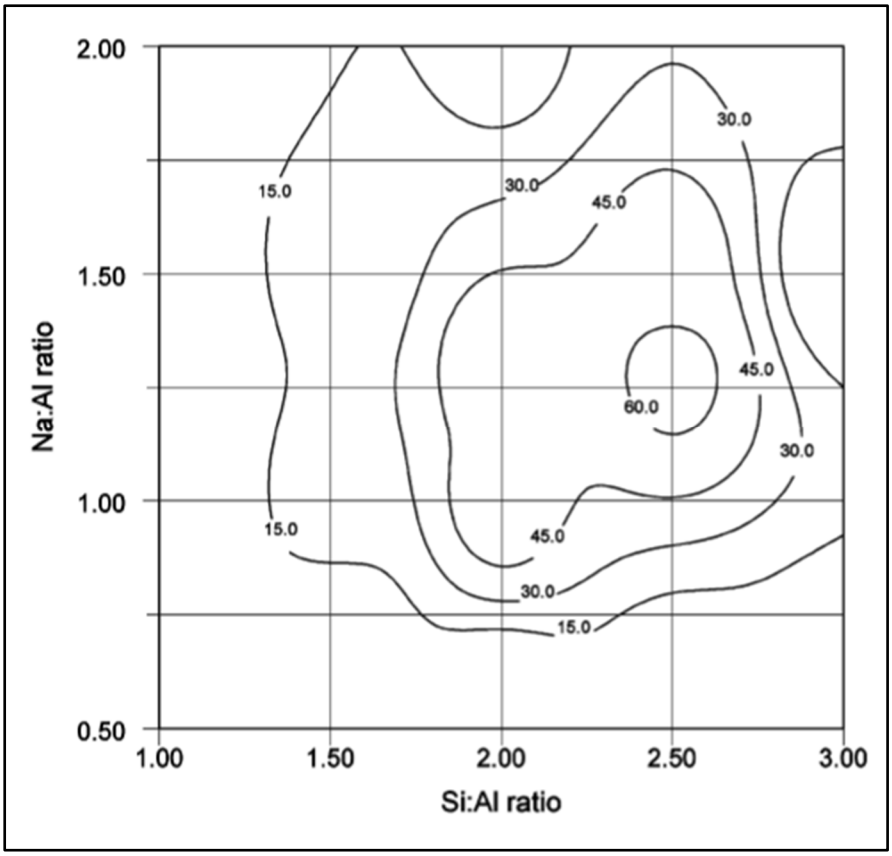

Figure 1.6 A contour map of the impact of compositional parameters on the compressive strength of alkali activated materials, adapted from Rowles & OConnor (2003)

In addition to acting as a potential source of silicon or aluminum, the type of activator influences the AAM gel chemistry and microstructure. The choice of alkali metal cation, typically sodium or potassium, has been observed to impact the average pore size of the resulting geopolymer (Hassan et al., 2019 ; Valencia Saavedra & Mejía de Gutiérrez, 2017). This result is implied by the difference in AAM structures discussed in Section 1.1.2 and the observation of this phenomenon corroborates that the ionic size of the charge balancing cations can influence the greater amorphous structure of the AAM. The type of activator anion can retard the alkali activation reactions. The lower solubility of some activator salts, such as sodium carbonate, causes a slower pH development in the AAM paste. This can influence the microstructure of the AAM, the phases present in the cured material, and the mechanical strength (Susan A. Bernal, Provis, et al., 2015 ; Fernández-Jiménez & Puertas, 2001 ; Mobasher, Bernal, & Provis, 2016). One study was also able to quantify the porosity created

by the decarbonization reaction from the disassociation of the sodium carbonate during the alkali activation reactions and utilize the created carbon dioxide to form a porous AAM (Alghamdi & Neithalath, 2018).

1.2.4 Production methods for AAM

Conventionally, AAM are produced through a multistep mixing and curing process. The production consists of five fundamental stages: (1) pretreatment of the precursor, (2) preparation of the activator solution, (3) mixing, (4) casting, and (5) curing. Within each stage, there are optional steps that have been shown to synergize with some, but not all, combinations of precursors and activators. The state-of-the-art best practices for producing AAM is highly dependent on the raw materials used. This has led sub-fields within this discipline to develop substantially different "best practices" for producing high-quality AAM. Though many extraneous and exotic processes have been demonstrated, this discussion will focus on summarizing the most relevant to the current state-of-the-art.

The first stage of the process involves bolstering the reactivity of the AAM precursor through pretreatments. Some precursors, such as fly ash, require no pretreatment and can be used as-is. However, even blast furnace slag, another high-quality precursor, must be milled to sub-millimeter particle sizes to achieve a sufficiently high reactivity. Milling and sieving to control the particle size is the most basic form of pretreatment. Reducing the particle size improves the dissolution rate of the alumina and silica from the precursor (Luukkonen et al., 2018). However, an excess quantity of fine particles can increase the water uptake in the powder. Excessively high dissolution of silica has also been observed to lead to unfavorable oligomer formation in AAM, which reduces their strength (van Deventer et al., 2007).

To reduce the reactivity of a precursor with high crystallinity, milling alone is not sufficient. Calcination is used to drive the thermal decomposition of the stable alumina and silica phases. For clay materials, calcination temperatures of around 600^{o}C are sufficient to achieve full oxide decomposition and excess temperature can cause recrystallization of stable oxides (J. Davidovits, 1991). However, for industrial by-products, particularly uncalcined emerging precursors such as bauxite residue, significantly higher temperatures of 800-1200^{o}C are

required to break crystalline phases into their reactive form (Lemougna, Wang, Tang, & Cui, 2017 ; Wu & Liu, 2012). At a commercial scale, calcination is typically conducted in a gas-fired rotary kiln which can reach such temperatures in a continuous production mode. After calcination, additional milling and sieving is required to ensure that the calcined materials are not excessively agglomerated. The calcination is a known hot-spot for the environmental impact of AAM and a significant contributor to their greenhouse gas emissions and total energy consumption (Joyce et al., 2018).

In parallel with precursor pretreatment, the activator is dispersed in water to form the highly alkaline activator solution. Activators are typically highly soluble and hygroscopic salts, such as sodium hydroxide. However, some activators, such as sodium carbonate, have lower solubility. In the activator solution, reactive alumina or silica can be added to modify the elemental composition of the final AAM. The alkaline activator solution is exceptionally caustic which makes it hazardous to handle in large volumes in a laboratory or commercial production facility. This has been identified as a major problem to the scalability of AAM and an obstacle to their adoption as a construction material (Luukkonen et al., 2018). The production of the activator solution can be entirely avoided by employing the so-called “one-part” mixing process, in which the activators are added directly to the precursor in a single mixing step.

The mixing process for the production of AAM is called “two-part” because it combines a solid component, precursor, and a pre-mixing liquid component, the activator solution, as shown in Figure 1.8(a). In the conventional two-part methodology, the activator solution and precursor are mixed together in a planetary or cement mixer until a homogenous paste is acquired. Conventional cement and concrete production, on the other hand, is called “one-part” because it requires only the addition of water to the dry components, thus making the mixing a single-step process. In two-part AAM, the handling and mixing of the activator solution significantly complicates the mixing process on a commercial level. Recently, one-part mixing processes have been demonstrated for AAM which eliminate the need to premix and handle the activator solution. This is achieved by using anhydrous powdered alkali salts as the activator and mixing the activator directly into the milled precursor, as shown in Figure 1.8(b).

By using dry activators, AAM can be produced by adding water to the premixed powders in a single mixing step in the same manner as is done for cement and concrete production.

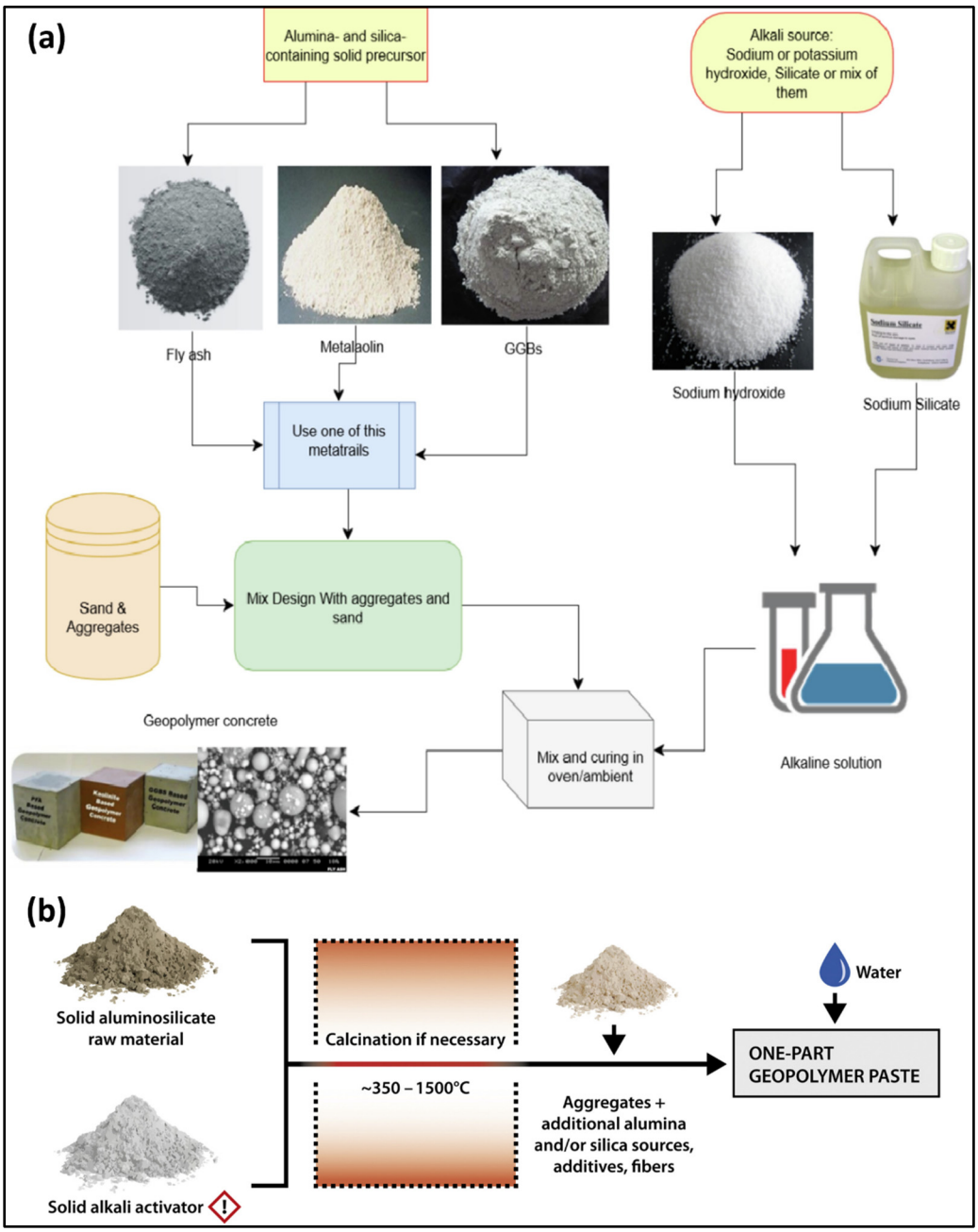

Figure 1.7 (a) A flowchart for the conventional two-part mixing process for AAM-derived industrial by-product precursors that do not require calcination, adapted from Hassan et al., 2019. (b) The simplified one-part mixing process for AAM, adapted from Luukkonen et al. (2018)

The use of one-part mixing simplifies the mixing process and eliminates the hazards of the preparation of the activator solution. However, while some researchers have been able to achieve equivalency between two-part and one-part AAM, the literature on the topic is inconsistent. Many studies have shown slower strength development in one-part AAM which has been attributed to a retarding effect from the concurrent dissolution of the activator and the precursor. (Susan A. Bernal, Nicolas, van Deventer, & Provis, 2015, p. ; Shi & Day, 1995). In contrast, other studies demonstrated accelerated strength development due to thermal acceleration from the exothermic activator dissolution raising the paste temperature during curing (Humad, Provis, & Cwirzen, 2017 ; Kovtun, Kearsley, & Shekhovtsova, 2015). Many researchers have reported lower final strength in one-part AAM due to incomplete dissolution of the reactive phases from the precursor (Escalante-García, Fuentes, Gorokhovsky, Fraire-Luna, & Mendoza-Suarez, 2003 ; Ke et al., 2016). The development of the best practices for one-part AAM is a current topic in the field and the related phenomena are still being studied. After mixing, the AAM paste is cast into molds and cured. Molds of plastic or metallic molds coated in petroleum jelly are suitable for the forming of AAM. The curing process is typically conducted under saturated humidity conditions at either room temperature or an elevated temperature below 100ºC. Many studies use room temperature curing for up to 28 days, following standards for cement pastes. However, most studies agree that AAM achieve higher final strength and density when cured at elevated temperatures (Duxson et al., 2007). This feature varies between precursors and is more significant in lower quality precursors where the reactivity is low. This is attributed to the increased solubility and improved reaction kinetics at elevated temperatures which allow the constituents of uncalcined precursors to react to form AAM more homogenously. The most common for elevated temperature curing is 60ºC, but it is often tested between 40ºC and 80ºC in the literature to determine the sensitivity of a precursor to this effect.

1.2.5 Bauxite residue as a precursor

Bauxite residue (BR) is a by-product of the Bayer process of aluminum production. Bauxite is an aluminum hydroxide-rich ore naturally found with other silicate minerals and iron oxides.

BR is the insoluble mineral oxides from this ore after the extraction of most of the aluminum (Power, Gräfe, & Klauber, 2011). Consequently, BR is primarily composed of alumina, silica, iron oxides, and sodium oxides along with trace metals and minerals present in the bauxite (Y. Liu, Lin, & Wu, 2007 ; S. Wang, Jin, Deng, & Xiao, 2021). BR is produced on a tremendous scale. Globally, it is estimated that current aluminum production results in over 150 million tons of BR being produced per year (IAI, 2021). Due to the alkalinity and potential ecotoxicity of BR, the by-product must be disposed of in specialized containment sites where it is contained indefinitely (Gräfe, Power, & Klauber, 2011 ; S. Rai, Bahadure, Chaddha, & Agnihotri, 2020). A global stockpile of 4 billion tons is believed to be currently contained in massive BR reservoirs distributed around the world (IAI, 2021). This is of particular import to Quebec which has a considerable aluminum industry and suffers from the continuous environmental cost of BR disposal.

The stockpile of BR continues to grow because only 3% of the production is currently used in conventional technology (Evans, 2016). It is anticipated that disposal volumes of BR will continue to increase annually unless a substantial development is made to recycle BR (Habert, 2014). Many studies have been conducted on different avenues for repurposing BR. As a concentrated mineral residue, BR contains minor fractions of valuable metals which can be extracted (Borra, Pontikes, Binnemans, & Van Gerven, 2015). The methodology has been applied to extract iron (Agrawal, Rayapudi, & Dhawan, 2018 ; Gu, Hargreaves, Jiang, & Rico, 2017), gallium (Ujaczki et al., 2019), alkalis (Kaußen & Friedrich, 2016 ; Yanxiu Wang et al., 2018), scandium (Anawati & Azimi, 2019, 2020), and other rare earth metals (Borra, Blanpain, Pontikes, Binnemans, & Van Gerven, 2016 ; Chaikin, Shoppert, Valeev, Loginova, & Napol'skikh, 2020). Attempts have also been made to valorize it as a raw material for sintered ceramics (Pontikes et al., 2009). However, a principal concern in the identification of a suitable end use for BR is an application that can take advantage of the large volume of BR production and consume the by-product at a scale that is relevant to its production scale.

The construction sector presents one of the strongest opportunities to match the large volume production of BR with a large volume application due to the massive scale of global cement consumption (Habert et al., 2020 ; Klauber, Gräfe, & Power, 2011 ; Pontikes & Angelopoulos, 2013). The construction industry has been successful in incorporating several industrial by-

products as partial cement replacements to mitigate the pollution of these by-products while simultaneously reducing the environmental footprint of cement production of the construction sector (Lothenbach, Scrivener, & Hooton, 2011). Numerous studies have applied this methodology to BR with mixed results. As part of this thesis, a quantitative analysis of the use of BR in cement production and as a supplementary cementitious material in concrete was conducted. The published journal article is presented in Annex I but excluded from the main text of the thesis because it is not directly related to alkali activated materials. In summary, the addition of BR to cement is possible, but only at low percentages due to the high alkalinity of BR. The alkalinity of BR induces alkali-silica reactions in concrete, leading to significant reductions in strength and durability (Hewlett & Liska, 2019 ; Venkatesh, Chand, & Nerella, 2019). An alternative binder is required to produce construction materials with higher contents of BR.

AAM are an alternative binder that are positively affected by the alkalinity of BR. This makes them a superior material chemistry for the valorization of large concentrations of BR as construction materials. BR has been heavily studied as an AAM precursor. Unfortunately, has shown low strength when used in its raw state as the only precursor, resulting in only 2-5 MPa of compressive strength, far below the requirements for construction (Dimas, Giannopoulou, & Panias, 2009 ; Zaharaki, Galetakis, & Komnitsas, 2016). This has been attributed to the high crystallinity and low reactive silica content of BR, giving the material low reactivity as a precursor (Wagh & Douse, 1991 ; Ye et al., 2016). Three general methodologies have been developed to bolster the reactivity of BR to achieve high-strength AAM, as visualized in Figure 1.8. Using the “supplemental precursor” method, Precast structural components such as paving blocks and masonry containing 20-30% BR have been demonstrated by diluting dried BR in fly ash (A. Kumar & Kumar, 2013). However, using higher contents of BR results in a drastic reduction in strength (G. Zhang, He, & Gambrell, 2010). This technique is limited by the content of BR that can be used and the reliance on large volumes of fly ash, once again brining AAM production into competition with the cement industry.

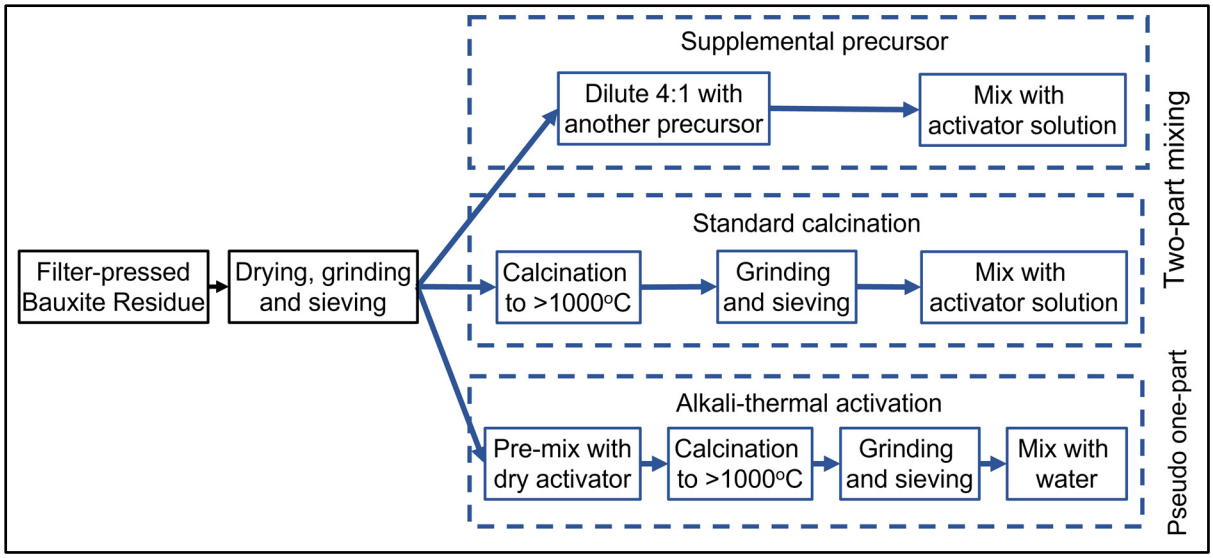

Figure 1.8 Summary of current methodologies for producing alkali activated materials from bauxite residue.

Through calcination, high-strength AAM containing 80-95% BR can be produced. These AAM can contain a desirably high content of BR. However, their production requires a two-part mixing process and high-temperature calcination of the BR. The two-part mixing process can be partially circumvented using the "alkali-thermal activation" method shown in Figure 1.8. However, in both cases, calcination at high temperature, typically above 1000°C is required to decompose the crystalline phases (Hertel, Van den Bulck, Blanpain, & Pontikes, 2022 ; Y. Liu et al., 2007). There have been notably few analyses that quantify the environmental impact of BR calcination at an industrial scale. It has been estimated that calcination releases 0.18-0.20 tons of CO_2 equivalent greenhouse gases and requires roughly 1.5 GJ of energy per ton of BR calcined. (Joseph Davidovits, 2002a ; Joyce & Björklund, 2019). Missing from prior life cycle analyses is the environmental impact of drying of the BR which can be estimated based on the theoretical heat of vaporization of water (2.3 MJ/kg) and the water content of BR (30%) to be at least 0.8 MJ and 0.09 tons of CO_2 emissions per ton of BR dried. No method has been yet demonstrated that can simultaneously create high-strength AAM containing a high concentration of BR without drying and calcination.

An additional challenge of utilizing BR in construction materials is its innate ecotoxicity. BR is highly alkaline complicating its disposal and presenting an ecological risk in the event of leaching into waterways. The formation of AAM eliminates this risk by forming water

insoluble N/C-A-S-H compounds from the reactive alkaline salts in BR. However, this requires full reaction of BR during alkali activation and a residual risk may be present if the alkali activation is incomplete. As a condensed mining by-product, BR also contains trace transition metals that are toxic to humans and wildlife (Y. Cui et al., 2019). Alkali activation is known to pacify the leaching of heavy metals from precursor materials through cationic exchange. A few studies have investigated the leaching of transition metals from BR AAM and showed that the leachate can be below the maximum allowable concentration for surface water (Nguyen et al., 2018, p. 20 ; M. Zhang et al., 2016). However, these works only studied AAM containing low contents of BR (e.g. 20%) and it is not known if the same leaching pacification will occur when the BR content is significantly increased. This thesis will address this research gap to measure the effectiveness of the pacification of alkali activation in AAM containing high contents of BR.

In the assessment of the leaching of metals, two types of methodologies exist: water-based and acid-based. Water leaching tests typically utilize neutral pH conditions over longer durations of time. In the province of Quebec, leaching behavior is determined by a water leaching-based test conducted with a high concentration of solid (1:4) for a duration of a week (QC CTEU-9). Acid-based leaching methodologies offer an accelerated aging test to quantify the leaching behavior under more aggressive conditions. The US Environmental Protection Agency uses method 1311 to determine the hazardous nature of leachate (EPA 1311). This methodology uses an acidic solution (pH 2.88) to accelerate the leaching within a shorter duration of 18 hours. In this thesis, both of these methodologies were used to assess the leaching behavior of BR AAM and are explained in detail in Section 2.2.

1.3 Applications and advantages

1.3.1 Structural applications

Due to their cement-like liquid state which hardens at room temperature, AAM are most frequently compared to cement. Since their discovery, AAM have been studied as an alternative to cement with the potential to utilize industrial by-products in the place of virgin

raw materials (Joseph Davidovits, 2002a). This has made AAM a premier low-carbon structural material with substantially lower environmental impact than cement (Ouellet-Plamondon & Habert, 2015 ; Shi et al., 2019). The construction sector has been estimated to create at least 8% of anthropogenic carbon dioxide emissions (Andrew, 2018). Of this, 50-60% are associated directly with the production of Portland cement, primarily from the decarbonization of calcite (Damtoft, Lukasik, Herfort, Sorrentino, & Gartner, 2008). This places cement production among the largest single technologies contributing to the increasing atmospheric levels of greenhouse gases. This has prompted, in recent decades, a concerted and multifaceted initiative to reduce the environmental impact of cement production (Habert et al., 2020).

Many studies have demonstrated means of reducing the emissions related to cement use by optimizing production conditions, minimizing water requirements, and modifying the clinker compositions. However, these methodologies fail to address 50-60% of the emissions that are related to the decarbonization of calcite, the principal raw material in Portland cement (Damtoft et al., 2008). So-called low-carbon binders offer alternative material platforms that can reduce or eliminate the need for calcite decarbonization, offering dramatic reductions in emissions. AAM are the most heavily studied low-carbon binder and they offer advantages in both environmental aspects and structural performance (Shi et al., 2019).

Early commercialization of AAM technology observed that the production of AAM has as low as 20% of the emissions of Portland cement (Joseph Davidovits, 2002a). More recent studies have mostly corroborated those results but showed that the environmental impact is strongly influenced by the precursor and activator used. This has led to a wide variation in the reported global warming potential of AAM compared to cement. Using calcined clays and high quantities of sodium silicate activator, AAM have been estimated to offer only modest improvements over cement, emitting roughly 80% compared to cement. However, dramatic improvements can be made by using high-quality industrial by-products which require little activator. In the best cases, the global warming potential of AAM has been calculated by life cycle assessment to be only 4-7% of that of cement, though differences in calculation methods have led to some variation in these results in the literature (Habert & Ouellet-Plamondon, 2016 ; Ouellet-Plamondon & Habert, 2015). This has reenforced the need to produce AAM

from non-virgin raw material sources, such as industrial by-products, and avoid calcination to maximize the environmental advantages of AAM over cement.

In addition to reducing the global warming potential, AAM offer physical, mechanical, and chemical advantages over ordinary cement. In the wet state, AAM pastes have similar physical characteristics to cement pastes, which means they are compatible with the same mixing and shaping equipment. They have improved workability and, for some precursors, better setting characteristics (Alonso, Gismera, Blanco, Lanzón, & Puertas, 2017 ; Jang, Lee, & Lee, 2014). AAM harden under ambient temperature conditions, in the same manner as cement, or can be cured rapidly at elevated temperatures (e.g. 60^{o}C) to reach full strength within 1 day (Provis et al., 2019 ; Suwan & Fan, 2017). This gives desirable process flexibility in the shaping and curing of AAM members.

After curing, AAM are high-strength structural materials with greater ultimate compressive strength than Portland cement (Y. Ding, Dai, & Shi, 2016 ; Part, Ramli, & Cheah, 2015). They have also been found to have higher tensile strength, lower modulus of elasticity, and lower Poisson's ratio, all favorable properties for structural components (K.-M. Lee, Choi, Choo, Choi, & Yoo, 2017 ; Noushini et al., 2016 ; Thomas & Peethamparan, 2015). AAM exhibit higher fracture resistance and greater localization of cracking, which makes the materials more resistant to failure (Dakhane, Das, Kailas, & Neithalath, 2016 ; Y. Ding, Dai, & Shi, 2018 ; Nath & Sarker, 2016). When used with aggregates to form concrete, AAM have higher fatigue resistance than ordinary concrete and have smaller aggregate-paste interfacial zones which contribute to corrosion and micro-cracking (Cândido et al., 2018 ; Mun Jae-Sung, Yang Keun-Hyeok, & Kim Si-Jun, 2016 ; San Nicolas & Provis, 2015). With these improved properties, it is theoretically possible to use lower quantities of AAM to achieve the same loadbearing specifications, reducing the cost and material requirements for construction.

AAM achieve greater density than cement, which contributes to their lower permeability and greater durability (Provis et al., 2015). AAM have enhanced chloride and acid resistance which are important qualities in many structural applications, particularly those in the range of ocean spray (Albitar, Mohamed Ali, Visintin, & Drechsler, 2017 ; Mehta & Siddique, 2016). Sources of magnesium can be incorporated into AAM without detrimentally effecting its properties and the content of magnesium has been found to form layered double hydroxide phases. These

phases have been observed to promote resistance to carbonation which resists corrosion. Magnesium-bearing phases are also believed to improve corrosion resistance by pacifying chloride through a chloride binding mechanism (Ke, Bernal, Hussein, & Provis, 2017 ; Ke, Bernal, & Provis, 2017). This extends the service life of AAM compared to cement, particularly in harsh environmental conditions.

1.3.2 Smart, self-sensing construction applications

Smart construction materials are a critical technology in the so-called "Industry 4.0" technological revolution. Smart construction materials are high-strength multifunctional structural components with self-healing or self-sensing functionality (Z. Tang, Li, Hu, Zhou, & Tam, 2019). Self-sensing is a material property that enables the continuous monitoring of a structural member's mechanical state. This enables the technique of structural health monitoring to use self-sensing members to detect changes in the load distribution in structures (P.-W. Chen & Chung, 1993). Structural health monitoring has been used as an advanced detection method for structural decay from micro-cracking, seismic damage, and corrosion (García-Macías & Ubertini, 2019 ; Lu & Li, 2011 ; Lu, Zhang, Li, & Dong, 2013). This provides a means to identify sites of defects and to apply preventative maintenance in a manner currently impossible with ordinary cement and concrete. The use of self-sensing construction materials will prolong the service life of buildings and infrastructure and revolutionize their maintenance (Tian, Li, Zheng, & Wang, 2019).

Self-sensing is typically achieved through measurements of the electrical conductivity of a material or device that is sensitive to strain. The use of external self-sensing devices can be retrofitted to existing structures or attached during construction with conventional materials. Strain gauges, optical fiber sensors, and piezoelectric transducers are used for this purpose (G. Y. Li, Wang, & Zhao, 2007 ; R. Wang, Gu, Mo, & Song, 2013 ; J. Zhao, Bao, Chen, & Kundu, 2016 ; X. Zhao, Li, Du, & Wang, 2008). However, the long-term stability of external sensors is questionable and their use raises safety concerns in structural applications due to the creation of a structural inhomogeneity at the site of attachment (Yoo, Kim, & Lee, 2018). Intrinsically self-sensing materials have been developed as an alternative to these external methods. These

self-sensing materials offer advantages in stability over a wider range of loading and environmental conditions (Chung, 2000 ; Reza, Batson, Yamamuro, & Lee, 2003 ; Sun, Liu, Li, & Hu, 2000). While the initial material costs may be greater, long-term projections predict lower maintenance costs compared to external sensor methods (Han, Zhang, Yu, Kwon, & Ou, 2011 ; Reza, Yamamuro, & Batson, 2004).

Self-sensing materials exhibit a strong relationship between their mechanical strain and their electrical conductivity, which allows measurements of their conductivity to act as an effective proxy to assess their current mechanical state. This relationship between strain and conductivity is an electromechanical phenomenon known as piezoresistivity. Alone, Portland cement has negligible piezoresistivity, making it unable to act as a self-sensing material. Over the last 20 years, technology has been developed to make cement piezoresistive by forming cement composites containing conductive carbon fiber or other conductive additives (Han, Ding, & Yu, 2015). Numerous studies have been conducted to identify the efficacy of different conductive additives and synergies between additives and dispersion techniques (Belli, Mobili, Bellezze, Tittarelli, & Cachim, 2018 ; Donnini, Bellezze, & Corinaldesi, 2018 ; Han, Zhang, Yu, Kwon, & Ou, 2012 ; C. Liu et al., 2019 ; Cecílie Mizerová, Kusák, Topolář, Schmid, & Rovnaník, 2021 ; Mohamed Saafi et al., 2014). A non-exhaustive list of examples is presented in Table 1.2. Self-sensing composites are characterized by the type and quantity of additive used as well as a measurement of their piezoresistivity, expressed as a percentage change in the measured conductivity.

Table 1.2 Examples of self-sensing composites and their piezoresistivity.

Reference	Binder	Conductive additive	Additive content (weight %)	Piezoresistivity (%)
(Azhari & Banthia, 2012)	Cement	Carbon fiber	15%	24%
(Donnini et al., 2018)	Cement	Carbon fiber	3%	10%
(Rehman, Ibrahim, Memon, Javed, & Khushnood, 2017)	Cement	Graphene	0.1%	42%
(Yoo, Kim, et al., 2018)	Cement	Carbon nanotubes	1%	33%
(Han et al., 2012)	Cement	Carbon nanotubes	0.5% 2%	40% 70%
(Deng et al., 2019)	AAM	Carbon fiber	0.3%	12%
(Mohamed Saafi et al., 2014)	AAM	Reduced graphene oxide	0.35%	16%

Self-sensing cement composites leverage highly conductive additives to achieve piezoresistivity. The piezoresistive behavior of these composites arises from the tunneling of electrons between the discrete conductive fibers or particles which are encapsulated in the insulating cement matrix (B. Chen, Wu, & Yao, 2004). The conductive additives form a disjointed conductive network within the composite where the electrical conductivity is dominated by the tunneling of electrons between the conductive particles. Since the tunneling phenomenon is highly sensitive to the barrier width, small changes can be detected in the spacing between the conductive particles such when the specimen is subjected to macroscopic mechanical strain (García-Macías, Castro-Triguero, Sáez, & Ubertini, 2018).

As seen in Table 1.1, AAM have been investigated alongside cement as a binder for self-sensing composites. However, they have seen relatively little attention compared to cement (Z.

Tang et al., 2019). While this methodology has been successful in producing self-sensing materials, the use of conductive additives raises many questions about the feasibility of these materials. Refined carbonaceous nanoparticles, such as carbon nanotubes, massively increase the raw material costs of the composites, up to one-hundred-fold compared to Portland cement (Gupta, Gonzalez, & Loh, 2017). The carbonaceous additives are highly hydrophobic and their uniform dispersion within the aqueous cement matrix is a challenge, even with the use of dispersion-assisting superplasticizers and ultrasonication techniques. Agglomeration from incomplete dispersion causes a deleterious and dangerous reduction in piezoresistive and mechanical properties (Han et al., 2012 ; J. Liu, Fu, Yang, & Gu, 2019). Finally, the additives reduce the durability of the composites by introducing a new mode of failure through a corrosion-assisted breakdown of the particle-matrix interface. Recent studies have reported substantial reductions in the piezoresistive and mechanical properties of self-sensing composites exposed to freeze-thaw or wet-dry testing (Ebrahimi, Daiezadeh, Zakertabrizi, Zahmatkesh, & Habibnejad Korayem, 2018 ; H. Li, Xiao, & Ou, 2008 ; H. Wang, Gao, & Liu, 2018).

The added cost, reduced durability, and low reproducibility of conventional self-sensing composites present a substantial obstacle to the deployment of smart construction materials. The intrinsic piezoresistivity of AAM presents an alternative to achieve self-sensing materials without the drawbacks created by the use of conductive additives. As mentioned in Section 1.3.3, a single study recently reported that AAM can exhibit high piezoresistivity as an intrinsic material property without the need for any conducting additive. This could signal a significant step forward for the field of smart construction materials and provide an avenue to scale-up AAM production in a unique application. However, the study has not yet been reproduced and the effect of compositional parameters on the piezoresistive properties of the AAM is entirely unknown.

The electrical properties of structural materials are becoming increasingly important in the development of smart materials (Dong, Li, Tao, & Wang, 2019 ; X Fu, Lu, & Chung, 1998). The high content of mobile alkali cations in AAM gives the materials unusual electromechanical behavior. Until recently, AAM were known to possess only negligible piezoresistivity, far less than what is required for self-sensing applications (Deng et al., 2019 ;

Cecílie Mizerová et al., 2021). However, a recent study identified that AAM can exhibit relatively high piezoresistivity under alternating current conditions, making them an ideal self-sensing material (M. Saafi et al., 2018). That study attributed the piezoresistive phenomenon in AAM to the piezoelectric effect, visualized in Figure 1.9. Applied compressive strain changes the diffusion pathways for the mobile alkali ions, resulting in a change in ionic conductivity which is measurable as piezoresistivity. While this hypothesis is harmonious with the conventional understanding of ionic mobility in AAM, no experimental or computation study has been conducted to corroborate this theory.

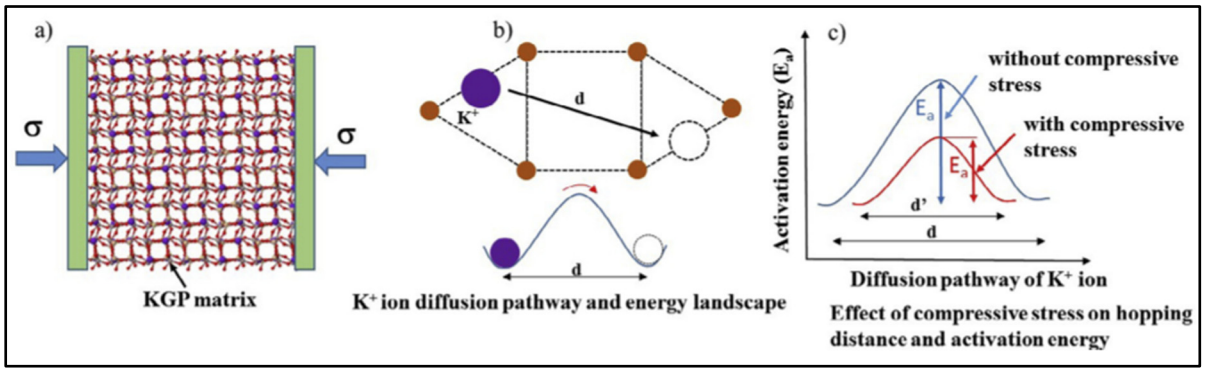

Figure 1.9 (a) A diagram of an AAM matrix under a compressive load, (b) the mechanism for electrical conductivity by ion diffusion between vacancies, and (c) a visualization of the change in activation energy to diffusion caused by the application of compressive stress. Adapted from M. Saafi et al. (2018)

The piezoresistivity of AAM is a unique advantage of this material among other construction materials. Cement and other low-carbon binders are not intrinsically piezoresistive and can only be made self-sensing through the addition of carbon fibers or other piezoresistive additives (Tian et al., 2019). The piezoresistivity of AAM adds another advantage to these materials over cement. However, only one prior study has documented the piezoresistivity of AAM (M. Saafi et al., 2018). This study did not report the mechanical properties of the AAM which are essential to the use of the AAM as a smart structural material. It also demonstrated piezoresistivity with only one composition with a potassium activator, which is uncommon in the study of high-strength AAM, and thus it is not known if this property is common in AAM or unique to a small compositional regime. For these reasons, the unique piezoresistivity of AAM among construction materials has not attracted the interest of researchers in the field.

1.3.3 Dielectric materials and energy storage applications

Dielectric materials are an essential type of electrical material primarily used as dielectric medium in capacitors for electronic and energy storage applications. The performance of a capacitor is directly proportional to the dielectric constant of the dielectric material. Thus, many studies have investigated materials and methods to maximize the dielectric constant and improve the performance of capacitors. Dielectric constant is a material property caused by the polarization of charged species within the material in the presence of an electric field. The external electric field induces a charge separation within the material leading to the formation of numerous dipolar moments, oriented along the external electric field lines. There are four principal types of polarization depending on the type of charged species being polarized: electronic, atomic, dipolar, and interfacial (Dakin, 2006). As visualized in Figure 1.10(a-d), polarization occurs across multiple scales of magnitude from subatomic in the case of electronic polarization to the scale of the grain size of the material for interfacial polarization. The strength of each type of polarization in a material is a fundamental material property determined by the mobility of each charged species. In the case of inorganic materials, dipolar and electronic polarization contribute negligibly to the total polarization. This is due to the nature of the chemical bonding which is predominantly covalent in inorganic materials (Jonscher, 1977). Covalent bonding is highly directional, which inhibits the rotational freedom of atoms and shared electrons to orient in the direction of an applied field. As such, the polarization in dielectric ceramics or alkali activated materials is primarily atomic and interfacial in nature. In atomic polarization, the crystallographic symmetry of charged ions in the material is influenced by an external electric field to form periodic dipoles within the crystal structure. In contrast, interfacial polarization is the product of ionic conduction to the grain boundary interfaces within the material, causing the accumulation of charged ions or ionic vacancies at the interfaces to create a polarization across each grain.

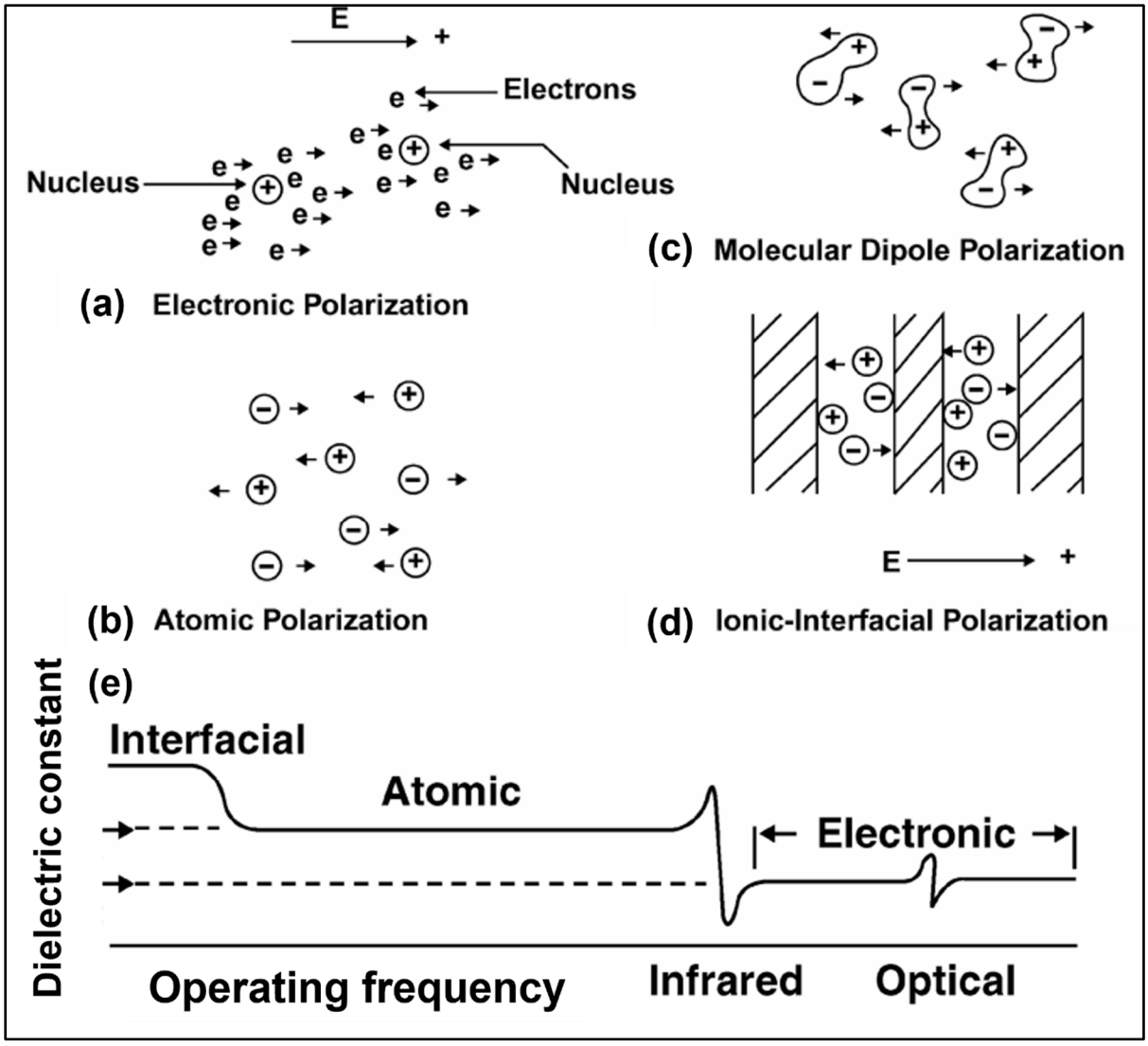

Figure 1.10 (a-d) a visualization of the polarization mechanisms responsible for dielectric constant and (e) the typical frequency dependence of dielectric constant for inorganic materials with labels of the dominant polarization mechanisms in each frequency regime, adapted from Dakin (2006)

In general, the dielectric polarization in solids is characterized by the Debye equation given by the expression:

$$\varepsilon(\omega) = \varepsilon_{\omega\to\infty} + \frac{\varepsilon_{\omega\to 0} - \varepsilon_{\omega\to\infty}}{1+i\omega\tau} \qquad \text{Equation 1.1}$$

Where $\varepsilon(\omega)$ is the dielectric constant at frequency ω, $\varepsilon_{\omega\to\infty}$ is the dielectric constant high frequency (the limit as frequency approaches infinity), $\varepsilon_{\omega\to 0}$ is the dielectric constant under direct current conditions (the limit as frequency approaches zero), i is the imaginary unit, and

τ is a material-specific constant known as the Deybe relaxation time. However, some solids, including AAM, are known to exhibit non-Debye behavior, sometimes represented as having multiple relaxation times attributed to different active polarization mechanisms. In extreme cases, the dielectric constant and dielectric loss does not approach a constant value as the applied frequency approaches zero. This phenomenon is known as low frequency dispersion is not well understood in the field.

Each type of polarization has a different relaxation rate, and thus is dependent on frequency in the case of oscillating external electric fields. This technique is utilized to deconvolve the contribution of each type of polarization to the total dielectric constant by analyzing the frequency dependence of the dielectric constant (Jonscher, 1981). The typical dielectric response of an inorganic material is shown in Figure 1.10(e), highlighting the frequency regimes where each type of polarization is dominant. The magnitude of the dielectric constant in each regime and the frequency at which transitions occur are properties of a material's chemical bonding and microstructure (Dakin, 2006). In practice for capacitor applications, specialized dielectric materials are designed to maximize the dielectric constant to improve energy storage capacity and minimize the dielectric loss to reduce energy loss. This thesis will focus on the study of the dielectric constant and the available material technologies that maximize this property.

Capacitors are a fundamental electronic component composed of a pair of electrodes and a dielectric material medium. The energy stored in a capacitor is proportional to the dielectric constant of the medium. Capacitors are a ubiquitous and versatile energy storage technology but are limited in their energy storage capacity compared to electrochemical and battery storage options (Hao, 2013). A comparison of different energy storage technologies is presented in Figure 1.11. Dielectric capacitors benefit from exceptional power density, allowing high charge and discharge rates. However, the energy density is orders of magnitude below that of battery technology. For decades, researchers have sought to improve the energy storage capacity of capacitors by developing new dielectric materials with higher dielectric constants. The vast majority of modern capacitors use polymer dielectrics with dielectric constants below 10 (Dakin, 2006 ; Zhou, Chu, Neese, Lin, & Zhang, 2007). However, dielectric ceramics have

significantly higher dielectric constants which can make them a superior material for energy storage devices with high energy density and high powder density.

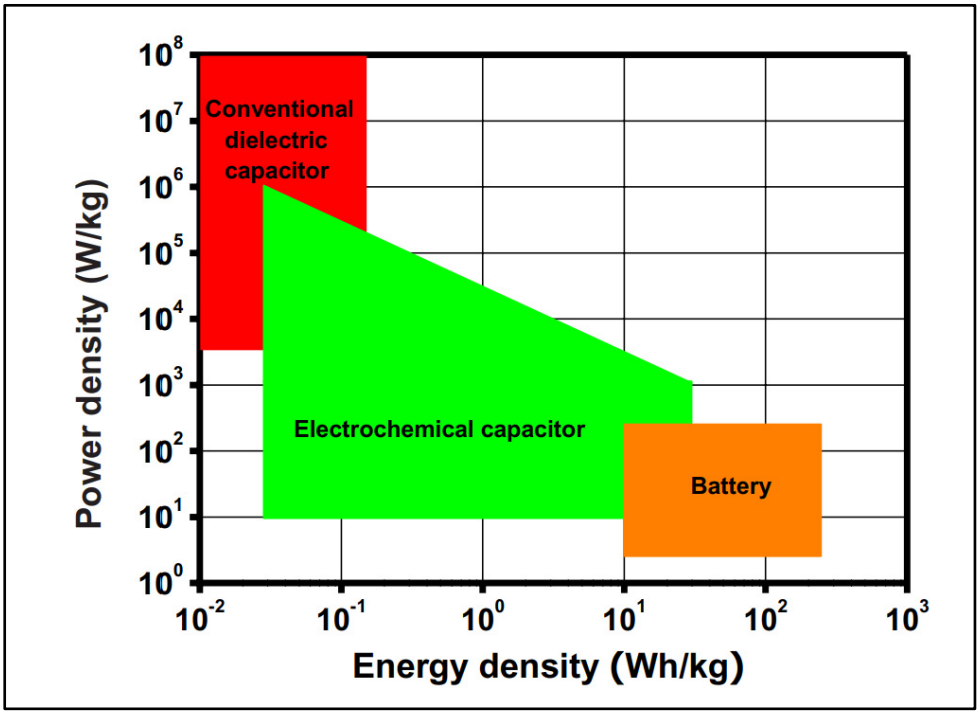

Figure 1.11 Comparison of the power density and energy storage capacity of the three primary categories of energy storage devices, adapted from Hao (2013)

Barium titanate is the oldest and most widely studied ceramic for dielectric applications. Early studies reported dielectric constants above 10^2 (Kokubo, 1970). Decades of research have been conducted to improve this property above 10^3 by refining the microstructure of the ceramic (Yao, Zhang, Yao, & Zhu, 1997). Other researchers have investigated other titanate ceramic compositions such as lead titanate, strontium titanate, and barium strontium titanate (Yadav & Gautam, 2014). The latter of the three can achieve dielectric constants as high as 10^4 (Jiwei, Xi, Xiaogang, Liangying, & Chen, 2002). Concurrently, calcium copper titanate was discovered in 2000 and is sometimes referred to as the "highest dielectric constant material" with dielectric constants up to 5×10^4 (Jesurani, Kanagesan, Velmurugan, & Kalaivani, 2012). This is a misnomer, as some exotically doped composites have been developed with dielectric

constants as high as 10^6 (Y. Zhang, Ma, Wang, Yuan, & Zhang, 2011). Table 1.3 summarizes the different types of conventional dielectric ceramics demonstrated in the literature.

Table 1.3 Examples of conventional dielectric ceramics and their dielectric constants.

Reference	Material	Dielectric constant
(Yao et al., 1997)	$BaTiO_3$	2 600
(Sooksaen, Reaney, & Sinclair, 2007)	$PbTiO_3$	500
(Kim, Kim, Yang, & Ohshima, 2005)	$SrTiO_3$	1 000
(Rhim, Hong, Bak, & Kim, 2000)	$Ba_{0.7}Sr_{0.3}TiO_3$	6 000
(Jiwei et al., 2002)	$Ba_{0.6}Sr_{0.4}TiO_3$	12 000
(Jesurani et al., 2012)	$CaCu_3Ti_4O_{12}$	50 000
(Y. Zhang et al., 2011)	$BaSrTiO_3$ – Lanthanum doped composite	100 000
(Hanjitsuwan, Chindaprasirt, & Pimraksa, 2011)	Na-AAM[1]	10 000
(Hanjitsuwan et al., 2014)	Na-AAM[1]	100 000
(M. Saafi et al., 2018)	K-AAM[2]	100 000 000

[1]: Na-AAM refers to an AAM which has been activated with a sodium activator.
[2]: K-AAM refers to an AAM which has been activated with a potassium activator.

Dielectric ceramics exhibit multiple advantages over polymer dielectrics. Their high dielectric constant presents the opportunity to improve energy storage capacity by multiple orders of magnitude. However, the principal drawback of dielectric ceramics that has prevented their dominance in the industry is cost (Hao, 2013). Dielectric ceramics with carefully controlled microstructures and compositions are far more expensive to produce. Casting ceramics into thin films is challenging and they require sintering to form a cohesive solid, which can damage the homogeneity of the film. Sintering is a high-temperature (typically in excess of 1000^{o}C) phenomenon of grain growth and grain reorientation used to strength ceramic materials after casting (Rahaman, 2017). Sintering is a high-cost and energy-intensive process that adds a substantial economic and environmental impact. This has limited the use of dielectric ceramics to niche applications where their environmental durability is required (Dakin, 2006).

While the mechanical properties of AAM have been investigated at some length, the electrical properties of these materials have attracted little attention in the literature. Only a handful of scientific reports have documented the conductivity or dielectric response of AAM. Those that have, shown in Table 1.3, have reported remarkably high values, meeting or exceeding that of refined dielectric ceramics. These AAM were are produced from fly ash, a by-product of coal combustion. This makes them a low-cost alternative with superior properties compared to the conventional ceramics. However, despite the high dielectric constants measured for AAM, no effort has been made in the literature to fabricate dielectric components from AAM except for the use of AAM as inert supports for ceramic powders (Essaidi et al., 2017 ; Hunpratub, Phokha, Maensiri, & Chindaprasirt, 2015). This is a gap in the literature on AAM, which could hold the key to a revolutionary step in capacitor performance.

A few researchers in the last decade have proposed the production of supercapacitors based on civil engineering materials (Meng & Chung, 2010 ; Junjun Zhang, Xu, & Zhang, 2016). The principal attraction of this technology is the opportunity for a ultra low-cost alternative to energy storage leveraging the affordability and high availability of construction materials. However, no similar studies have been conducted on AAM despite their high dielectric constant. The dielectric properties of AAM are sensitive to the alkali content in the AAM and with optimization of this parameter, the dielectric constant can be increased to 10^5 (Hanjitsuwan et al., 2014). One study demonstrated that the use of potassium activators can boost the dielectric constant to as high as 10^8, but the property is highly sensitive to operating frequency (M. Saafi et al., 2018). These results highlight the potential of AAM as a dielectric material but the cause for the difference in dielectric constants between AAM is unknown. It has been postulated that the dielectric constant may be additionally affected by other compositional parameters in AAM, such as the silicon/aluminum ratio (Si/Al) and the type of activator. However, no prior study has explored this topic. In this thesis, this hypothesis will be investigated to determine the relationship between the dielectric constant and the compositional parameters which govern the chemistry of potassium AAM for the purpose of identifying the optimal composition for future study.

1.4 Conclusion: challenges and opportunities in AAM technology

AAM offer numerous advantages over cement as a construction material. They have improved strength and durability, reduce the requirements for virgin raw materials, lower greenhouse gas emissions, and may even have smart "self-sensing" properties. AAM are not a new technology and have been heavily studied for decades. However, in this time, only a handful of infrastructure installations worldwide have made the switch to AAM. This thesis seeks to address two major obstacles to the commercial scale-up of the AAM industry by improving techniques to utilize emerging precursors and studying the unique properties of AAM to identify new applications.

The competition for high-quality precursor materials has stymied the development of AAM production infrastructure. Concurrently with the development of AAM technology to valorize industrial by-products such as fly ash and blast furnace slag as AAM precursors, the cement industry has developed means to utilize the same by-products as supplementary cementitious materials (Juenger & Siddique, 2015 ; Lothenbach et al., 2011). This has created unfavorable competition for limited volumes of these by-products. A solution to this competition is to develop technology to valorize by-products that are incompatible with cement as AAM precursors. This avenue of research has driven the discovery of the so-called emerging precursors discussed in Section 1.2.1. The most promising methodology is to utilize large volume by-products that contain high contents of alkali metals. Alkali metals, such as sodium salts, detrimentally impact the mechanical properties of cement and concrete but are beneficial to AAM by reducing the required amount of activator (Hewlett & Liska, 2019 ; Venkatesh et al., 2019). BR is a promising raw material that meets these criteria and has no other proven reuse case to compete with. BR is a by-product of aluminum production which has a globally significant presence in Quebec. However, the current methods for producing BR are lacking and call attention to two other obstacles to the production.

Traditional methods for producing BR AAM, as discussed in Section 1.2.4, rely on calcination and two-part mixing. Calcination is an energy-intensive process that is used to increase the reactivity of a precursor at the cost of high expense and emissions. It has been identified as a "hot-spot" in the life cycle analysis of BR and a potential non-starter for valorization options

(Joyce et al., 2018 ; Joyce & Björklund, 2019). Two-part mixing, similarly, has been critically received by many researchers as incompatible with modern cement mixing equipment and a source of considerable safety hazards arising from the activator solution (Luukkonen et al., 2018). The current state-of-the-art for producing BR AAM heavily relies on these two techniques (Hertel & Pontikes, 2020). The first part of this thesis proposes a new technique for using BR as an effective precursor for AAM without calcination or two-part mixing methodologies. This work presents an improved methodology to produce AAM from this highly available precursor, to address this obstacle to AAM commercialization.

The second obstacle to AAM commercialization is the lack of small-volume high-value applications which can serve as stepping stones to develop AAM production infrastructure. The cement industry benefits from the pre-eminence of Portland cement in construction and the economy-of-scale of exceedingly large production volumes (Andrew, 2018). This has made the application of cement replacement an exceedingly difficult one for AAM to break into. However, this can be solved by developing alternative use cases for AAM to provide a gentle on-ramp to scale up AAM production and supply chains. To accomplish this goal, new applications of AAM must be identified in which cement is not a direct competitor.

AAM have many unique properties that can be leveraged for applications beyond construction. Numerous studies have investigated the chemical applications of AAM and their potential applications as catalysts or adsorbents (Sazama, Bortnovsky, Dědeček, Tvarůžková, & Sobalík, 2011). However, none of these applications have been successfully commercialized on a large scale. In this thesis, the less-studied electrical properties of AAM have been investigated and two new promising applications have been discovered. An investigation of the electromechanical behavior of AAM revealed that AAM can act as intrinsic self-sensing materials. This has applications as a smart construction material to replace conventional cementitious composites and enable structural health monitoring in the next generation of infrastructure projects. In parallel, a thorough study of the dielectric behavior of AAM revealed dramatically high polarizability which can be leveraged to create AAM-based supercapacitors. These potential applications as high-value self-sensing or dielectric materials can help to develop an AAM industry and realize the full potential of AAM in construction and beyond.

CHAPTER 2

METHODOLOGY

2.1 Materials and methods for mixing, curing, and mechanical testing

For this thesis, alkali activated materials (AAM) were produced from bauxite residue (BR), fly ash, and metakaolin. The BR was supplied by Rio Tinto from their production facility in Jonquière, Québec. The fly ash was supplied by Titan America Inc., tradename ProAsh®. Two metakaolins were tested, one from Poraver GmbH. under the tradename Metapor® and another Metastar 501HP® from Imerys S.A. These four raw materials were used precursors to prepare AAM and the equivalent oxide compositions of the four precursors are presented in Table 2.1. The term precursor will be used to refer to these four raw materials in this and subsequent chapters. These values were used in the calculations of the elemental compositions of the AAM, as described in subsequent sections. The BR was received and utilized in its filter-pressed form. The water content of the BR was measured to be 25.4%. The AAM were activated with one or a combination of four activators: sodium hydroxide (NaOH), sodium metasilicate (Na_2SiO_3), potassium hydroxide (KOH), and potassium carbonate (K_2CO_3). All of the activators were reagent grade, anhydrous solids supplied by Sigma Aldrich. In the AAM, silica fume was added to increase the reactive silica content. The silica fume was measured to have a moisture content of 4.8% which was accounted for in the mix design. Reagent-grade, anhydrous calcium hydroxide was added to some AAM as a source of supplemental calcium. AAM were prepared using different proportions of these raw materials. The best proportions to maximize the compressive strength were determined through a sequential optimization of compositional factors known to influence the strength of AAM (Luukkonen et al., 2018):

1) Type of precursor or proportion of precursors used in multi-precursor blends;
2) Content of total activator used;
3) Type of activator or proportion of activators used in multi-activator blends;
4) Content of water.

To accomplish the objectives of each sub-section of the thesis, different series of arrays of AAM compositions were prepared. These are described in detail in Chapters 2.2, 2.3.1, and 2.4.

Table 2.1 Equivalent oxide composition of the precursors

Effective Oxide Constituent	Weight Percentage (%)			
	Bauxite residue[1]	ProAsh Fly ash[2]	Metapor Metakaolin[3]	Metastar 501HP Metakaolin[4]
Silicon oxide	5.0	55.3	57.9	46.5
Aluminum oxide	55.7	21.4	24.9	49.5
Iron oxide	11.9	10.2	0.84	0.4
Calcium oxide	0.02	3.4	4.24	-
Magnesium oxide	0.01	0.98	0.45	-
Sodium oxide	0.01	0.96	7.67	0.2
Potassium oxide	0.01	2.11	0.56	0.2
Sulfur oxide	0.1	0.92	0.06	-

[1]: as per (El Gass Hamza, 2020)
[2]: as per (Alizadeh, 2016)
[3]: as per (Poraver, 2019)
[4]: as per (Imerys, 2019)

The AAM were prepared using a one-part mixing methodology to maximize the scalability of the process in future production and avoid complications and hazards arising from the use of separate activator solutions. The mixing methodology is referred to as “one-part” because the precursors, activators, and other additives were added simultaneously to the mixing chamber and mixed in a single step. The mixer was a planetary mixer compliant with cement industry standard ASTM C305 (ASTM International, 2020a). The mixtures were mixed for eight minutes ($\pm$ 0.5 minutes) at 45 rpm until a homogenous paste was achieved. After mixing, the resulting pastes were immediately cast into stainless steel or polyoxymethylene molds coated with petroleum jelly to prevent adhesion. The molds were sealed to prevent loss of moisture

during curing. The physical and mechanical properties of the AAM were assessed in accordance with ASTM standards. The ultimate compressive strength was measured following ASTM standard C109 (ASTM International, 2020b). Compressive testing was conducted on 5-centimeter cube specimens. Compressive testing was conducted at a constant loading of 1 kN/second. Flexural strength was assessed by ASTM C348 (ASTM International, 2021a, p. 348). Square rods of dimension 40 x 40 x 160 mm were tested in three-point flexure under a constant loading of 0.004 kN/second. As an internal standard to facilitate comparison, the mechanical properties were assessed after curing at 60ºC for seven days in a saturated humidity environment. Curing at elevated temperatures has been generally found to improve the mechanical properties of AAM and 60ºC is the most common temperature found in the literature (Hertel & Pontikes, 2020 ; W. Hu, Nie, Huang, Shu, & He, 2018 ; Lemougna et al., 2017).

2.2 Preparation of alkali activated materials from bauxite residue

The principal challenge in this portion of the study was to develop a mixing methodology and compatible AAM composition that could be prepared in a “true” one-part mixing method. The challenge was to improve upon all earlier studies by circumventing the need for calcination, but also to use BR in its raw filter-pressed form without drying or milling. This methodology builds upon the one prior study in the literature which prepared AAM from the slurry filtrate of BR without drying and milling (Arnout, Hertel, Liard, Lootens, & Pontikes, 2017). This earlier study utilized wet BR, but only at a low content (24%). This thesis presents an improved methodology that not only achieves substantially greater mechanical properties but also dramatically improve the BR content to above 70%.

To maximize the content of BR that could be utilized in the AAM, the composition of the AAM was optimized. The optimization was conducted by sequentially optimizing a series of parameters known to strongly influence the mechanical properties of AAM: (1) activator content, (2) water/binder ratio, (3) precursor type, (4) precursor content, (5) curing conditions, (6) activator type, and (7) calcium content. A non-exhaustive of the most important compositions tested is presented in Table 2.2. Compressive strength of each composition was

measured and the composition which exhibited the highest strength was taken as the optimum for this parameter and adopted into the composition for the testing of subsequent parameters. To examine the impact of curing conditions, compositions FA-20 and FA-30 were cured at room temperature for up to 28 days and at 80ºC, in addition to the standard curing conditions. The compressive strength of these specimens was tested after one, three, and five days (± 2 hours) of curing to assess the curing rate and strength development under different curing conditions.

Table 2.2 Compositions of alkali activated bauxite residue.

Parameter	Sample ID	Precursor	Bauxite residue (wt%)[1]	Precursor (wt%)	Sodium hydroxide (wt%)	Sodium metasilicate (wt%)	Calcium hydroxide (wt%)
Activator content	FA-20-6a	ProAsh Fly ash	78.1	15.0	5.5	0	0
	FA-20-8a		75.3	14.7	7.2	0	0
	FA-20-10a		72.7	14.2	10.6	0	0
	FA-30-6a		70.5	22.7	6.7	0	0
	FA-30-8a		69.3	22.3	8.4	0	0
	FA-30-10a		68.1	22.0	9.9	0	0
Precursor type and content	MP-10	Metapor	89.2	7.4	3.4	0	0
	MP-20		82.2	15.3	2.4	0	0
	MP-30		74.7	23.9	1.4	0	0
	MS-10	Metastar	88.5	7.3	4.2	0	0
	MS-20		80.8	15.1	4.1	0	0
	MS-30		72.7	23.2	4.0	0	0
	FA-10	ProAsh Fly ash	88.7	7.4	4.0	0	0
	FA-20		81.2	15.1	3.7	0	0
	FA-30		73.2	23.4	3.3	0	0
Activator type	FA-20-2s	ProAsh Fly ash	80.5	15.1	2.1	2.3	0
	FA-20-3s		80.2	15.1	1.3	3.4	0
	FA-20-4s		79.9	15.0	0.6	4.5	0
	FA-30-2s		72.6	23.4	2.0	2.0	0
	FA-30-3s		72.3	23.3	1.2	3.1	0
	FA-30-4s		72.1	23.2	0.5	4.2	0
Calcium content	FA-20-1c	ProAsh Fly ash	80.6	15.0	3.6	0	0.7
	FA-20-2c		79.5	14.8	3.6	0	2.1
	FA-20-3c		78.4	14.6	3.5	0	3.4
	FA-30-1c		72.5	23.2	3.3	0	1.1
	FA-30-2c		71.7	22.9	3.3	0	2.1
	FA-30-3c		71.0	22.7	3.2	0	3.1

[1]: Wet bauxite residue weight including 25.4% water

After optimization, the highest performing composition, FA-20-2c, was tested in a pug-mill style mixer. The pug mill was a Peter Pugger® brand mixer operating at 15 rpm. The

components were added simultaneously and mixed in a single mixing step for twenty minutes (± 0.5 minutes). After mixing, the resulting paste was extruded out of the pug mill, shaped, and cured under the standard conditions explained above. This mixer was observed to have superior synergy with the one-part mixing methodology for producing high-strength BR AAM.

In addition to the mechanical properties assessment, characterization was conducted of the physical properties and leaching behavior best compositions of BR AAM. The open porosity of the AAM was measured by water adsorption following ASTM C373 (ASTM International, 2018a). AAM specimens were dried and evacuated under 95 kPa (13.8 psi, 28 in Hg) of vacuum to remove air from the open pores. While maintaining the vacuum, deionized water was added. After breaking the vacuum, the surface water was removed, and the water adsorption was calculated as a percent difference in weight compared to the dry weight. The skeletal density of the AAM was measured using an Anton Paar Ultrapyc® pycnometer. These two measurements were used to calculate the percentage of open porosity using the following formula:

$$\%\, Porosity_{open} = \frac{W_A\, D_S}{D_W + W_A\, D_S} \qquad \text{Equation 2.1}$$

where W_A is the percent water absorption, D_s is the skeletal density of the inorganic polymer, and D_w is the density of deionized water. The pore volume and pore size distribution within the AAM was measured by mercury porosimetry using a Micromeritics Autopore® mercury porosimeter. Intrusion and extrusion were measured over a pressure range of 10 kPa to 227 MPa. The Washburn equation was applied to quantify the pore size distribution between 120 microns and 50 nm. The surface characteristics were measured by isothermal nitrogen adsorption using a Micromeritics Gemini®. The Brunauer-Emmet-Teller theory was applied to quantify the surface area and the micropore size distribution was computed by the Barret-Joyner-Halenda method.

The leaching performance of the AAM and the constituent raw materials were characterized in accordance with US EPA method 1311 and Quebec method CTEU-9 (QC MELCC, 2012 ; US EPA, 2015a). Method 1311 simulates leaching in an acidic environment for the purposes of identifying hazardous materials and CTEU-9 simulates water leaching. For both methods, dried specimens were ground and sieved below 75 microns. For method 1311, the samples were mixed with a 2.88 pH solution prepared with acetic acid at a ratio of 1:20 sample/solution

and mixed at 30 rpm for 18 hours (± 0.5 hours). For method CTEU-9, the samples were mixed with 7.0 pH deionized water at a ratio of 1:4 sample/solution and mixed at 30 rpm for 7 days (± 0.5 hours). After mixing, both leachates were extracted and filtered through 0.45-micron glass filters. A portion of each leachate was acidified to pH of 1 using nitric acid to stabilize the leached metals for analysis. The quantity of leached metals was quantified for sodium, aluminum, chromium, iron, nickel, copper, zinc, arsenic selenium, cadmium, and lead using a ThermoFisher Scientific® inductively coupled plasma mass spectrometer. The remainder of each leachate was analyzed with an ion-specific electrode for fluoride content.

2.3 Optimizing the intrinsic self-sensing in alkali activated materials

2.3.1 Compositions and measurement method for piezoresistivity

This thesis investigates the intrinsic self-sensing properties of AAM for the purposes of (1) determining how common the feature is among AAM of different types, (2) identifying the optimum composition of AAM to maximize the self-sensing performance, and (3) examining the mechanisms which make this property manifest in AAM. The first two of these goals were addressed by preparing an array of AAM compositions varying 4 key parameters: (1) precursor type, (2) activator type, (3) activator content, and (4) silica content. The compositions tested are listed in Table 2.3. Three precursors, fly ash, metakaolin, and blast furnace slag were compared at a single composition. A specimen of Portland cement with water/binder ratio of 0.35 was also prepared as a reference. The activator type was selected from sodium hydroxide or potassium hydroxide to determine which alkali cation was preferred to maximize the piezoresistivity. A few compositions using an alternative activator anion, potassium carbonate, were also tested for comparison. The activator content was examined by varying the effective sodium:aluminum (Na/Al) elemental ratio between 0.8 and 1.2. Finally, the silica content, represented as the silicon:aluminum (Si/Al) elemental ratio, was varied between 2.5 and 3.2. The alkali cation, Na/Al ratio, and Si/Al ratio were examined in a full factorial design, resulting in 18 different compositions being tested.

Table 2.3 Compositions of self-sensing AAM

Sample ID	Precursor	Mass (g)					
		Precursor	Silica fume	NaOH	KOH	K_2CO_3	Deionized water
FA-0.8-2.5	ProAsh Fly Ash	500	41	62	0	0	152
FA-0.8-2.85		500	85	62	0	0	161
FA-0.8-3.2		500	130	62	0	0	169
FA-1.0-2.5		500	41	79	0	0	152
FA		500	85	79	0	0	161
FA-1.0-3.2		500	130	79	0	0	169
FA-1.2-2.5		500	41	96	0	0	152
FA-1.2-2.85		500	85	96	0	0	161
FA-1.2-3.2		500	130	96	0	0	169
0.8/2.5		500	41	0	93	0	114
0.8/2.85		500	85	0	93	0	120
0.8/3.2		500	117	0	93	0	127
1/2.5		500	41	0	119	0	116
1/2.85		500	85	0	119	0	123
1/3.2		500	117	0	119	0	129
1.2/2.5		500	41	0	146	0	118
1.2/2.85		500	85	0	146	0	125
1.2/3.2		500	117	0	146	0	131
C-33		500	85	0	79	43	120
C-67		500	85	0	40	86	129
C-100		500	85	0	0	129	138
MK	Metapor	500	143	185	0	0	445
BFS	Blast furnace slag	500	0	38	0	0	241
Cement	Portland cement	500	0	0	0	0	138

To measure the piezoresistivity, AAM specimens were prepared with embedded electrodes. The 5-centimeter cube molds used for compressive strength testing were modified with a bracket to hold two galvanized stainless-steel mesh electrodes in the center of one of the cube faces. The electrodes had a wire thickness of 0.61 mm (23 gauge) and a mesh size of 6.73 mm

(mesh size #3). The electrodes were cut to a size of 50 mm x 100 mm and embedded 50 mm into the cubes and 10 mm apart (± 0.5 mm), as shown in Figure 2.1. These specimens were cured for the standard seven days (± 2 hours) at 60ºC under saturated humidity and then were dried for an additional seven days (± 2 hours) at 60ºC in a dry oven. This gentle drying process removes excess surface water from the specimens that could interfere by surface conduction with the measurement of the electrical resistance without recrystallizing the native hydrates in the AAM.

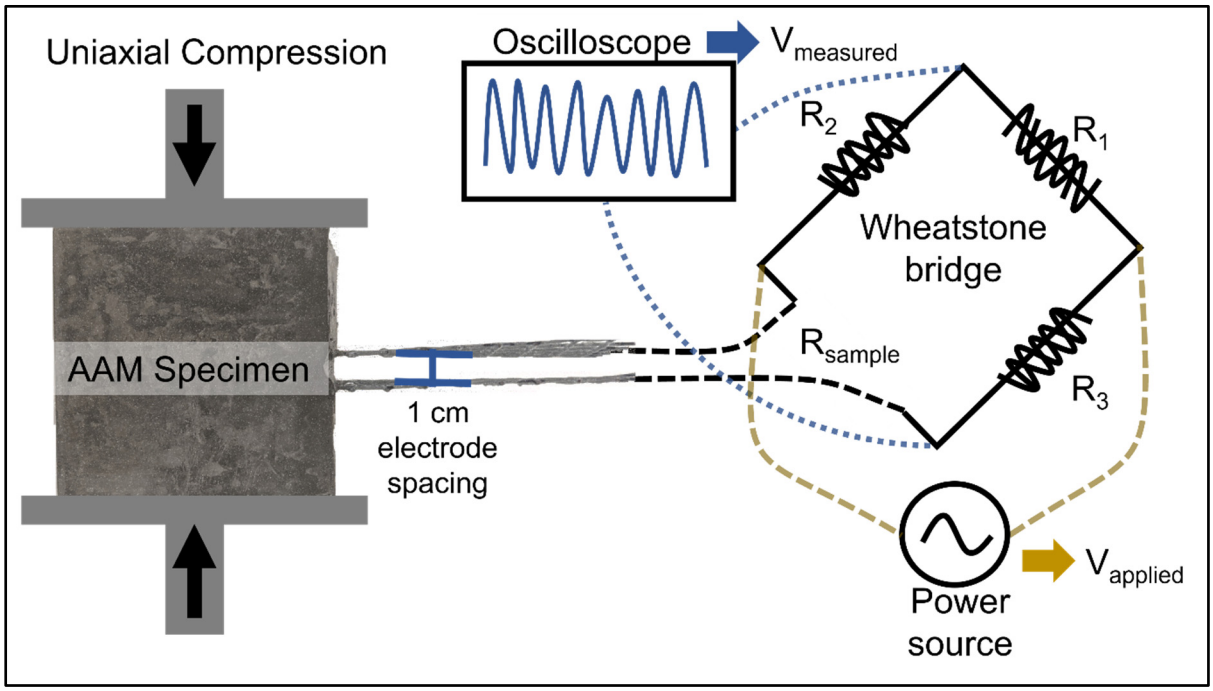

Figure 2.1 The experimental set-up used to measure the piezoresistivity of alkali activated materials.

The electrical resistance between the electrodes was measured using a Wheatstone bridge. A Wheatstone bridge is a basic electronic circuit of three resistors used to measure the resistance of an unknown sample under an alternating current (Hoffmann, 1974). A power source of 10 volts was applied at 10 Hz, 10 kHz, and 10 MHz across the bridge, and the sample resistance (R_{sample}) was measured at each frequency using the following equation, derived from Ohms law:

$$R_{sample} = R_3 \frac{R_2 - \frac{V_{measured}}{V_{applied}}(R_1+R_2)}{R_1 + \frac{V_{measured}}{V_{applied}}(R_1+R_2)} \qquad \text{Equation 2.2}$$

where R_1, R_2, and R_3 are the resistances of the bridge resistors in the orientation shown in Figure 2.1, $V_{applied}$ is 10 Volts, and $V_{measured}$ is the voltage across the sample measured with an oscilloscope. The real component of each voltage was monitored with an InfiniiVision 3034A oscilloscope from Aligent Technologies®, correcting for the phase shift between the applied and measured voltages. Resistors of 860 kΩ ($\pm$ 10%) were used in the Wheatstone bridge to approximate the expected resistance of the AAM, based on literature values, and to maximize the accuracy of the measurement (Hanjitsuwan et al., 2011). The specimens were compressively stressed at intervals of 1 MPa up to 10 MPa in an orientation orthogonal to the electrodes, as shown in Figure 2.1. At each interval, the electrical resistance was measured to quantify the gradual change in resistance with increasing applied load.

In addition to the mechanical and piezoresistive measurements, Fourier transform infrared spectroscopy and scanning electron microscopy were conducted to characterize the specimens. Fourier transform infrared spectroscopy was conducted to ensure homogeneity and full reactivity of the raw materials. A full spectrum of 400 cm^{-1} to 4000 cm^{-1}, with a focus on the range of 700 cm^{-1} to 1300 cm^{-1}, where the characteristic peaks of the alkali activation and inorganic polymer condensation reactions occur. In particular, the infrared spectroscopy is expected to show a decrease in the band centered at 1093 cm^{-1} which corresponds to the Si-O-(Si,Al) vibration. Literature measurements show that, for fly ash AAM, the alkali activation reactions can be confirmed by a decrease in wavenumber of this band. However, the magnitude of this decrease has been disputed in the literature with final band positions of fly ash AAM being reported in the range between 958 cm^{-1} and 1025 cm^{-1} (W. K. W. Lee & van Deventer, 2003 ; Rees et al., 2007). A corresponding decrease in the intensity of the 818 cm^{-1} band, corresponding to δ vibrations in the O-Al-O of reactive AlO_4 phases and 468 cm^{-1} of Si-O-Si bonds is also expected to confirm the consumption of reactive alumina and silica phases into the AAM. Micrographs of the fracture surfaces were acquired by scanning electron microscopy to characterize the homogeneity of the experimental specimen. Energy dispersive spectroscopy was conducted to confirm that uniform distribution of activator was achieved in the one-part mixing process.

2.3.2 Computational modeling of the piezoresistivity

The piezoresistive phenomenon in AAM is far from well understood and has only been documented in two prior studies in the scientific literature. Only one of these studies presented an explanation for the piezoresistivity, which attributed the property to ionic conductivity which could be theoretically enhanced under compressive strain (M. Saafi et al., 2018). However, this theory is strictly conjecture and no experimental or computation proof has been presented to substantiate the strain-sensitivity of ionic conductivity in general nor in the specific case of AAM. This thesis seeks to address this research gap and provide a computational result that can either corroborate or disprove this hypothesis. Since conductivity must either be in the form of electrons or ions, it logically follows that the nature of the piezoresistivity can be determined by modeling the electrical conductivity of the AAM. A computational model of ionic conductivity is practically impossible due to the still limited understanding of the nature of the AAM structure. However, modeling the electrical conductivity is a feasible endeavor because the quantum mechanics of electronic mobility are well understood.

To model the electrical conductivity of AAM, the Kubo-Greenwood theorem of conductivity was applied. The Kubo-Greenwood theorem is a quantum mechanical expression derived from perturbation theory given by:

$$\sigma(\omega) = \frac{2ie^2\hbar^3}{m_e^2 V}\sum_{m,m'}\frac{\Delta f_{m'm}}{\Delta\epsilon_{mm'}}\frac{\langle m|\nabla|m'\rangle\langle m'|\nabla|m\rangle}{(\Delta\epsilon_{mm'}-\hbar\omega+i\delta/2)} \qquad \text{Equation 2.3}$$

Where σ is the electrical conductivity, ω is the perturbation frequency, m_e is the mass of an electron, V is the unit cell volume, m and m' represent each pair of atoms, δ is a constant related to the average inter-collision time, f is the Fermi-Dirac occupation number, and ϵ is the corresponding eigenvalue (Greenwood, 1958 ; Kubo, 1957). When the Kubo-Greenwood theorem is applied to a structure of atoms, it computes the overlap of electron orbitals for each pair of atoms and the conductivity of electrons through the structure in the presence of a Dirac impulse. The method for applying this theorem to computational structures of materials is described extensively in the work by *Calderin et al.* (Calderín, Karasiev, & Trickey, 2017).

Interested readers are directed to that manuscript for an exhaustive explanation of the methodology. This theorem has been used to model the conductivity of idealized metals (Dufty, Wrighton, Luo, & Trickey, 2018). However, it has not been previously applied to amorphous inorganic materials, such as AAM.

Since the Kubo-Greenwood theorem computes the conductivity under an infinite frequency Dirac function, it can be thought of as the instantaneous conductivity of a material without any movement of the atoms or ions within the structure. This makes the theorem ideal for the contribution of the electronic conductivity without contribution from the ionic conductivity present in experimental measurements. In addition, the atomic structures used for the Kubo-Greenwood theorem are free of the atomic defects and grain boundaries present in real materials. For this reason, the computation yields the conductivity of the material without contribution from contact resistance, intergranular resistance, or interfacial conduction. In this way, the computed conductivity by the Kubo-Greenwood theorem is the theoretical conductivity of a perfect single-crystal version of the material.

A recent article by *Zhang et al.* published the results of a molecular dynamics simulation of an AAM with an elemental composition of 1 Na: 1 Al: 3 Si (M. Zhang et al., 2018). The atomic positions from this model were used to model a 240-atom structure of AAM, representing a 1.5-nanometer cube. The atoms were relaxed using the Broyden-Fletcher-Goldfarb-Shanno algorithm using the process described by *Fletcher* (Fletcher, 2013). The relaxation minimizes the free energy of the structure to ensure that the model accurately represents an equilibrium AAM structure without thermal excitation. The relaxed structure was imported into the open-source software Quantum Espresso, and the electrical conductivity was calculated using the Kubo-Greenwood theorem. The piezoresistivity of the structure was determined by artificially straining the model at intervals of 0.2% up to 0.8%. At each interval, the new strained structure was imported into Quantum Espresso and the conductivity calculation was repeated to determine the change in conductivity at each interval of strain.

2.4 Characterizing the dielectric behavior of alkali activated materials

The investigation of the dielectric properties of AAM in this thesis seeks to (1) determine if the exceptional dielectric constant reported by *Saafi et al.* (10^8) is representative of potassium AAM, (2) document the compositional-property relationships for AAM with respect to the dielectric behavior, and (3) identify the optimal composition of potassium AAM to maximize the dielectric constant. To explore these three topics, an array of potassium AAM compositions was prepared considering three compositional factors: (1) activator anion, (2) activator content, and (3) silica content. As explained in Section 2.3, the activator content is a means to modulate the sodium:aluminum (Na/Al) elemental ratio, and the silica content modifies the silica:alumina (Si/Al) elemental ratio. The Na/Al ratio was varied from 0.8 to 2.0, while the Si/Al ratio was varied between 2.3 and 3.2. The list of compositions tested with different combinations of activator, Na/Al ratio, and Si/Al ratio is presented in Table 2.4 while maintaining a constant water/binder ratio of 0.18.

Table 2.4 Composition of alkali activated materials for dielectric characterization

Sample ID	Mass (g)				
	Fly ash	Silica fume	Potassium hydroxide	Potassium carbonate	Deionized Water
H-0.8-2.5	100	7.8	18.6	0	17.6
H-1-2.5	100	7.8	25.0	0	17.7
H-1.2-2.5	100	7.8	29.3	0	17.8
H-1.4-2.5	100	7.8	34.6	0	17.9
H-0.8-2.85	100	15.8	18.6	0	18.9
H-1-2.85	100	15.8	25.0	0	19.0
H-1.2-2.85	100	15.8	29.3	0	19.0
H-1.4-2.85	100	15.8	34.6	0	19.1
H-1-2.3	100	3.6	25.0	0	17.0
H-1-2.7	100	12.1	25.0	0	18.4
H-1-3	100	20.5	25.0	0	19.7
H-1-3.2	100	24.7	25.0	0	20.4
H-1.4-2.3	100	3.6	34.6	0	17.2
H-1.4-2.7	100	12.1	34.6	0	18.5
H-1.4-3	100	20.5	34.6	0	19.9
C-0.8-2.5	100	7.8	0	18.9	24.1
C-1-2.85	100	15.8	0	27.0	25.6
C-1.2-2.85	100	15.8	0	31.6	26.4
C-1.4-2.85	100	15.8	0	37.7	27.5
C-1.6-2.85	100	15.8	0	43.2	28.5
C-1.8-2.85	100	15.8	0	49.0	29.5
C-2-2.85	100	15.8	0	56.5	30.9
C-1-2.3	100	3.6	0	27.0	23.4
C-1-2.5	100	7.8	0	27.0	24.2
C-1-2.7	100	12.1	0	27.0	24.9
C-1-3	100	20.5	0	27.0	26.4
C-1-3.2	100	24.7	0	27.0	27.2
C-1.4-2.3	100	3.6	0	37.7	25.3
C-1.4-2.5	100	7.8	0	37.7	26.1
C-1.4-2.7	100	12.1	0	37.7	26.8
C-1.4-3	100	20.5	0	37.7	28.3
C-1.4-3.2	100	24.7	0	37.7	29.1

Each AAM composition was mixed following the standard one-part mixing procedure and shaped into disks for the characterization of the electrical properties. The AAM pastes were cast into polyoxymethylene molds to form disks that were 40 mm in diameter and 2 mm in thickness (± 0.5 mm), as shown in Figure 2.2. The AAM were cured for two days (+2 hours) in a 60ºC oven at saturated humidity to prevent inhomogeneity due to moisture loss. After curing, the specimens were polished with 200-grit alumina sandpaper to ensure that the outer surfaces were sufficiently smooth. The specimens were then dried for one day (+2 hours) in a dry oven at 60ºC to remove surface moisture that could cause surface conduction to interfere with the measurement. The specimens were removed from the drying oven and immediately transferred into zip-top plastic bags to prevent the accumulation of humidity on the surface before the measurements could be completed.

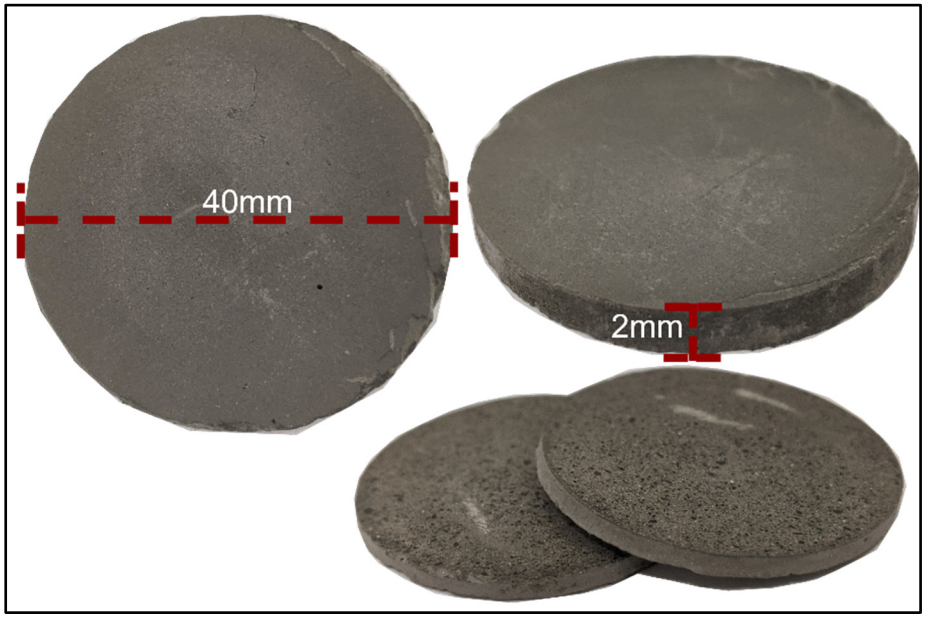

Figure 2.2 AAM specimen prepared for broadband dielectric spectroscopy

Broadband dielectric spectroscopy was used to quantify the electrical and dielectric properties of each AAM specimen. The disk-shaped specimens were sandwiched between brass electrodes and inserted into a Novocontrol Technologies GmbH dielectric spectrometer. A quadratic profile wave of amplitude three volts was applied cyclically at room temperature at

frequencies between 0.1 Hz and 1 MHz. Each composition was tested in quadruplicate. The dielectric constant, dielectric loss, and conductivity were measured at each frequency. The loss tangent is a dimensionless engineering parameter used to characterize the dielectric loss independent of the geometry. The loss tangent is the ratio of the dielectric loss and dielectric constant and was calculated at each frequency. In this study, the loss tangent is used to assess the relative change between the dielectric constant and the dielectric loss constant as a function of frequency and to characterize changes in the frequency dependence as a function of the composition.

As a supplemental measurement, cyclic voltammetry was conducted on select compositions of AAM which showed high dielectric constants. The specimens were prepared in an identical manner as described in Section 2.3.1 for producing specimens for piezoresistivity samples. The specimens were 5-centimeter cubes with galvanized stainless-steel electrodes embedded 1-centimeter ($\pm$0.5 mm) apart in the middle of one of the cube faces. Cyclic voltammetry measurements were conducted using a 2450 SourceMeter from Keithley Instruments with a voltage of $\pm$1 volts and a scan speed of 1 Hz.

CHAPTER 3

VALORIZATION OF UNMODIFIED, FILTER-PRESSED BAUXITE RESIDUE AS A PRECURSOR FOR ALKALI ACTIVATED INORGANIC POLYMERS IN A ONE-PART MIXING PROCESS

Michael Di Mare[1] and Claudiane M. Ouellet-Plamondon[1]

[1] Department of Construction Engineering, École de Technologie Supérieure, 1100 Rue Notre-Dame Ouest, Montréal (QC), Canada

Paper published in the *Journal of Cleaner Production*, January 2023 (with modifications)

3.1 Introduction

Researchers have struggled to develop a suitable reuse case for bauxite residue (BR) for decades. BR is a large volume by-product of the Bayer process of aluminum production and is produced at a scale of 150 million tons per year, worldwide (IAI, 2021). Less than 3% of the BR produced is reused with current technology (Evans, 2016). The remainder is disposed of in specialized containment sites where it must be contained indefinitely due to its ecotoxicity (Gräfe et al., 2011 ; S. Rai et al., 2020). The global accumulation of BR is a rapidly growing challenge, and the worldwide storage of this waste is projected to reach 4 billion tons in 2022 (IAI, 2021). The field of construction is the most viable candidate to valorize BR at sufficiently large volumes to match its production volume (Di Mare et al., 2021 ; Klauber et al., 2011 ; Pontikes & Angelopoulos, 2013). There is a sustained and multifaceted effort underway to reduce the environmental impact of construction and construction materials by any means necessary (Habert et al., 2020). The reuse of BR in construction materials synergizes with this goal and presents a large-scale application to valorize BR. Unfortunately, the high alkalinity of BR induces alkali-silica reactions when used in cement, the most prominent construction material, leading to significant reductions in strength and durability (Hewlett & Liska, 2019 ;

Venkatesh et al., 2019). This has stymied the use of BR in cement in large volumes to mitigate the accumulation of this harmful waste

Alkali activated materials (AAM) are an environmentally friendly alternative to cement that are not negatively influenced by high alkalinity. AAM are synthesized from industrial by-products, called precursors, and have an 80% lower greenhouse warming potential compared to Portland cement (Habert & Ouellet-Plamondon, 2016). This is a sorely needed reduction in environmental footprint for the construction industry. Attempts to utilize BR alone as an AAM precursor achieved only than 2 – 5 MPa of strength, far below the requirements for construction (Dimas et al., 2009 ; Zaharaki et al., 2016). Unlike conventional AAM precursors, BR has relatively high crystallinity and low reactive silica content (Wagh & Douse, 1991 ; Ye et al., 2016). Many studies have proposed techniques to make BR more similar to conventional precursors using various combinations of calcination, chemical modification, and micronization (Hertel, Iacobescu, Blanpain, & Pontikes, 2016 ; Y. Hu et al., 2019 ; Ke, Bernal, Ye, Provis, & Yang, 2015 ; Ye et al., 2014). However, these processes, particularly calcination, add substantial capital and operating expenses which make the reuse of BR in this manner economically unviable (Hertel & Pontikes, 2020). An alternative is to blend BR with conventional AAM precursors, typically with high dilution ratio such as 4:1 (i.e., 20% BR). It has been largely concluded that the use of greater contents of BR is detrimental to the mechanical integrity of the AAM (A. Kumar & Kumar, 2013 ; Yuancheng Li, Min, Ke, Liu, & Tang, 2019 ; G. Zhang et al., 2010). However, this is not a long term solution because of the competition for high quality precursors, such as metakaolin, blast furnace slag and coal fly ash, which can also be used as supplementary cementitious materials in blended cement (Duxson & Provis, 2008). This competition for raw materials plagues the deployment of all AAM in construction and could be remedied by the development of AAM containing high contents of BR.

Another obstacle for AAM in construction is the reliance on a two-step mixing processes. AAM are classically made by the preparation of an activator solution, a highly caustic mixture of sodium salts and water, which is subsequently mixed with the precursor in a separate mixer. This two-step process, called “two-part”, has been strongly criticized as incompatible with the single-step (“one-part”) mixing technology used for cement, and safety concerns have been

raised about the preparation and handling of the caustic activator solution in an industrial environment (Luukkonen et al., 2018). To date, no study of BR AAM has attempted a true one-part mixing process. The closest approximation is the so-called “alkali-thermal” process in which BR is mixed with the activator before calcination and grinding to yield a water-reactive premixed powder which can be used in one-part mixing equipment (Ke et al., 2015 ; Ye et al., 2016). This remains a far cry from a true one-part mixing and the added processing costs in alkali-thermal and other techniques reduce the advantages of using BR in AAM.

The development of a one-part methodology for BR is further complicated by the high-water content of the by-product. BR is disposed of from alumina production facilities as a slurry or filter-pressed solid, containing at least 25% water. Developing an alkali activation methodology which could utilize BR in its wet state would improve the economic viability of scale-up and production. However, only one study in the literature has produced AAM from wet BR without drying and only with a low content of BR (24%) (Arnout et al., 2017). In this study, a true one-part AAM methodology is demonstrated that simultaneously valorizes BR in its wet filter-pressed state without pretreatment while utilizing up to three times the BR content found in comparable studies. The objectives are to maximize the content of BR and investigate the properties of the resulting AAM, including mechanical strength, permeability, and leaching behavior. The goal is to present a production methodology that maximizes the viability of cost-effectively reusing BR in large volumes as a construction material while minimizing competition for precursors with other parts of the construction sector.

3.2 Materials and Methods

3.2.1 Materials

Alkali activated materials (AAM) were prepared from filter-pressed bauxite residue (BR) and a supplemental precursor: fly ash or metakaolin. The BR from the Bayer process was used in the wet filter-pressed form, as received from Rio Tinto, without drying or other modification. Fly ash (FA) with the tradename ProAsh® was supplied by Titan America LLC. Poraver GmBH supplied metakaolin, tradename Metapor® (MP), blended with glass fines to achieve

the same silica content as fly ash. Imerys S.A. supplied MetaStar 501HP (MS), a high-performance metakaolin. The supplemental precursors were blended with the BR in ratios of 1:9, 2:8, and 3:7 of precursor/dry BR by weight, accounting for the content of water in the BR. The water content of the BR was measured to be 25.4%. The minimum water/binder ratio was set by the water content in the BR and, thus, was 0.31, 0.27, and 0.24, depending on the ratio of the precursors. Additional deionized water, in intervals of 0.2 water/binder ratio up to 0.42, was added if necessary to maintain workability while minimizing the water content.

Table 3.1 Chemical composition of the bauxite residue, fly ash, and metakaolin raw materials

Equivalent oxide composition (%), dry	Filter-pressed bauxite residue (BR)	ProAsh fly ash (FA)	Metapor metakaolin (MP)	Metastar 501HP metakaolin (MS)
Al_2O_3	74.7	21.4	24.9	46.4
SiO_2	6.7	55.3	57.9	50.6
Na_2O	0.01	1.0	7.7	0.2
K_2O	0.01	2.1	0.6	0.2
CaO	0.03	3.4	4.2	-
MgO	0.01	0.9	0.5	-
Fe_2O_3	16.0	10.2	0.8	0.4
TiO_2	1.5	-	1.1	1.5
Moisture content (%)	25.4	-	0.5	0.7

The AAM were activated with a blend of anhydrous, reagent-grade sodium hydroxide and sodium metasilicate. Sodium hydroxide was used as the primary activator and was tested in a range of dosages between 3% and 24%. In some compositions, sodium metasilicate was partially substituted while maintaining a constant molar sodium content, described as Na / Al ratio, to achieve different silicon contents (Si / Al ratio). In other compositions, anhydrous, reagent-grade calcium hydroxide was added as a supplemental source of calcium to modify the Ca / Si ratio. A non-exhaustive list of compositions of AAM is given in Table 3.2. The compositions are described by their mixing proportions (% weight) and by their elemental proportions to facilitate reproduction of the technique.

Table 3.2 Compositions of alkali activated materials prepared with filter-pressed bauxite residue.

Parameter	Sample ID	Precursor	BR (wt%) [1]	Precursor (wt%)	NaOH (wt%)	Sodium silicate (wt%)	CaOH (wt%)	Na/Al ratio[2]	Si/Al ratio[2]	Ca/Si ratio[2]	W/B ratio[3]
Precursor type	MP-10	Metapor	89.2	7.4	3.4	0	0	0.1	0.14	0.05	0.31
	MP-20		82.2	15.3	2.4	0	0	0.1	0.22	0.06	0.33
	MP-30		74.7	23.9	1.4	0	0	0.1	0.31	0.06	0.33
	MS-10	Metastar	88.5	7.3	4.2	0	0	0.1	0.13	0.00	0.34
	MS-20		80.8	15.1	4.1	0	0	0.1	0.19	0.00	0.36
	MS-30		72.7	23.2	4.0	0	0	0.1	0.25	0.00	0.42
	FA-10	ProAsh Fly ash	88.7	7.4	4.0	0	0	0.1	0.14	0.03	0.31
	FA-20		81.2	15.1	3.7	0	0	0.1	0.22	0.04	0.27
	FA-30		73.2	23.4	3.3	0	0	0.1	0.31	0.05	0.24
Activator content	FA-20-6a	ProAsh Fly ash	78.1	15.0	5.5	0	0	0.2	0.22	0.04	0.27
	FA-20-8a		75.3	14.7	7.2	0	0	0.3	0.22	0.04	0.27
	FA-20-10a		72.7	14.2	10.6	0	0	0.4	0.22	0.04	0.27
	FA-30-6a		70.5	22.7	6.7	0	0	0.2	0.31	0.05	0.24
	FA-30-8a		69.3	22.3	8.4	0	0	0.3	0.31	0.05	0.24
	FA-30-10a		68.1	22.0	9.9	0	0	0.4	0.31	0.05	0.24
Activator type	FA-20-2s	ProAsh Fly ash	80.5	15.1	2.1	2.3	0	0.1	0.24	0.04	0.27
	FA-20-3s		80.2	15.1	1.3	3.4	0	0.1	0.25	0.04	0.27
	FA-20-4s		79.9	15.0	0.6	4.5	0	0.1	0.26	0.04	0.27
	FA-30-2s		72.6	23.4	2.0	2.0	0	0.1	0.33	0.05	0.27
	FA-30-3s		72.3	23.3	1.2	3.1	0	0.1	0.34	0.05	0.27
	FA-30-4s		72.1	23.2	0.5	4.2	0	0.1	0.35	0.05	0.27
Calcium content	FA-20-1c	ProAsh Fly ash	80.6	15.0	3.6	0	0.7	0.1	0.22	0.19	0.27
	FA-20-2c		79.5	14.8	3.6	0	2.1	0.1	0.22	0.24	0.27
	FA-20-3c		78.4	14.6	3.5	0	3.4	0.1	0.22	0.28	0.27
	FA-30-1c		72.5	23.2	3.3	0	1.1	0.1	0.31	0.17	0.27
	FA-30-2c		71.7	22.9	3.3	0	2.1	0.1	0.31	0.20	0.27
	FA-30-3c		71.0	22.7	3.2	0	3.1	0.1	0.31	0.22	0.27

[1]: Wet bauxite residue weight including 25.4% water
[2]: Molar ratio accounting for contributions of all components.
[3]: Water binder ratio, accounting for the water content in the bauxite residue and added water

3.2.2 Mixing procedures and optimization methodology

The AAM were prepared in a true one-part mixing procedure using BR in its wet, filter-pressed state, as received from the supplier. The BR was mixed with fly ash or metakaolin, the activators, and, if necessary, additional water and calcium hydroxide in a single step. The mixing was conducted in a planetary mixer used for cement mortars, compliant with ASTM C305 (ASTM International, 2020a). The mixture was mixed for eight minutes at 45 rpm until a homogenous paste was achieved. The paste was immediately cast into 5 cm stainless steel cube molds and compacted in accordance with ASTM C109 (ASTM International, 2020b). The molds were sealed to prevent moisture loss and cured in a saturated humidity chamber at 60ºC for seven days. Curing at elevated temperature has been generally found to improve the mechanical properties of BR AAM and 60ºC is the most common temperature found in the literature (Hertel & Pontikes, 2020 ; W. Hu et al., 2018 ; Lemougna et al., 2017). To examine the impact of curing conditions, additional AAM were cured at 80ºC and curing times of one, three, and five days were tested to assess the curing rate and its effect on the strength development. One set of specimens was additionally cured in a saturated humidity chamber at 23ºC for 28 days, to compare to the typical curing conditions of cement.

The composition of the AAM was optimized to maximize the BR content while targeting a compressive strength above 10 MPa. The optimization was conducted by sequentially varying variables in the composition to determine the values which yielded the highest strength. The variables tested, in order, were: (1) activator content, (2) water/binder ratio, (3) precursor type, (4) precursor content, (5) curing conditions, (6) activator type, and (7) calcium content. A non-exhaustive list of compositions tested is given in Table 3.2, categorized by the compositional parameter under examination. The results, similarly, have been grouped by parameter in Figures 3.2 and 3.3 and Tables 3.3 and 3.4. During the optimization, both 20% and 30% fly ash gave favorable results and, for subsequent variables, both compositions, called FA-20 and FA-30, were tested to explore potential synergies.

3.2.3 Characterization methods

After curing, the 5 cm cube specimens were tested for mechanical, physical, and leaching properties. Compressive strength was assessed in accordance with ASTM C109 under constant compressive loading of 1 kN/s (ASTM International, 2020b). The specimens were tested in triplicate and the error bars in subsequent figures depict the standard deviation. The physical properties were assessed by water adsorption, pycnometry, mercury intrusion porosimetry, and isothermal nitrogen adsorption. Water adsorption measurements were conducted to determine the quantity of open porosity in the material, following ASTM C373 (ASTM International, 2018a). Specimens were dried and evacuated under 95 kPa (13.8 psi, 28 in Hg) of vacuum to remove air from the open pores. While maintaining the vacuum, deionized water was added. After breaking the vacuum, the surface water from the water-impregnated specimens was removed and the water adsorption was calculated as a percent difference of the change in weight from the dry state. The skeletal density of the material was measured using an Anton Paar Ultrapyc® pycnometer. These two measurements were used to calculate the percentage of open porosity using the following formula:

$$\%\ Porosity_{open} = \frac{W_A\ D_s}{D_w + W_A\ D_s} \qquad \text{Equation 3.1}$$

where W_A is the percent water absorption, D_s is the skeletal density of the AAM, and D_w is the density of deionized water. The pore volume was confirmed by mercury porosimetry using a Micromeritics Autopore® mercury porosimeter. Intrusion and extrusion were measured over a pressure range of 10 kPa to 227 MPa. The Washburn equation was applied to quantify the pore size distribution between 120 microns and 50 nm. Isothermal nitrogen adsorption was conducted using a Micromeritics Gemini®. The Brunauer-Emmet-Teller theory was applied to quantify the surface area and the micropore size distribution was computed by the Barret-Joyner-Halenda method.

The leaching performance of the AAM and the constituent raw materials were characterized in accordance with US EPA method 1311 and Quebec method CTEU-9 (QC MELCC, 2012 ; US EPA, 2015a). Method 1311 simulates leaching under acidic environment for the purposes of identifying hazardous materials and CTEU-9 simulates water leaching. For both methods,

dried specimens were ground and sieved to below 75 microns. For method 1311, the samples were mixed with a 2.88 pH solution prepared with acetic acid at a ratio of 1:20 sample/solution and mixed at 30 rpm for 18 hours. For method CTEU-9, the samples were mixed with 7.0 pH deionized water at a ratio of 1:4 sample/solution and mixed at 30 rpm for 7 days. After mixing, both leachates were extracted and filtered through 0.45-micron glass filters. A portion of each leachate was acidified to pH of 1 using nitric acid to stabilize the leached metals for analysis. The quantity of leached metals was quantified for sodium, aluminum, chromium, iron, nickel, copper, zinc, arsenic selenium, cadmium, and lead using a ThermoFisher Scientific® inductively coupled plasma mass spectrometer. The remainder of each leachate was analyzed with an ion specific electrode for fluoride content.

3.3 Results and Discussion

3.3.1 True one-part mixing and environmental benefits

Mitigating the global accumulation of bauxite residue (BR) requires the reuse large volumes of BR cost-effectively. Different processes have been proposed to transform BR into a construction material and a visualization comparing the process schemes is shown in Figure 3.1. In yellow, the methods to use BR as a clinker additive or supplementary cementitious material are shown. In the clinker, BR can be added in fractions of a percent as a source of calcium, aluminum, and iron (Tsakiridis, Agatzini-Leonardou, & Oustadakis, 2004). In concrete, it can be included up to 25% as a supplementary cementitious material in a raw or calcined state, but causes degradation in the mechanical strength and the durability (Ghalehnovi, Roshan, Hakak, Shamsabadi, & de Brito, 2019a ; Pontikes & Angelopoulos, 2013). This limits the viability of these methodologies in production.

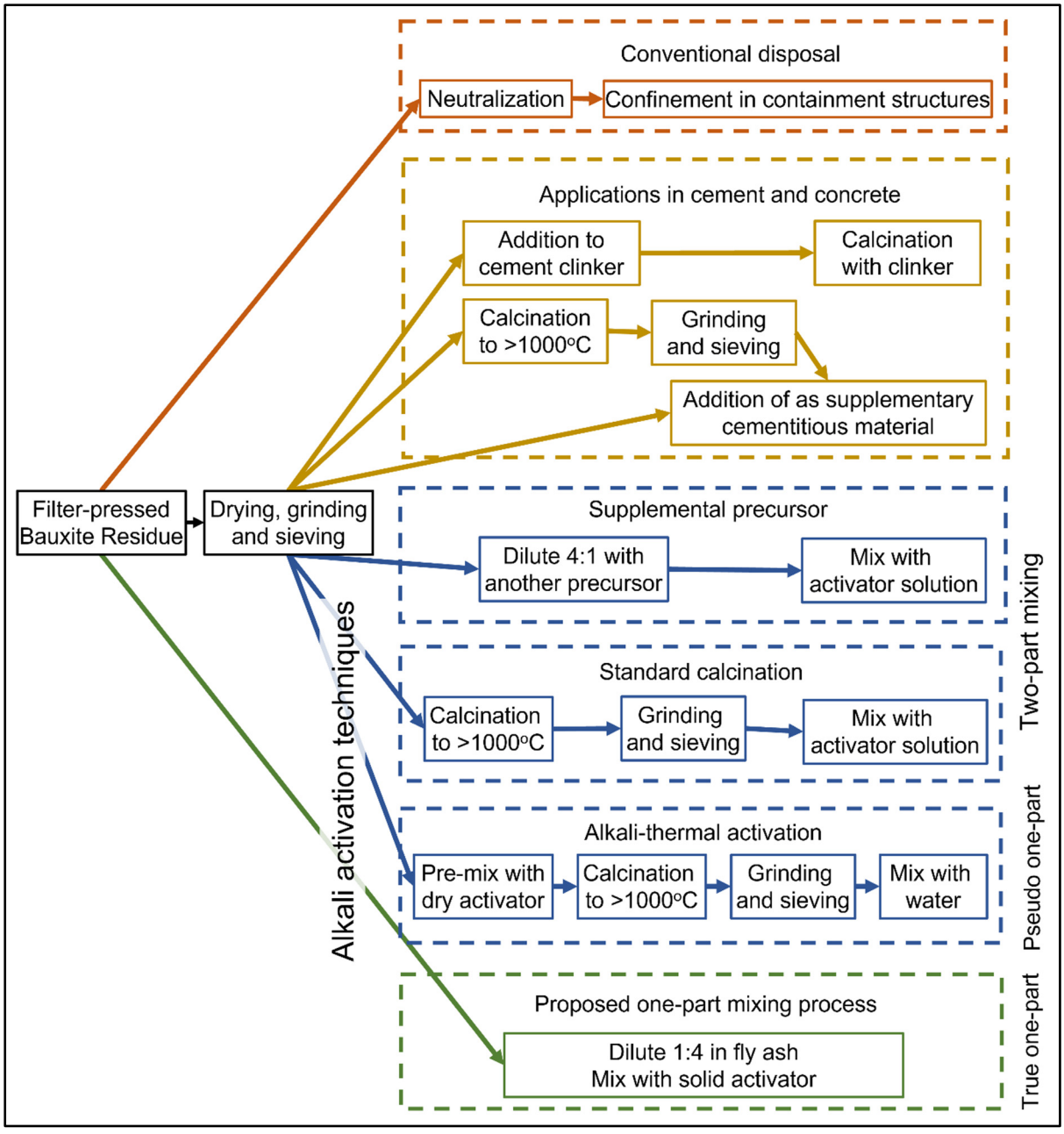

Figure 3.1 Comparison of processing schemes for the disposal of bauxite residue (orange), its use in cement (yellow), the production of alkali activated materials by conventional methods (blue), and the proposed one-part process (green).

Alkali activation methods, shown in blue in Figure 3.1, can utilize significantly greater BR content than is possible with cement. Precast structural components such as paving blocks and masonry containing 20-30% BR have been demonstrated by diluting dried BR in fly ash (A.

Kumar & Kumar, 2013). However, using higher contents of BR results in a drastic reduction in strength (G. Zhang et al., 2010). Standard calcination methods can create AAM containing 80-95% BR but requires a two-part mixing process which has been criticized for low scalability (Hertel, Blanpain, & Pontikes, 2016 ; Luukkonen et al., 2018). While this aspect can be marginally improved with alkali-thermal activation, both standard calcination and alkali-thermal activation require calcination above 1000ºC to thermally decompose the crystalline phases of BR at create reactive amorphous phases for stronger alkali activation (Hertel et al., 2022 ; Ke et al., 2015 ; Ye et al., 2016).

There have been notably few analyses in the literature to quantify the environmental impact of BR calcination at an industrial scale. An early study of kaolin AAM estimated that calcination releases 0.17 tons of carbon dioxide per ton of AAM precursor and an additional 0.02 tons CO_2 / ton worth of electricity is required to grind the calcined material (Joseph Davidovits, 2002a). This agrees well with recent estimates of the energy consumption required to grind and calcine BR, based on modern technology currently in use for the production of cement (Joyce et al., 2018 ; Joyce & Björklund, 2019). With use of the US EPA emission database, the energy consumption can be converted to equivalent CO_2 emissions, as shown in Table 3.3. The energy cost and emissions caused by grinding and calcination reduce the advantages of utilizing BR AAM as a construction material.

Table 3.3 Energy consumption and emissions estimates for each preprocessing step used in conventional alkali activation techniques

Processing step	Energy consumption (MJ / ton of BR)	Equivalent CO_2 Emissions (ton CO_2 / ton of BR)[4]
Drying	769[1]	0.09
Grinding	158[2]	0.02
Calcination	1 469[3]	0.18
Total	2 396	0.29

[1]: Calculated from the BR water content, the heat of vaporization, and the specific heat capacity of water from (Stallard & Amis, 1952).
[2]: Estimated by (Joyce & Björklund, 2019) from milling reports for cementitious materials.
[3]: Estimated by (Joyce et al., 2018) from an interpolation of clinker calcination studies.

[4]: Calculated from the energy consumption using the United States Environmental Protection Agency Greenhouse Gases Equivalencies Calculator (EPA, 2021).

The cost and environmental impact of drying is an another obstacle for the valorization BR due to the high content of water (30%) present in the by-product (Pontikes & Angelopoulos, 2013). All conventional methods to valorize BR in cement or AAM require the complete removal of this water, but no prior study has quantified the cost or impact of drying. Using the theoretical heat of vaporization (2.3 MJ/kg) and heat capacity (4.2 kJ/kg ºC) of water, the minimum energy consumption of the drying process can be calculated to be 770 MJ / ton of BR and creates 50% of the emissions of calcination (Stallard & Amis, 1952). The omission of the drying step from prior life cycle assessments has led to an underestimate of the environmental impact of conventional methodologies. The drying step has avoided scientific scrutiny despite the high energy cost because there is no demonstrated alternative. Only one prior study has succeeded in producing AAM from BR without drying and only with a relatively low content (24%) of BR (Arnout et al., 2017). The potential emissions savings in eliminating the drying, grinding, and calcination steps presents a great opportunity to maximize the advantages of BR in AAM.

The one-part mixing process demonstrated in this study accomplishes precisely this goal to offer multiple advantages over conventional alkali activation. The process, shown in green in Figure 3.1, eliminates the need for drying, grinding, and calcination of the BR to form an AAM. Combined, this avoids as much as 0.29 tons of CO_2 emissions per ton of BR valorized and the substantial operating expenses associated with the 660 kWh (2.4 GJ) per ton required to preprocess BR for conventional alkali activation methods. Moreover, after compositional optimization, the BR was tripled compared to the earlier study by *Arnout et al.*, creating an AAM with exceptionally high BR content (>70%). This was accomplished using a blend of solid activators and a single step mixing process that maximizes scalability and cost-effectiveness.

3.3.2 Compositional optimization of the one-part process

To rigorously demonstrate the one-part mixing method, a compositional optimization was conducted to maximize the BR content in the AAM while maintaining compressive strength above 10 MPa. Preliminary tests using the one-part methodology were conducted by blending fly ash and wet BR with different activator contents and water / binder ratios. A low activator content of 4%, significantly lower than the quantity required for alkali-thermal activation, maximized the compressive strength to 12.6 and 8.3 MPa, respectively, as shown in Figure 3.2(a) (Y. Hu et al., 2019 ; Ke et al., 2015). This trend between the strength and the activator content is as expected for AAM. Low activator content reduces the total aluminum dissolved from the fly ash and BR. However, excessive activator raises the pH and causes unfavorable oligomer formation in the gel, reducing the final strength of the AAM (Duxson & Provis, 2008 ; Provis et al., 2015). The low content of activator required indicates the high availability of the reactive alumina and silica phases in the BR without need for grinding to reduce the particle size. Added water was found to significantly reduce the compressive strength, even at the optimized activator content, as shown in Figure 3.2(b). Subsequent compositions were tested at the minimum water / binder ratio to maximize the strength by adding no additional water beyond the inherent in the BR.

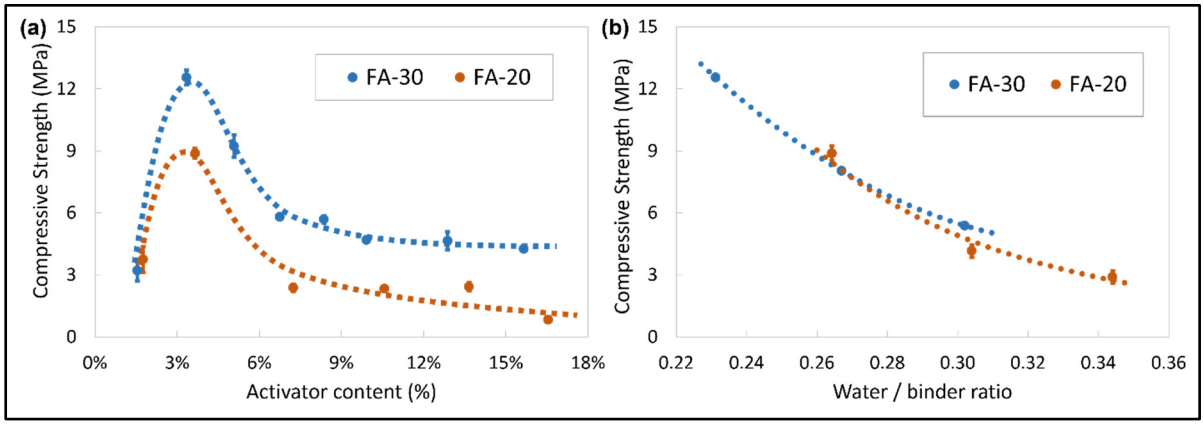

Figure 3.2 The compressive strength in MPa of AAM with varying (a) activator content and (b) water/binder ratio.

Metakaolin-based AAM were prepared by exchanging the fly ash for two types of metakaolin while maintaining the optimum activator content and minimum water/binder ratio to preserve workability. Metapor is a metakaolin product produced for the cement industry containing glass fines to make the silica content equivalent to fly ash. Metastar is a high-reactivity conventional metakaolin with a greater water demand. Table 3.4 compares the compressive strength of the AAM to evaluate the compatibility of the precursors. Both metakaolin yielded inferior mechanical strength compared to the fly ash at the same dosages (10%, 20%, or 30%). The silicon to aluminum (Si/Al) ratio is included in Table 3.4 to illustrate that the reduction in strength is not related to a change in the availability of reactive silicon or aluminum provided by the metakaolin. Metapor, with its greater content of reactive silica, gave greater performance than Metastar at each dosage level. However, this trend better correlated to the water demand of the two sources of metakaolin and the corresponding water/binder ratio required to achieve workability. The excess water, added to achieve workability in the metakaolin AAM in the wet state, limited the final strength in the hardened state consistent with the trend presented in Figure 3.2(b).

Table 3.4 Compressive strengths of AAM with each precursor with constant activator content.

Sample ID	Precursor : Dry BR[1]	Precursor	Si/Al ratio[2]	Water/binder ratio[3]	Compressive strength (MPa)[4]
FA-10	10% : 90%	ProAsh	0.14	0.31	2.7
MP-10		Metapor	0.14	0.31	2.6
MS-10		Metastar	0.13	0.34	1.3
FA-20	20% : 80%	ProAsh	0.22	0.27	8.3
MP-20		Metapor	0.22	0.33	5.5
MS-20		Metastar	0.19	0.36	3.1
FA-30	30% : 70%	ProAsh	0.31	0.24	12.6
MP-30		Metapor	0.31	0.33	4.3
MS-30		Metastar	0.25	0.42	3.1

[1]: Weight ratio of supplemental precursor to the BR, neglecting the water content of the BR.
[2]: Molar ratio accounting for contributions of all components.
[3]: Water binder ratio, accounting for the water content in the BR and added water
[4]: Measured after 7 days of curing at 60ºC.

The fly ash AAM showed good compatibility with the one-part mixing process, prompting further investigation of the effect of the curing rate and activator composition. Curing at 60ºC was adopted as a reference because it is the most common temperature for elevated curing in the literature (Hertel & Pontikes, 2020). At this temperature, the strength develops gradually reaching a plateau at seven days, as shown in Figure 3.3(a). Curing at 80ºC increases the final strength by at least 20%, shown in Figure 3.3(b), and accelerates the process, achieving final strength within five days. Room temperature curing was found to be incompatible with this AAM, granting the AAM only a few MPa in the first month. This is consistent with other studies of BR and fly ash blends which exhibited significantly greater strength development under heated curing conditions than ambient ones (W. Hu et al., 2018).

The activator content was varied by blending anhydrous sodium metasilicate and sodium hydroxide while maintaining a constant molar sodium content. With this technique, the strength was improved by up to 35% but the optimum activator blend was found to vary based on the content of fly ash, as shown in Figure 3.3(c). Prior studies using two-part mixing methods corroborate the effect of adding reactive silicate to modify the AAM composition and bolster the mechanical strength (W. Hu et al., 2018). The addition of calcium salts have similarly been found to improve AAM strength, in certain dosages, due to the formation of sodium/calcium alumina-silica-hydrates (N/C-ASH) gels which have a greater degree of crosslinking (Chindaprasirt et al., 2018). No prior study has applied this principle to BR AAM. In the higher FA composition, the strength increased by up to 15%. However, in the case of lower fly ash which has lower silica content, the added calcium primarily competes with sodium for bonding sites, leading to diminishing strength through the same mechanism that weakens cement.

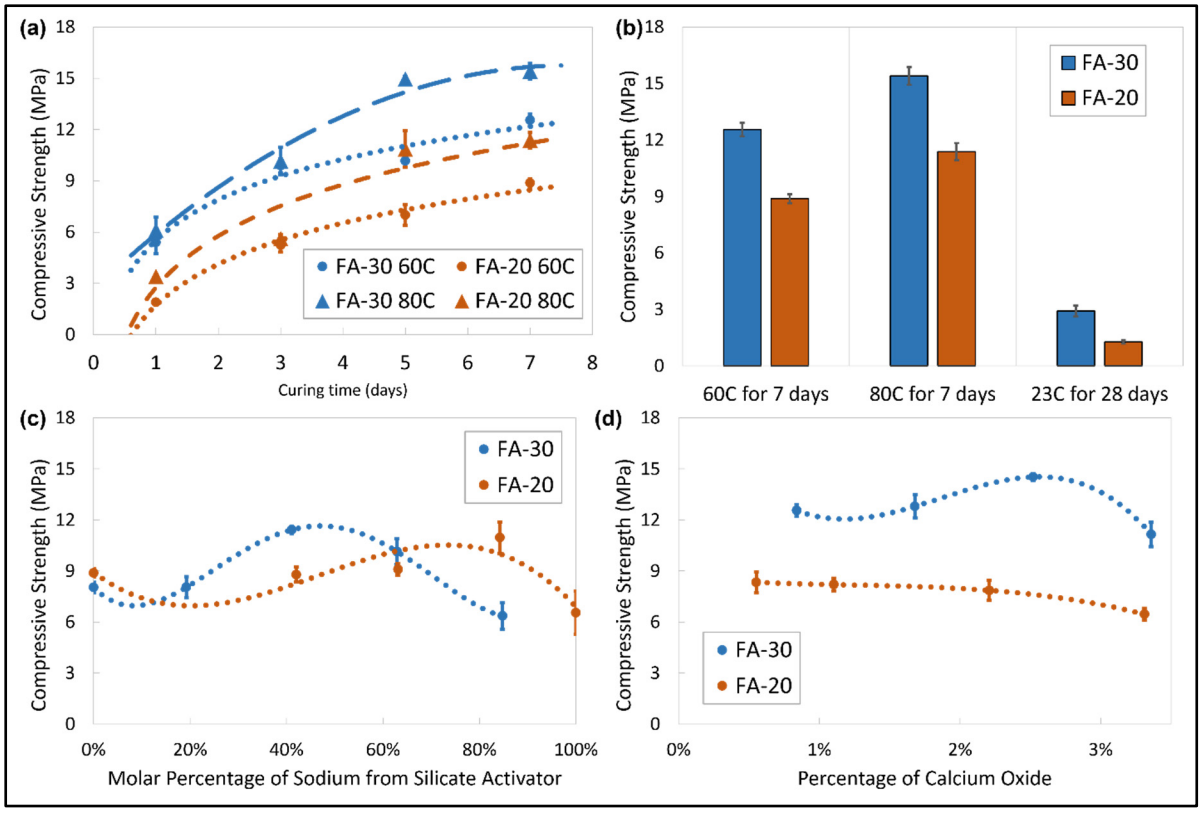

Figure 3.3 (a) The strength development and the (b) final compressive strength in MPa of AAM under different curing conditions. The compressive strength of AAM based on (c) the activator composition and (d) the total calcium content, maintaining constant activator content and water/binder ratio.

With compositional optimization, the one-part mixing process produced AAM with high BR content. The specimen FA-20-4s was composed of 76% BR and exhibited compressive strength above 11 MPa. Only a few studies in the literature have produced AAM containing a comparable quantity of BR without calcination. These studies reached only 5-7 MPa using two-part mixing methodologies (Zhang 2010, Li 2019). Two-part methodologies utilizing calcination to bolster the reactivity of BR as the sole precursor have been shown to exhibit strength between 6-9 MPa (Hairi, Jameson, Rogers, & MacKenzie, 2015 ; Ye et al., 2014). However, greater properties have been obtained through the combined thermal and chemical modification of BR with calcination (Hertel, Blanpain, et al., 2016 ; Hertel, Iacobescu, et al., 2016). Results comparable to those of two-part methods have been achieved with pseudo-one-part alkali-thermal activation of BR to reach strengths of 7-10 MPa (Ke et al., 2015 ; Ye et al.,

2016). The one-part AAM produced in this study meets or exceeds the strength of those in the literature while eliminating the need for calcination.

With a compressive strength of 11 MPa, the one-part AAM exceeds the requirements for ASTM C62-NW (ASTM International, 2017) which mandates 8.6 MPa for interior bricks. BR AAM are a circular economy solution to brick masonry to reduce the environmental impact of construction without compromising mechanical properties. AAM require less virgin raw materials than clay bricks or cement blocks. The one-part mixing process eliminates the drying, grinding and heat treatment required for brick sintering or cement clinker production, maximizing the advantages of BR-based construction materials.

3.3.3 Effect of composition on porosity and surface area

Measurements of the water absorption were conducted as a preliminary assessment of the differences in microstructure caused by the compositional parameters. The results are presented in Table 3.5 alongside the corresponding compressive strength, to illustrate the lack of correlation between these two properties. The results are grouped by the compositional parameter being investigated, which reveals that only the change in the precursor type and the activator content substantially affect the porosity of the AAM. Metakaolin AAM are 14% more porous than their fly ash counterparts. This agrees with prior studies of AAM microstructures and the enhanced mesoporosity in metakaolin AAM (Provis et al., 2015). Changes in water/binder ratio also contribute to this change, as all AAM were prepared with the minimum content of water necessary to achieve workability, but the heightened water demand of the metakaolin necessitated greater water content. Changes to the activator type, corresponding to variation in the Si/Al ratio, or the calcium content, corresponding to the Ca/Si ratio, showed minimal effect on the porosity despite significant influence on the compressive strength. However, with lower activator contents, the porosity also increased by 20%, despite significant improvement in compressive strength. This confirms that the greater strength is not caused by densification, but instead form stronger alkali activation reaction between the BR particles. The water absorption-based porosity measurements were used to identify which AAM

compositions were most important for further microstructural characterization by mercury intrusion porosimetry and isothermal nitrogen adsorption.

Table 3.5 Summary of the porosity measurements.

Parameter	Sample ID	Na/Al ratio[1]	Si/Al ratio[1]	Ca/Si ratio[1]	Compressive strength[2] (MPa)	Porosity[2] (%)
Precursor type	MS-20	0.1	0.19	0	3.1	39
	MP-20	0.1	0.22	0.06	5.1	41
	FA-20	0.1	0.22	0.05	8.3	35
	FA-30	0.1	0.31	0.05	12.6	34
Activator content	FA-20-6a	0.2	0.22	0.05	2.4	34
	FA-20-10a	0.4	0.22	0.05	2.4	33
	FA-30-6a	0.2	0.31	0.05	5.8	28
	FA-30-10a	0.4	0.31	0.05	4.6	27
Activator type	FA-20-2s	0.1	0.24	0.05	8.8	35
	FA-20-4s	0.1	0.26	0.05	11.2	32
	FA-30-2s	0.1	0.33	0.05	11.4	34
	FA-30-4s	0.1	0.35	0.05	6.4	34
Calcium content	FA-20-1c	0.1	0.22	0.19	7.9	35
	FA-20-3c	0.1	0.22	0.28	6.5	34
	FA-30-1c	0.1	0.31	0.17	14.5	35
	FA-30-3c	0.1	0.31	0.22	11.1	35

[1]: molar ratio accounting for contributions of all components.
[2]: measured after 7 days of curing at 60ºC.

Mercury intrusion porosimetry was conducted to characterize the microstructure of the highest-performing AAM. The cumulative pore volume, shown in Figure 3.4(a), reveals that the alkali activation of BR creates micron-sized pores from the inter-particle macropores during the

recondensation reaction. The addition of these macropores dramatically increases the permeability and reduces the tortuosity compared to BR, shown in Figure 3.4(c,d). This effect diminishes with higher contents of fly ash which reduces the pore size and reduces total porosity by up to 25%. The log differential intrusion, presented in Figure 3.4(b), highlights the monomodal pore size distribution in both the BR and the AAM, and allows the quantification of the pore size reduction from 200 nm to 100 nm with increasing fly ash content.

Control of the porosity of AAM improves their function as construction materials. Construction materials benefit from low thermal conductivity, which is dependent on the porosity, to improve the passive thermal insulation of structures. The BR AAM produced from the one-part mixing process exhibit porosity between 30-40%, comparable to prior studies of metakaolin and fly ash AAM. At this level of porosity, the thermal conductivity is between 0.71 and 0.49 W/mK (Kamseu et al., 2012 ; Lassinantti Gualtieri, Cavallini, & Romagnoli, 2016), which is up to 80% lower than conventional concrete (Wadsö, Karlsson, & Tammo, 2012). This an additional advantage of BR AAM for improving insulation and long-term energy savings.

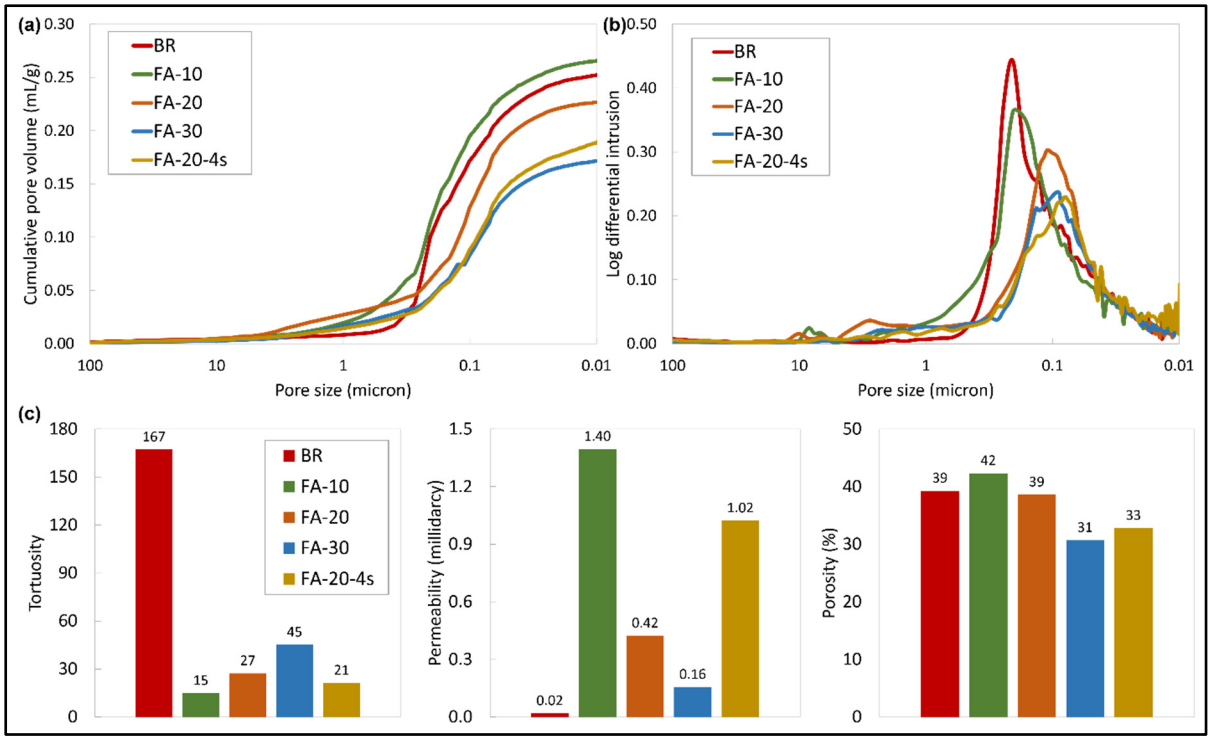

Figure 3.4 (a) Cumulative pore volume (mL/g) and (b) log differential intrusion for unreacted BR and AAM containing different proportions of fly ash. (c) The (c) tortuosity, permeability (millidarcy), and total porosity (volume %) of unreacted BR and each AAM.

The mercury intrusion porosimetry revealed that the permeability and surface area can be improved through the addition of a silicate activator. The composition FA-20-4s exhibited 100x greater permeability than BR and 35% higher strength than FA-20. The silicate activator also increased the mesopore volume by as much as 50%. However, the accuracy of mercury intrusion porosimetry is reduced in the mesopore range. To confirm these findings, isothermal nitrogen adsorption was conducted to accurately measure the volume and size distribution of mesopores. Nitrogen adsorption is capable of measuring pore volume with high accuracy but is limited to the mesopore size range (2-50 nm). The cumulative mesopore volume measurements, shown in Figure 3.5(a), reveal that FA-20-4s exhibits mesoporosity more similar to BR than the other AAM. Figure 5(b) reveals that the mesopore volume of FA-20-4s is the same as FA-20 from 20-40 nm, and then mimics the microstructural texture of raw BR at lower pore sizes. This causes the specimen to have up to 60% higher surface area than the other AAM.

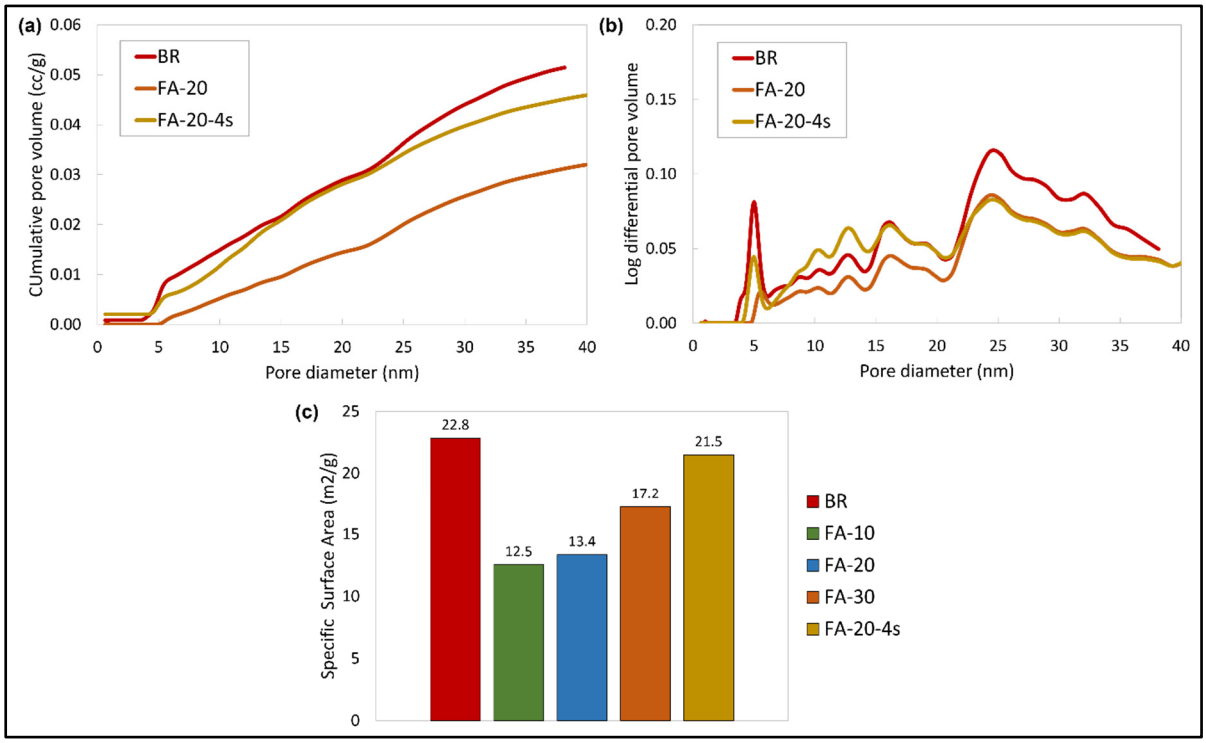

Figure 3.5 (a) Cumulative (mL/g) and (b) log differential mesopore volume distributions for unreacted BR and AAM measured isothermal nitrogen adsorption. (c) The specific surface area of each specimen in m2/g.

Enhanced permeability and surface area are valuable properties for multifunctional applications involving adsorption. BR has been demonstrated as an adsorbent for wastewater treatment of metals, such as manganese and copper, and organic pollutants (Yongchao Li, Huang, Xu, Ma, & Guo, 2020 ; Qi et al., 2018 ; Yongfeng Wang et al., 2020). Recently, a BR AAM has been shown to maintain its adsorbent properties while dramatically improving its permeability (Hertel, Novais, Murillo Alarcón, Labrincha, & Pontikes, 2019). BR AAM are a low cost and low environmental impact adsorbent which mitigate the low permeability that makes the direct use of BR unviable. Improving the surface area increases the active sites for adsorption which makes the AAM more effective as an adsorbent. The combination of high strength and improved adsorbent properties creates an opportunity to make multifunctional construction materials from BR with structural and water purifying properties.

3.3.4 Leaching performance of one-part alkali activated materials

The valorization of BR is dependent upon the pacification of trace metallic pollutants in the raw material (Gräfe et al., 2011). Many trace metals in BR are regulated by water standards and the leaching from BR AAM must be below the maximum allowable concentrations. While recrystallization reactions tend to cause the exclusion of impurities to grain boundaries which can increase leaching, alkali activated has been observed to be effective at stabilizing metallic impurities through cationic exchange (Vance & Perera, 2009). The influence of these two competing mechanisms was investigated by comparing the leaching of the AAM to the unreacted raw materials, BR and fly ash, in a weighted average. The leaching from the AAM, shown in Figure 3.6, was found to be as much as five times lower for most of the metallic pollutants compared to the raw materials. However, for nickel and selenium, the leaching was slightly enhanced indicating that cationic exchange is not successful in entrapping these impurities. Notably, composition FA-20-4s which exhibited substantially greater permeability, did not suffer from greater leaching. This agrees with prior studies of BR AAM leaching and confirms that the metallic pollutants present in BR can be effectively pacified by the alkali activation (Nguyen et al., 2018).

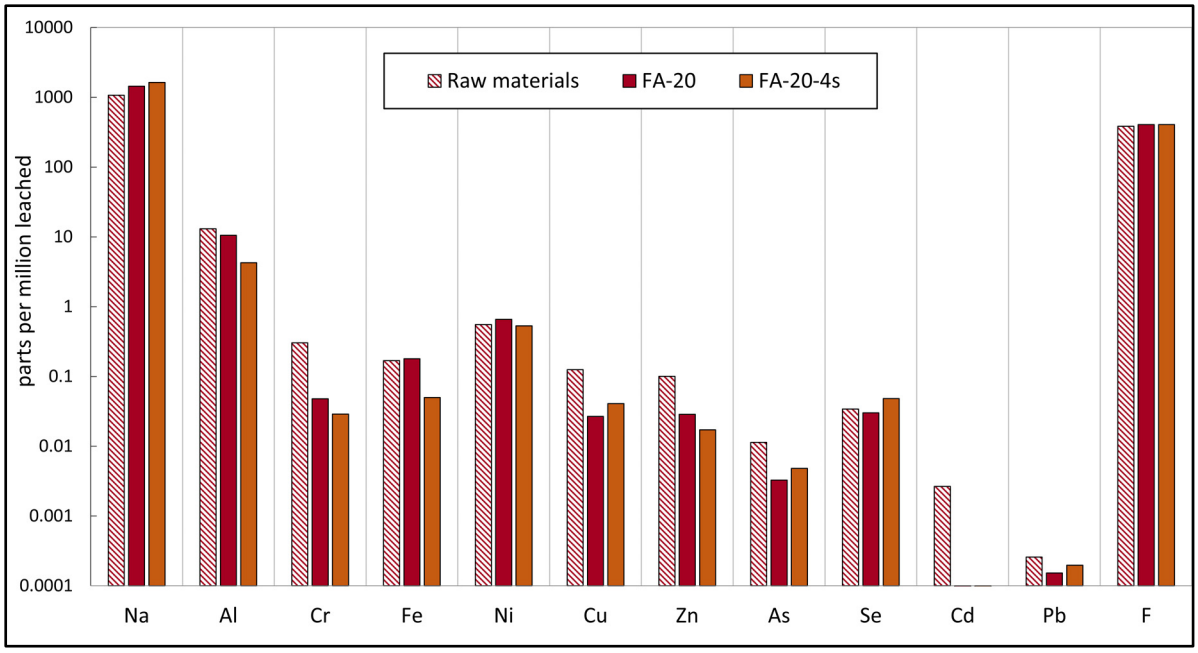

Figure 3.6 A comparison of the leaching of unreacted BR and fly ash with AAM under US EPA method 1311 conditions.

Leaching tests were conducted under acidic and neutral conditions and the results for the three highest performing AAM are listed in Table 3.6. Notably, the compositions FA-20 and FA-30 exhibited very similar leaching despite having different BR contents. This further supports the conclusion that the pollutants in the BR are being well stabilized. Contrary to expectations, the more aggressive acidic conditions led to lower leaching for many pollutants than neutral conditions. This is due to the difference in the duration of the tests. The US EPA standard 1311 is an accelerated leaching test using harsher acidic solutions and a short duration of only 18 hours. In contrast, the Quebec water leaching tests are conducted over seven days which gives more stable metallic pollutants time to disassociate from the AAM and be leached out. In particular, this is true for iron, arsenic and selenium; three metals which should be given closer attention in subsequent studies. Nevertheless, the one-part AAM leached substantially less than prior studies of two-part BR AAM. The leaching of arsenic, cadmium, and lead was reduced by a factor >100x and copper and chromium were reduced by a factor of at least 3 compared to (M. Zhang et al., 2016) and (Nguyen et al., 2018), despite these studies only using low contents (20-30%) of BR. To verify the safety of this level of leaching, the concentrations of

leached pollutants were compared to the maximum allowable concentrations for surface water in Quebec, also given in Table 3.6 (Quebec, 2021). The leachate from the one-part AAM was substantially below the required levels and this confirms that the process was successful it mitigating the ecotoxicity of BR.

Table 3.6 Leaching performance of three AAM in acidic and neutral water solutions compared to the Quebec surface water standards.

Pollutants	Maximum allowable limit (ppm)[1]	Concentration in leachate (ppm)					
		FA-30		FA-20		FA-20-4s	
		Acid[2]	Water[3]	Acid[2]	Water[3]	Acid[2]	Water[3]
Sodium	-	1338	1558	1444	2562	1630	3846
Aluminum	-	19.2	113	10.5	3.3	4.3	0.9
Chromium	-	0.06	0.20	0.05	0.17	0.03	0.19
Iron	-	0.40	17.4	0.18	1.14	0.05	0.44
Nickel	260	0.91	0.10	0.66	0.08	0.53	0.04
Copper	7.3	0.03	0.16	0.03	0.22	0.04	0.36
Zinc	67	0.04	0.09	0.03	0.14	0.02	0.04
Arsenic	340	0.006	2.36	0.003	2.42	0.005	2.15
Selenium	62	0.053	0.47	0.030	0.39	0.048	0.38
Cadmium	1.1	<0.0002	0.027	<0.0002	0.022	<0.0002	0.020
Lead	34	0.0003	0.005	0.0002	0.002	0.00020	0.0004
Fluoride	4000	406	15.4	407	24.9	406	25.6

[1]: as per Quebec standard for resurgent surface water (Quebec, 2021).
[2]: leachate under acidic conditions described by US EPA method 1311 (US EPA, 2015a).
[3]: leachate extracted under deionized water testing conditions described by Quebec CTEU-9 (QC MELCC, 2012).
"–" indicates that the maximum concentration is not defined by the standard.

3.4 Conclusion

A cost-effective reuse application for bauxite residue (BR) is a paradigm shift in the treatment of this industrial by-product. The one-part mixing methodology demonstrated in this study is the best avenue to valorize BR as an alkali activated material (AAM) for construction applications. This is the first technique developed that utilizes high contents of BR (>70%) in its raw filter-pressed form. This simultaneously increases the BR content by as much as three times while eliminating the significant environmental impact of drying and grinding, and the low scalability of conventional two-part mixing methods. One-part AAM containing 80% bauxite residue achieved as high as 11 MPa of compressive strength. This strength was double that of prior studies using comparable two-part methods without calcination and exceeds the ASTM requirements for C62-NW bricks. The results show a synergy between one-part mixing techniques with producing suitably strong materials for masonry applications while meeting surface water leaching standards. One-part AAM are a circular economy solution to brick and cement masonry that can improve the environmental impact of both the construction and aluminum industries worldwide.

CHAPTER 4

HIGH STRENGTH CONSTRUCTION MATERIAL FROM RAW BAUXITE RESIDUE BY ONE-STEP ALKALI ACTIVATION

Michael Di Mare[1] and Claudiane M. Ouellet-Plamondon[1]

[1] Department of Construction Engineering, École de Technologie Supérieure, 1100 Rue Notre-Dame Ouest, Montréal (QC), Canada

Paper published in *Journal of Sustainable Metallurgy*, December 2022 (with minor changes)

4.1 Introduction

Bauxite residue is a globally accumulating waste product, and the development of a valorization technique is needed as a long-term solution to mitigate its production. The lack of valorization options for bauxite residue (BR) is a gap in the sustainability of the aluminum industry, recognized in the international 2022 Circularity Gap Report and by the Aluminum Stewardship Initiative, a global non-profit organization advocating for the sustainability in aluminum production. The global aluminum industry produces 150 million tons of BR per year, but less than 3% of the waste is reused by current technology (Evans, 2016). The field of construction is in sore need of greener construction materials with lower consumption of virgin raw materials and environmental impact (Di Mare et al., 2021 ; Habert et al., 2020). Replacing the virgin raw materials with BR simultaneously reduces the environmental footprint of both the construction and the aluminum sectors. However, the high alkalinity of BR severely limits the content that can be used in concrete without compromising the mechanical integrity by detrimental alkali-silica reactions (Hewlett & Liska, 2019 ; Venkatesh et al., 2019). An alternative binder chemistry is required to utilize large concentrations of BR in construction materials.

Alkali activation of BR can produce construction materials with higher proportions of BR than is possible with Portland cement. Alkali activated materials (AAMs) have received heavy scientific scrutiny as an environmentally friendly alternative to cement. The principal challenge in producing BR-based AAM is maximizing the BR content while meeting the ASTM standards for construction materials which require the compressive strength to exceed 28 MPa. A plethora of studies have investigated the optimal chemical and phase compositions to meet this requirement (Hertel & Pontikes, 2020 ; Hertel et al., 2022 ; Ye et al., 2017). However, comparatively few studies have evaluated process-property relationships for the alkali activation of BR as a means of achieving this goal. In this study, a new mixing methodology is demonstrated that utilizes a pugmill compressive mixer traditionally used only for the production of ceramic pottery. In a novel discovery, compressive mixing synergizes strongly with the alkali activation of BR and allows the production of high-strength AAMs containing 77% BR. This methodology eliminates the need for the energy-intensive process of calcination and triples the proportion of BR compared to other fly ash-based BR AAM techniques (Arnout et al., 2017 ; A. Kumar & Kumar, 2013). The strength development, microstructure, and leaching behavior of this new BR AAM have been characterized to assess the viability of the AAM as a construction material.

4.2 Experimental procedures

Alkali activated materials (AAMs) were prepared from bauxite residue using a one-step mixing procedure. Filter-pressed bauxite residue (BR) was produced in Quebec, Canada, and received in its raw, wet state from Rio Tinto. The water content in the BR was measured to be 25.4%. Fly ash from Titan America, tradename ProAsh®, was used as a supplementary binder. The chemical composition and density of the BR and fly ash used are given in Table 4.1. Anhydrous, reagent-grade calcium hydroxide (slaked lime) was added to moderate the calcium content. A combination of anhydrous, reagent grade sodium metasilicate and sodium hydroxide were used as alkali activators. The components were added in the quantities specified in Table 4.2 to the mixing chamber and mixed without any drying, pretreatment, premixing, or modification. All the components were mixed simultaneously in a single step in

a Peter Pugger® brand pugmill operating at 15 rpm. After mixing for twenty minutes, the resulting paste was extruded out of the pugmill, shaped, and cured, as shown in Figure 4.1. To comply with ASTM standard C109 (ASTM International, 2020b), the paste was cast into 5 cm stainless steel molds and sealed to prevent moisture loss. Curing was conducted at 60ºC in a saturated humidity chamber. The compressive strength was measured after 1, 3, and 7 days under constant loading of 1 kN/sec, as per ASTM C109.

Table 4.1 Chemical composition of the bauxite residue and fly ash raw materials

Equivalent oxide composition (%), dry	Bauxite residue	Fly ash
Al_2O_3	74.7	21.4
SiO_2	6.7	55.3
Na_2O	0.01	1.0
Fe_2O_3	16.0	10.2
CaO	0.03	3.4
Moisture content (%)	25.4	-
Specific gravity	2.79	2.65

Table 4.2 Composition of the alkali activated material

Component	Quantity (g)
Raw bauxite residue	5000
Grade C fly ash	933
Calcium hydroxide (slaked lime)	217
Sodium metasilicate	283
Sodium hydroxide (lye)	36

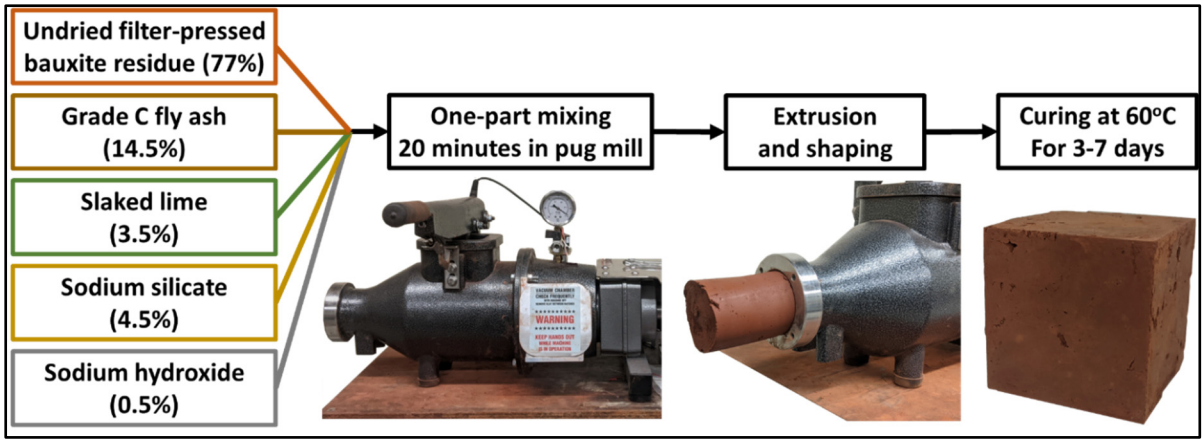

Figure 4.1 One-step mixing, extrusion and curing process used for the production of high strength alkali activated materials containing 77% unmodified filter-pressed bauxite residue.

The microstructure of the AAM was characterized using mercury intrusion porosimetry and isothermal nitrogen adsorption. The AAM was dried and gently fragmented into 5-10 mm pieces for microstructural analysis to avoid undue distortion of the microstructure. The macropore size distribution, total porosity, permeability, and density were measured using a Micromeritics Autopore® porosimeter. The volume of mesopores was characterized by the Barret-Joyner-Halenda method and the specific surface area was calculated by Brunauer-Emmet-Teller theory with a Micromeritics Gemini® analyzer. The leaching behavior of the AAM was assessed in accordance with EPA method 1311 and Quebec method CTEU-9 (QC MELCC, 2012 ; US EPA, 2015a). The AAM was ground and sieved below 75 microns. For method 1311, the ground sample was combined with a 2.88 pH solution prepared with acetic acid at a ratio of 1:20 by weight and mixed for 18 hours. For method CTEU-9, the ground sample was mixed at a ratio of 1:4 with a 7.0 pH solution of deionized water for 7 days. Mixing was conducted in polypropylene vials, at 30 rpm, in the manner specified by both leaching standards. After mixing, the leachate solutions were filtered with 0.45-micron glass filters. A portion of each solution was acidified to pH of 1 using nitric acid and analyzed for trace metals with a ThermoFisher Scientific® inductively coupled plasma mass spectrometer. The remaining portion of each solution was analyzed for fluoride content using an ion-specific electrode.

4.3 Results and discussion

The pugmill mixing procedure produced alkali activated materials (AAMs) with exceptionally high strength. The specimens exceed 30 MPa, as shown in Figure 4.2(a), after only 3 days of heated curing; gaining more than 90% of their final strength in this time. The strength of the AAM exceeds the 28 MPa required by ASTM standards for several applications as precast structural components including concrete barriers (C825 (ASTM International, 2019b)), retaining wall members (C915, C1776 (ASTM International, 2018b, 2022b)), underground utility, wastewater and storm drain structures (C858, C913, C1504 (ASTM International, 2019a, 2020d, 2021b)), manhole sections (C478 (ASTM International, 2020c)), septic tanks (C1227 (ASTM International, 2022c)), and brick masonry (C62 (ASTM International, 2017, p. 62)). This presents a variety of applications for environmentally friendly structural materials composed primarily of BR.

A key advantage of the pugmill methodology is the use of BR in its raw, filter-pressed state, as received from the aluminum production facility. The pugmill methodology does not require the BR to be dried and milled to bolster reactivity. This deviates significantly from conventional methodologies and allows all the mixing to be conducted in a single step without additional pretreatment stages; greatly simplifying the production process. The only similar study in the literature to use undried BR limited the BR content to 24% (Arnout et al., 2017). With the new methodology, the proportion of BR can be tripled to 77% while maintaining high strength. The compressive strength is five times greater than comparable studies of BR-fly ash AAMs prepared with traditional two-part mixing methodologies which achieved only 5 – 7 MPa when containing 70-80% BR (Yuancheng Li et al., 2019 ; G. Zhang et al., 2010). This demonstrates the synergy between the compressive pugmill mixing and the stronger alkali activation reactions in the BR without the need for additional processes to improve the reactivity, such as milling and calcination.

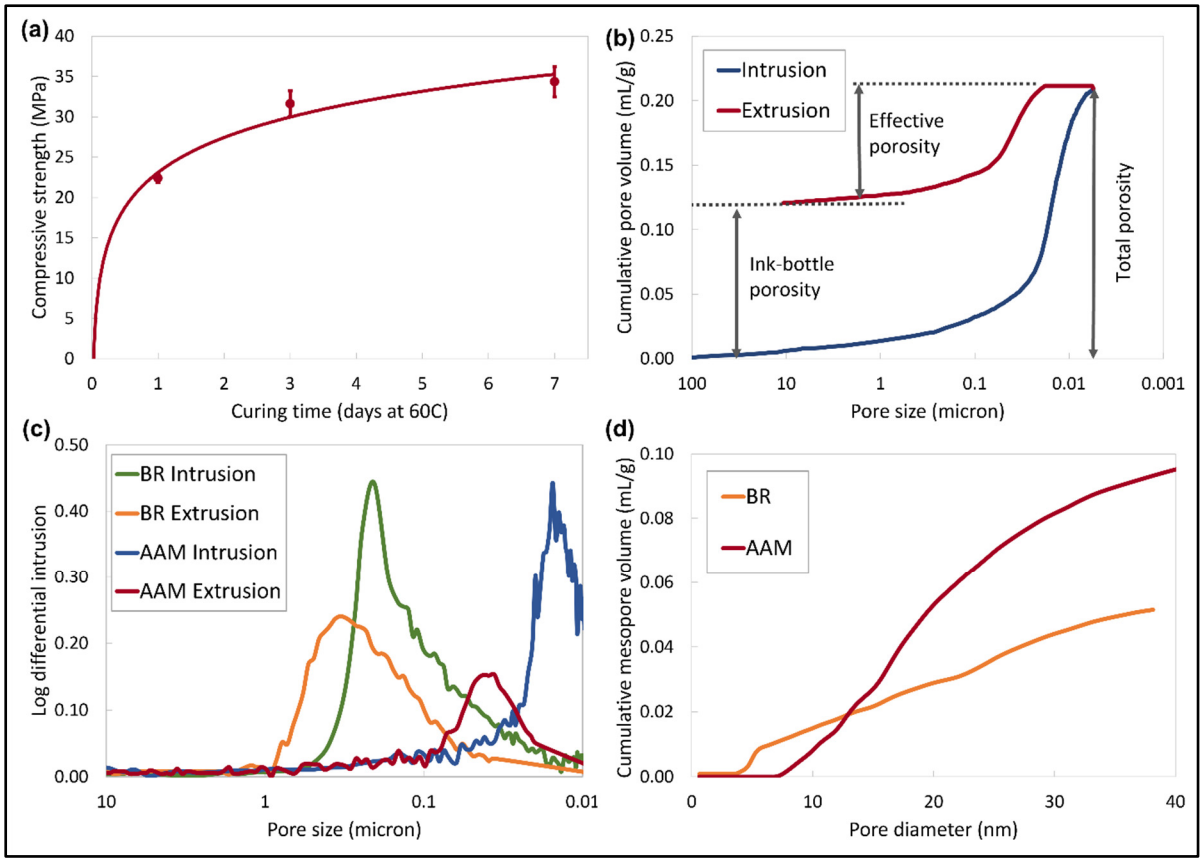

Figure 4.2 (a) The compressive strength in MPa of alkali activated materials (AAM) during heated curing. (b,c) Mercury porosimetry showing (b) the intrusion and extrusion of the AAM in mL/g and (c) the pore size and neck size distributions in microns of the AAM and bauxite residue (BR). (d) The mesopore volume in mL/g of the AAM measured using isothermal nitrogen adsorption.

To characterize the microstructure of the material, the AAM was analyzed by mercury porosimetry and nitrogen adsorption. The intrusion and extrusion of the AAM, shown in Figure 4.2(b), a reveal a strong ink-bottle effect. This indicates a high degree of constriction between the true pore diameters and connective pore necks. While the total porosity of the AAM is 34%, the effective porosity is less than half of this because of this constriction. The pore size distribution, illustrated in Figure 4.2(c), is monomodal. The extrusion of the AAM specimen reveals that the median pore size is 40 nm, and the intrusion shows that the pores are linked by necking points of diameter 15 nm. The pores are significantly smaller than raw BR which has pores of 300 nm and less constriction. The increased mesopore volume of the AAM is confirmed by isothermal nitrogen adsorption, shown in Figure 4.2(d), which shows that it is

more than twice that of raw BR. The microstructural properties calculated from the porosimetry are listed in Table 4.2. The permeability is increased by more than one hundred-fold, making the AAM a borderline semi-pervious material (Bear, 1988).

Table 4.3 The properties of the alkali activated material after seven days of curing at 60ºC compared to raw bauxite residue.

Property	Bauxite residue	Alkali activated material
Compressive strength (MPa)	-	34.4
Total porosity (%)	39.3	34.3
Effective porosity (%)	28.6	14.9
Permeability (millidarcy)	0.02	5.63
Bulk density (mg/L)	1.54	1.64
Skeletal density (mg/L)	2.54	2.49
Specific surface area (m^2/g)	22.8	24.9

The valorization of bauxite residue presents a unique challenge due to its ecotoxicity (Gräfe et al., 2011). Prior studies have shown that alkali activation is effective at stabilizing trace toxins in BR, making the AAM safe for use (Bobirică et al., 2020 ; Nguyen et al., 2018 ; M. Zhang et al., 2016). However, no prior study has investigated the leaching of AAM which contained high contents (>50%) of BR. In this study, an accelerated acid leaching test (EPA 1311) and a water-based leaching test (QC CTEU-9) were conducted to determine the safety of this unique AAM containing 77% BR (QC MELCC, 2012 ; US EPA, 2015a). A summary of the results is shown in Figure 4.3, alongside the maximum allowable concentrations for surface water in Quebec, Canada, where the BR was produced (Quebec, 2021). The alkali activation was successful in stabilizing the trace pollutants in the BR, making them unavailable for leaching. The results under both acidic and neutral leaching conditions were similar and varied based on the specific pollutant. In general, the EPA 1311 procedure yielded lower leaching due to the lower sample / solution ratio. In all cases, the leaching of the AAM was significantly below the maximum allowable concentration, demonstrating that the AAM can be used as a construction material without risk of ecotoxicity.

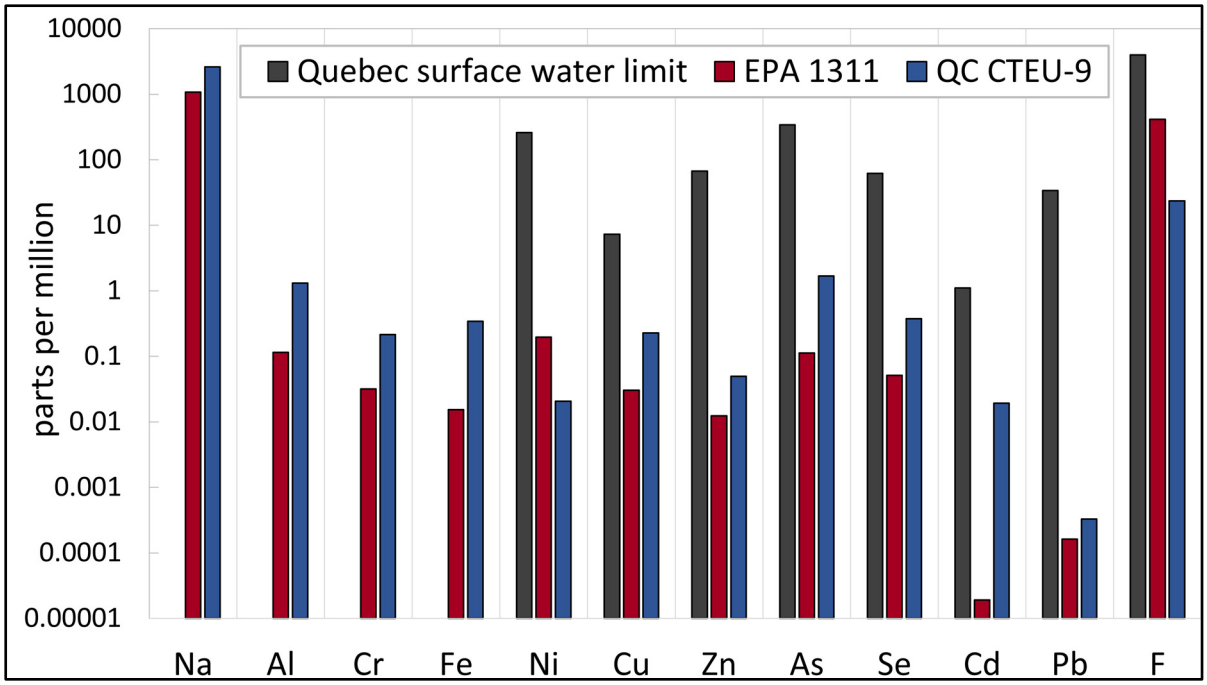

Figure 4.3 The water leaching (QC CTEU-9) and accelerated acid leaching (EPA 1311) behavior of the alkali activated material compared to the maximum allowable concentrations for resurgent surface water in Quebec in parts per million. The limit for sodium, aluminum, chromium, and iron are not defined by the standard.

4.4 Conclusion

The bauxite residue (BR) alkali activated materials (AAMs) are an environmentally friendly construction material that addresses the circularity gap that exists in aluminum production and improves the sustainability of both the aluminum and construction sectors. With the novel pugmill mixing methodology demonstrated in this work, AAMs can be produced containing 77% unmodified BR, eliminating the need for costly and energy-intensive preprocessing steps. The AAMs reach 34 MPa in only three days of curing, exceeding ASTM requirements in numerous standards for retaining walls, brick masonry, and wastewater infrastructure. Leaching analysis confirms that the strong alkali activation effectively pacifies the ecotoxicity of the BR. With this new mixing methodology, BR AAMs are a circular economy solution to reduce the impact of the aluminum sector on the environment by valorizing large contents of BR as an environmentally friendly construction material.

.

CHAPTER 5

HIGHLY PIEZORESISTIVE, SELF-SENSING, ONE-PART POTASSIUM ACTIVATED INORGANIC POLYMERS FOR STRUCTURAL HEALTH MONITORING

Michael Di Mare[1] and Claudiane M. Ouellet-Plamondon[1]

[1] Department of Construction Engineering, École de Technologie Supérieure, 1100 Rue Notre-Dame Ouest, Montréal (QC), Canada

Paper published in *Materials Today Sustainability*, October 2022 (with minor changes)

5.1 Introduction

Structural health monitoring is an emerging technology in construction that will fundamentally change the maintenance and repair of concrete buildings. The technology relies on the deployment of self-sensing construction materials in structural members which are capable of reporting changes in their mechanical state. This enables real-time monitoring of structural changes due to corrosion, seismic damage, or structural decay (Tian et al., 2019). With improved information, structural health monitoring will make the repair of infrastructure localized and preventive: stopping sites of decay before the impact is systemic (Reddy, Kavyateja, & Jindal, 2021). This will substantially reduce the cost of maintenance and prolong the service life of concrete structures and infrastructure. The deployment of structural health monitoring is limited by the availability of self-sensing construction materials. Two principal obstacles that stymie the availability of these materials are high cost and low scalability. These problems arise because Portland cement is not intrinsically self-sensing. It must be combined with conductive additives, preferably fibers such as carbon fiber, to form a self-sensing composite. Cement composites are self-sensing through their piezoresistivity: a measurable reduction in electrical resistance during compression. Carbon fiber-cement composites can

achieve piezoresistivity of 10-30% which is suitable for a variety of self-sensing applications (Azhari & Banthia, 2012 ; M. Chen, Gao, Geng, Zhang, & Liu, 2017 ; Donnini et al., 2018). However, the reliance on conductive fibers to form self-sensing composites poses multiple problems for the deployment of this technology in the construction sector.

The piezoresistivity of cement composites arises from the tunneling of electrons between the conductive fibers. Cement is an insulating matrix, and the electrical conductivity of cement composites is dominated by the tunneling between the fibers (García-Macías et al., 2018). The tunneling effect is strongly influenced by the distance between the fibers, which is minutely reduced under compressive strain, leading to a macroscopic piezoresistivity. However, because of the extreme sensitivity to the distance fiber spacing, the piezoresistivity of cement composites is highly vulnerable to dispersion irregularities (Galao, Baeza, Zornoza, & Garcés, 2014 ; Han et al., 2012). This has led the reported piezoresistivity of cement composites in the literature to vary substantially due to inconsistencies in dispersion methods. In one example, a change in the superplasticizer was reported to increase the piezoresistivity by more than 10x (Han et al., 2012). This presents a problem for the scalability of the technology in the field of construction. Inconsistencies in mixing with different equipment and volumes of production could easily compromise the self-sensing performance.

Proponents of self-sensing cement composites have ambitiously touted these materials as a cost-saving and green solution for the future of construction. Cement production is the singularly largest material contributor to global greenhouse gas emissions (Andrew, 2018). Structural health monitoring will prolong the service life of concrete structures thereby reducing maintenance costs and cement consumption. However, few studies have quantified the economic and environmental impact of the conductive fibers required to produce self-sensing cement composites (Gupta et al., 2017 ; Papanikolaou, Arena, & Al-Tabbaa, 2019). Many techniques have been investigated to reduce the quantity of conductive fiber required to achieve high piezoresistivity. The most effective method, the use of carbon nanotubes, reduces the required fiber content by at least a factor of 10 (Yoo, Kim, et al., 2018). However, the use of nanoparticles amplifies the dispersion sensitivity and the economics of this technique remain uncertain. One study concluded that the use of carbon nanotubes in this manner would increase

the cost of cement composites by a factor of 100x compared to ordinary concrete (Gupta et al., 2017).

Additional complications arise from the physical properties of cement composites and the manner of measuring their piezoresistivity. Carbonaceous additives, including carbon fiber and carbon nanotubes, substantially reduce the workability of cement (Banfill, Starrs, Derruau, McCarter, & Chrisp, 2006 ; Bhojaraju, Mousavi, Brial, DiMare, & Ouellet-Plamondon, 2021 ; H. Wang, Gao, & Wang, 2017). Recent studies have shown that the piezoresistivity of self-sensing cement composites has limited longevity due to breakdown at the fiber-matrix interface (H. Li et al., 2008 ; H. Wang et al., 2018). Another problem arises from the conventional manner of measuring piezoresistivity. The vast majority of piezoresistivity measurements are conducted under cyclic loading conditions, where the resistance is measured with direct current while the compressive load is oscillated (Han et al., 2015). This method simulates applications involving transient changes in compression, such as vehicle detection on roadways (Han, Yu, & Kwon, 2009). Cyclic loading, however, is not representative of structural health monitoring applications where gradual changes in static loading indicate corrosion or structural decay. The effectiveness of a self-sensing material for structural health monitoring is better simulated using static loading conditions. However, very few studies have employed static load testing because of the high polarization of cement. Polarization causes the measured electrical resistance under direct current measurements to increase with time which distorts the measurements of the piezoresistivity (Xuli Fu, Ma, Chung, & Anderson, 1997). Methodologies utilizing alternating currents, such as the one proposed by *Vaidya et al.*, remedy this polarization problem but have not seen widespread adoption in the field (Vaidya & Allouche, 2011).

The high cost, low scalability, and questionable longevity have stalled the implementation of self-sensing cement composites and, to date, there is no real-world infrastructure that employs this technology (Tian et al., 2019). There is a distinct need for an alternative self-sensing material without the problems of cement composites. Very recently, a promising candidate for this role has been found in alkali activated materials (AAMs). First documented by *Saafi et al.*, AAMs exhibit piezoresistivity as an intrinsic material property and, thus, do not require need for conductive fibers to act as self-sensing construction materials (M. Saafi et al., 2018). Prior

studies of AAMs without conductive fibers did not measure any piezoresistivity using direct current (Deng et al., 2019 ; Cecílie Mizerová et al., 2021). However, the work by *Saafi et al.* innovated by using an alternating current-based measurement method to avoid the detrimental impact of polarization. With this methodology, AAMs were found to be piezoresistive under static loading conditions, making them ideal self-sensing materials for structural health monitoring applications.

In addition to intrinsic piezoresistivity, AAMs offer numerous advantages over cement as a sustainable structural material. AAMs are natural composites formed from so-called AAM precursors, rich in reactive aluminosilicates. AAMs have been extensively studied as an environmentally friendly cement alternative because several industrial by-products, such as fly ash and blast furnace slag, can be used as AAM precursors (Duxson & Provis, 2008). This causes AAMs to have up to 80% lower global warming potential than Portland cement (Habert & Ouellet-Plamondon, 2016). Many studies on AAMs have demonstrated better workability (Alonso et al., 2017 ; Jang et al., 2014), higher strength (Y. Ding et al., 2016 ; Part et al., 2015), and greater durability (Susan A Bernal & Provis, 2014 ; Jian Zhang, Shi, Zhang, & Ou, 2017) than cement. However, the properties of an AAM are strongly influenced by its chemistry. Generally, AAM are known to be composed of NASH (sodium-aluminum-silicon-hydrate) or KASH (potassium-aluminum-silicon-hydrate) gels which form amorphous polymer chains. The chemistry of these polymer chains can be defined by its alkali content, typically described as an alkali / aluminum or alkali / silicon ratio, and its mer structure, defined by the silicon / aluminum ratio. These two compositional parameters determine the number of bridging oxygens and the proportion of siloxo to di-siloxo mers within the polymer structure (J. Davidovits, 1991).

These compositional factors have a strong impact on the mechanical and electrical properties of AAMs (Hanjitsuwan et al., 2014 ; Rowles & O'connor, 2003). Their relationship to piezoresistivity, an electromechanical property, is entirely unknown. The original work by *Saafi et al*. demonstrated intrinsic piezoresistivity of only a single composition of potassium AAM (K-AAM) (M. Saafi et al., 2018). A recent study has corroborated the measurement and test methodology using a sodium AAM, with lower piezoresistivity (Di Mare, Inumerable, Brisebois, & Ouellet-Plamondon, 2022). However, no investigation has confirmed the intrinsic

piezoresistivity of potassium AAMs nor determined the effect of composition on the piezoresistivity of AAMs. This study seeks to address these two research gaps and determine the optimum composition of potassium AAMs to maximize the piezoresistive performance.

5.2 Materials and methods

5.2.1 Materials

K-AAMs were prepared by the alkali activation of fly ash. ProAsh® fly ash from Titan America was used and composed of 21.4 wt% aluminum oxide, 55.3 wt% silicon oxide, and 1.0 wt% sodium oxide. An array of AAMs compositions was prepared to achieve potassium / aluminum (K/Al) elemental molar ratios between 0.8 and 1.2, and silicon / aluminum (Si/Al) elemental molar ratios between 2.5 and 3.2. The elemental and mixing proportions of the compositions tested are listed in Table 5.1. The samples were identified with a sequence of two numbers: the K/Al ratio and the Si/Al ratio. Silica fume (4.8% moisture) was added to modulate the Si/Al ratio. Dry reagent grade potassium hydroxide (12% moisture) was the primary activator. For samples C-33, C-67, and C-100, the 33%, 67%, or 100% of the potassium hydroxide was substituted for anhydrous reagent grade potassium carbonate while maintaining the same K/Al ratio. A constant water / binder (W/B) ratio of 0.20 was maintained for all samples to achieve a flowable paste across the range of compositions. The water / binder ratio is defined by the weight ratio of the total water content to the dry weight of the other components that form the AAM. Specimen were demarcated by an identifier composed of their K/Al ratio followed by their Si/Al ratio. For example, the specimen with K/Al ratio of 1.0 and Si/Al ratio of 3.2 were identified as “1.0/3.2”, as specified in Table 5.1

Table 5.1 Summary of the alkali activated materials prepared

Sample ID	K / Al ratio[1]	Si / Al ratio[1]	W / B ratio[2]	Fly ash (g)	Silica fume (g)	Potassium hydroxide (g)	Potassium carbonate (g)	Deionized water (g)
0.8/2.5	0.8	2.50	0.20	500	41.2	92.5	0	113.7
0.8/2.85	0.8	2.85	0.20	500	85.4	92.5	0	120.4
0.8/3.2	0.8	3.20	0.20	500	116.7	92.5	0	127.1
1/2.5	1.0	2.50	0.20	500	41.2	119.2	0	115.8
1/2.85	1.0	2.85	0.20	500	85.4	119.2	0	122.5
1/3.2	1.0	3.20	0.20	500	116.7	119.2	0	129.2
1.2/2.5	1.2	2.50	0.20	500	41.2	145.9	0	117.9
1.2/2.85	1.2	2.85	0.20	500	85.4	145.9	0	124.6
1.2/3.2	1.2	3.20	0.20	500	116.7	145.9	0	131.4
C-33	1.0	2.85	0.20	500	85.4	79.4	43.0	119.6
C-67	1.0	2.85	0.20	500	85.4	39.6	86.2	128.8
C-100	1.0	2.85	0.20	500	85.4	0	129.3	138.0

[1]: Elemental molar ratios accounting for the contributions of all components.

[2]: The water / binder ratio.

5.2.2 Mixing and curing procedure

The K-AAMs were mixed in a one-part (single-step) mixing methodology in a planetary cement mixer compliant with ASTM International standard C305 (ASTM International, 2020a, p. 305). A one-part methodology based on cement mixing technology was used to maximize the scalability of the process within the current construction industry and circumvent the scalability limitations caused by the two-part mixing of AAMs (Luukkonen et al., 2018). The dry powders and water were added simultaneously to the mixer and mixed for six minutes at 45 rpm until a homogenous paste was formed. After mixing, the paste was immediately cast into steel molds coated with petroleum jelly to inhibit adhesion. The molds were sealed in zip-

top plastic bags to prevent moisture loss and cured at 60ºC for seven days under saturated humidity conditions to ensure complete hardening. Elevated temperature curing is known to be beneficial for the development of high-strength AAMs and is particularly important for one-part AAMs (Luukkonen et al., 2018 ; Suwan & Fan, 2017).

For mechanical assessment, 50 mm cube specimens were produced in accordance with ASTM C109 (ASTM International, 2020b, p. 109) and 40 mm x 40 mm x 160 mm square rods were prepared for testing as per ASTM C348 (ASTM International, 2021a, p. 348). A sample of each AAM was ground for Fourier transform infrared spectroscopy. For measurement of the piezoresistivity, molds for 50 mm cube specimens were modified with a bracket to hold a pair of electrodes in place during curing. The electrodes were galvanized stainless steel mesh cut to size 50 mm x 100 mm with a wire thickness of 0.61 mm (23 gauge) and mesh size 6.73 mm (mesh #3). The electrodes were embedded 50 mm into the cubes and held parallel at 10 mm apart in the center of one face of the specimen in the manner shown in Figure 1. Before measurement of the piezoresistivity, the specimen with the embedded electrodes were left to dry in a dry oven at 60ºC for an additional seven days. This drying process gently removed excess surface water from the AAM specimens that could interfere with the resistance measurement through surface conduction without damaging or recrystallizing the native hydrates within the AAMs.

5.2.3 Characterization methods

The compressive strength was measured in triplicate with a constant loading rate of 1 kN/sec, following ASTM C109 (ASTM International, 2020b, p. 109). The flexural strength was measured on square rod samples with a constant loading of 0.048 kN/sec, as per C348 (ASTM International, 2021a, p. 348). Fourier transform infrared spectroscopy was conducted to confirm the complete dissolution of the activator and added silica fume to achieve the targeted elemental proportions in the AAM. A full spectrum was measured across the range 400 cm^{-1} to 4000 cm^{-1}, with special attention being paid to 700 cm^{-1} to 1300 cm^{-1}, where the characteristic peaks of the alkali activation reaction and recondensation reactions occurred.

To measure the piezoresistivity, compressive stress was applied to the AAM specimen with the embedded electrodes at intervals of 1 MPa up to 10 MPa. Compressive stress was applied orthogonal to the orientation of the electrodes, as shown in Figure 5.1, such that the distance between the electrodes was reduced by the compressive strain. All measurements were made in triplicate at ambient temperature using samples gently dried using the aforementioned procedure to minimize surface conduction. At each interval of stress, the electrical resistance between the embedded electrodes was measured using a Wheatstone bridge. A Wheatstone bridge is a basic electronic circuit of three resistors used to measure the resistance of an unknown sample under an alternating current. A power source of 10 volts was applied at 10 Hz, 10 kHz, and 10 MHz across the bridge, and the sample resistance (R_{sample}) was measured at each frequency using the following equation, derived from Ohms law:

$$R_{sample} = R_3 \frac{R_2 - \frac{V_{measured}}{V_{applied}}(R_1+R_2)}{R_1 + \frac{V_{measured}}{V_{applied}}(R_1+R_2)} \qquad \text{Equation 5.1}$$

where R_1, R_2, and R_3 are the resistances of the bridge resistors in the orientation shown in Figure 5.1, $V_{applied}$ is 10 Volts, and $V_{measured}$ is the voltage across the sample measured with an oscilloscope. The sample voltage was monitored with an InfiniiVision 3034A oscilloscope from Aligent Technologies®. Resistors of 860 kΩ were used in the Wheatstone bridge to approximate the expected resistance of the AAM, based on literature values (Di Mare & Ouellet-Plamondon, 2022), and to maximize the accuracy of the measurement.

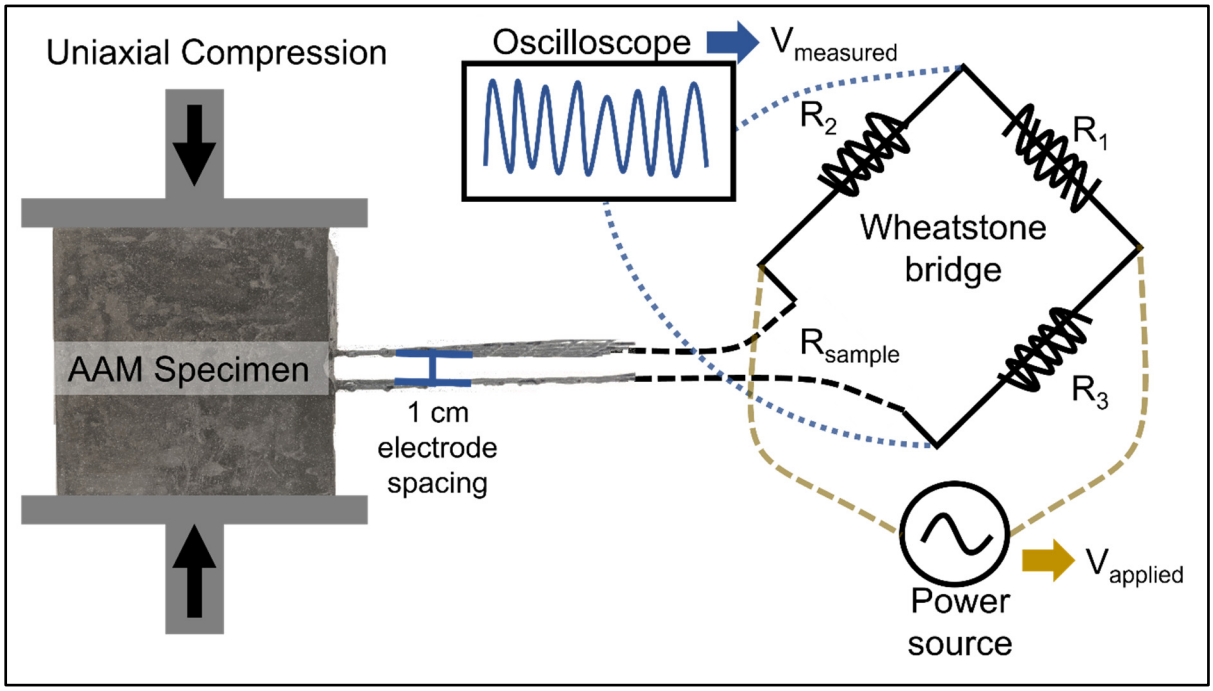

Figure 5.1 The experimental set-up for the measurement of the piezoresistivity of the alkali activated materials using a Wheatstone bridge, oscilloscope, and alternating current power source.

Following convention, the piezoresistivity of the AAMs was quantified as the fractional change in resistance (FCR) and its derivatives, the stress sensitivity coefficient and the gauge factor (Han et al., 2015). The three parameters are defined by the following equations:

$$FCR = \frac{R_\sigma - R_0}{R_0} \quad \text{Equation 5.2}$$

$$Stress\ sensitivity = \frac{FCR}{\sigma} \quad \text{Equation 5.3}$$

$$Gauge\ factor = \frac{FCR}{\varepsilon} \quad \text{Equation 5.4}$$

where R_σ is the sample resistance measured at a compressive loading of σ, R_0 is the resistance across the unstressed sample, and ε is the compressive strain. FCR is the clearest representation of the piezoresistivity, but it is dependent on the applied stress. Most commonly, only the maximum FCR measured at the maximum compressive load is discussed. Stress sensitivity and gauge factor serve as comparative tools for comparing materials tested under different levels of compressive loading (Han et al., 2015).

5.3 Results and discussion

5.3.1 The intrinsic piezoresistivity of AAMs

The intrinsic piezoresistivity of AAMs is an opportunity to make affordable and environmentally friendly, self-sensing construction materials from industrial by-products. AAMs are a cost-competitive alternative to ordinary Portland cement and their production from industrial by-products, such as the fly ash utilized in this study, offer a substantially reduced carbon footprint for a construction material. The discovery of their self-sensing functionality presents an added advantage which could see the rapid incorporation of smart construction materials in all forms of construction. This is possible because their self-sensing behavior is intrinsic and is achieved without the added cost of additives or the exotic coating methods required by conventional self-sensing technology (W. Li, Dong, Guo, Wang, & Shah, 2022). However, the intrinsic piezoresistivity in AAMs is a recent discovery and the field is not yet aware of the remarkable potential.

The piezoresistivity of AAMs has escaped scientific scrutiny thus far because its detection requires a non-standard measurement method. AAMs have been previously studied as an alternative binder to cement for self-sensing composites with carbon fiber and other conductive additives (Z. Tang et al., 2019). Nearly every study in the literature has omitted reporting the piezoresistivity of neat AAMs, AAMs without any additive, as a baseline. This is presumably because the high dielectric polarization of neat AAMs makes the measurement of the electrical resistance highly inconsistent under direct current conditions (Di Mare & Ouellet-Plamondon, 2022). This has led to the erroneous conclusion that AAMs are not intrinsically piezoresistive (Z. Tang et al., 2019). However, this hypothesis was disproven by the recent publication by *Saafi et al.* that measures the piezoresistivity using alternating current (M. Saafi et al., 2018). Without the obscuration of polarization, AAMs exhibit relatively high piezoresistivity as an intrinsic property.

Competing theories exist on the nature of the intrinsic piezoresistivity in AAMs. The property has been likened to the piezoelectricity of AAMs, another electromechanical property, which

is caused by the high mobility of alkali cations within the amorphous KASH structure (C. Lamuta, Bruno, Candamano, & Pagnotta, 2017 ; Caterina Lamuta, Candamano, Crea, & Pagnotta, 2016 ; M. Saafi et al., 2018). The alkali cations, typically sodium or potassium depending on the alkali activator, charge balance the aluminosilicate polymer network in AAMs, and are free to migrate between adjacent sites (J. Davidovits, 1991). A recent publication, corroborating the results of *Saafi et al.*, alternatively proposed that the piezoresistivity is not dominated by the ionic movement but instead by changes in the electronic mobility (Di Mare et al., 2022). However, these two works disagree on the magnitude of the measured piezoresistivity. The works did not use the same composition and it is well known that the properties of an AAM are strongly influenced by its composition. No study has yet determined what factor or combination of factors controls the piezoresistivity of AAMs.

The most significant difference between the AAMs in the two prior publications is their alkali activator. *Saafi et al.* tested potassium activated fly ash (K-AAMs) while the other used the more common sodium activated fly ash (Na-AAMs) (Di Mare et al., 2022 ; M. Saafi et al., 2018). Na-AAMs and K-AAMs are typically modeled as modified nepheline and leucite crystals, visualized in Figure 2(a). The different size of the activator cation has a substantial impact on the symmetry of the crystal structure and its geometry. To quantify the role of activator cation in the piezoresistivity, two compositions of AAMs were prepared with identical alkali / aluminum (alkali/Al) and silicon / aluminum (Si/Al) ratios using sodium hydroxide and potassium hydroxide as activators. The piezoresistivity of the samples was measured as the samples were compressed at intervals up to 10 MPa and the results are presented in Figure 2(b-d). Both specimens exhibited acceptable compressive strength, above 30 MPa, and high piezoresistivity. With these properties, both AAMs would make suitable materials for structural health monitoring applications.

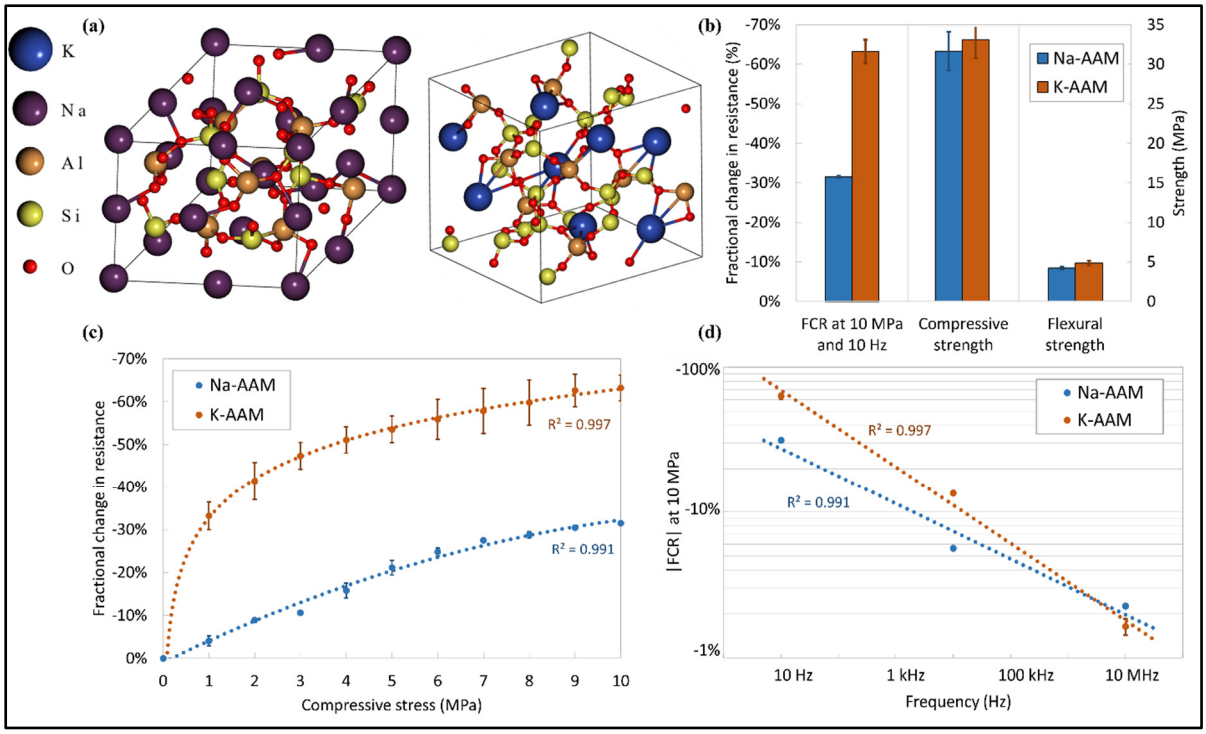

Figure 5.2 (a) Visualizations of the Nepheline and Leucite crystal structures. (b) A comparison of the piezoresistivity and mechanical properties of the sodium and potassium alkali activated materials. (c,d) The fractional change in resistance of sodium (Na-AAM) and potassium (K-AAM) alkali activated materials with alkali/Al ratio of 1.0 and Si/Al ratio of 2.85.

The K-AAMs in Figure 2(c) had a significantly greater piezoresistive response than the Na-AAMs equivalent, suggesting that KASH gels are favorable to NASH equivalents. The K-AAMs reached a FCR >60%. This is a substantial improvement over typical cement composites, which generally yield 10-30% FCR, similar to the Na-AAMs measured here (W. Li, Qu, Dong, Mishra, & Shah, 2022). While the Na-AAM is a good self-sensing material, the result confirms that the piezoresistivity is strongly influenced by the activator cation. It agrees with the prior two studies that potassium is a preferred activator for self-sensing AAMs, giving higher FCR. The FCR was also found to decline following an exponential curve at higher frequencies, as has been previously reported (Di Mare et al., 2022). However, the magnitude of the FCR measured for this K-AAM was dramatically higher than that measured by *Saafi et al.* in their work, which was 16-22% at the same frequency and compression (M. Saafi et al.,

2018). This indicates that additional compositional factors are involved in controlling the piezoresistivity of K-AAMs.

5.3.2 Compositional optimization to maximize the piezoresistivity of AAMs

The alkali content (K/Al) and chain structure (Si/Al) of the KASH in AAM strongly impact the physical, mechanical and electrical properties of AAMs (Hanjitsuwan et al., 2014 ; Rowles & O'connor, 2003). To investigate the impact of these compositional factors on the piezoresistivity, an array of compositions was prepared to expand around the initial K-AAM composition in a full factorial design. The piezoresistivity measurements at each frequency are presented in Table 2. As with the initial Na-AAM and K-AAM compositions, the piezoresistivity of the AAMs declines following a power function with frequency. The FCR was reduced below 20% at 10 kHz and became negligible in the MHz range. This trend was consistent for all of the compositions and not influenced by any of the compositional factors. At 10 Hz, exceptionally high FCR was measured for all the compositions. All the compositions were above 45% and the highest reached 67% FCR.

Table 5.2 The electrical resistance and piezoresistivity of an array of potassium activated materials

Sample ID	Resistance under a 0 MPa load (MΩ)[1]	Resistance under a 10 MPa load (MΩ)[1]	Fractional change in resistance under a 10 MPa load (%)		
			at 10 Hz	at 10 kHz	at 10 MHz
0.8/2.5	0.615	0.316	48.8	9.5	0.2
0.8/2.85	0.766	0.269	67.0	17.0	0.7
0.8/3.2	0.794	0.431	54.1	14.2	0.5
1/2.5	0.703	0.290	58.2	11.9	0.5
1/2.85	0.786	0.323	61.1	11.9	1.0
1/3.2	0.843	0.391	53.5	11.0	0.8
1.2/2.5	0.694	0.340	48.7	10.5	0.3
1.2/2.85	0.617	0.293	57.4	17.7	0.1
1.2/3.2	0.616	0.286	50.9	17.1	0.1

[1]: Electrical resistance measured with a testing frequency of 10 Hz between electrodes 10 mm apart.

Interpreting these results involves deconvolving the composition into its constituent elemental ratios. AAMs across the compositional range followed similar FCR trends with applied stress, shown in Figure 3(a). The piezoresistivity shows some nonlinearity at low stress but becomes linear at higher levels of compression. This trend, like the frequency dependence, was not influenced by the composition. The FCR measured under a compressive load of 10 MPa, showed strong dependence on both compositional factors. The FCR was improved by varying the Si/Al ratio, and an optimum was found at the midpoint of the array, 2.85. The Si/Al ratio governs the chain structure of the KASH in the AAMs. When the Si/Al ratio is between 2 and 3, the AAM is composed of a mixture of siloxo and di-siloxo mers. Above 3.0, the AAM is saturated with silica, and the excess forms crosslinking silate groups between the polymer chains (J. Davidovits, 1991). The results, shown in Figure 3(c), reveal that the piezoresistivity is maximized when the Si/Al ratio is between 2.7 and 3.0, with the FCR declining parabolically

away from the optimum. This indicates that a minority of siloxo mers distributed in a matrix of predominately di-siloxo mers is preferable for developing a KASH chain structure with strain-sensitive conductivity. An absence of siloxo mers or an excess of di-siloxo mers reduces the piezoresistive response. The optimum Si/Al ratio appears to be influenced by the K/Al ratio, which also strongly impacts the piezoresistivity.

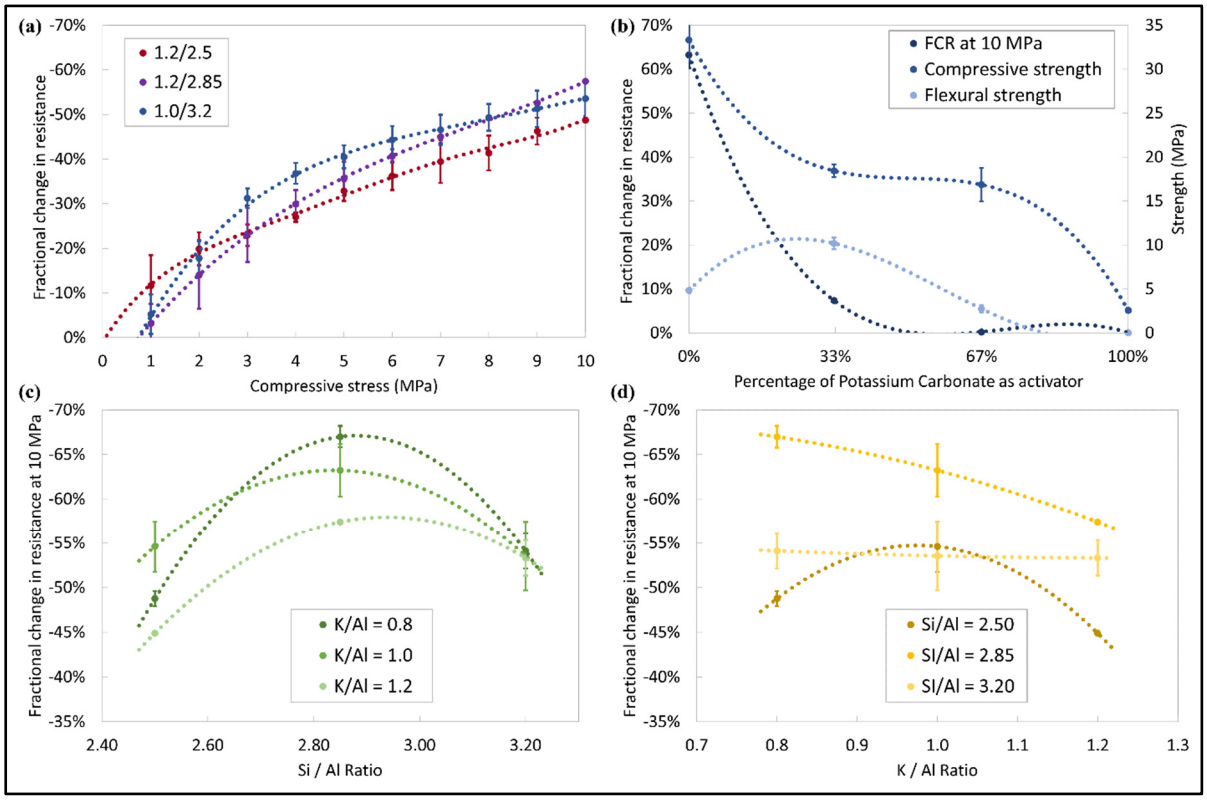

Figure 5.3 (a) The fractional change in resistance with compressive stress for AAM with different compositions. (b) The effect of potassium carbonate as an alternative activator on the piezoresistivity and the strength of the AAM. A comparison of the piezoresistivity under a compressive load of 10 MPa and with an alternating current source at 10 Hz for AAM with different (c) K/Al ratios and (d) Si/Al ratios.

The K/Al ratio has a more complicated relationship with the piezoresistivity, as shown in Figure 3(d). Potassium ions in an AAM act as charge balancing species, localized around alumina tetrahedra. When the K/Al ratio is above 1.0, there is a supersaturation of potassium ions. Contrary to expectations, this does not improve the piezoresistive response despite improving the conductivity, as listed in Table 2. Instead, the piezoresistivity declines above

1.0, indicating that these extra-stoichiometric potassium ions are mobile but not sensitive to strain. For K/Al below 1.0, the presence of potassium vacancies increases the number of bridging oxygens to compensate for the charge imbalance. When there are more siloxo mers in the KASH structure, an increase in bridging oxygens causes a reduction in the piezoresistivity. However, near the optimum Si/Al ratio the trend is reversed. A K/Al ratio below parity significantly improves the FCR up to 67%, suggesting that bridging oxygens play a critical role in the strain-sensitive conduction pathways that cause the piezoresistivity. This gives insight into the mechanisms of the intrinsic piezoresistivity in AAMs though the computational modeling of AAMs is limited and a more thorough investigation of this topic is required for a deeper analysis of the piezoresistive mechanisms (Di Mare et al., 2022).

The K/Al and Si/Al are not independent factors in controlling the piezoresistivity of the AAMs. Both factors significantly influence the piezoresistivity and their interdependence must be considered in the design of self-sensing AAMs. To visualize the relationship, the results over the full array of compositions are presented in a 3-dimensional rendering and 2-dimensional contour plot in Figure 4. In this figure, the lowest valley, shown in red, gives the greatest FCR and thus the best piezoresistivity. While there is some apparent symmetry in the topography, the relationship, even in this relatively small compositional range, is complex and dependent on both factors. This visualization allows for the facile identification of the most desirable compositional ranges to investigate for self-sensing AAMs. On the surface, it may seem that further reduction in the K/Al would be preferable for self-sensing applications. However, there are trade-offs with the mechanical properties, discussed in Section 3.3, which make this avenue impractical.

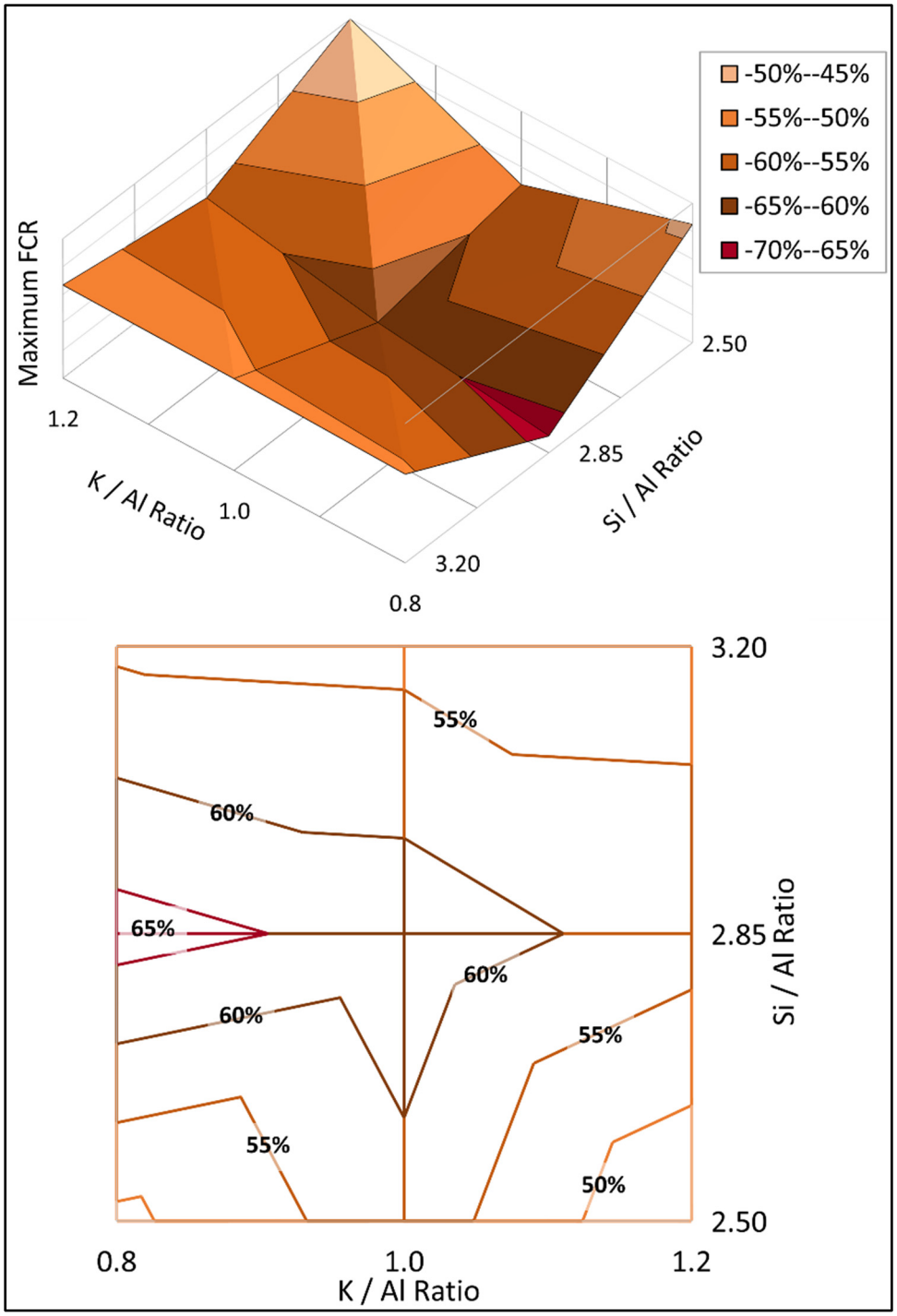

Figure 5.4 The compositional dependence of the piezoresistivity of alkali activated materials measured under a compressive load of 10 MPa and with an alternating current source of 10 Hz, shown as a 3D rendering and a 2D contour plot.

Another compositional factor that can influence the mechanical properties is the activator anion. The activator in a K-AAM is a salt of potassium and the anion in the activator can influence the mechanical properties, setting rate, and environmental impact of an AAM (Susan Andrea Bernal, 2016). A recent study of K-AAMs revealed that the electrical properties are strongly influenced by the activator anion. In that study, the conductivity was improved by several orders of magnitude by replacing the potassium hydroxide activator with potassium carbonate (Di Mare & Ouellet-Plamondon, 2022). To probe the effect of the activator anion on the piezoresistivity, a series of AAMs were prepared to partially substitute the primary activator, potassium hydroxide, for potassium carbonate between 33% and 100%, while maintaining the same elemental composition. The results, presented in Figure 3(b), show that the piezoresistivity and compressive strength decline sharply when potassium carbonate is used as the activator. The AAM, which gave a very high performance with potassium hydroxide, loses all of its piezoresistivity when 67% and 100% of the activator is potassium carbonate. This is caused by the substantially higher conductivity of the potassium carbonate AAMs achieving an effect similar to the percolation threshold in conventional cement composites (García-Macías et al., 2018). The network of conductivity becomes continuous for potassium carbonate AAMs, and resistance becomes no longer susceptible to strain. Thus, the piezoresistivity vanishes. This observation indicates the importance of the activator anion and other factors known to influence the conductivity when optimizing self-sensing AAMs.

5.3.3 The outlook for self-sensing AAMs for structural health monitoring

Self-sensing construction materials must achieve high piezoresistivity and high mechanical strength. However, a quantified definition of “high piezoresistivity” is yet to be defined. Self-sensing construction materials are in their infancy and they have not yet been tested in real-world infrastructure projects (Tian et al., 2019). As such, no criterion has been established for the level of FCR required for structural health monitoring applications. Materials with higher FCR should have significantly improved sensitivity to detect changes in compressive loading. In principle, this reduces the threshold for the early detection of corrosion or damage. Thus, maximizing the FCR improves the self-sensing performance, and no upper limit has been

identified. In contrast, mechanical requirements are well established and vary based on the application. For load-bearing structural members, an ultimate compressive strength of 28 MPa is required (ASTM International, 2020b, p. 109). However, the requirements are lower for other applications such as bricks (20.7 MPa) and non-load-bearing members (4.1 MPa) (ASTM International, 2017, 2022a, p. 129). For self-sensing materials, maximizing the FCR must be balanced by maintaining the required mechanical properties for construction applications.

The mechanical and piezoresistive properties of the three compositions of K-AAMs with the highest FCR are listed in Table 5.3. These AAMs share the optimum Si/Al ratio which was shown to give the highest piezoresistive performance. Though the composition '0.8/2.85' exhibited the greatest FCR, the compressive strength decreased dramatically at lower K/Al. This trend is consistent with other studies of the effect of the alkali/aluminum ratio on compressive strength (Rowles & O'connor, 2003). The composition '1/2.85' has a superior combination of properties because it achieves high piezoresistivity and sufficient strength to be used in load-bearing members.

Table 5.3 The piezoresistivity and mechanical properties of the optimal compositions of alkali activated materials

Sample ID	Compressive strength (MPa)	Flexural strength (MPa)	Fractional change in resistance[1] (%)	Stress sensitivity (MPa^{-1})	Gauge factor
0.8/2.85	12.9	3.3	67.0	0.067	39.3
1.0/2.85	33.3	4.8	63.2	0.063	95.7
1.2/2.85	20.5	3.9	57.4	0.057	53.5

[1]: measured under a compressive load of 10 MPa with a 10 Hz alternating current source

The intrinsic piezoresistivity of K-AAMs creates a unique opportunity to create a superior self-sensing construction material without the drawbacks of conventional composites. With compositional optimization, the piezoresistivity can be more than tripled compared to the original study by *Saafi et al* (M. Saafi et al., 2018). The K-AAMs developed in this study outperformed nearly every AAM composite containing carbon fiber, carbon nanotubes, or

graphene in the literature. Many studies dispersing carbonaceous additives in AAMs have reported only roughly 5% FCR (Perry, Saafi, Fusiek, & Niewczas, 2015 ; Vilaplana, Baeza, Galao, Zornoza, & Garcés, 2013). However, studies with greater dispersion and high concentrations of fibers have reached FCR of 15-30% (Deng et al., 2019 ; Mohamed Saafi et al., 2014 ; Vaidya & Allouche, 2011). These results are on par with cement composites that have reported FCR between 10 and 30% using various dosages and combinations of conductive additives (Azhari & Banthia, 2012 ; Donnini et al., 2018 ; C. Liu et al., 2019 ; Yoo, Kim, et al., 2018). Though there are some examples in the literature of piezoresistive composites with FCR comparable to that of K-AAMs, 40-70%, the methods required to prepare these composites involve extreme dispersion-assistance or exotic coating methods to achieve this property (Bi, Liu, Shen, Hu, & Zhang, 2017 ; Han et al., 2012). Intrinsically piezoresistive K-AAMs offer a distinct advantage in the simplicity of their production.

Structural health monitoring technology is stagnant because self-sensing construction materials have not yet been able to make the transition from laboratory development to scalable production. This is a consequence of the distinct challenge in scaling the technology used to make conventional self-sensing composites. Even small quantities of highly refined conductive fibers can dramatically inflate the cost of the composites and the sustainability of cement composites has not received scientific attention (Gupta et al., 2017 ; Papanikolaou et al., 2019). Moreover, the composites have questionable longevity and reproducibility which is an unacceptable tradeoff in loadbearing structures where consistency and long-term performance are of paramount importance (H. Li et al., 2008 ; H. Wang et al., 2018). The construction industry is ill-equipped to utilize the high-energy dispersion techniques required to achieve consistent properties in these composites and this creates a tremendous obstacle to the widespread adoption of these technologies (Han et al., 2015 ; Reddy et al., 2021). Intrinsically piezoresistive K-AAMs are a much-needed alternative to cement composites. They can be prepared in a standard cement mixer in a single-step process without exotic additives, maximizing their scalability in the construction sector. Their piezoresistivity dwarfs conventional composites without the added cost, complexity, and environmental impact of added carbon fiber. This makes K-AAMs the most promising self-sensing material for the smarter and greener construction of the future.

5.4 Conclusion

AAMs are an alternative self-sensing material that will revolutionize the field of smart construction materials. Conventional self-sensing composites are limited in scalability because of the conductive additives required. AAMs dramatically improve on this approach by achieving high piezoresistivity intrinsically, without the need for any additives. This presents a far greener, more scalable, and more affordable alternative to conventional composites without sacrificing mechanical integrity. The self-sensing capability of AAMs has not received scientific attention previously because of the sensitivity of this property to composition. More investigations are needed on the measurement set-up, material composition, and the benchmark to other materials. This study presents a compositional optimization for potassium AAMs based on fly ash using a one-part (single-step) mixing process in a standard cement mixer. This makes AAMs a drop-in replacement for ordinary construction materials while adding smart functionality to enable structural health monitoring and improve sustainability.

CHAPTER 6

HIGH STRENGTH, SELF-SENSING CONSTRUCTION MATERIALS FROM ONE-PART ALKALI ACTIVATED MATERIALS

Michael Di Mare[1] and Claudiane M. Ouellet-Plamondon[1]

[1] Department of Construction Engineering, École de Technologie Supérieure, 1100 Rue Notre-Dame Ouest, Montréal (QC), Canada

Paper submitted for publication, July 2022 (with minor changes)

6.1 Introduction

Self-sensing construction materials will revolutionize structural maintenance and prolong the service life of infrastructure around the globe. Self-sensing is a functional material property that enables continuous assessment of a structural member. This can be used to rapidly identify sites of damage and corrosion to deploy localized and preventative maintenance in a manner currently impossible. However, current self-sensing materials made from cement composites are prohibitively expensive for practical applications in construction and recent studies have found them to have low durability (Ebrahimi et al., 2018 ; Gupta et al., 2017 ; H. Li et al., 2008). This has prevented the commercialization of self-sensing construction products. This study overcomes this obstacle by demonstrating a new type of high-performing, self-sensing materials made without costly conductive additives. Exceptionally high self-sensing properties can be obtained without compromising mechanical integrity in a promising new alternative for the future of smart self-sensing construction.

Self-sensing is a smart property made possible by the combination of a material and a compatible nondestructive test. The state-of-the-art for self-sensing construction materials relies on piezoresistivity (Tian et al., 2019). Piezoresistivity is an uncommon electromechanical property that causes a material's mechanical strain state and electrical

resistance to be proportional. For piezoresistive structural members, measurements of the electrical resistance are a facile nondestructive test to detect changes in load distribution. In a laboratory setting, piezoresistivity is measured under either cyclic or static loading conditions. Cyclic loading conditions utilize an oscillating mechanical load to simulate vibrations or transient loads for applications such as traffic monitoring, seismic detection, and border security (García-Macías & Ubertini, 2019 ; Han et al., 2009 ; Z. Zhang, Huang, Bridgelall, Palek, & Strommen, 2015). Static conditions imitate applications in structural health monitoring and corrosion detection in which the change in loading is gradual and piezoresistivity is used to detect structural settling and decay (Downey, D'Alessandro, Ubertini, & Laflamme, 2018 ; Lu et al., 2013). Structural health monitoring has been championed as an up-and-coming construction technology since its first proposition in 1993 (P.-W. Chen & Chung, 1993). However, the technology has not seen any real-world commercialization due to the limited scalability of the current state-of-the-art piezoresistive construction materials.

Conventional piezoresistive materials are composites of Portland cement containing a conductive additive. Piezoresistivity in the composite arises from the electronic tunneling between discrete conductive particles within the insulating cement matrix. During mechanical compression, strain reduces the distance between the conductive particles enhancing tunneling and causing a measurable reduction in electrical resistance (García-Macías et al., 2018). This technique has been applied to create piezoresistive composites with carbon fiber, carbon black, carbon nanotubes, and graphene derivatives (Belli et al., 2018 ; Donnini et al., 2018 ; Han et al., 2012 ; C. Liu et al., 2019 ; Cecílie Mizerová et al., 2021 ; Mohamed Saafi et al., 2014). However, with all of these carbonaceous additives, three common problems persist with piezoresistive composites: affordability, reproducibility, and longevity. These refined carbonaceous additives are expensive to produce in large volumes and have been estimated to increase the price of piezoresistive composites by one-hundred-fold (Gupta et al., 2017). Reproducible dispersion of the hydrophobic additives is challenging, even with the use of dispersion-assisting superplasticizers and ultrasonication techniques (Han et al., 2012 ; J. Liu et al., 2019). Agglomeration from incomplete dispersion can cause a deleterious reduction in the mechanical properties which can threaten the integrity of the structural members. Finally,

the particle-matrix interface, which is responsible for the piezoresistivity, is susceptible to corrosion-assisted failure. Recent studies have reported substantial reductions in the mechanical durability of self-sensing composites and a short operational lifespan for their piezoresistivity due to breakdown at the conductive particle-matrix interface (Ebrahimi et al., 2018 ; H. Li et al., 2008 ; H. Wang et al., 2018). The deployment of structural health monitoring in construction will require reimagining the production of piezoresistive construction materials to reduce cost, ensure reproducible production, and guarantee a long operating life. The most straightforward solution is to develop a new piezoresistive material which does not rely on carbonaceous additives to function.

Alkali activated materials (AAMs) are a low-carbon binder technology whose piezoresistive properties are not well understood. AAMs have been heavily studied as an environmentally friendly alternative to Portland cement. They can be produced from industrial by-products which can give them up to a 70% reduction in global warming potential compared to cement (Habert & Ouellet-Plamondon, 2016). The physical and mechanical properties of AAMs are strongly sensitive to elemental composition and many studies have optimized the composition of AAMs to maximize their mechanical properties (Provis et al., 2019 ; Rowles & O'connor, 2003). At optimal compositions, AAMs can have greater mechanical properties and improved durability compared to Portland cement (Y. Ding et al., 2016 ; Jian Zhang et al., 2017). These properties, in conjunction with their lower carbon footprint, have attracted a great deal of interest for their use in construction.

In a remarkable discovery, AAMs were recently found to be intrinsically piezoresistive without requiring carbonaceous additives. This was first reported in 2018 for a potassium-activated fly ash AAM and subsequently corroborated in 2019 with a sodium-activated slag AAM (Rovnaník, Kusák, Bayer, Schmid, & Fiala, 2019 ; M. Saafi et al., 2018). The fly ash-based AAM exhibited three times more piezoresistivity than the slag-based AAM, up to 26% fractional change in resistance (FCR). The reason for the difference in piezoresistivity between these two AAMs is unknown and may be related to the use of different precursor materials, different alkali activators, and different elemental compositions. No study has yet identified the dependence of piezoresistivity on the compositional factors of AAMs. To truly propose intrinsically piezoresistive AAMs as a solution for self-sensing construction products, a more

thorough analysis must be conducted on the prevalence of this uncommon electromechanical property across a range of AAM compositions to identify factors that influence performance. Sodium activators are preferred for AAMs because of their lower environmental impact and higher mechanical properties than potassium-based equivalents (Hosan et al., 2016 ; N. Li et al., 2019). The initial study on potassium-activated fly ash did not measure the compressive strength of the AAM, which is a critical property for construction applications. A composition must be identified which can simultaneously achieve high piezoresistivity and high strength without compromising the scalability advantages of AAMs over conventional cement composites.

The unique intrinsic piezoresistivity of AAMs was previously unnoticed because it is not compatible with the most common measurement method for piezoresistivity. Piezoresistivity is typically measured using a direct-current source under cyclic loading conditions. However, under these conditions, AAMs exhibit less than 2% FCR, comparable to Portland cement (Cecílie Mizerová et al., 2021 ; Rovnaník et al., 2019). Instead, AAMs were found to be piezoresistive only under static loading conditions and when measured with an alternating current. This exemplifies the need for compatibility between the self-sensing material and the nondestructive test methods. AAMs are an ideal piezoresistive construction material for structural health monitoring applications without the drawbacks of cement composites.

In the last two years, four review articles on the topic of self-sensing materials have dedicated entire sections to discussing the potential of intrinsically piezoresistive AAMs and the implications of this technology on the field (Huang & Sun, 2021 ; Nalon et al., 2022 ; Tian et al., 2019 ; Vlachakis, Perry, & Biondi, 2020). However, with only two examples of this phenomenon in the literature, the topic is far from well established. Moreover, both of the prior studies tested only a single AAM each and no study has determined the effect of compositional factors on the piezoresistivity. This study seeks to address this research gap by applying the same methodology used to optimize the composition for mechanical and electrical properties of AAMs to its piezoresistivity (Hanjitsuwan et al., 2014 ; Rowles & O'connor, 2003). This work will develop piezoresistive AAMs using a one-part, single-stage mixing process that can be easily reproduced in a conventional cement mixer to maximize the scalability of this technology. In doing so, the present study will identify the factors that influence

piezoresistivity in AAMs, determine the optimum composition for creating AAMs that have high strength and high piezoresistivity, and demonstrate the feasibility of producing self-sensing construction materials using a facile one-part process.

6.2 Experimental methods

6.2.1 Materials

Alkali activated materials (AAM) were prepared by the alkali activation of three different raw material precursors: metakaolin, blast furnace slag, and fly ash. The metakaolin was characterized to be composed of, in oxide equivalent weight percent, 46.5% aluminum oxide, 49.5% silicon oxide, and 0.20% sodium oxide. The slag was ground, granulated, and composed of 10.3% aluminum oxide, 38.6% silicon oxide, and 0.43% sodium oxide. The fly ash was composed of 21.4% aluminum oxide, 55.3% silicon oxide, and 0.96% sodium oxide. Mixtures were prepared of the precursors with silica fume (4.8% moisture), anhydrous reagent grade sodium hydroxide, and deionized water to achieve the proportions specified in Table 6.1. A specimen of Portland cement was prepared with water / binder ratio of 0.35 as a reference.

Table 6.1 Summary of alkali activated inorganic polymer compositions prepared

Sample ID	Precursor used	Na/Al ratio	Si/Al ratio	W/B ratio[1]	Precursor (g)	Silica fume (g)	NaOH (g)	Water (g)
MK	Metakaolin	1.0	1.50	0.70	500	143	185	445
BFS	Blast furnace slag	1.0	3.20	0.45	500	0	38	241
FA	Fly ash	1.0	2.85	0.25	500	85	79	161
Cement	Portland cement	-	-	0.35	500	0	0	138
FA-0.8-2.5	Fly ash	0.8	2.50	0.25	500	41	62	152
FA-0.8-2.85	Fly ash	0.8	2.85	0.25	500	85	62	161
FA-0.8-3.2	Fly ash	0.8	3.20	0.25	500	130	62	169
FA-1.0-2.5	Fly ash	1.0	2.50	0.25	500	41	79	152
FA-1.0-3.2	Fly ash	1.0	3.20	0.25	500	130	79	169
FA-1.2-2.5	Fly ash	1.2	2.50	0.25	500	41	96	152
FA-1.2-2.85	Fly ash	1.2	2.85	0.25	500	85	96	161
FA-1.2-3.2	Fly ash	1.2	3.20	0.25	500	130	96	169

[1]: Water to binder ratio, accounting for the moisture content of all solid components.

The composition of the AAM can be described by the precursor and the elemental proportions: sodium:aluminum (Na/Al) and silicon:aluminum (Si/Al). These molar ratios are calculated from the oxide composition of each constituent. To determine which precursor is preferred for piezoresistive applications, four initial compositions (MK, BFS, FA, Cement) were prepared, one from each precursor. The elemental ratios and water / binder ratios were selected from typical values found in the literature to accommodate the significantly different water demand

and Si/Al ratio in the precursors (Provis et al., 2019). To investigate the impact of each of the elemental ratios on the piezoresistivity, eight additional compositions of alkali activated fly ash were prepared. The compositions formed a factorial array around the initial composition FA in the range between 0.8 – 1.2 Na/Al and 2.5 – 3.2 Si/Al while maintaining a constant water / binder ratio. The compositions, listed in Table 6.1, were identified by "FA-Na/Al-Si/Al" for each specimen.

6.2.2 Preparation methods

The specimens were prepared following a one-part mixing methodology to maximize the compatibility of the process with conventional concrete production methods. The dry powders were mixed with water in a single mixing step using a planetary mixer that is compliant with ASTM C305 (ASTM International, 2020a, p. 305). The resulting paste was cast into stainless steel molds coated with petroleum jelly to prevent adhesion. The molds were immediately sealed to prevent moisture loss and cured under saturated humidity conditions. Three types of molds were used to prepare specimens. 50 mm cube specimens were prepared for compressive strength testing, as per ASTM C109 (ASTM International, 2020b, p. 109). 40 mm x 160 mm square rods were prepared for flexural strength testing, in accordance with ASTM C348 (ASTM International, 2021a, p. 348). For piezoresistivity, 50 mm cube molds were modified with a bracket to maintain a pair of electrodes in parallel in the center of one of the faces. The electrodes were galvanized stainless steel mesh, with a wire thickness of 0.61 mm (23 gauge), and mesh size of 6.73 mm (mesh #3). The electrodes were cut to be 50 mm in width and 100 mm in length and inserted to embed 50 mm of the length in the AAM cube. The bracket held the electrodes at a parallel spacing of 10 mm for the duration of the curing to yield the specimens shown in Figure 6.1. All of the specimens were cured at 60ºC for seven days under saturated humidity conditions to achieve their final properties. In addition, the specimens with the embedded electrodes were gently dried at 60ºC for another seven days in a dry oven after curing to remove excess water which could interfere with the resistance measurements through surface conduction. This gentle drying process ensured water removal without damaging the phase or recrystallizing the aluminosilicate hydrates native to the AAM.

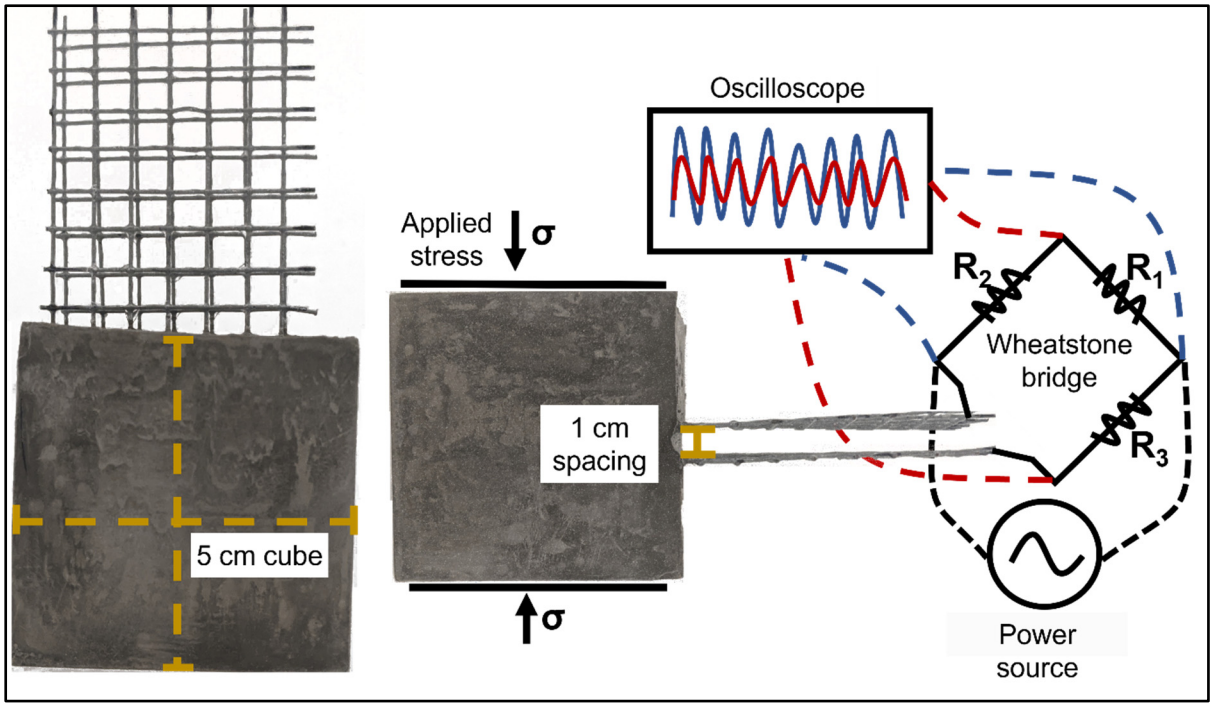

Figure 6.1 Alkali activated material specimens with embedded electrodes and the experimental measurement setup used for piezoresistivity measurement.

6.2.3 Strength and piezoresistivity measurements methods

The AAM specimens were assessed for their mechanical and piezoresistive properties. The compressive strength of the cube specimen was measured following ASTM C109 (ASTM International, 2020b, p. 109). The measurement was conducted in triplicate with a loading rate of 1 kN/sec. The square rods were tested in flexure in accordance with ASTM C348 and a loading rate of 0.048 kN/sec (ASTM International, 2021a, p. 348). The electrical resistance of the specimens with the embedded electrodes was measured by connecting the electrodes to a Wheatstone bridge circuit composed of an alternating current power source, a Wheatstone bridge, and an oscilloscope in the manner shown in Figure 6.1.

A Wheatstone bridge circuit is a standard electrical circuit that can be used to measure an unknown resistance under an alternating current (Hoffmann, 1974). The bridge was composed of resistors with a resistance of 860 kΩ. This resistance was selected to closely approximate the expected resistance of the AAM, based on literature values, to maximize the accuracy of

the Wheatstone bridge measurement (Hanjitsuwan et al., 2014). The power source applied 10 Volts at 10 Hz, 10 kHz, and 10 MHz. At each frequency, the electrical resistance was measured. The Wheatstone bridge was composed of resistors with resistance. An InfiniiVision 3034A oscilloscope (Agilent Technologies®) was used to measure the voltage across the two sides of the bridge. The resistance of the AAM specimen was calculated from those voltage measurements using the following equation, derived from Ohms Law:

$$R_{sample} = R_3 \frac{R_2 - \frac{V_m}{V_i}(R_1 + R_2)}{R_1 + \frac{V_m}{V_i}(R_1 + R_2)} \quad \text{Equation 6.1}$$

where R_1, R_2, R_3 are the bridge resistors, shown in the orientation given in Figure 6.1, V_i is the voltage across the known resistors R_1 and R_2 which is equal to the applied voltage, and V_m is the voltage drop across the sample.

The measurement of the resistance was conducted on the specimen under ambient conditions and a series of compressive loadings. The specimens were compressed in the orientation parallel to the electrodes, as shown in Figure 6.1, to measure the piezoresistivity. The resistance was measured at compressive loading up to 10 MPa at an interval of 1 MPa. At each loading, the resistance was measured at each frequency. The piezoresistivity was quantified, by convention, as the fractional change in resistance (FCR), stress sensitivity coefficient, and gauge factor, defined by:

$$FCR = \frac{R_\sigma - R_0}{R_0} \quad \text{Equation 6.2}$$

$$Stress\ sensitivity = \frac{FCR}{\sigma} \quad \text{Equation 6.3}$$

$$Gauge\ factor = \frac{FCR}{\varepsilon} \quad \text{Equation 6.4}$$

Where R_σ is the resistance measured under compressive loading σ, R_0 is the resistance of the same sample under ambient conditions, and ε is the mechanical strain. All measurements were conducted in triplicate at room temperature and the error bars in the subsequent figures depict the standard deviation.

6.2.4 Characterization methods

Fourier transform infrared spectroscopy was conducted to ensure homogeneity and full reactivity of the raw materials. A full spectrum of 400 cm^{-1} to 4000 cm^{-1}, with a focus on the range of 700 cm^{-1} to 1300 cm^{-1}, where the characteristic peaks of the alkali activation and inorganic polymer condensation reactions occur. Micrographs of the fracture surfaces were acquired by scanning electron microscopy to characterize the homogeneity of the experimental specimen. Energy dispersive spectroscopy was conducted to confirm that uniform distribution of activator was achieved in the one-part mixing process.

6.3 Results and discussion

6.3.1 Influence of precursor on piezoresistivity

The fractional change in resistance (FCR) of a piezoresistive material quantifies its capacity to detect abnormal strain in-situ. Though there is no established level of FCR required for self-sensing applications, higher FCR gives the self-sensing member greater detection resolution. Thus, the objective of all studies of piezoresistive materials is to maximize the FCR while maintaining compressive strength above 30 MPa to be suitable for construction applications (Tian et al., 2019). The methodology demonstrated in this study utilizes alternating current to accurately measure the FCR of the self-sensing specimen under static loading conditions. Static loading conditions are the most representative of structural health monitoring applications where self-sensing members are used to detect gradual structural decay and sites of corrosion (P.-W. Chen & Chung, 1993 ; Han et al., 2015). This is made possible with greater accuracy than before through the novel use of the alternating current test methodology explained in Section 2.3.

With this measurement methodology, it is possible to accurately measure the piezoresistivity of highly polarizing alkali activated materials (AAMs) without interference from the polarization. AAMs can be prepared from a variety of different aluminosilicate sources, known as precursors, and the type of precursor is known to have a substantial influence on the

properties of the AAMs (Duxson & Provis, 2008). In Figure 1(a) it is shown that this trend extends to piezoresistivity. The three precursors, fly ash, metakaolin, and blast furnace slag, produced AAMs with substantially different FCR across the same range of compressive loading. The blast furnace slag AAM exhibits negligible piezoresistivity, comparable to inert Portland cement shown here as a baseline. This is significantly lower than the 8% FCR reported in the prior study (Rovnaník et al., 2019). This is likely due to the high iron content in the slag used in the study to which the piezoresistivity was attributed.

The other precursors exhibited significantly greater piezoresistivity. The metakaolin AAM had a moderate FCR of 8%. However, the metakaolin AAM exhibited a relatively constant FCR above 5 MPa, only increasing from 2% over the latter half of the range. This was undesirable because it limited the stress sensitivity of the AAM and, thus, the capacity to detect small changes in stress. The fly ash AAM exhibited significantly higher FCR, up to 31%, and greater linearity which made it a superior piezoresistive material. Notably, the trend between precursors for piezoresistivity was the opposite of the generally accepted trend for mechanical strength (Duxson & Provis, 2008 ; Provis et al., 2019). Fly ash AAMs, which are generally weaker at optimized compositions than slag AAMs and metakaolin AAMs, exhibited greater self-sensing performance, demonstrating that strong alkali activation reactions were not a good indicator of high piezoresistive response. Additional experiments were conducted based on the fly ash AAMs to examine ways to further enhance its FCR.

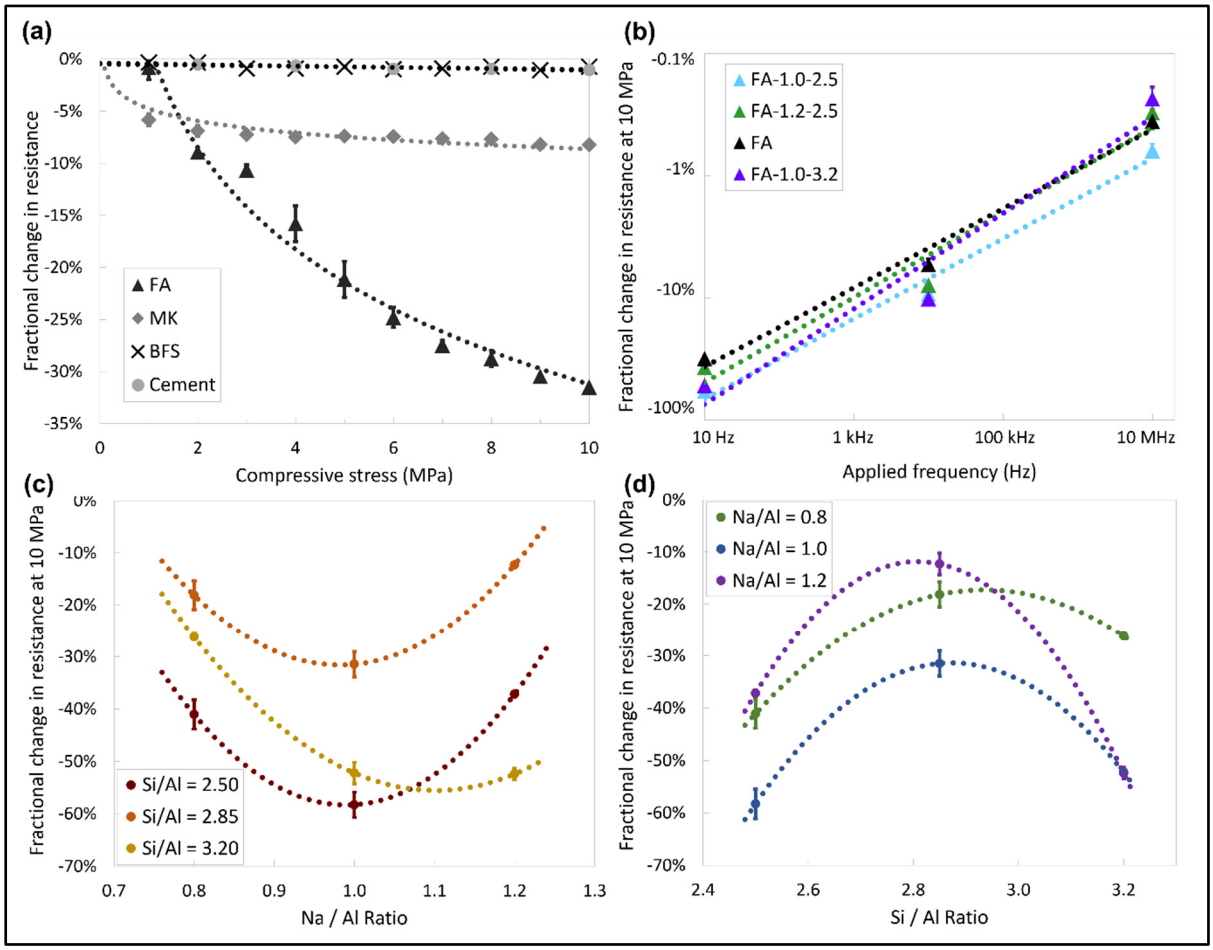

Figure 6.2 (a) Comparison of the piezoresistivity of alkali activated materials prepared from different precursors. The effect of (b) measurement frequency, (c) sodium/aluminum ratio, and (d) silicon/aluminum ratio on the piezoresistivity of alkali activated fly ash at 10 MPa.

The use of the alternating current technique added an additional variable to test in the optimization of the methodology: the testing frequency. As previously mentioned, AAM have been reported to have different levels of intrinsic piezoresistivity based on the testing conditions. This necessitated the simultaneous optimization of a self-sensing AAM and its optimal testing conditions. With conventional direct current measurements, fly ash AAM exhibited negligible piezoresistivity without the addition of conductive additives, with FCR below 1% (Deng et al., 2019 ; Cecílie Mizerová et al., 2021). However, *Saafi et al.* reported as much as 26% intrinsic FCR for potassium activated AAM by using alternating current (M.

Saafi et al., 2018). *Saafi et al.* observed that the FCR declined at higher frequencies, but failed to discuss this phenomenon further. To examine this phenomenon, fly ash AAM were tested at alternate frequencies and the results are shown in Figure 6.2(b). The FCR was found to decline in a consistent power function with a coefficient of 0.33. This trend was true across all of the fly ash compositions, with comparable frequency dependence. Testing at low frequency yielded greater piezoresistivity and future studies which apply this methodology must be consistent with the frequency to make accurate comparisons.

6.3.2 Effect of the composition on the piezoresistivity of alkali activated fly ash

The piezoresistivity, like most properties of alkali activated materials (AAM), may be dependent on the elemental composition in addition to the precursor type. To examine this possibility, a factorial array of compositions was prepared centered on the initial fly ash AAM which exhibited high FCR. The compositions were defined by their sodium/aluminum (Na/Al) and silicon/aluminum (Si/Al) ratios. The results, shown in Table 6.2, revealed that both factors strongly influence the electrical resistance and fractional change in resistance (FCR). With the optimal composition, identified as FA-1.0-2.5 by its elemental ratios, an FCR of up to 58% was obtained. This demonstrated that despite not correlating with mechanical strength trends, the piezoresistivity of AAM was strongly influenced by its chemistry.

Table 6.2 Electrical resistance and fractional change in resistance (FCR) measured for piezoresistive alkali activated fly ash specimens, organized by their elemental composition.

Sample ID	Na / Al ratio	Si / Al ratio	Resistance at ambient (kΩ)[1]	Resistance at 10 MPa (kΩ)[1]	FCR at 10 MPa (%)[1]
FA-0.8-2.5	0.8	2.50	549.4	323.1	41.1
FA-0.8-2.85	0.8	2.85	237.0	193.9	18.1
FA-0.8-3.2	0.8	3.20	708.7	547.8	22.7
FA-1.0-2.5	1.0	2.50	784.4	363.4	58.3
FA	1.0	2.85	816.8	560.7	31.5
FA-1.0-3.2	1.0	3.20	717.4	339.1	52.2
FA-1.2-2.5	1.2	2.50	489.3	306.6	37.2
FA-1.2-2.85	1.2	2.85	230.0	184.2	12.3
FA-1.2-3.2	1.2	3.20	704.0	404.0	52.4

[1]: measured at 10 Hz

The Na/Al and Si/Al ratios are typically discussed separately in the study of AAM because they govern different aspects of the inorganic polymer's chemistry. AAM are composed of NASH (sodium-aluminum-silicon-hydrate) gels and the relative proportion of the components in this gel strongly influence the inorganic polymer's structure. The Na/Al ratio controls the content of sodium ions which act as charge balancing cations, localized around alumina tetrahedra within the inorganic polymer chains. It has been suggested that the mobility of hydrated sodium ions is responsible for the intrinsic piezoresistivity and piezoelectricity of AAM (Caterina Lamuta et al., 2016). Varying the Na/Al ratio creates sodium vacancies or super-stoichiometric cations which influences the ionic mobility. Greater Na/Al has been reported to increase the conductivity of AAM by as much as a factor of 10 (Hanjitsuwan et al., 2014). On the other hand, the Si/Al ratio controls the monomers and oligomers that form during the recondensation reaction to form the inorganic polymer network. Between $2 < Si/Al < 3$, AAM are composed of a mixture of sialate-siloxo and sialate-disiloxo monomers. For $Si/Al > 3$, sialate-disiloxo monomers become crosslinked by excess sialate groups (J. Davidovits, 1991 ; van Deventer et al., 2007).

Prior studies have extensively reported on the effect of the elemental ratios on the mechanical properties of AAM, but no study to date has investigated their impact on the piezoresistivity (Rowles & O'connor, 2003). In Figure 6.2(c,d), both factors have a strong impact on the piezoresistivity of the AAM, but their influence appears to be independent. For the Na/Al ratio, a clear optimum is observed at 1.0, independent of the Si/Al ratio. A 20% reduction in the sodium ion content, when Na/Al ratio is 0.8, reduces the FCR by approximately 40% at all Si/Al ratios. This indicates that not all the sodium ions contribute to the piezoresistivity and that reducing the total sodium content disproportionately reduces the mobile ions that are responsible for this phenomenon. Increasing the Na/Al ratio to 1.2 causes a similar magnitude reduction in FCR due to oversaturation and low vacancy content. The sodium ions migrate through a charge hopping mechanism, which can be obstructed by a lack of vacancies (Caterina Lamuta et al., 2016). The FCR is maximized when a stoichiometric content of sodium is present and can be reduced by excess sodium ions or vacancies.

The Si/Al ratio in inorganic polymers determines the composition of the monomers and their crosslinking. At a Si/Al of 2.5, there are an equal proportion of sialate-siloxo and sialate-disiloxo monomers, containing two silica tetrahedra and three silica tetrahedra, respectively (J. Davidovits, 1991). A mixture of monomer types creates a more disordered AAM and this enhances the mobility responsible for piezoresistivity. A similar increase in chemical disorder occurs when the Si/Al exceeds 3.0, wherein excess silate groups induce crosslinking between polymer chains (J. Davidovits, 1991). This irregular crosslinking increases the disorder in the amorphous NASH structure. The results, shown in Figure 6.2(d), indicate that a more disordered NASH structure is preferred for piezoresistivity. The FCR is increased by a factor of 2-4 in these regimes compared to the midpoint, for all Na/Al ratios.

In an effort to correlate the changes AAM chemistry responsible for higher FCR, spectroscopic and microscopic analyses were conducted. Fourier transform infrared spectroscopy has been successfully used to characterize alkali activation of fly ash (W. K. W. Lee & van Deventer, 2003 ; Rees et al., 2007). The reaction causes a characteristic peak shift in a broad peak centered around 1070 cm^{-1}, which corresponds to Si-O-(Al,Si) bond vibration. In fully reacted AAM, the recondensation reaction in alkali activation shifts this peak to a lower wavenumber around 1000 cm^{-1} (W. K. W. Lee & van Deventer, 2003). For this study, inorganic polymers

of varying Na/Al and Si/Al ratios were tested, and their spectra were compared to determine if infrared spectroscopy could identify the chemical cause of the variation in FCR. However, the results, depicted in Figure 6.3(a,b), show that compositional changes have minimal effect on the spectra despite the large difference in piezoresistive performance between the compositions. The characteristic peak shift can be observed from 1030 cm^{-1} to 990 cm^{-1}. There is variation in peak breadth with different Si/Al ratios, as shown in Figure 6.3(b). This is consistent with the changing proportion of sialate-siloxo and sialate-disiloxo monomers which have different peak positions. Other peaks, such as the two shown around 770 cm^{-1}, are present in the unreacted fly ash, indicating that they are inert impurities. One atypical peak was observed at 850 cm^{-1} in FA-1.0-2.85, which corresponds to O-Al-O vibration caused by an alumina impurity (Rees et al., 2007). No change in the spectra can be identified which correlates with the piezoresistive performance.

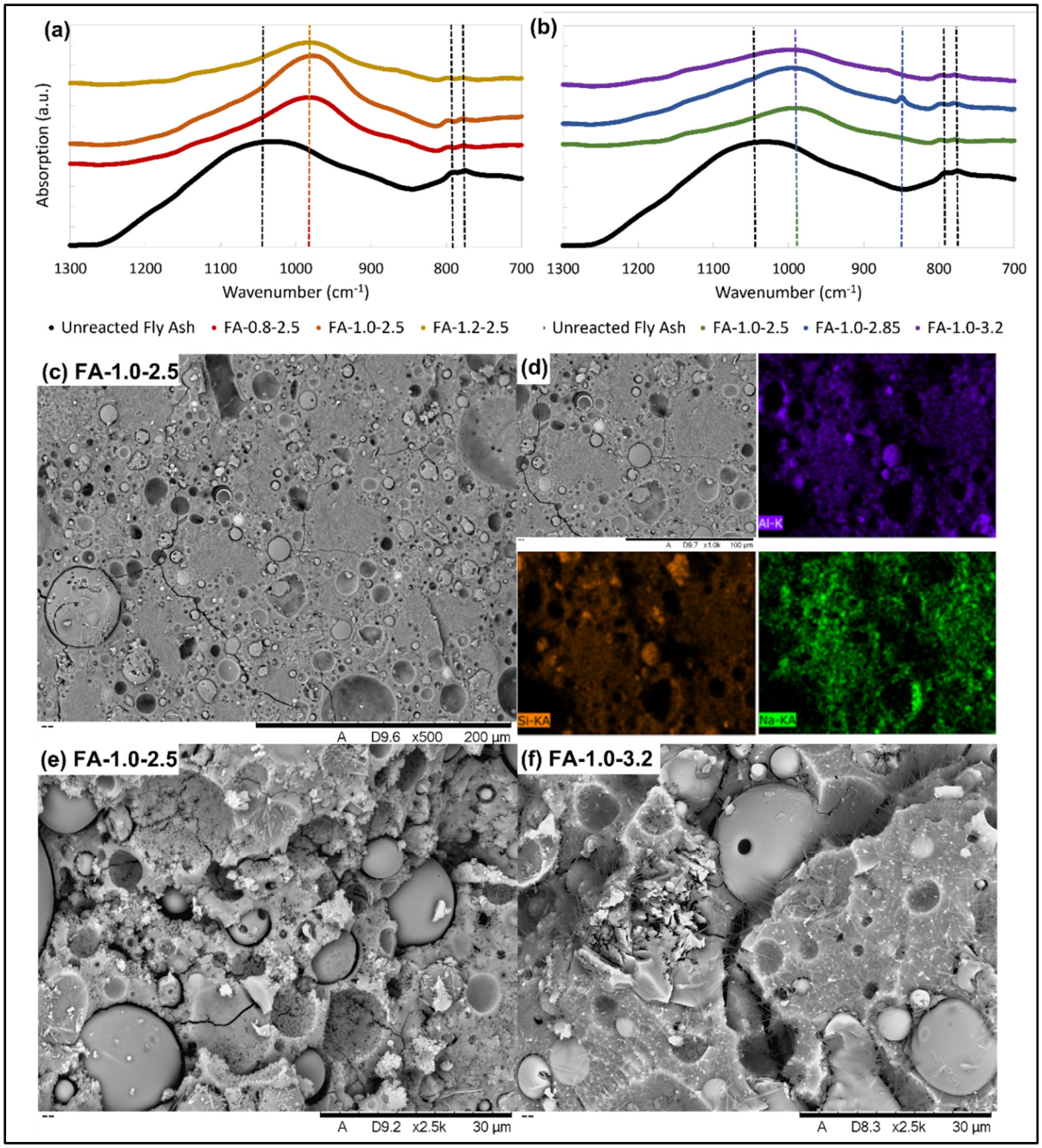

Figure 6.3 Fourier transform infrared spectra of unreacted fly ash and alkali activated fly ash with (a) varying Na/Al ratio and (b) varying Si/Al ratio. (c,d) Low magnification (500x) scanning electron fracture surface micrograph and energy dispersive spectroscopy mapping for Al, Si, and Na of specimen FA-1.0-2.5. (e,f) High magnification (2.5kx) scanning electron fracture surface micrographs of specimens FA-1.0-2.5 and FA-1.0-3.2.

Microstructural analysis by scanning electron microscopy was conducted for different compositions of AAM to confirm their homogeneity. Low magnification microscopy of the fracture surfaces, shown in Figure 6.3(c), revealed smooth trans-granular fracture indicating a well-reacted AAM. A small content of unreacted fly ash can be seen as spherical defects. The silica fume cannot be seen in the micrographs, demonstrating that the one-part mixing methodology that was used dispersed the dry components uniformly. Energy dispersive spectra were collected, such as those shown in Figure 6.3(d), to further confirm the homogeneity. The elemental maps for the major components, Al, Si, and Na, show agreement with each other and the texture of the corresponding micrograph. This indicates that the activator was homogeneously dispersed, resulting in an even distribution of sodium within the specimen.
Scanning electron microscopy was used to assess the microstructure of the AAM to correlate changes with the FCR. Higher magnification micrographs, such as those shown in Figure 6.3(e,f), illustrate the difference in microstructure at different Si/Al ratios. At a low Si/Al ratio, a higher surface area inorganic polymer is obtained with sub-micron porosity. Above Si/Al of 3.0, this porosity disappears due to greater crosslinking between particles, creating a lower texture microstructure, which can be seen in Figure 6.3(f). This type of microstructural feature has been correlated to changes in mechanical strength (Provis et al., 2015). However, both compositions shown in Figure 6.3(e,f) exhibited FCR, demonstrating that high FCR can occur with or without this microstructure. No microstructural feature could be identified as an indicator of high piezoresistive performance.

6.3.3 Optimization and prospects

This study is the first to demonstrate the intrinsic piezoresistivity of sodium-based alkali activated materials (AAM). The results are substantially higher than the maximum of 26% fractional change in resistance (FCR) reported for potassium-based AAM (M. Saafi et al., 2018). The FCR was found to vary considerably with the choice of precursor and elemental composition. The FCR of fly ah AAM can vary between 12-58% by varying the Na/Al and Si/Al ratios. The elemental ratios were found to be roughly, but not strictly, independent with some greater irregularity when the Si/Al ratio is >3.0 and crosslinking is prevalent. A

multivariable illustration of this relationship is shown in Figure 6.4 as a 3D rendering and a contour plot.

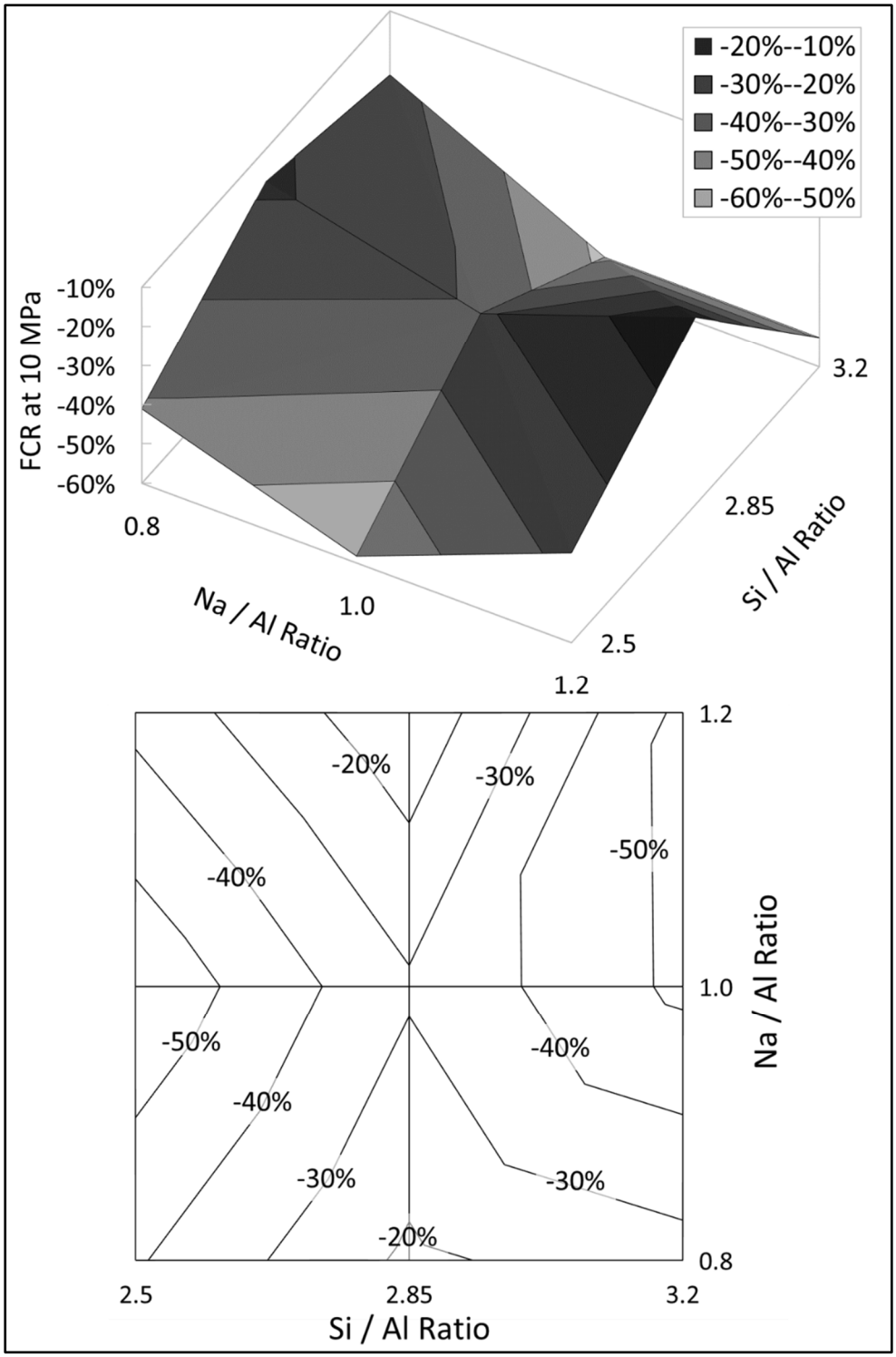

Figure 6.4 (a) A three-dimensional rendering and (b) a contour plot of the fractional change in resistance (FCR) at 10 MPa and 10 Hz across an array of elemental compositions of alkali activated fly ash defined by their Na/Al and Si/Al ratios.

From the factorial array, three AAM compositions were identified which yielded FCR above 50% and were considered the best candidates for self-sensing applications. The mechanical and piezoresistive properties of these compositions are given in Table 6.3. Smart construction materials must exhibit both high FCR and high compressive strength. Of the three compositions, FA-1.0-2.5 was the optimal exhibiting the greatest FCR and compressive strength of all of the AAM. The compressive strength significantly exceeds the 28 MPa required to replace concrete and is comparable to so-called high-performance fly ash AAM (Provis et al., 2019). This composition is the best candidate for use as a self-sensing construction material.

Table 6.3 Comparison of the mechanical and the piezoresistive properties of the best compositions of alkali activated fly ash.

Sample ID	Compressive strength (MPa)	Flexural strength (MPa)	FCR at 10 MPa[1]	Stress sensitivity (MPa^{-1})	Gauge factor
FA-1.0-2.5	53.3	2.6	58.3	0.058	141.3
FA-1.0-3.2	32.4	3.9	52.2	0.052	76.9
FA-1.2-3.2	23.5	4.4	52.4	0.052	56.0

[1]: measured at 10 Hz

The optimal composition, FA-1.0-2.5, exhibits intrinsic piezoresistivity without any additives, which is comparable to or better than conventional piezoresistive composites. Prior studies have investigated the use of AAM as a matrix material for piezoresistive composites containing carbon fiber, carbon black, graphene, and conductive aggregates. With 0.3% addition of carbon fiber or reduced graphene oxide, AAM composites have been produced with FCR between 7-16% and gauge factors of up to 44 (Deng et al., 2019 ; Mohamed Saafi et al., 2014). The highest performing piezoresistive composites required the addition of both 0.3% carbon fiber and 35% conductive aggregate to achieve FCR up to 48% at 10 MPa (Ma et al., 2020). However, this effect is primarily caused by the high content of conductive aggregate and the FCR was measured to reduce to 13%. The intrinsic piezoresistivity documented in this study represents a strict improvement over AAM composites by achieving comparable or higher FCR and gauge

factors without the need for conductive additives. This eliminates the need for chemical dispersants and ultrasonication required to disperse the hydrophobic additives and the added costs of these materials, offering a more practical smart construction material.

Intrinsically piezoresistive AAM offer a similar advantage over conventional cement composites. Piezoresistive cement composites have been heavily studied using carbon fiber, carbon black, graphene oxides, carbon-coated conductive aggregates, and combinations of these conductive additives. Carbon fiber, the most popular additive, typically yields composites with 5-20% FCR depending on the carbon fiber content and the quality of the dispersion (Azhari & Banthia, 2012 ; Belli et al., 2018 ; Donnini et al., 2018). With carbon nanotubes, the fiber content can be reduced to 0.1% and below, but the reliance on dispersion-assisted mixing increases to ensure homogeneity in the composite (Han et al., 2012 ; G. Y. Li et al., 2007 ; C. Liu et al., 2019 ; Yoo, You, Youn, & Lee, 2018). Structural applications have a low tolerance for inhomogeneity, and fiber additives, including carbon fiber and carbon nanotubes, have profound effects on the workability and mechanical strength of concrete. This is compounded by the reported reductions in durability for piezoresistive cement composites, leading researchers to question the viability of cement composites in self-sensing applications (Ebrahimi et al., 2018 ; H. Li et al., 2008 ; H. Wang et al., 2018).

Intrinsically piezoresistive AAM eliminate these drawbacks while exhibiting exceptionally high FCR. The intrinsic piezoresistivity of AAM has been overlooked due to their incompatibility with direct current testing methods. However, with a facile switch to alternating current, AAM can be a high-performing self-sensing construction material without the added cost, durability, or dispersion problems that arise from the use of conductive additives. The AAM of this study were prepared in a one-part mixing methodology using a planetary mixer recommended by the ASTM for reproducing the existing cement processing technology used in large-scale production. This maximizes the feasibility of scaling up this technology for effective and cost-efficient application as a smart construction material

6.4 Conclusions

Alkali activated materials (AAM) exhibit high intrinsic piezoresistivity without the addition of conventional conductive additives. This piezoresistivity has been previously overlooked due to the high polarizability of AAM distorting the measurement of the conductivity under direct current conditions. The piezoresistive performance, like the mechanical properties, is dependent on the precursor and the elemental composition of the AAM but follow different trends. Alkali activated fly ash was found to exhibit the greatest self-sensing properties and, with optimization of the sodium/aluminum and silicon/aluminum elemental ratios, the fractional change in resistance was enhanced to 58% at 10 MPa. Piezoresistive AAM were produced with a facile, one-part mixing methodology compatible with existing concrete technology and without the need for the costly conductive additives used in conventional composites. AAM are superior self-sensing construction materials and deserve further investigation for structural health monitoring applications.

CHAPTER 7

COMBINED EXPERIMENTAL AND COMPUTATIONAL PREDICTION OF THE PIEZORESISTIVITY OF ALKALI ACTIVATED INORGANIC POLYMERS

Michael Di Mare[1], Nathaniel Inumerable[2], Patrick Brisebois[1] and Claudiane M. Ouellet-Plamondon[1]

[1] Department of Construction Engineering, École de Technologie Supérieure, 1100 Rue Notre-Dame Ouest, Montréal (QC), Canada
[2] Department of Materials Science and Engineering, University of Illinois at Urbana-Champaign, Urbana, IL, 61801, USA

Paper published in *Journal of Physical Chemistry C*, July 2022 (with minor changes)

7.1 Introduction

Smart building materials are multifunctional construction materials designed to improve the maintenance of structures and prolong the working life of buildings (Tian et al., 2019). They are typically high mechanical strength materials that have been modified with additives to impart self-healing or self-sensing properties. Self-sensing is an intelligent material property wherein the material supports a nonintrusive detection method that allows continuous assessment of the material's mechanical state. Self-sensing building materials can detect pressure, vibrations, and abnormal strain in a structural member. This has led to their proposal for a wide variety of applications including structural health monitoring, corrosion detection, seismic damage detection, traffic sensing, and border security monitoring (P.-W. Chen & Chung, 1993 ; García-Macías & Ubertini, 2019 ; Lu et al., 2013 ; Jinrui Zhang et al., 2015). However, the additives used to impart self-sensing properties severely limit the affordability and the durability of the materials (Gupta et al., 2017 ; H. Li et al., 2008 ; H. Wang et al., 2018). In this work, alkali activated inorganic polymers are demonstrated to exhibit self-sensing behavior intrinsically, circumventing the drawbacks of self-sensing additives while

maintaining high mechanical strength. To understand the origin of this unusual property, the electrical conductivity of inorganic polymers was modeled from first principles by quantum mechanical perturbation theory.

Conventional self-sensing building materials are composites of an inorganic matrix material, most commonly Portland cement, and a conductive additive, typically carbon fiber (Tian et al., 2019). The self-sensing property is achieved through the piezoresistivity of the composite, in which the electrical conductivity of the composite is sensitive to strain-induced changes in the tunneling distance between the conducting carbon fibers. This methodology requires a high content of carbon fiber (e.g. 15%) and is sensitive to the dispersion of the fibers and changes in the fiber-matrix interface, which has drawn questions about its affordability, reproducibility, and longevity of composites as self-sensing building materials (Azhari & Banthia, 2012 ; Han et al., 2015). An ideal improvement would be the identification of a building material that is self-sensing intrinsically, without the need for conductive additives. In one recent study, a potassium activated inorganic polymer was shown to exhibit this property, but the extent of its presence in other alkali activated inorganic polymers and the mechanisms behind the intrinsic piezoresistivity are unknown (M. Saafi et al., 2018).

Alkali activated materials are amorphous inorganic polymers with ceramic-like properties, formed through a polycondensation reaction of aluminum and silicon oxides dissolved in the presence of a high pH activator (van Deventer et al., 2007). Their elemental composition is analogous to zeolites, but they are formed at room temperature which has attracted many comparisons to Portland cement (Provis & Van Deventer, 2009). Generally, they exhibit high mechanical properties and are considered a low-cost and environmentally friendly alternative to Portland cement because they can be synthesized from industrial by-products that are rich in aluminum and silicon oxides, such as blast furnace slag and coal fly ash (Duxson & Provis, 2008). Alkali activated inorganic polymers have been investigated as a matrix material for self-sensing composites with conductive additives (Deng et al., 2019 ; C. Mizerová, Rovnaník, Kusák, & Schmid, 2021 ; Cecílie Mizerová et al., 2021 ; Mohamed Saafi et al., 2014). However, their intrinsic piezoresistivity was found to be negligible with conventional measurement methods.

Conventionally, piezoresistivity is measured under direct current conditions with cyclic loading of compressive stress. Cyclic loading simulates how a self-sensing material may behave in applications with transient loads, such as in traffic monitoring (Jinrui Zhang et al., 2015). This has created a challenge to the deployment of self-sensing building materials in other applications of interest, such as structural health monitoring and corrosion detection, in which loading changes are static. Despite interest in these applications, few studies have measured piezoresistivity under static conditions and it has been observed that some piezoresistive materials are only self-sensing under cyclic loading (Han et al., 2015 ; Z. Tang et al., 2019).

This investigation seeks to develop a new understanding of the intrinsic piezoresistivity of alkali activated inorganic polymers. Unlike for conventional self-sensing composites, the mechanisms behind intrinsic piezoresistivity are not known. Modeling of the theoretical properties of inorganic polymers only recently became possible due to molecular dynamics simulations of the complex amorphous structure (M. Zhang et al., 2018). The goal of this study is to, for the first time in the scientific literature, use a structural model of an inorganic polymer to compute a theoretical property. The piezoresistivity is calculated by applying the Kubo-Greenwood theorem, a first-principles quantum mechanical expression for electrical conductivity. The Kubo-Greenwood theorem has never previously been applied to a complex amorphous material and the results are corroborated by experimental measurements. An improved experimental methodology has been developed to accurately measure the intrinsic piezoresistivity of inorganic polymers under static loading conditions. The results present inorganic polymers as an environmentally friendly alternative for smart building materials without the drawbacks of conventional composites.

7.2 Experimental methods

Experimental specimens of inorganic polymer were prepared through the alkali activation of fly ash (ProAsh®, Separation Technologies Inc.). The specimens were prepared in triplicate using sodium metasilicate and silica fume to achieve an elemental ratio of 1.1:1:3 Na/Al/Si (sodium/aluminum/silicon). A water/binder ratio of 0.25 was used to form a flowable paste.

The mixture was prepared in a low-shear mixer and cast into stainless steel molds which were sealed to prevent moisture loss during curing. Specimen for mechanical properties were prepared and tested in accordance with ASTM C109 and ASTM C348 (ASTM International, 2020b, p. 01, 2021a, p. 348). For piezoresistivity specimens, 5 cm cube molds were modified with a bracket to maintain two steel mesh electrodes at a spacing of 1 cm apart. The specimens were cured in a saturated humidity chamber at 60ºC for 7 days to ensure complete reaction. Prior to piezoresistivity measurements, excess moisture was gently removed without damaging the native hydrates by drying at 60ºC for 7 days in a dry oven. For comparison, a piezoresistivity specimen of Portland cement was prepared with a water/binder ratio of 0.3 at cured at room temperature for 28 days prior to testing.

The piezoresistivity was calculated by measuring the conductivity of the specimens with an alternating current source, adapted from the method described by *Saafi et al*. (M. Saafi et al., 2018). The electrical properties were measured using the experimental setup shown in Figure 7.1(c). Compressive stress was applied at 1 MPa intervals up to 10 MPa in a direction orthogonal to the orientation of the electrodes. At each interval, the conductivity was measured using a Wheatstone bridge containing resistors of 860 kΩ and a 10-volt alternating current source between 10 Hz and 10 MHz. The resistance of the bridge resistors was selected to be close to the expected resistance of the specimen, based on published values for other alkali activated fly ash inorganic polymers, to maximize the accuracy of the measurement (Hanjitsuwan et al., 2011). The source voltage, V_{source}, and the voltage across the electrodes, $V_{electrodes}$, were measured using an InfiniiVision® 3034A oscilloscope (Agilent Technologies Inc.) and the sample resistance, R_{sample}, was calculated using the following equation, derived from Ohms law:

$$R_{sample} = R_3 \frac{R_2 - \frac{V_{electrodes}}{V_{source}}(R_1 + R_2)}{R_1 + \frac{V_{electrodes}}{V_{source}}(R_1 + R_2)} \qquad \text{Equation 7.1}$$

where R_1, R_2, and R_3 are the resistances of the of the bridge resistors in the configuration shown in Figure 7.1(c). The self-sensing piezoresistivity was quantified, by convention, as the fractional change in resistance (FCR) defined by:

$$FCR\ (\sigma, \varepsilon) = \frac{R_o - R_{\sigma,\varepsilon}}{R_o} \qquad \text{Equation 7.2}$$

where ρ_o is the unstrained resistivity, and $\rho_{\sigma,\varepsilon}$ is the resistivity at stress σ or strain ε, respectively.

7.3 Theoretical calculations

A structural model of an alkali activated inorganic polymer was generated from the molecular dynamics simulation presented by *Zhang et al.* (M. Zhang et al., 2018). A 240 atom structure, representing at 1.5 nm cube of inorganic polymer, was modeled in the opensource software Quantum Espresso. The structure achieved the elemental ratio of 1.1:1:3 Na/Al/Si and an H_2O/Al_2O_3 ratio of 10.75. The structure was relaxed using the Broyden-Fletcher-Goldfarb-Shanno algorithm to minimize the free energy as described by *Fletcher* (Fletcher, 2013). Following the methodology explained by *Calderin et al.* Quantum Espresso was used to compute the theoretical electrical conductivity of this structure and a projector augmented wave pseudopotential was assumed for each atom (Calderín et al., 2017). The self-consistent field calculations were conducted to establish boundary conditions. This calculation was solved iteratively for the kinetic energy (Wfc) and potential energy (Rho) cut-offs in ranges of 40-95 and 300-800, respectively, using 111 kpoint and David diagonalization for each element present in the inorganic polymer. The self-consistent field parameters are given in Table 7.1 and were used in Quantum Espresso to solve the Kubo-Greenwood theorem of electrical conductivity.

Table 7.1 Self-consistent field calculation results for the alkali activated inorganic polymer.

Element	Wfc	Rho
Sodium	85	750
Aluminum	75	450
Silicon	85	750
Hydrogen	65	700
Oxygen	45	600

The Kubo-Greenwood theorem is a quantum mechanical expression that describes the transport coefficient of electrons through a structure for a perturbation of frequency ω (Greenwood, 1958 ; Kubo, 1957). In the general case, the electrical conductivity, σ, is given by the expression:

$$\sigma(\omega) = \frac{2ie^2\hbar^3}{m_e^2 V}\sum_{m,m'}\frac{\Delta f_{m'm}}{\Delta\epsilon_{mm'}}\frac{\langle m|\nabla|m'\rangle\langle m'|\nabla|m\rangle}{\left(\Delta\epsilon_{mm'}-\hbar\omega+i\delta/2\right)} \qquad \text{Equation 7.3}$$

for each pair of atoms, m and m', where f is the Fermi-Dirac occupation number, ϵ is the corresponding eigenvalue, δ is a constant related to the average inter-collision time, and V is the unit cell volume. The theorem was solved with the given parameters and structure using the methodology described by *Calderin et al.* (Calderín et al., 2017). Interested readers are directed towards that manuscript for an in-depth explanation. Notably, the application of the Kubo-Greenwood theorem yields the theoretical conductivity of the material, under the assumption of no atomic movement and no interfacial contributions (Dufty et al., 2018). The theoretical self-sensing behavior of the inorganic polymer was calculated by applying artificial strain to the structural model. The structure was strained at intervals up to 0.8%. At each interval, the Kubo-Greenwood theorem was applied to yield a new strained conductivity and the piezoresistivity was quantified as fractional change in resistance (FCR).

7.4 Results and discussion

In this study, a novel method is demonstrated to measure the piezoresistivity of smart building materials. The method is adapted from the work presented by *Saafi et al*., which demonstrated intrinsic piezoresistivity in an inorganic polymers using alternating current conditions (M. Saafi et al., 2018). Alternating current eliminates the effect of polarization in insulating materials, such as inorganic polymers, which causes the conductivity to decline over time during the measurement (Han et al., 2015). Inorganic polymers have high polarizability making them particularly susceptible this form of systemic error (Hanjitsuwan et al., 2011). Polarization has lead other investigators to conclude that piezoresistivity in inorganic polymers can only be observed under cyclic loading conditions, which is impractical for most applications of in-situ self-sensing (Z. Tang et al., 2019). However, it has been recently

demonstrated that piezoresistive composites can be used under static loading conditions with alternating current (Mohamed Saafi et al., 2014).

This study demonstrates that this methodology can be used to measure the intrinsic piezoresistivity of inorganic polymers under static loading conditions. The electrical resistance was measured with an alternating current source using a Wheatstone bridge and oscilloscope, as shown in Figure 7.1(c). At a testing frequency of 10 Hz, the measurements could be conducted rapidly and reliably, leading to minimal standard deviation, depicted as error bars in the figures. This methodology was used to assess the piezoresistivity of the alkali activated inorganic polymer and Portland cement. The piezoresistivity was quantified as the fractional change in resistance (FCR) at each compressive stress interval in Figure 7.1(a). The inorganic polymer exhibited strong piezoresistivity, up to 12.2% FCR at 10 MPa. The FCR closely follows a logarithmic trend (R^2>0.98) with a stress sensitivity coefficient of 0.05 MPa^{-1}.

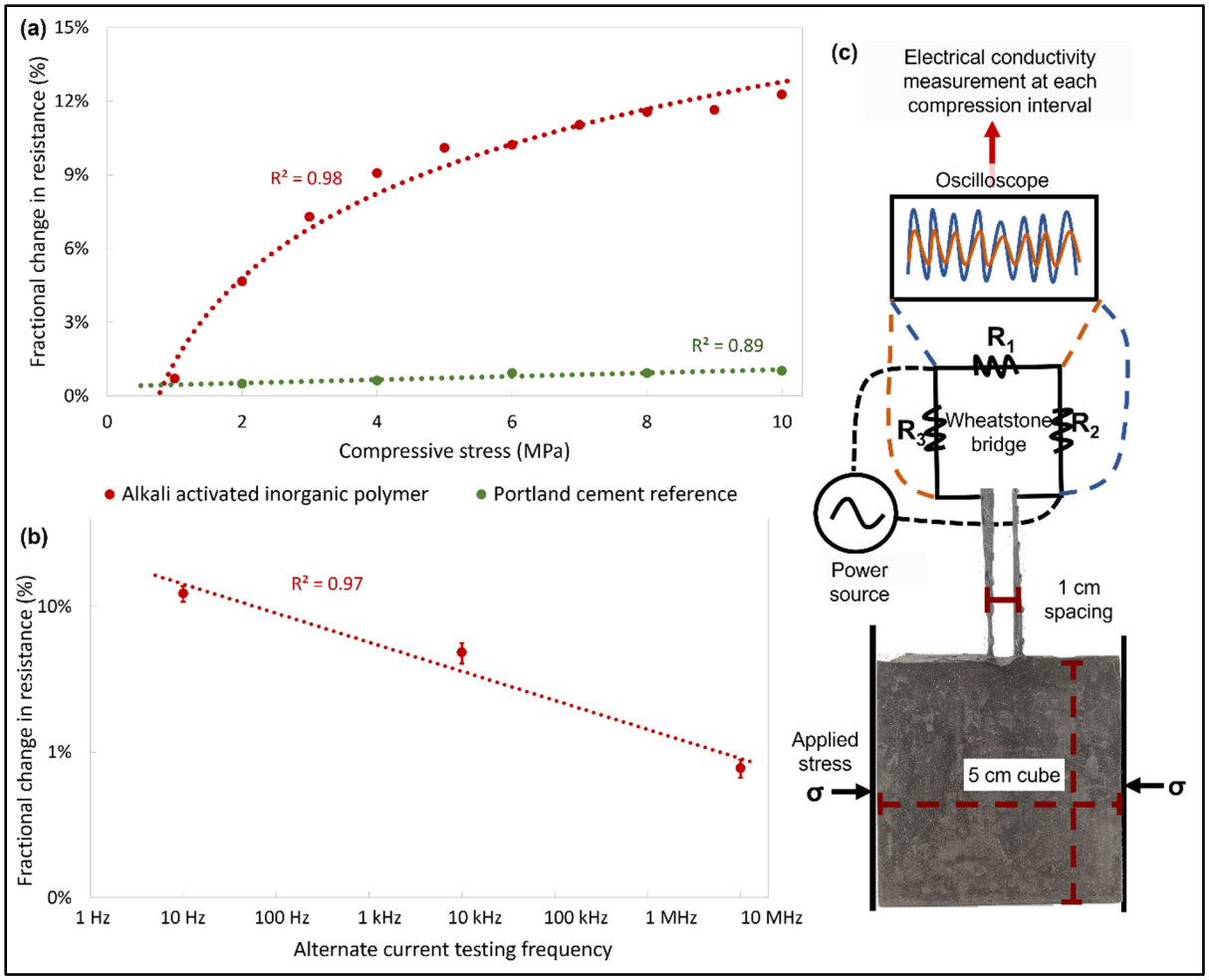

Figure 7.1 (a) The piezoresistivity of alkali activated inorganic polymer and Portland cement at 10 Hz, (b) the frequency dependence of the piezoresistivity of inorganic polymers at 10 MPa, and (c) the experimental method for the piezoresistivity measurement.

The piezoresistivity of the inorganic polymer was significantly higher than prior studies of inorganic polymers under cyclic loading. Inorganic polymers without conductive additives have FCR below 1% when measured with direct current under a cyclic loading (C. Mizerová et al., 2021 ; Cecílie Mizerová et al., 2021). The results shown in Figure 7.1(a) reveal that the use of alternating current increases the measurable FCR by a factor of 10. For comparison, Portland cement is known to not be piezoresistive under direct current conditions and the results show it is not improved with the use of alternating current (Han et al., 2015). This result presents an opportunity for the future use of inorganic polymers as self-sensing materials.

However, the frequency dependence of the piezoresistivity, shown in Figure 7.1(b), reveals a more complicated relationship.

While direct current conditions diminish the FCR of inorganic polymers, so too does the use of high alternating currents. The piezoresistivity of the inorganic polymers was found to closely follow a power function (R^2>0.97) with frequency and be maximized at low frequencies. This can be understood as a combination of multiple phenomena. The conductivity of alkali activated materials is known to vary over several orders of magnitude as a function of testing frequency (Hanjitsuwan et al., 2011). It is reasonable to infer that not all of the conductive species in inorganic polymers contribute to the piezoresistivity. The frequency dependence of the piezoresistivity implies that the conductive species responsible for piezoresistivity are diminished at higher frequencies more so than other conductive species in the inorganic polymer.

Moreover, the disappearance of the piezoresistivity under direct current conditions can be understood as a artifact of polarization. Inorganic polymers are known to have high polarizability and this quality leads to a time-dependent reduction in conductivity under direct current conditions. In prior studies, this artifact has counteracted the increasing in conductivity due to piezoresistivity, leading researchers to conclude that inorganic polymers are not intrinsically piezoresistive. However, with the use of alternating current, the polarization manifests as a phase shift in the results which can be accounted for to eliminate this artifact and accurately observe the intrinsic piezoresistivity of the inorganic polymers.

An operating frequency of 10 Hz was selected as a compromise of rapid measurement speed, to avoid fluctuations in the compressive loading of the specimen, and the high piezoresistive response of the material. Future studies that employ this methodology must be consistent with the measurement frequency to make faithful comparisons. At this frequency, a good FCR of 12.2% was measured for the inorganic polymer giving it an intrinsic piezoresistivity that rivals piezoresistive composites. The results are in the range of the 16.5% FCR of inorganic polymer composites containing graphene and the 7% FCR of carbon fiber composites at 10 MPa (Deng et al., 2019 ; Mohamed Saafi et al., 2014). The intrinsic FCR of inorganic polymers is comparable to the 13-20% FCR that has been achieved with cement composites containing carbon fiber and carbon nanotubes at 10 MPa (Azhari & Banthia, 2012 ; S. Ding, Ruan, Yu,

Han, & Ni, 2019). Inorganic polymers are superior because they reach similar FCR intrinsically, without the added cost, environmental impact, or durability reduction caused by carbon fiber addition.

Understanding the piezoresistive mechanisms within inorganic polymers requires modeling electrical changes in the structure during strain. Prior studies have suggested, without evidence, that the strong piezoresistive response in inorganic polymers originates from the ionic conductivity of alkali cations through the amorphous structure (Caterina Lamuta et al., 2016 ; M. Saafi et al., 2018). This study seeks to challenge that conjecture and prove that the piezoresistivity arises, at least in part, from changes in electron mobility. To accomplish this goal, the electrical properties were modeled from first principles using the Kubo-Greenwood theorem. This is a first-of-its-kind computation of the theoretical conductivity of an amorphous ceramic-like material. The computation does not consider the conduction or movement of ions, assuming fixed atomic positions (Dufty et al., 2018). This will elucidate the electron mobility contribution to the piezoresistivity as artificial strains are applied to the structure.

The modeled alkali activated inorganic polymer has the same elemental ratio (1.1:1:3 Na/Al/Si) as the experimental specimens that were tested. The relaxed model is shown in Figure 7.2(a). The piezoresistivity, quantified as the fractional change in resistance (FCR), was computed at four intervals of strain, up to 0.8%. The piezoresistivity is shown in Figure 7.2(b) to increase linearly (R^2>0.99) up to 14% FCR with a strain sensitivity coefficient of 17.8. This definitively proves that inorganic polymers exhibit piezoresistivity as an intrinsic material property, not caused by an undocumented phase or other phenomena.

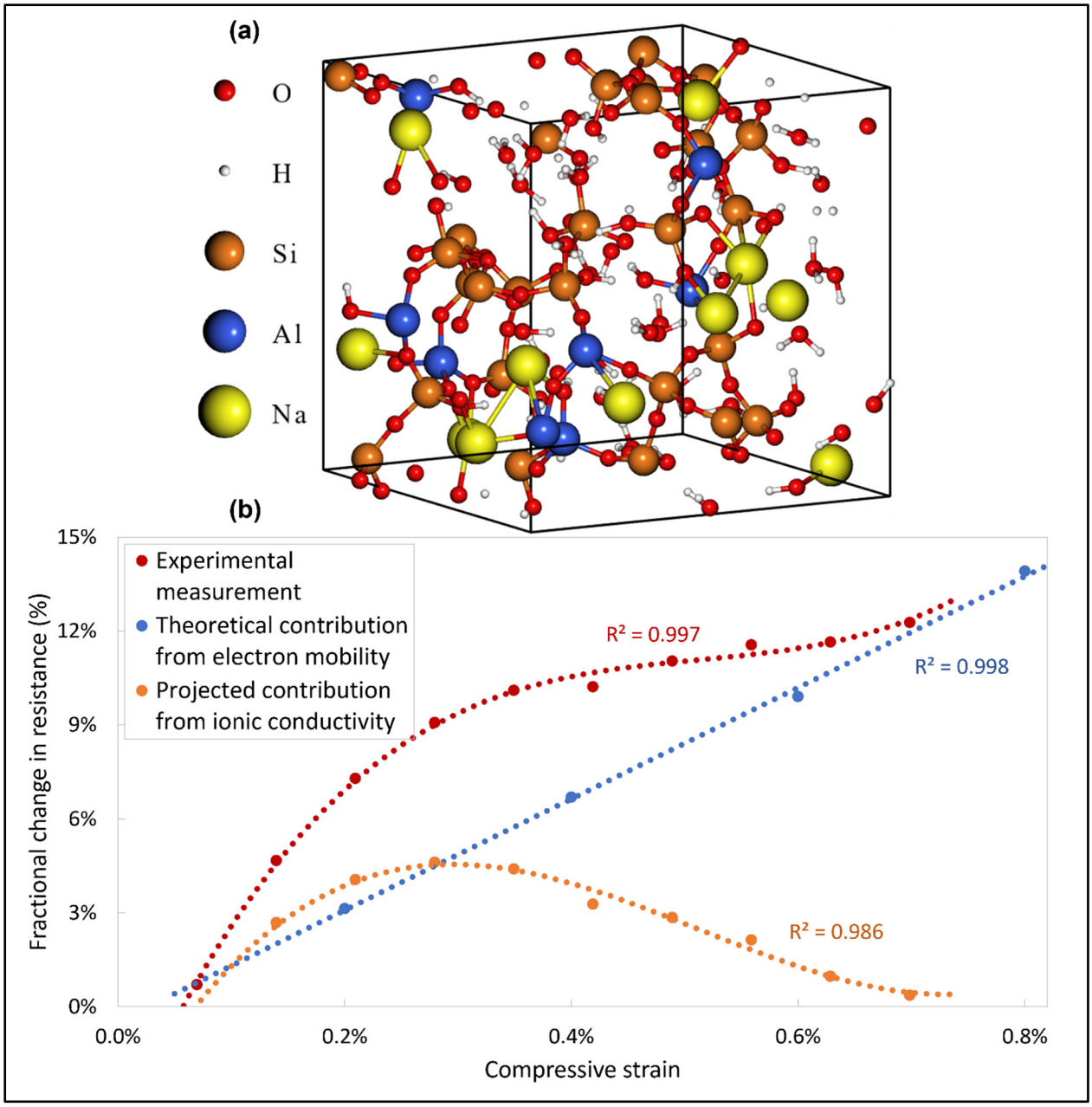

Figure 7.2 (a) The structural model of the alkali activated inorganic polymer of elemental ratio 1.1:1:3 Na/Al/Si after relaxation in Quantum Espresso and (b) the theoretical piezoresistivity of the inorganic polymer and the contribution from the ionic conductivity.

The result also proves that changes in electron mobility are a major contributor to the piezoresistive response. However, the electrical contribution to the piezoresistivity, calculated computationally, is lower than what was measured experimentally, particularly at low strains.

A reasonable hypothesis is that the difference between the computationally predicted and experimentally measured piezoresistivity can be attributed to the ionic conductivity of the alkali activated inorganic polymer, which is not considered in the computational model. Conductivity can arise as a result of electrical or ionic mobility and both types of conductivity can be increased by strain to contribute to the piezoresistivity. While the computational model predicts a theoretical electrical contribution, the ionic contribution can be estimated by taking the difference between the theoretical calculation and the experimental results. The contribution of the ionic conductivity, as shown in Figure 7.2(b), is significant at small strains but declines at high strain values. Charge hopping mechanisms for ionic mobility are enhanced when strain is applied because the distance between neighboring sites is reduced (Caterina Lamuta et al., 2016). However, at higher strains, the conduction pathways are constricted, resulting in lower ionic mobility. The ionic contribution becomes negligible at higher strains and the experimentally measured FCR converges with the predicted piezoresistivity due to the electronic mobility. The two factors together result in the nonlinear piezoresistive behavior that is observed experimentally.

Smart building materials are required to exhibit high mechanical properties, excellent durability, and useful self-sensing properties. Alkali activated inorganic polymers have been extensively studied in the literature as a cement alternative with greater mechanical properties and durability than Portland cement (Susan A Bernal & Provis, 2014). The compressive and flexural strengths of the experimental specimen investigated in this work were measured to be 31.9 and 3.90 MPa, respectively. This meets the requirements for infrastructure applications and is consistent with typical values for alkali activated fly ashes (Provis et al., 2019). With high strength and intrinsic piezoresistivity, this inorganic polymer is a competitive alternative to cement composites proposed for smart building materials. The use of alkali activated materials as piezoresistive building materials circumvents the challenges facing conventional cement-carbon fiber composites including high cost, dispersion reproducibility, and limited durability (Gupta et al., 2017 ; Han et al., 2015 ; H. Wang et al., 2018). Alkali activated inorganic polymers are a superior smart building material. The measurement method and theoretical model for the intrinsic piezoresistivity presented in this work create a framework for future investigations into this novel material solution. Future studies should apply

compositional modifications to the inorganic polymer to bolster the mechanical properties and investigate the impact of these compositional changes on the piezoresistive behavior.

7.5 Conclusion

Alkali activated inorganic polymers are a superior smart building material with high mechanical strength and intrinsic self-sensing behavior. However, to date, they have been overlooked because their structure and properties are not well understood. In this study, a combined theoretical and experimental approach has been applied to elucidate the nature of the intrinsic piezoresistivity of alkali activated inorganic polymers. The results shed light on the origin of this property in inorganic polymers and demonstrate a methodology that can be used to investigate the theoretical properties of other smart building materials. Alkali activated inorganic polymers offer a superior combination of strength and self-sensing behavior compared to conventional cement composites, without the need for self-sensing additives.

CHAPTER 8

THE EFFECT OF COMPOSITION ON THE DIELECTRIC PROPERTIES OF ALKALI ACTIVATED MATERIALS: A NEXT GENERATION DIELECTRIC CERAMIC

Michael Di Mare[1] and Claudiane M. Ouellet-Plamondon[1]

[1] Department of Construction Engineering, École de Technologie Supérieure, 1100 Rue Notre-Dame Ouest, Montréal (QC), Canada

Paper published in *Materials Today Communications*, July 2022 (with minor changes)

8.1 Introduction

The transition to intermittent renewable energy sources, such as solar and wind power, creates a demand for high-capacity energy storage systems that are low-cost to install and maintain. Energy storage technology is divided into dielectric capacitors, electrochemical capacitors, and batteries; each with different ranges of specific energy density and power density capabilities. Dielectric capacitors are ubiquitous, versatile, and competitive in cost but limited in their energy storage capacity (Hao, 2013). For decades, researchers have sought to improve the energy storage capacity by developing new dielectric materials with higher dielectric constants. To date, the greatest dielectric constants have been achieved with calcium copper titanate and barium strontium titanate which can, under precise compositional and fabrication specifications, reach dielectric constants above 10^5 (Jesurani et al., 2012 ; Y. Zhang et al., 2011). In this work, a facile method is described to produce a novel dielectric material at a bulk scale which surpasses the most refined dielectric ceramics and achieves dielectric constants above 10^9. This could improve the energy storage capacity of dielectric capacitors by a factor of one thousand and revolutionize static energy storage systems.

Improved dielectric constants translate to an enhanced energy storage capacity. The energy stored in a dielectric capacitor is proportional to dielectric constant. Great increases in dielectric constant have been found in conventional dielectric ceramics, e.g. barium titanate, by carefully controlling the elemental composition of the ceramic (Hao, 2013). Refinement of the composition is responsible for improvement in barium titanate dielectric constants from around 100 to above 10^3 (Kokubo, Kung, & Tashiro, 1968 ; Yao et al., 1997). However, this methodology of compositional control has not been applied to all dielectric materials. Alkali activated materials (AAM) are a class of amorphous materials with physical and chemical properties similar to ceramics. They are known to exhibit high dielectric constants but have been generally overlooked as dielectric materials due to their cement-like mechanical and setting properties (Hanjitsuwan et al., 2011). In this study, a four-factor compositional optimization was conducted in a factorial experimental design to maximize the dielectric constant of AAM. The results exceeded expectations and yielded a dielectric AAM with polarizability far exceeding that of dielectric ceramics.

Dielectric ceramics are categorized as linear dielectrics, ferroelectrics, relaxor ferroelectrics, or antiferroelectrics based the hysteresis in their polarization. The hysteresis arises from remnant polarization during charging and discharging which leads to nonrecoverable energy loss (S. Liu, Shen, Hao, & Zhai, 2019). The majority of research attention has been focused on ferroelectrics (e.g. barium titanate) and antiferroelectrics (e.g. perovskite ceramics) because of the high dielectric constants of these materials. In contrast, linear dielectrics exhibit no hysteresis in their polarization resulting in greater energy recovery (S. Liu et al., 2019). This behavior occurs in centrosymmetric crystals, such as aluminum oxide, and glasses. Linear dielectrics have desirable high breakdown voltages, but their application is limited by their lower saturated polarization due to relatively low dielectric constants (Hao, 2013). Few studies have overcome this obstacle by discovering new centrosymmetric or amorphous materials with linear dielectric behavior and high dielectric constants.

The search for new linear dielectric requires the recognition of novel materials. Research in dielectric ceramics is predominantly focused on incremental improvements in the elemental optimization of perovskite ceramics (S. Liu et al., 2019 ; Yadav & Gautam, 2014). These studies do not address the fundamental challenges in scalability and cost which limit the

deployment of high performing dielectric ceramics in energy storage infrastructure. Prior studies that have proposed creative material solutions to address these challenges, such as cement-based supercapacitors (Meng & Chung, 2010 ; Junjun Zhang et al., 2016), have received little attention from the electronic ceramics community. Thus, it has been without fanfare that the dielectric constants of AAM have been reported to be above 10^4 (Hanjitsuwan et al., 2011 ; Malkawi, Al-Mattarneh, Achara, Mohammed, & Nuruddin, 2018), despite this property exceeding the performance of ferroelectric ceramics. AAM are construction-grade materials, boasting low cost, high production volumes, and low environmental impact (Joseph Davidovits, 2002b). Their use as an alternative dielectric addresses a fundamental challenge in the production of affordable energy storage systems.

The lack of understanding of the dielectric behavior of AAM has led to the neglect of their potential. Unlike dielectric ceramics which are stable over large ranges of frequency, the dielectric polarization in AAM is understood to arise, not from dipoles, but from interfacial polarization. As such, the large dielectric constant of AAM has been interpreted as a consequence of ionic mobility of super-stoichiometric alkali cations within the amorphous structure (Caterina Lamuta et al., 2016). This causes AAM to have relatively high loss tangents and strong frequency dependence in their permittivity (Hanjitsuwan et al., 2014, 2011). The composition of the AAM plays a large role in the dielectric behavior (Hanjitsuwan et al., 2014 ; Malkawi et al., 2018). AAM are amorphous aluminosilicate materials composed of NASH (sodium-aluminum-silicon-hydrate) or KASH (potassium-aluminum-silicon-hydrate) gels. These gels for crosslinked inorganic polymers with complex chemistry, strongly influenced by the proportion of the elemental components in the NASH or KASH gels. These composition of an AAM is defined by the alkali:aluminum:silicon ratio, the type of alkali ion, and the type of activator (J. Davidovits, 1991). Preliminary studies have shown for sodium AAM that increasing the alkali content (Na/Al ratio) can increase the dielectric constant to nearly 10^5 and that switching from sodium to potassium can offer further enhancement (Hanjitsuwan et al., 2014 ; M. Saafi et al., 2018). However, the scientific literature on the dielectric properties of AAM is incomplete. There have been very few published studies on the dielectric behavior of AAM and the effect of compositional parameters beyond the alkali content on the dielectric properties is entirely unknown.

This study addresses this gap in the literature to explore the synergy between different compositional factors and maximize the dielectric constant of AAM. A four-factor optimization was conducted to determine the effect of alkali content (K/Al ratio), monomer KASH structure (Si/Al ratio), activator anions, and testing frequency on the dielectric constant, loss tangent, and ionic conductivity. The permittivity is known to be sensitive to frequency and the results will seek to support the hypothesis that this relationship is connected to the ionic conductivity. The effect of the alkali content is known for sodium AAM but has not been studied in potassium AAM. The monomer KASH structure is determined by the ratio of silica and alumina tetrahedra and is known to have a large impact on the mechanical strength and density but has never been previously considered in the study of the dielectric properties of AAM (Rowles & O'connor, 2003). Finally, the activator anion influences the mechanical strength, setting time, and environmental impact of AAM, but the effect of their chemistry on the dielectric polarization has not been studied (Susan A. Bernal, Nicolas, et al., 2015 ; Fernández-Jiménez & Puertas, 2001 ; N. Hu, Bernsmeier, Grathoff, & Warr, 2017). These four factors were studied with a factorial experimental design to elucidate the synergies between each factor. This analysis comprehensively establishes the optimal composition of potassium AAM to maximize the dielectric constant.

8.2 Experimental procedures

To measure the dielectric properties, specimens of alkali activated material (AAM) were prepared by the alkali activation of fly ash (ProAsh®, Separation Technologies LLC). The fly ash was composed of 55.3% silicon oxide, 21.4% aluminum oxide, 10.2% iron oxide, 3.4% calcium oxide, and 2.1% potassium oxide. The silicon:aluminum ratio of the AAM was modified by the addition of silica fume to the fly ash. The silica fume was deagglomerated in a pulverizing pan prior to addition to ensure dispersion and measured to have a moisture content of 4.8%. Two reagent grade potassium salts were tested separately as activators: potassium hydroxide (12% moisture) and potassium carbonate (0.1% moisture). Specimens were prepared in arrays of potassium:aluminum (K/Al) and silicon:aluminum (Si/Al) ratios with each activator, centered around the composition 1:1:2.85 (K/Al/Si). This composition was

previously reported to exhibit a high dielectric constant (M. Saafi et al., 2018). The water content was kept constant at a liquid to solids ratio of 0.18 to ensure flowable AAM pastes across the compositional range.

Table 8.1 Composition of experimental specimens.

Sample ID	Activator anion	K / Al ratio	Si / Al ratio	Fly ash (g)	Silica fume (g)	Activator (g)	Water (g)
H-0.8-2.5	Hydroxide	0.8	2.5	100	7.8	18.6	17.6
H-1-2.5	Hydroxide	1.0	2.5	100	7.8	25.0	17.7
H-1.2-2.5	Hydroxide	1.2	2.5	100	7.8	29.3	17.8
H-1.4-2.5	Hydroxide	1.4	2.5	100	7.8	34.6	17.9
H-0.8-2.85	Hydroxide	0.8	2.85	100	15.8	18.6	18.9
H-1-2.85	Hydroxide	1.0	2.85	100	15.8	25.0	19.0
H-1.2-2.85	Hydroxide	1.2	2.85	100	15.8	29.3	19.0
H-1.4-2.85	Hydroxide	1.4	2.85	100	15.8	34.6	19.1
H-1-2.3	Hydroxide	1.0	2.3	100	3.6	25.0	17.0
H-1-2.7	Hydroxide	1.0	2.7	100	12.1	25.0	18.4
H-1-3	Hydroxide	1.0	3.0	100	20.5	25.0	19.7
H-1-3.2	Hydroxide	1.0	3.2	100	24.7	25.0	20.4
H-1.4-2.3	Hydroxide	1.4	2.3	100	3.6	34.6	17.2
H-1.4-2.7	Hydroxide	1.4	2.7	100	12.1	34.6	18.5
H-1.4-3	Hydroxide	1.4	3.0	100	20.5	34.6	19.9
C-0.8-2.5	Carbonate	0.8	2.5	100	7.8	18.9	24.1
C-1-2.85	Carbonate	1.0	2.85	100	15.8	27.0	25.6
C-1.2-2.85	Carbonate	1.2	2.85	100	15.8	31.6	26.4
C-1.4-2.85	Carbonate	1.4	2.85	100	15.8	37.7	27.5
C-1.6-2.85	Carbonate	1.6	3.0	100	15.8	43.2	28.5
C-1.8-2.85	Carbonate	1.8	3.0	100	15.8	49.0	29.5
C-2-2.85	Carbonate	2.0	3.0	100	15.8	56.5	30.9
C-1-2.3	Carbonate	1.0	2.3	100	3.6	27.0	23.4
C-1-2.5	Carbonate	1.0	2.5	100	7.8	27.0	24.2
C-1-2.7	Carbonate	1.0	2.7	100	12.1	27.0	24.9
C-1-3	Carbonate	1.0	3.0	100	20.5	27.0	26.4
C-1-3.2	Carbonate	1.0	3.2	100	24.7	27.0	27.2
C-1.4-2.3	Carbonate	1.4	2.3	100	3.6	37.7	25.3
C-1.4-2.5	Carbonate	1.4	2.5	100	7.8	37.7	26.1
C-1.4-2.7	Carbonate	1.4	2.7	100	12.1	37.7	26.8
C-1.4-3	Carbonate	1.4	3.0	100	20.5	37.7	28.3
C-1.4-3.2	Carbonate	1.4	3.2	100	24.7	37.7	29.1

The mixing of the AAM paste was conducted in a low shear mixer with a radial flow impeller. The AAM were prepared with a one-part mixing methodology to enhance the scalability of the process. The powders, fly ash, silica fume, and activator, were gently premixed by hand until a homogenous powder was obtained which achieves the desired elemental ratio (K/Al/Si). Then, deionized water was added to achieve the targeted liquid to solid ratio. The mixture was mixed for five minutes at 200 rpm until a homogenous paste was obtained. The paste was immediately cast into polyoxymethylene molds. Disks of diameter 40 mm and thickness 2 mm were prepared for broadband dielectric spectroscopy, as shown in Figure 8.1(d). The samples of each composition were cured at 60ºC for two days in a sealed environment to prevent moisture loss. Subsequently, they were dried at 60ºC for one day to remove surface moisture without decomposing the native hydrates in the AAM.

In the performance of a dielectric, two material properties must be considered: the dielectric constant and the loss tangent. The dielectric constant is directly proportional to the energy storage capacity of a capacitor. The loss tangent quantifies the amount of energy that is lost to heat during charging. The dielectric properties and conductivity of the specimens were measured by broadband dielectric spectroscopy (Novocontrol Technologies GmbH) at room temperature. A quadratic profile wave of amplitude three volts was applied cyclically at room temperature at frequencies between 0.1 Hz and 1 MHz. Specimens were prepared in quadruplicate and averaged to produce the results shown. Additional specimens were prepared for cyclic voltammetry. The pastes were mixed in an identical manner and cast into 5 cm cubes. A mounted bracket was used to maintain a pair of stainless-steel mesh electrodes in parallel at a spacing of 1 cm apart. The specimens were cured in a sealed environment, to prevent moisture loss, and then dried in the same manner described above. Cyclic voltammetry was conducted using a source measurement unit (2450 SourceMeter, Keithley Instruments) with a triangular voltage profile magnitude $\pm$1 Volts and a scan speed of 1 Hz.

8.3 Results and discussion

8.3.1 Dielectric properties of potassium hydroxide activated fly ash

Broadband dielectric spectroscopy analyzes the frequency dependence of the electrical and dielectric properties of a material. The dielectric behavior of alkali activated materials (AAM) is known to vary significantly with frequency (Malkawi et al., 2018). The frequency dependence of the dielectric constant, loss tangent, and conductivity for four AAM is shown in Figure 8.1. The relationships agree with previously reported trends for AAM (Hanjitsuwan et al., 2014, 2011). The dielectric constant, Figure 8.1(a), exhibited two slopes: a nearly constant dielectric constant above 10 kHz and a constant exponential increase at lower frequencies. Above 100 kHz, the dominant polarization mechanism was dipolar, caused by local shifts in the ions within the amorphous AAM structure. This is corroborated by the two-regime conductivity shown in Figure 8.1(c). At high frequencies, the conductivity was predominantly electronic, while at low frequencies the conductivity approached a lower, constant value indicating that it was caused by mobility of alkali ions, particularly potassium, which were loosely bound to alumina tetrahedra in the KASH structure (J. Davidovits, 1991). Greater ionic conduction at low frequency drove ionic-interfacial polarization, which is responsible for the high dielectric constants reached at low frequency. Notably, the dielectric constant continued to rise at low frequencies without approaching a constant value. This indicated that the AAM exhibited low frequency dispersion and the dielectric behavior cannot be accurately modeled using traditional Debye relaxation models. This polarization was caused by the electrostatic accumulation of ions along interfaces and grain boundaries within the AAM, due to ionic conduction in the presence of the external electric field (Dakin, 2006). The contribution of this polarization was enhanced at low frequencies because the greater period gave more ions time to migrate to the interfaces, increasing the total polarization.

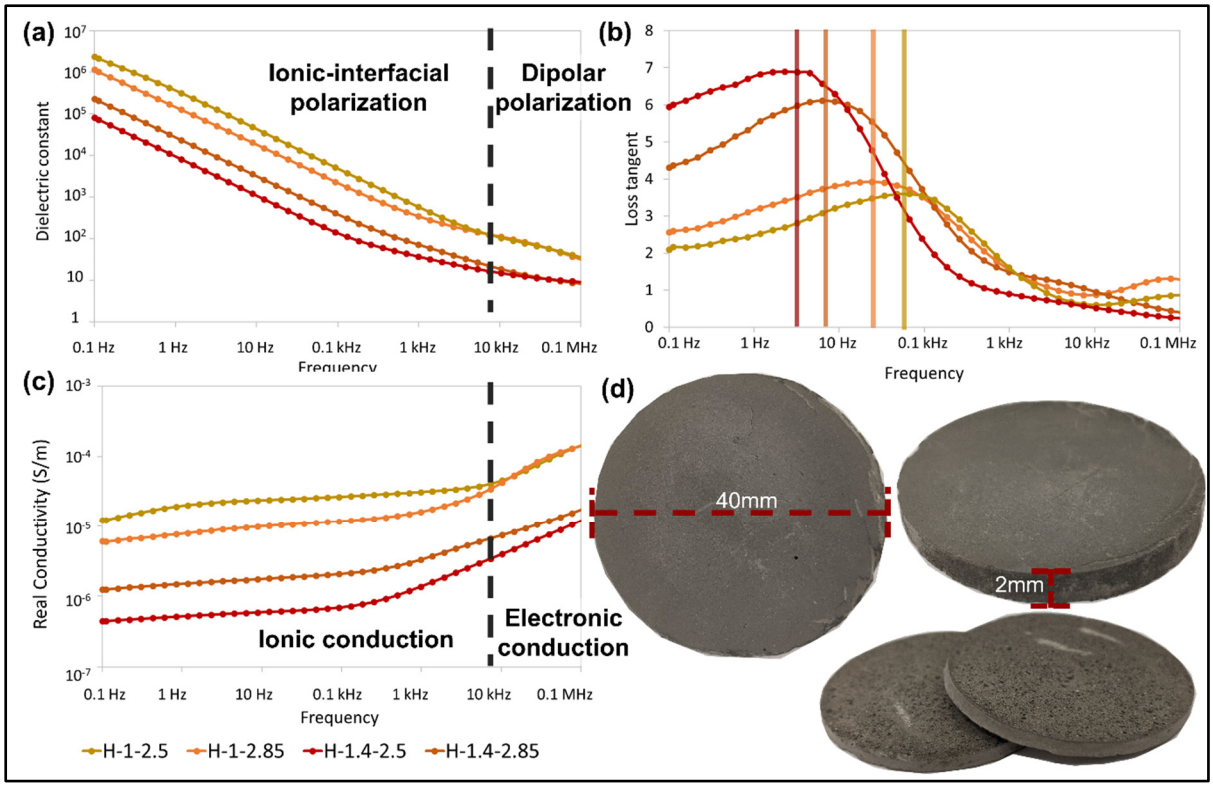

Figure 8.1 Broadband dielectric spectroscopy of potassium hydroxide AAM with different elemental compositions, defined by the K/Al/Si ratio, for (a) dielectric constant, (b) loss tangent, and (c) conductivity. (d) AAM experimental specimen prepared for analysis.

The energy loss during polarization is represented as loss tangent, shown in Figure 8.1(b), the ratio of the dielectric loss and dielectric constant. The loss tangent is a material property influenced by the bonding and molecular structure of the KASH gel. Interestingly, the loss tangent declined at lower frequencies, despite the presence of strong low frequency dispersion in the AAM. This is promising for the practical use of AAM at low frequencies with minimal dielectric loss. The changing position of the peak in loss tangent, highlighted by the vertical lines in Figure 8.1(b), are an indication of structural differences between the amorphous AAM and the influence of the elemental proportion on the KASH gel (Goracci, Monasterio, Jansson, & Cerveny, 2017). The shift in the loss tangent peaks confirms the impact of the elemental proportions of the AAM on the dielectric properties, which can also be seen in the dielectric constant and conductivity. The four AAM shown in Figure 8.1 form two pairs based on their potassium:aluminum (K/Al) ratio, indicating that this factor has a significant influence on the

dielectric properties and conductivity. This trend agreed with previous reports of the effect of alkali content in sodium-based AAM (Hanjitsuwan et al., 2014). However, the silicon:aluminum (Si/Al) ratio, which has not been considered in any previous study, could also be seen to have a substantial impact on both the dielectric constant and the conductivity.

Table 8.2 Summary of dielectric properties of potassium hydroxide activated inorganic polymers based on their elemental ratio.

Sample ID	K / Al ratio	Si / Al ratio	Dielectric constant at 0.1 Hz	Dielectric constant at 50-60 Hz	Conductivity at 50-60 Hz (S/m)
H-0.8-2.5	0.8	2.5	5.0×10^{3}	1.2×10^{2}	3.0×10^{-9}
H-1-2.5	1.0	2.5	1.5×10^{6}	1.0×10^{3}	1.6×10^{7}
H-1.2-2.5	1.2	2.5	7.2×10^{3}	8.0×10^{1}	3.1×10^{-9}
H-1.4-2.5	1.4	2.5	1.2×10^{4}	7.1×10^{1}	5.2×10^{-9}
H-0.8-2.85	0.8	2.85	3.7×10^{3}	1.1×10^{2}	2.4×10^{-9}
H-1-2.85	1.0	2.85	5.5×10^{5}	9.7×10^{2}	1.5×10^{-7}
H-1.2-2.85	1.2	2.85	7.4×10^{4}	2.3×10^{2}	2.2×10^{-8}
H-1.4-2.85	1.4	2.85	4.3×10^{4}	1.2×10^{2}	1.7×10^{-8}
H-1-2.3	1.0	2.3	5.5×10^{3}	6.2×10^{1}	2.8×10^{-9}
H-1-2.7	1.0	2.7	1.7×10^{5}	3.7×10^{2}	4.8×10^{-8}
H-1-3	1.0	3.0	8.0×10^{3}	1.2×10^{2}	5.2×10^{-9}
H-1-3.2	1.0	3.2	4.5×10^{3}	8.5×10^{1}	2.9×10^{-9}
H-1.4-2.3	1.4	2.3	2.1×10^{5}	3.0×10^{2}	4.6×10^{-8}
H-1.4-2.7	1.4	2.7	6.1×10^{3}	5.6×10^{1}	3.2×10^{-9}
H-1.4-3	1.4	3.0	2.6×10^{3}	4.0×10^{1}	1.8×10^{-9}

To further the effect of these two elemental ratios on these two properties, an array of compositions was tested with varying combinations of K/Al and Si/Al ratios. The dielectric constant and conductivity in the 50-60 Hz range, which is of principle interest in conventional energy storage, is given in Table 8.2. The dielectric properties were found to be strongly dependent on the elemental ratios. There is a strong correlation between the compositions

which exhibited higher dielectric constant with greater conductivity. This further supports the hypothesis proposed by other works that the large dielectric polarization of AAM is caused by ionic conductivity and ionic-interfacial polarization (Caterina Lamuta et al., 2016). The composition H-1-2.5 exhibited the highest dielectric constant, 10^3 at 50-60 Hz. This is comparable to barium titanate at the same frequency (Kokubo et al., 1968 ; Yadav & Gautam, 2014 ; Yao et al., 1997). However, unlike barium titanate and other ferroelectric ceramics, the dielectric constant is dramatically increased at low frequency. The dielectric constant, shown in Figure 8.1(a), exponentially increases at lower frequencies and can reach exceedingly high values at pseudo-direct current conditions, such as 0.1 Hz. At 0.1 Hz, the H-1-2.5 composition reaches a dielectric constant of 10^6, which is 1000 times higher than barium titanate and 200 times higher than barium strontium titanates (Jiwei et al., 2002 ; Rhim et al., 2000 ; Yadav & Gautam, 2014 ; Yao et al., 1997 ; Q. Zhang, Cui, Dong, & Du, 2009). The increased dielectric constant at low frequencies occurs in all compositions, as shown in Table 8.2, and is enhanced for compositions which are more favorable to polarization at 50-60 Hz.

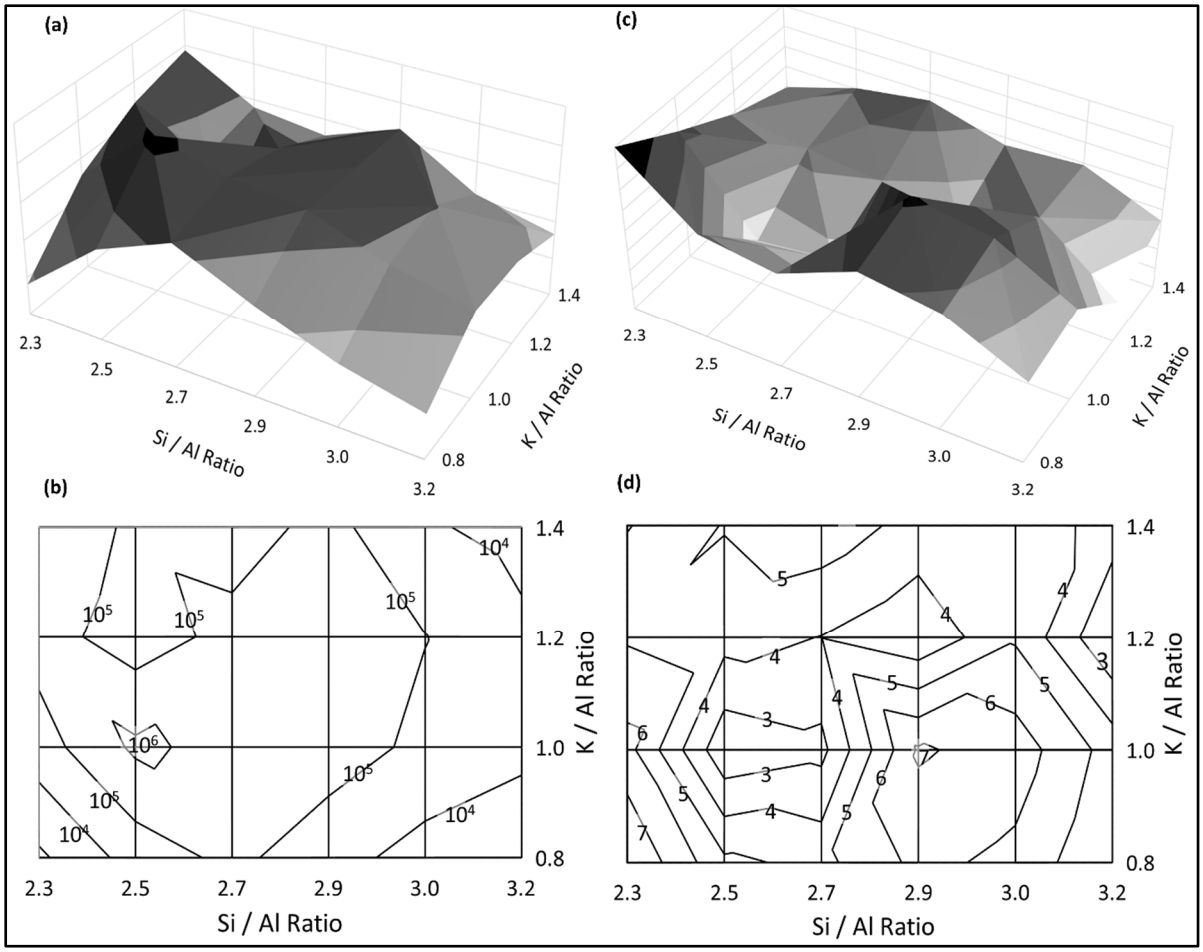

Figure 8.2 (a,b) The compositional dependence of the dielectric constant at 0.1 Hz visualized as (a) a 3D rendering and (b) a contour plot. (c,d) The loss tangent at 0.1 Hz illustrated with (c) a 3D rendering and (d) a contour plot across the compositional array

To map the effect of the elemental ratios on the dielectric constant and understand the effect of the KASH composition on the dielectric properties, the dielectric properties at 0.1 Hz were visualized in the manner shown in Figure 8.2. The effect of the K/Al and Si/Al ratios are not independent, as shown in the 3D rendering and contour plot of Figure 8.2(a,b), with a maximum that is interdependent on both factors. Prior literature on the topic has solely considered the impact of alkali content (K/Al) on the dielectric constant (X.-M. Cui, Zheng, Han, Su, & Zhou, 2008 ; Hanjitsuwan et al., 2014). However, Figure 8.2(b) clearly shows that both the alkali content and the monomer KASH structure (Si/Al) are equally important. In the range of Si/Al ratio 2.0 to 3.0, AAM are understood to be composed of a mixture of sialate-

siloxo and silate-disiloxo monomers (J. Davidovits, 1991). For potassium hydroxide AAM, the maximum was observed at a Si/Al ratio 2.5, indicating that dielectric polarization is maximized when an even distribution of the two types of monomers is present within the AAM. For the optimum composition, H-1-2.5, the 10^6 dielectric constant measured surpasses the highest dielectric constant reported for sodium AAM by a factor of one hundred (Hanjitsuwan et al., 2014).

There is a correlation between the compositional dependence of the dielectric constant and the loss tangent. The highest dielectric constant and lowest loss tangent are found at the same composition. This is a desirable combination of energy storage applications that seek to store large energy densities while minimizing charging losses. The loss tangent, shown in Figure 8.2(c,d), does not share precisely the same compositional dependence as the dielectric constant. Moreover, the loss tangent for the potassium hydroxide AAM, even at the optimized composition of H-1-2.5, is significantly higher than is desired for the application of a linear dielectric. While post-treatment methodologies, such as calcination (X. Cui, Liu, He, Chen, & Zhou, 2011), may be capable at reducing the loss tangent, they add cost and processing complexity which reduces one of the key advantages of AAM over conventional dielectric ceramics. A more desirable solution is the discovery of a better AAM composition which further improves the dielectric properties.

8.3.2 Maximizing the dielectric constant with potassium carbonate activated fly ash

In search of alkali activated materials (AAM) with high dielectric constant and low loss tangent, an alternative potassium activator was investigated. An array of potassium carbonate AAM was prepared with varying K/Al and Si/Al ratios and analyzed by broadband dielectric spectroscopy. The dielectric properties and conductivity exhibited equivalent frequency dependence to potassium hydroxide AAM discussed previously. However, the dielectric constant and conductivity were significantly higher than the AAM activated with potassium hydroxide, as shown in Table 8.3. At 50-60 Hz, the dielectric constant exceeds 10^6 for some compositions and at the optimum composition, C-1.4-2.85, the dielectric constant reaches 10^9

at 0.1 Hz, a 1000-fold increase over that of the potassium hydroxide AAM. This is the highest dielectric constant ever reported for a ceramic-like dielectric.

Table 8.3 Summary of the dielectric properties of potassium carbonate activated inorganic polymers based on their elemental ratio.

Sample ID	K / Al ratio	Si / Al ratio	Dielectric constant at 0.1 Hz	Dielectric constant at 50-60 Hz	Conductivity at 50-60 Hz (S/m)
C-0.8-2.5	0.8	2.5	8.8×10^{6}	2.3×10^{4}	2.5×10^{-4}
C-1-2.85	1.0	2.85	5.7×10^{6}	7.5×10^{3}	9.9×10^{-5}
C-1.2-2.85	1.2	2.85	6.7×10^{8}	4.2×10^{6}	3.8×10^{-2}
C-1.4-2.85	1.4	2.85	1.1×10^{9}	3.5×10^{6}	2.1×10^{-2}
C-1.6-2.85	1.6	3.0	2.0×10^{8}	2.5×10^{5}	3.2×10^{-3}
C-1.8-2.85	1.8	3.0	2.2×10^{8}	3.5×10^{5}	6.5×10^{-3}
C-2-2.85	2.0	3.0	1.0×10^{8}	2.1×10^{5}	3.1×10^{-3}
C-1-2.3	1.0	2.3	8.0×10^{7}	3.4×10^{5}	3.9×10^{-3}
C-1-2.5	1.0	2.5	2.7×10^{7}	3.8×10^{4}	7.3×10^{-4}
C-1-2.7	1.0	2.7	1.2×10^{6}	2.4×10^{3}	3.6×10^{-5}
C-1-3	1.0	3.0	1.7×10^{5}	3.1×10^{2}	4.3×10^{-6}
C-1-3.2	1.0	3.2	1.5×10^{2}	4.8×10^{1}	6.6×10^{-8}
C-1.4-2.3	1.4	2.3	8.1×10^{7}	1.8×10^{5}	2.1×10^{-3}
C-1.4-2.5	1.4	2.5	8.1×10^{6}	5.6×10^{4}	5.9×10^{-4}
C-1.4-2.7	1.4	2.7	7.8×10^{6}	1.1×10^{4}	1.7×10^{-4}
C-1.4-3	1.4	3.0	2.5×10^{7}	4.3×10^{4}	7.8×10^{-4}
C-1.4-3.2	1.4	3.2	1.3×10^{7}	1.9×10^{4}	3.1×10^{-4}

Comparing the results of Table 8.2 and Table 8.3 based on the elemental ratios reveals that the activator anion has a large impact on the polarizability of the AAM. The effect of activator anion has never been previously investigated or reported for electrical or dielectric properties. The results also indicate that the optimal elemental ratios, which give the highest dielectric constant, are different for different activators. To elucidate the changing compositional

relationships, the dielectric properties of the potassium carbonate AAM were visualized in Figure 8.3 in a manner to mimic Figure 8.2. For this activator, the optimum K/Al ratio is shifted to 1.4, indicating that a supersaturation of potassium ions enhances the ionic conduction which is responsible for the ionic-interfacial polarization. As was found with the potassium hydroxide AAM, the loss tangent and dielectric constant are inversely related, which is a desirable for dielectric applications, and the loss tangent is reduced to 1.3. The exceptionally high dielectric constant of potassium carbonate AAM warrants additional investigation to leverage this property.

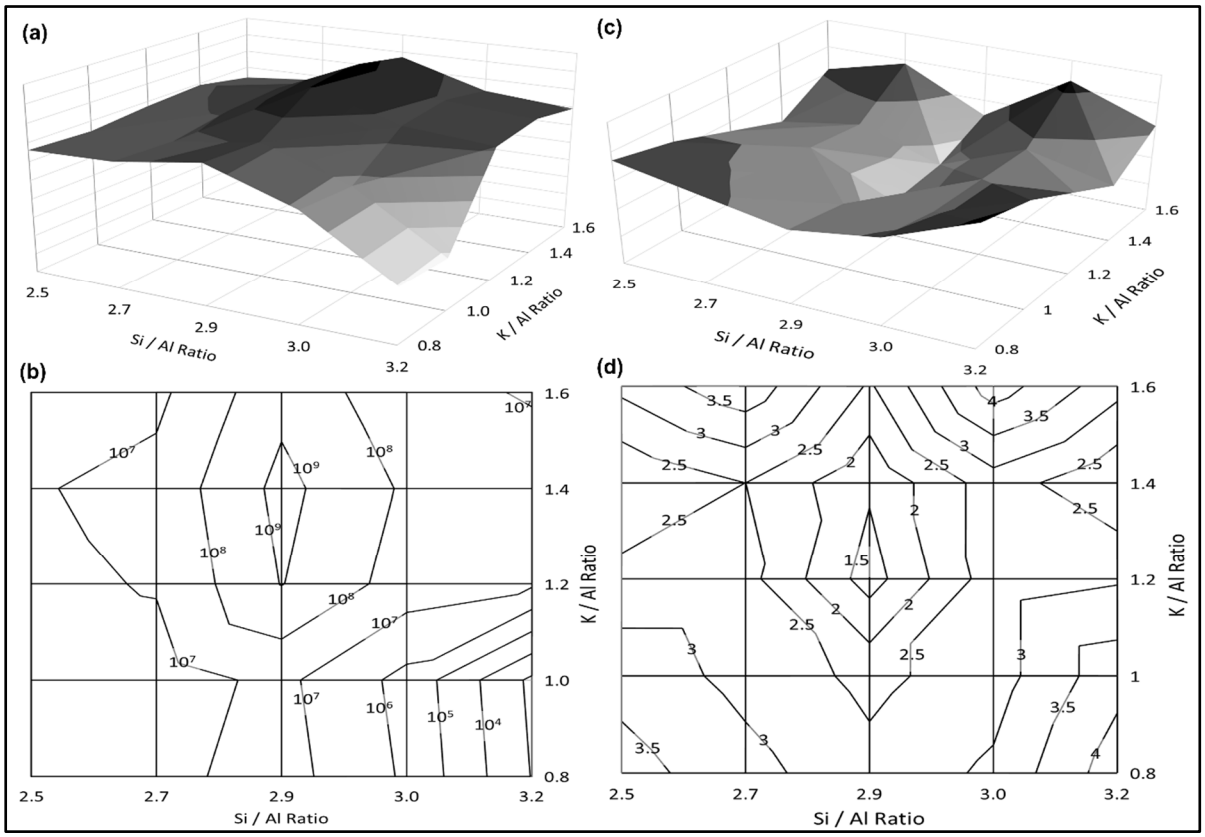

Figure 8.3 (a,b) The dielectric constant of potassium carbonate AAM at 0.1 Hz visualized in (a) a 3D rendering and (b) a contour plot. (c,d) The loss tangent at 0.1 Hz illustrated with (c) a 3D rendering and (d) a contour plot across the compositional array.

With the optimal composition, potassium carbonate AAM exhibit the greatest dielectric constant ever reported in the literature of ceramic dielectrics. To date, calcium copper titanates

have been extensively investigated since their discovery in 1967 and are regarded as the highest polarizing dielectric material (Deschanvres, Raveau, & Tollemer, 1967 ; U. S. Rai, Singh, Mandal, & Singh, 2014). This ceramic can have a dielectric constant as high as $5x10^4$ at room temperature and low frequency (50 Hz) (Jesurani et al., 2012). Only a few precisely doped ceramic composites have been documented to surpass this record and reach dielectric constants of 10^5 (Shankar & Deshpande, 2011 ; Y. Zhang et al., 2011). Potassium carbonate AAM offers an unprecedented leap in dielectric constant. This could increase energy storage capacity of capacitors by as much a million times. Moreover, the AAM are produced without the need for chemical vapor deposition, hydrothermal crystallization, high temperature sintering, or virgin raw materials. A lack of sustainability in energy storage technology is a recognized concern (Acar, 2018). Dielectric AAM are a major step towards an energy storage technology for sustainable and circular economy. However, realizing this opportunity will require future studies to develop new fabrication methods and to better understand the dielectric loss in AAM.

8.3.3 Ionic conductivity and energy storage mechanisms

Despite the improvement offered by the potassium carbonate activator, alkali activated materials (AAM) continue to exhibit high loss tangent. Reducing the loss tangent further will require a deeper understanding to the nature of the polarization and dielectric relaxation in AAM. Addressing these underlying questions will require additional investigation outside of the scope of this work, whose objective is to determine the optimum composition of AAM. The results of this study can create a framework for a future investigation into the dielectric mechanisms of AAM. Prior literature on the topic has concluded that the great dielectric polarization in AAM is a consequence of their high ionic conductivity (Caterina Lamuta et al., 2016 ; M. Saafi et al., 2018). Alkali ions, in this case potassium, act as a charge-balancing species within the amorphous network of the AAM, localized around the alumina tetrahedra. Ionic conduction occurs through charge hopping mechanisms which allow the cations to move to adjacent sites (Caterina Lamuta et al., 2016). For potassium carbonate AAM, enhanced dielectric polarization was observed when the alkali content (K/Al) was greater than 1.0. This implies that an excess of potassium cations contributes to improved ionic conductivity, which

enhances the dielectric response. This implies the hypothesis that maximizing the conductivity simultaneously maximizes the dielectric constant.

This hypothesis is supported by measurements of the conductivity across the compositional range of elemental ratios. The conductivity of each AAM specimen was measured and the results, at 0.1 Hz, were visualized in Figure 8.4 for each activator. Comparing Figure 8.4(a,b) and Figure 8.2(a,b) reveals a strong positive correlation between the conductivity and dielectric constant for potassium hydroxide AAM. The maxima and minima occur at the same compositions and the overall curvature is identical. The same is true for potassium carbonate AAM, shown in Figure 8.4(c,d) and Figure 8.3(a,b). The results corroborate the theory that the ionic conductivity strongly contributes to the dielectric polarization. The conductivities of the potassium carbonate AAM were found to be significantly higher than for potassium hydroxide AAM, reaching 38 mS/m (380 μS/cm) for composition C-1.2-2.85. Notably, this is only one tenth the value reported for some fast ionic conductors (He, Zhu, & Mo, 2017). A future study may consider the possibility of improving upon this to create an affordable and sustainable AAM ionic conductor.

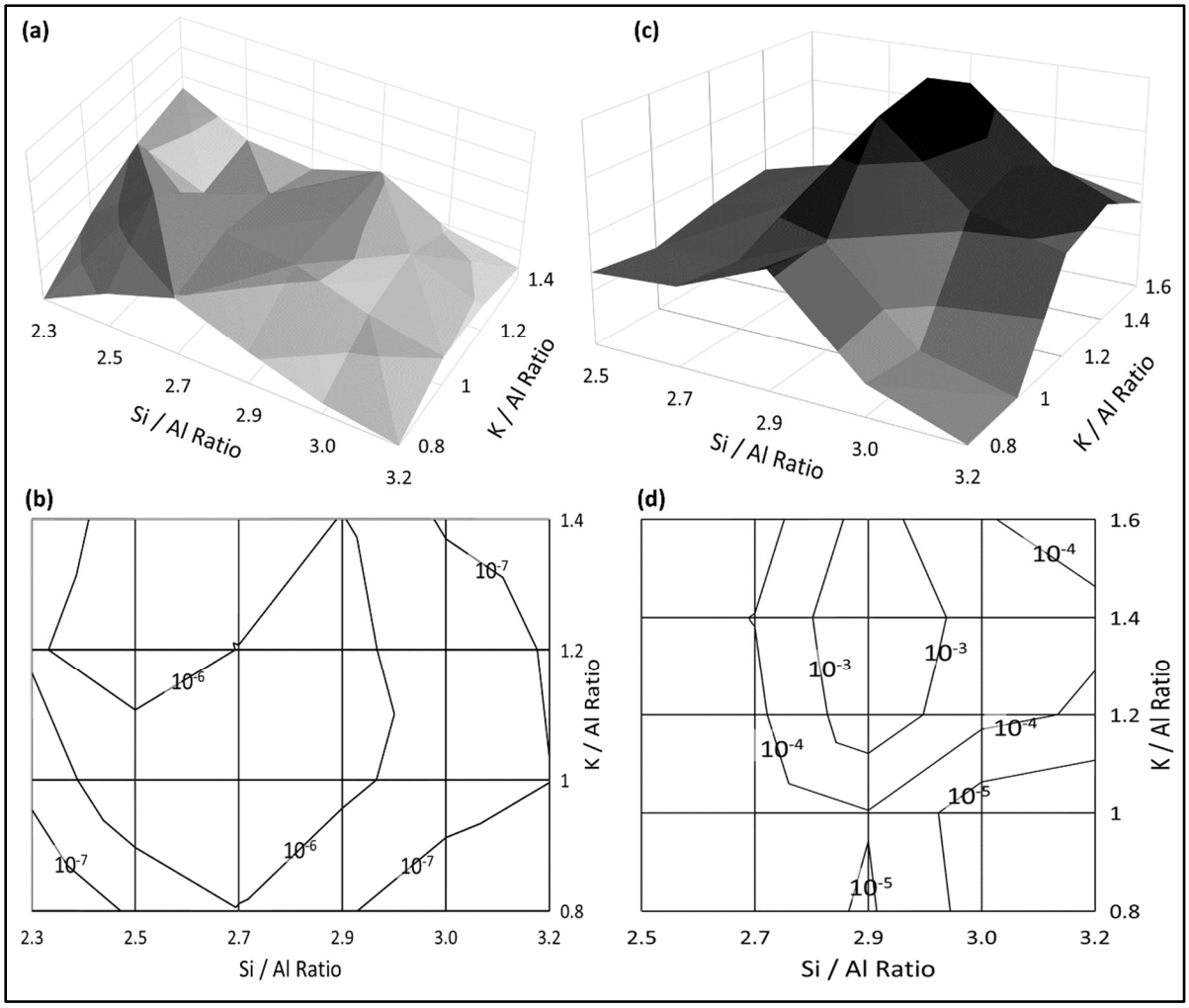

Figure 8.4 The conductivity (in S/m) of (a,c) potassium hydroxide activated and (b,d) potassium carbonate AAM, illustrated in 3D renderings and contour plots.

Ionic conduction in AAM leads to interfacial polarization and charge accumulation on the electrodes. Prior literature has explained energy storage within AAM through a conduction-adsorption mechanism (M. Saafi et al., 2018). Mobile alkali ions accumulate on grain boundaries within the AAM and adsorb on the anode. The ionic accumulation results in the formation of a double layer capacitor on the electrode surfaces, as visualized in Figure 8.5(d). This mechanism is more kinetically favored at low frequencies, where the ions have more time to move, which explains the strong frequency dependence of the dielectric polarization. To measure this phenomenon, cyclic voltammetry was conducted on the AAM specimens.

The charge accumulation mechanism which occurs in AAM is fundamentally different than the energy storage mechanism responsible for the behavior of ferroelectric ceramics, such as barium titanate. Unlike barium titanate, AAM are amorphous and cannot have the required space group symmetry for the ferroelectric phenomenon. Thus, energy storge of AAM must be assessed differently than it is done for ferroelectrics. The cyclic voltammetry measurements, shown in Figure 8.5, offer an alternative measurement to the conventional polarization-electric field (*p*-*E*) analysis used to measure energy storage in ferroelectric and antiferroelectric dielectrics. In this measurement, the enclosed area in each curve is a measurement of the energy stored during the polarization of the AAM specimen. A larger enclosed area indicates the formation of a stronger double layer capacitor within the AAM. The method is employed qualitatively to determine the relative strength of the AAM as an energy storage medium.

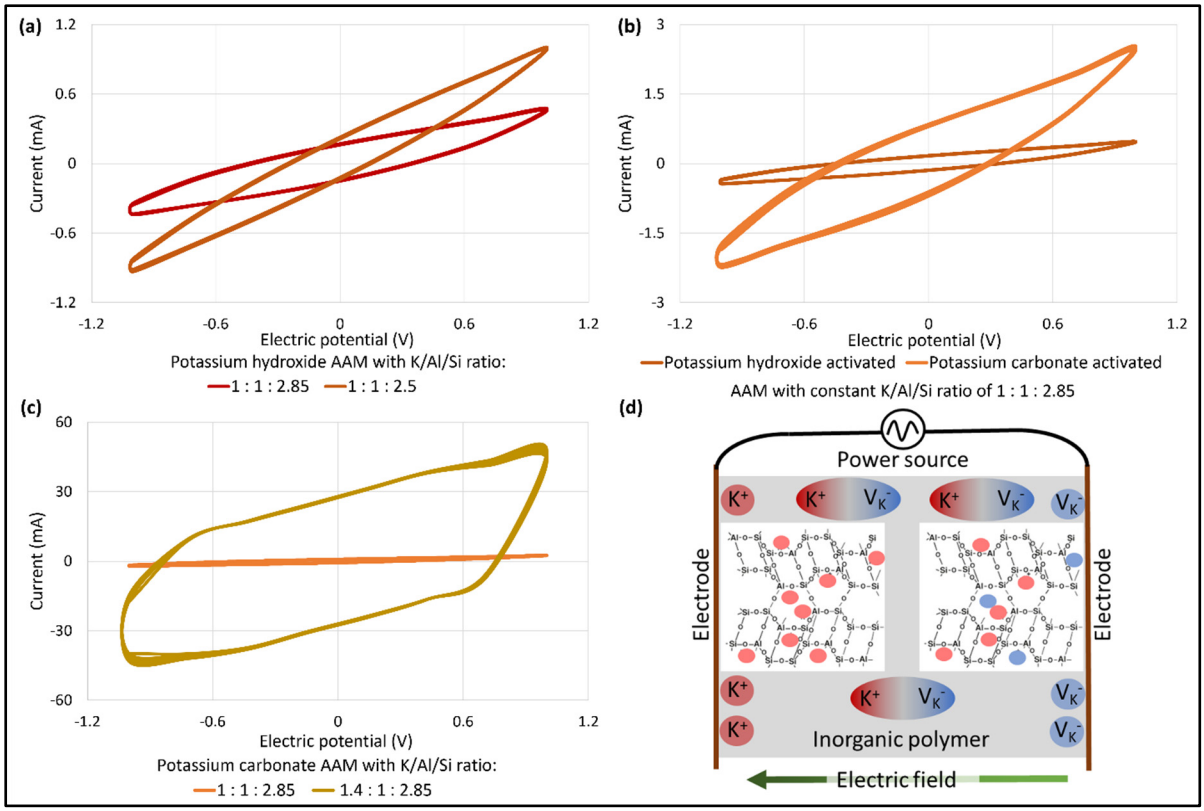

Figure 8.5 Cyclic voltammetry at 1 Hz of (a) two potassium hydroxide AAM with different elemental compositions, (b) two AAM with different activators but equivalent elemental composition, (c) two potassium carbonate AAM with different elemental compositions. (d) Graphical illustration of dipole formation and ionic conduction to the electrodes. The AAM structure was adapted from Davidovits (2013), shared under creative commons CC BY-SA 3.0.

The cyclic voltammetry measurements compare pairs of AAM specimens with different dielectric constants. Figure 8.5(a) compares two potassium hydroxide AAM specimens: one with dielectric constant 10^5 and the other with 10^6. Comparing this figure to the results in Table 8.2, an increase in enclosed area in the cyclic voltammetry curve correlates to the composition with the greater dielectric constant. This correlation continues in Figure 8.5(b), where a much larger difference in enclosed area is observed between AAM prepared with different activators which coincides with a significantly larger increase in dielectric constant. All of these enclosed areas are dwarfed by that of the optimal composition of potassium carbonate AAM, shown in Figure 8.5(c). The larger enclosed area indicates a substantially greater accumulation of

charges at the electrodes. This supports the hypotheses that ionic conduction and adsorption are occurring in the AAM with higher dielectric constants, resulting in greater energy storage.

8.3.4 Next steps: continuous casting methods for alkali activated films

Alkali activated materials (AAM) offer a promising solution for high density energy storage in environmentally friendly linear dielectric capacitors. However, their development cannot advance without suitable fabrication methods to produce AAM films. This will enable quantitative measurements of the energy storage capacity and estimates of the production costs compared to conventional alternatives. This topic deserves thorough investigation and is outside the scope of this study. However, due to the importance of this topic as the pivotal next step in the development of AAM dielectrics, a summary of the most suitable fabrication methods has been included here to promote the topic for subsequent study. The ideal methods for producing AAM films must be able to produce comparable thicknesses to that of barium titanate or other dielectric ceramics and support a continuous production to maximize the scalability and affordability of the production. Two methodologies have been identified that meet these ideal requirements, visualized in Figure 8.6.

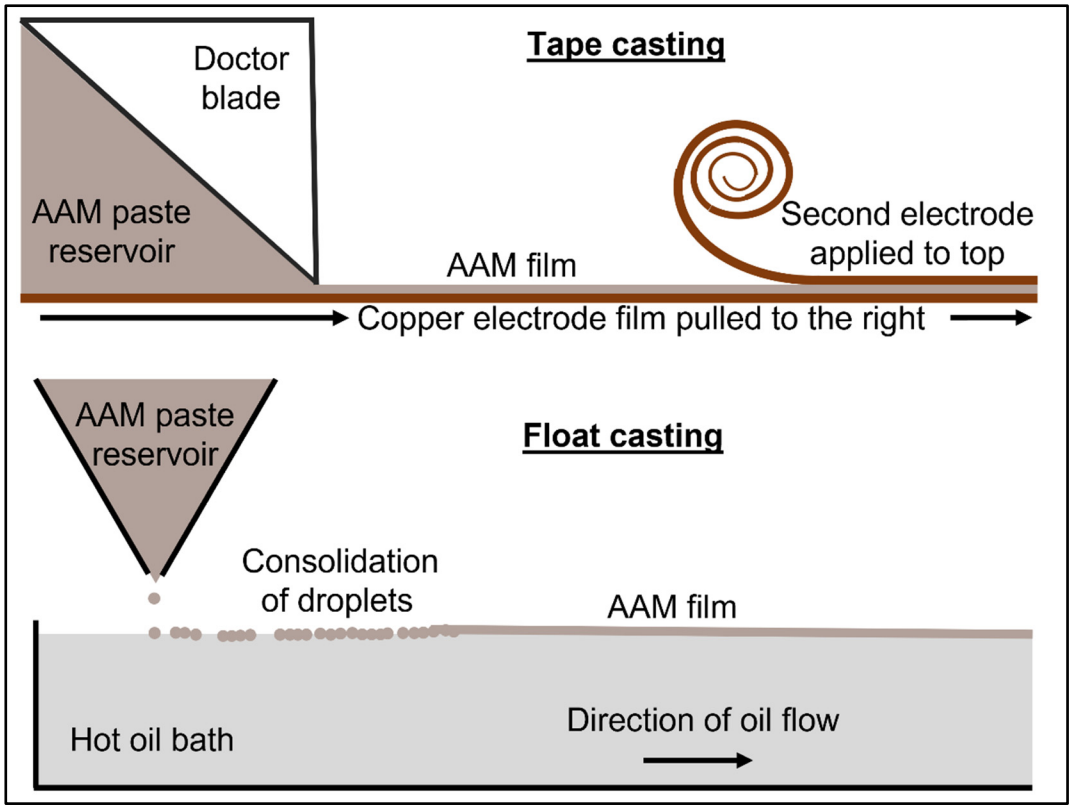

Figure 8.6 Illustration of tape casting and float casting methods for the continuous fabrication of alkali activated material films.

The two ideal methodologies are tape casting and float casting, conventionally used to produce ceramic greenware and glass panes. Tape casting technique uses a doctor blade and a moving substrate to create continuous films. Tape casting has been demonstrated with AAM for other applications to produce film thicknesses below 100 microns (Bulatova et al., 2014 ; Tok, Boey, & Lam, 2000). Further refinement of the doctor blade angle, substrate speed, and rheological properties of AAM will be able to reduce this thickness. A similar process refinement has been conducted on barium titanate to produce film thicknesses as low as 3 microns. These films have been deemed suitable for capacitor applications and are advantageous because of the low cost and high throughput of tape casting (Nava Quintero, Guillemet, Aguilar-Garib, Reyes Melo, & Durand, 2012). In float casting, droplets are cast onto a non-miscible liquid and allowed to consolidate into a film. A similar drip casting method has already been applied to AAM using a hot polyethylene glycol bath to achieve setting within 30 minutes of casting (Q.

Tang, Ge, Wang, He, & Cui, 2015). Float casting has been successfully implemented for the production of zeolite membranes with film thicknesses as low as 1.7 microns (Aoki, Kusakabe, & Morooka, 2000 ; Kiesow et al., 2013).

The development of film casting methods for AAM will enable future studies to build AAM capacitors and accurately assess the maximum energy storage capacity. The energy stored in a capacitor is proportional to the dielectric constant and inversely proportional to the thickness. High performing dielectric ceramics are generally synthesized on the scale of 1 micron or, preferably, sub-micron thickness (Hao, 2013). This level of thickness may be impossible with tape or float casting, but the million-fold improvement in dielectric constant offered by AAM gives significant room for flexibility in thickness. While conventional dielectric capacitors have energy density below 0.1 Wh/kg, a 10-micron film of potassium carbonate AAM could have an energy density of 10^3 Wh/kg, surpassing the energy density of batteries and that of liquid fuels (Hao, 2013 ; S. Liu et al., 2019). Moreover, AAM are a low-cost, environmentally friendly alternative to conventional dielectric ceramics that can be prepared from non-virgin raw materials, shaped with continuous production processes, and cured without energy intensive sintering. Combining these advantages with dramatic improvement in energy density is a revolutionary development for energy storage technology.

8.4 Conclusions

Alkali activated materials (AAM) present a unique opportunity to create high storage dielectric capacitors in a circular economy, recycling industrial wastes into value-added products. AAM are produced from by-product aluminosilicate wastes and, previously, their dielectric properties have received very little scientific attention. This manuscript describes the methods to produce and optimize AAM with exceptionally high dielectric constants, up to 10^9. This is the highest dielectric constant ever reported in a ceramic-like material. Future studies must develop new film casting methods to produce homogenous and uniform AAM dielectric capacitors. With tape or float casting methods, low-cost circular economy AAM capacitors could achieve energy storage capacities comparable to conventional batteries. This is more than a thousand-fold improvement over conventional capacitors. AAM dielectric capacitors

are an environmentally conscious solution to energy storage and warrant further recognition and investigation.

CHAPTER 9

DISCUSSION OF THE RESULTS

9.1 A one-part mixing methodology for bauxite residue alkali activated materials

Alkali activated materials (AAM) have numerous advantages over cement which could see them have many potential applications in the construction sector. The construction industry is in sore need of green solutions to reduce the environmental impact of cement production (Habert et al., 2020). Among the advantages of AAM are lower greenhouse gas emissions and a reduced need for virgin raw materials (Habert & Ouellet-Plamondon, 2016). However, AAM technology has not been able to replace the entrenched cement industry because of the low availability of the high-quality industrial by-products needed to produce AAM (Duxson & Provis, 2008). This scarcity issue is aggravated by competition for these by-products with the cement industry, which has developed means to utilize them as supplementary cementitious materials (Juenger & Siddique, 2015 ; Lothenbach et al., 2011). The present solution to this problem is to develop new methods to use other by-products that are produced in large volumes and with whom there is no competition with the cement industry.

Bauxite residue (BR) is a perfect match for these criteria. BR is a large volume by-product of the Bayer process of aluminum production, produced in volumes of 150 million tons per year with no large-scale valorization options (Evans, 2016 ; IAI, 2021). BR contains a relatively high content of alkali metal which gives it low compatibility with conventional cement production (Venkatesh et al., 2019). The challenge in utilizing AAM is its relatively low reactivity during alkali activation. Low reactivity is not a problem that is unique to BR and there exist several methodologies for improving the reactivity of a precursor. The problem is that the conventional methodologies all add substantial cost and/or require the use of large volumes of high-quality industrial by-products which recreates the scarcity and cross-competition problems that BR was being used to avoid.

The specific objectives of this section of the research are as follows:

1) Develop a new methodology to transform bauxite residue into a high-strength AAM.

a) Explore techniques that can valorize large volumes of bauxite residue without expensive, energy-intensive, or low scalability technologies.
b) Conduct a compositional optimization to maximize the bauxite residue content in AAM while maintaining sufficient strength to meet construction standards.

These objectives were accomplished, and the results were composed in two published journal articles. In Chapter 3, a new methodology is presented to valorize BR as an AAM without the high added processing costs or raw material requirements that are drawbacks of the conventional methods. The new method is a truly one-part mixing technique that can transform BR directly from its wet state, straight from the aluminum production line, into a high-strength AAM material, without drying, milling, or calcination. The one-part methodology improves upon the methods of a prior study that used a different wet form of BR in low concentrations (24%) in conjunction with another industrial by-product (Arnout et al., 2017). The one-part method is effective for AAM containing between 70-80% BR, offering a dramatic improvement in BR content and minimizing the quantity of other materials required. Chapter 3 presents the results of a compositional optimization for the new one-part methodology. Chapter 4 explains how an alternative mixer technology can be synergistically used to boost the compressive strength of the BR AAM above 30 MPa. At this level of strength, the AAM, which is 76% BR, meets ASTM standards for precast structural components including retaining walls and underground wastewater infrastructure. This presents a bright opportunity to valorize large volumes of BR and simultaneously reduce the environmental impact of the construction sector.

9.2 Self-sensing applications of alkali activated materials

In addition to the need for new precursor materials, the deployment of alkali activated materials (AAM) as a cement replacement in construction requires the scaling up of production infrastructure and supply chains. Cement production benefits considerably from its massive economy-of-scale, improving efficiency from raw material extraction to transport of the final product. The efficiency of this scale of production keeps costs down even in the face of theoretically superior alternatives, such as AAM. To date, this has posed an insurmountable

obstacle to the scale-up of AAM production as a cement replacement. A solution to this problem is the creation of smaller unique applications for AAM that cement cannot compete in. These smaller applications can act as stepping stones to bridge the gap between pilot production and the massive production scale required to effectively compete with cement.

Smart construction materials are an ideal application for this purpose. This is an application adjacent to general construction, but one that cement is not well suited for due to cost and durability concerns. Smart construction materials are high-strength materials that serve in loadbearing structural members but add unique multifunctionality (Z. Tang et al., 2019). Self-sensing is one of the most common categories of smart construction materials. Self-sensing materials are typically piezoresistive and this property allows external detection of fluctuations or changes in the mechanical loading of a self-sensing structural member in-situ (Tian et al., 2019). This is used in building and infrastructure maintenance to enable structural health monitoring, an emerging technology that allows the detection and localization of sites of decay or corrosion in a building to facilitate localized and preventative maintenance (García-Macías & Ubertini, 2019).

While the concept of structural health monitoring has been around for decades, current construction has yet to adopt it (P.-W. Chen & Chung, 1993 ; Tian et al., 2019). This is because the state-of-the-art technology for self-sensing materials relies on forming composites of a highly conductive additive, such as carbon fiber, with an insulating binder, most commonly cement. This technology is prone to many complications, primarily high added cost and low reproducibility (Han et al., 2015). A recent study by *Saafi et al.* identified a revolutionary alternative based on AAM (M. Saafi et al., 2018). The work demonstrated that AAM can exhibit self-sensing piezoresistivity as an intrinsic material property, without the need for any conductive additives. This valuable property has not been studied extensively thus far because it only manifests under alternating current conditions and, thus, cannot be observed with a standard impedance meter. A low-cost, highly reproducible self-sensing construction material is a paradigm shift in the use of smart construction materials in real infrastructure. However, no study since has corroborated the results of *Saafi et al.* or provided any explanation as to the origin of this unusual property in AAM. Thus, this thesis seeks to address this topic by reproducing the results of *Saafi et al.* and expounding upon this field of study. The specific

objectives of this section of the thesis, maintaining the numbering presented in the introduction, are as follows:

2) Identify new applications to serve as a stepping stone to scale up AAM production.
    a) Examine the self-sensing behavior of AAM, investigate its prevalence across a range of compositions, and optimize its performance.
    b) Computationally model the piezoresistivity in AAM to mechanistically explain the origin of its self-sensing properties.

The first sub-objective, 2(a), was accomplished and the results were composed in two journal articles. Chapter 5 is a published journal article describing an investigation of the piezoresistivity of potassium AAM derived from fly ash to corroborate the results of *Saafi et al.* The study finds that potassium AAM are intrinsically piezoresistive, as expected, and that the piezoresistivity can be improved substantially by controlling the composition of the AAM. In Chapter 6, the investigation is continued to study the impact of the precursor and activator types. Sodium AAM are far more common in the field than potassium AAM which *Saafi et al.* first studied. It was unknown if the piezoresistivity is a common property among AAM or unique to potassium AAM. Moreover, the study by *Saafi et al.* neglected to consider the mechanical properties of the AAM, which are critical for applications of smart construction materials. The results in Chapter 6 revealed that both precursor and activator types are important to piezoresistive behavior. An optimal composition of sodium AAM derived from fly ash was identified which exhibits both very high piezoresistivity (>50%) and very high compressive strength (>50 MPa).

Accomplishing the second sub-objective, 2(b), required an investigation of the origin of piezoresistivity in AAM, which was published in another journal article, Chapter 7. Intrinsic piezoresistivity is an unusual property in a material. No explanation of the property of AAM has been presented in the literature that has been supported with experimental or computational evidence. This is made more complicated by the relatively limited resources in understanding the precise structure of an AAM. Only with recent computational advancements has the modeling of the complex structures of AAM become possible with molecular dynamics. Utilizing recent literature on the modeled structures of AAM, Chapter 7 presents a computation of the theoretical piezoresistivity of an AAM structure. The results align relatively well with

experimental data and suggest that the intrinsic piezoresistivity measured experimentally in AAM is a consequence of both ionic and electronic contributions. The methodology presented in Chapter 7 is the first attempt in the literature to directly correlate computational and experimental measurements of the intrinsic piezoresistivity of a material. Hopefully, it will provide a means for future investigators in this field to support their experimental results with computational explanations.

9.3 Dielectric applications of alkali activated materials

While researching the electromechanical behavior of alkali activated materials (AAM) for self-sensing applications, a curious gap in the literature was identified on the dielectric properties of AAM. AAM have been reported to have very high dielectric constants between 10^4-10^5 (Hanjitsuwan et al., 2014). The study by *Saafi et al.* that discovered the intrinsic piezoresistivity of potassium AAM also documented dielectric constants as high as 10^8 (M. Saafi et al., 2018). These dielectric constants are substantially higher than traditional dielectric ceramics, such as barium titanate (10^2-10^3), barium strontium titanate (10^3-10^4), and calcium copper titanate (10^4) (Jesurani et al., 2012 ; Yadav & Gautam, 2014). Since the energy storage density of a capacitor is directly proportional to the dielectric constant of the medium, AAM could provide a dramatic improvement in energy storage technology if the technology was developed to utilize them as a dielectric.

There is a long history of investigating AAM as a low-cost alternative to ceramic materials. The original study by *Davidovits* that discovered AAM was searching for an alternative to ceramic-based flame retardants (Joseph Davidovits, 2002b). More recently, the properties of zeolite materials have been mimicked by AAM for the purposes of catalysis and adsorption (Khalid, Lee, Park, Abbas, & Lee, 2018 ; Zheng, Ma, Zhang, & Li, 2019). AAM have also been investigated as an alternative or intermediary in the production of specialty ceramics (Bell, Driemeyer, & Kriven, 2009b ; Liguori, Aprea, Roviello, & Ferone, 2019). The key advantages of AAM in these applications are the capacity to shape the AAM in a liquid state and to harden the AAM to full strength and density without pressing or sintering. Liquid

casting and room temperature hardening make AAM easier to produce and avoid difficulties arising from the milling to shape or sintering shrinkage of traditional ceramics.

In the field of dielectrics, AAM offer the same advantages as in other applications. However, AAM have not yet attracted attention as an alternative to dielectric ceramics. In fact, very few articles in the literature have even reported the dielectric properties of AAM. The potential value of a low-cost dielectric material has been recognized by some researchers to propose exotic supercapacitor designs (Meng & Chung, 2010 ; Junjun Zhang et al., 2016). If realized, this could type of energy storage device could bring produce high energy density capacitors with storage capabilities comparable to or exceeding those of modern batteries. Far more research on the topic is required before this technology could be proven. In particular, the uncommon potassium AAM investigated by *Saafi et al.* are the highest dielectric constants ever reported in the literature. This thesis continues the investigation of the dielectric properties of AAM through the following objective, maintaining the numbering presented in the introduction:

2) Identify new applications to serve as a stepping stone to scale up AAM production.
    c) Determine the effect of compositional parameters on the dielectric properties of AAM and optimize the properties for dielectric applications.

This objective was accomplished, and the results were published in a journal article. Chapter 8 provides an in-depth examination of the dielectric properties of potassium AAM and its relation to the composition. The work corroborates the results of *Saafi et al.* by measuring the dielectric response of 32 AAM compositions and investigating the effect of different compositional parameters using a factorial design. It was found that the dielectric constant of AAM is strongly influenced by the composition and the operational frequency. The AAM exhibited non-Debye polarization behavior with strong low frequency dispersion. This type of polarization is not well understood in the literature and further study will be required to understand the polarizability of AAM. Nevertheless, at the optimal composition, an AAM with a dielectric constant as high as 10^9 was discovered. These results lay a foundation for future studies to investigate the best fabrication methods to produce AAM films and AAM-based capacitors. This creates a new application for AAM outside of the realm of construction and could have substantial implications as a low-cost energy storage technology in the future.

CONCLUSION

This thesis investigates the methods and properties of alkali activated materials (AAM) to propose new means to produce them and new applications in which they commercially succeed. The overall goal of this work was to address a research question which has challenged investigators in the field: what can be done to improve the commercializability of AAM and support the development of a robust AAM industry? AAM are a versatile class of materials that boast low environmental impact and can offer green solutions for a variety of different applications. However, despite their advantages, AAM have not yet been scaled up commercially to compete with their primary rival, Portland cement. The motivation of this research was to provide a feasible avenue for the scale-up of AAM. This challenge was undertaken with a two-pronged approach. In one part, a novel methodology was developed to valorize bauxite residue as a raw material for AAM. This serves to reduce the competition for raw materials between AAM production and cement production to make the scale-up more economically viable. In the other prong, the electrical and electro-mechanical properties of AAM were investigated in search of new applications in which AAM can excel. The gaps in the literature on the electrical properties of AAM create the opportunity to identify new applications for AAM to expand into, without creating competition with cement. The intent is that they may serve as a bridge to ramp up AAM production and reduce the gap between pilot and viable full-scale production.

The specific objectives of this thesis were as follows:

1) Develop a new methodology to transform bauxite residue into a high-strength AAM.
    a) Explore techniques that can valorize large volumes of bauxite residue without expensive, energy-intensive, or low scalability technologies.
    b) Conduct a compositional optimization to maximize the bauxite residue content in AAM while maintaining sufficient strength to meet construction standards.

2) Identify new applications to serve as a stepping stone to scale up AAM production.
    a) Examine the self-sensing behavior of AAM, investigate its prevalence across a range of compositions, and optimize its performance.

b) Computationally model the piezoresistivity in AAM to mechanistically explain the origin of its self-sensing properties.
c) Determine the effect of compositional parameters on the dielectric properties of AAM and optimize the properties for dielectric applications.

The objective of working with bauxite residue was to develop a new methodology for producing AAM that would improve the feasibility of a commercial scale-up. While many conventional methodologies exist for producing AAM from bauxite residue, these methods produce materials that are either too weak for structural applications, contain only a low content of bauxite residue, or require costly energy-intensive processes to function. The process described in Chapter 3 accomplishes Objective 1(a) by demonstrating an alternative methodology that is facile, eschews energy-intensive calcination treatments, and contains substantially more bauxite residue than possible with other methodologies. The work detailed in Chapter 4 continues the study of this new process to propose a thorough compositional and process optimization, as prescribed by Objective 1(b). AAM were produced that contained 76% bauxite residue and reached over 30 MPa of compressive strength, far exceeding the expected results. The new process triples the bauxite residue content in the AAM compared to other studies of the same strength and quadruples the compressive strength of the AAM compared to studies with the same proportion of bauxite residue to fly ash. Moreover, in a novel advantage, the new process is effective without drying and milling of the bauxite residue, offering additional energy and greenhouse gas emissions savings. The methodology developed in this work maximizes the advantages the economic and environmental advantages of producing AAM from bauxite residue for structural applications. The results of these studies maximize the economic and environmental advantages of producing high-strength AAM from bauxite residue to accomplish Objective 1.

The electrical and electromechanical behavior of AAM was investigated to identify new applications for these materials. The goal, as defined by Objective 2, is to develop applications that can serve as stepping stones to bridge the gap between pilot production and the massive economy-of-scale required to compete with cement. The electrical and electromechanical properties of AAM have not seen significant scientific study. The importance of these properties to the field of multifunctional materials creates the opportunity to innovate on AAM

material design to produce smart, multifunctional construction materials as a new application of AAM technology. An investigation of the electromechanical properties of AAM revealed that AAM exhibit an unusual and valuable self-sensing property that can be leveraged to create smart construction materials. The study detailed in Chapter 5 sought to corroborate the discovery of this property and thoroughly document the prevalence of this behavior in different types of AAM. Chapter 6 continues this investigation with the discovery that the combination of mechanical and self-sensing properties can be improved with further compositional optimization. These two chapters, taken together, satisfy Objective 2(a) in providing the first exploratory study of the self-sensing behavior of AAM in the literature.

However, understanding the self-sensing behavior of AAM proved to be a challenge. The electromechanical properties were strongly influenced by compositional factors but did not correlate to the microstructural mechanisms known to dictate the mechanical and physical properties of AAM. Attempts to characterize the chemistry of the AAM to continue refining the self-sensing properties were met with limited success due to the absence of suitable characterization techniques for analyzing AAM containing a high content of iron. Nevertheless, a thorough investigation was conducted to develop new means of examining the origin of the valuable self-sensing properties of AAM. To accomplish Objective 2(b), a new computational methodology was developed to quantitatively model the piezoresistivity of AAM which is responsible for their self-sensing performance. Chapter 7 presents a first-of-its-kind computational model that can be used to explain the mechanistic origin of piezoresistivity in AAM and other self-sensing materials. These works together, propose AAM as a robust multifunctional material that can exhibit self-sensing performance comparable to or exceeding that of the best self-sensing composites. This is particularly significant because AAM express high self-sensing behavior without the need for conventional additives which simultaneously circumvents the principal challenges of high cost, low reproducibility, and low durability that have prevented conventional self-sensing composites from being implemented in real-world infrastructure. This makes AAM a unique solution for this field and makes self-sensing smart materials an ideal application for the scale-up of AAM production.

A more exotic application was found in the study of the dielectric properties of AAM. There exists a significant gap in the literature surrounding the dielectric properties of AAM. The

properties have not been well documented, and the prior studies have neglected to consider the potential value of AAM as a dielectric material. Chapter 8 details an investigation of these properties and the results revealed that AAM have among the highest polarizability of any reported material. Dielectric constants as high as 10^9 were measured, surpassing all dielectric ceramics by at least four orders of magnitude. There is much still to learn about the dielectric polarization mechanisms in AAM before these materials can be used in practice. The dielectric properties were found to be highly sensitive to the composition of the AAM and to the operating frequency. The AAM exhibited non-Debye polarization and relaxation behavior with a strong contribution from low frequency dispersion, a type of polarization not well understood in the field. Nevertheless, if the dielectric performance of AAM can be realized in a practical capacitor, it will revolutionize capacitive energy storage technology. These results document the optimal composition and operating parameters to maximize the dielectric properties of AAM to satisfy Objective 2(c). This lays the groundwork for future investigations of AAM as dielectric materials and represents the tip of what may be a significant field of study and application for AAM in the future.

The contributions of this research to the scientific literature can be summarized by the following:

- Demonstration of a new process to valorize bauxite residue in its raw form without the need for cost-prohibitive pre-processing techniques;
- Compositional optimization of bauxite residue AAM using the new methodology to maximize the bauxite residue content while exceeding mechanical strength requirements for precast structural members and ensuring neutralization of ecotoxic metal leaching;
- Thorough documentation of the piezoresistivity of AAM and the means for utilizing it self-sensing mechanism for smart construction applications;
- Identification of the compositional factors which effect the self-sensing properties of AAM;
- Demonstration of a novel computational methodology for studying the theoretical self-sensing behavior of materials;
- New understanding of the impact of compositional factors on the dielectric properties of AAM;

- Optimization of an AAM to achieve a dielectric constant in excess of 10^9, the highest reported dielectric polarization in the literature.

Taken together, these different prongs of research present a bright future for AAM technology. AAM represent a low-cost and environmentally friendly alternative to cement and other ceramic materials. Green material solutions are in sore need in the construction sector and AAM have the capacity to fulfill this need. The new applications in smart materials and electronic capacitors achieve the objective to identify new markets into which AAM production can be expanded. The novel production methodology that has been developed allows large volumes of bauxite residue to be transformed as never-before into a structural strength AAM. This maximizes the economic and environmental incentives to valorize bauxite residue and reduce the pollution of an industrial sector that is significant to Quebec's economy. The results demonstrate how the unique compositional flexibility of AAM can be leveraged to both improve their viability in established construction applications as well as develop new applications to expand their use in other sectors.

RECOMMENDATIONS

This thesis opens new avenues for the future research of alkali activated materials (AAM) that can and should be further investigated. Below, recommendations are presented for subsequent studies, organized by topic and chapter.

The research on bauxite residue AAM presented in Chapter 3 is part of a larger research effort currently being funded by a Mitacs Accelerate grant in collaboration with Rio Tinto. The subsequent stages of this research will investigate porosity control techniques for producing high permeability AAM from bauxite residue and the chemical reactivity of these materials as adsorbents. This work seeks to create a greener and lower-cost alternative to traditional adsorbent materials by utilizing a AAM containing a high content of unmodified bauxite residue. In addition to these topics of study, the bauxite residue AAM should be investigated for structural applications. The one-part mixing methodology that was developed was more successful than expected at producing high-strength AAM. This presents an opportunity for structural applications of this AAM. However, to realize these applications additional studies must be conducted into the durability of this material. Freeze-thaw, accelerated aging, and corrosion resistance are among the durability measurements that would be required to assess the suitability for different structural applications. Additionally, the effervescence of this AAM should be measured to determine the AAM's capacity to adsorb CO_2. Raw bauxite residue and other AAM are both known to passively adsorb CO_2 under ambient conditions, and this must be measured to accurately assess the material's environmental footprint. Better characterization of the raw materials, the intermediary NASH gels, and the final AAM chemistry will facilitate greater reproducibility of the results. This will be significant for the utilization of this technique in other locations as the composition of by-product raw materials, including bauxite residue and fly ash, are known to vary significantly across regions and continents. Finally, there is need for a full life cycle analysis to quantify the sustainability advantages of valorizing BR in this manner.

On the topic of self-sensing AAM, further investigation is required to develop the application side for the self-sensing materials. Self-sensing materials remain an academic topic with little commercial scale-up. The high-strength, self-sensing AAM presented in Chapter 6 solves

many of the most significant challenges that have prevented the commercialization of self-sensing construction products. However, the commercial market for these products does not yet exist. Subsequent academic investigations and pilot trials must be conducted to demonstrate the best methods for integrating self-sensing materials into ordinary construction methods. These future works will create the groundwork for a new market of smart bricks and smart construction components for which AAM will be a green material solution. In addition, the durability of both the mechanical and piezoresistive properties of AAM must be investigated to determine the longevity of the product. It is currently unknown how stable the self-sensing properties of AAM are with time or how they may be influenced by environmental conditions. Assessing these factors will provide a more comprehensive perspective on the applications in which self-sensing AAM are superior to more traditional self-sensing cement composites. Moreover, additional characterization of the NASH gel and AAM chemical structure will be necessary to develop further understanding of the nature of the self-sensing behavior of AAM and continue to refine their physical and piezoresistive properties.

Finally, for dielectric applications of AAM, additional study is required on the origin of the dielectric behavior and on the optimal fabrication methods of AAM. More in-depth study of the fundamental polarization phenomena will illuminate the nature of the dielectric response of AAM and improve reproducibility of the properties. This will require more extensive crystallographic and dielectric characterization of the AAM to extract the fundamental relationships between the chemistry and the properties. In the application of AAM for energy storage, accurately measuring the energy storage capacity of AAM will require the creation of AAM thin films. As discussed in Chapter 8.3.4, the production of homogenous, defect-free thin films will require the thorough optimization of the production parameters. Once optimal production methods can be established, the critical properties such as the energy storage capacity and the breakdown voltage, which are functions of the film thickness and homogeneity, can be measured. These steps are necessary to accurately compare AAM to current energy storage technology and realize their potential advantages over dielectric ceramic capacitors.

ANNEX I

A calculator for valorizing bauxite residue in the cement industry

Michael Di Mare,[1] Valerie Nattrodt Monteiro,[1] Victor Brial,[1] Claudiane Ouellet-Plamondon,[1] Sebastien Fortin,[2] Katy Tsesmelis,[3] Marcelo Montini,[4] Diego Rosani[5]

[1] Department of Construction Engineering, University of Quebec, École de technologie supérieure, Montréal, QC, H3C 1K3, Canada.
[2] Rio Tinto, Aluminium Technology Solutions – ARDC, 1955 boul. Mellon, Jonquière, QC, Canada
[3] Mining & Refining, International Aluminium Institute, 2 Duke Street, St James, London, United Kingdom
[4] Norsk Hydro Brasil, 549 Gentil Bittencourt Avenue, Belém, Para State, Brazil
[5] RosCon - Cement Consulting, v. L. da Vinci 41, 22100 COMO, Italy

Paper published in *Cleaner Materials*, August 2021

I - 1 Introduction

Bauxite was defined in 2020 as a critical raw material by the European Commission due to its massive scale of consumption (Blengini, Latunussa, Eynard, Torres de Matos, & Wittmer, 2020). Bauxite residue (BR) is an industrial by-product produced in large volumes globally but without a substantive reuse case (Evans, 2016). This has resulted in a growing global stockpile in dedicated containment systems which is expected to reach 4 billion tons by 2022 (IAI, 2021). There is a growing need to develop avenues for recycling BR. However, few applications present the opportunity to reuse the material at a scale that is relevant to its production volume. A notable exception is the potential use of BR as an additive in the synthesis of ordinary Portland cement (X. Liu & Zhang, 2011). Due to the massive scale of Portland cement production globally, the ability to incorporate BR in cement, even as a minor component, would mitigate the growth of the global stockpile of BR.

Moreover, the utilization of bauxite residue (BR) has received attention for its potential value as a cost-saving additive to produce cement with lower environmental footprints. Many studies have considered BR in different forms and proportions in cement mixes. BR has shown promise as both a replacement ingredient in the raw meal in cement production and as a supplementary cementitious material (SCM) (Ghalehnovi, Roshan, Hakak, Shamsabadi, & de Brito, 2019b ; R.-X. Liu & Poon, 2016 ; Tsakiridis et al., 2004). However, the best practices for utilizing BR in cement have not been established. There are many extrinsic factors, such as transportation, power costs, and environmental taxes, which complicate the calculation of the added value of valorizing BR. These factors influence the economic incentive to utilize this material. In this study, a systematic quantification of these factors has been developed into a computational algorithm for determining the suitability of incorporating BR into cement production on a plant-by-plant basis.

Bauxite residue is a by-product obtained during the production of alumina using the Bayer process (Power et al., 2011). Bauxite, the aluminum hydroxide bearing ore, is found in nature commingled with silicate minerals, iron oxides, titanium oxides, and many other minor or trace elements. Consequently, bauxite residue is composed of a combination of insoluble mineral oxides that are present in the extracted ore (Y. Liu et al., 2007 ; S. Wang et al., 2021). BR may be classified as a hazardous material due to its caustic nature. This arises from the considerable content of soluble sodium phases (hydroxide and carbonates) and complicates the disposal and containment of this by-product. Techniques have been developed to concentrate the residue through filter pressing (Angelopoulos, Balomenos, & Taxiarchou, 2016). Life cycle assessments have been conducted of bauxite residue disposal to quantify its costs to the environment and the advantages of disposal and containment technologies (Joyce & Björklund, 2019 ; S. Rai et al., 2020). However, the substantial scale of bauxite residue production has made disposal, containment, and pacification efforts for the material a challenge.

Bauxite residue is produced on a tremendous scale. Globally, it is estimated that current aluminum consumption results in the annual production of over 150 million tons of BR (IAI, 2021). However, it is estimated that less than 3% of bauxite residue is used in conventional technology (Evans, 2016). This creates a strong imperative to develop new avenues for valorizing this material. Many studies have been conducted on different avenues for

repurposing bauxite residue. As a concentrated mineral residue, BR contains minor fractions of valuable metals which can be extracted (Borra et al., 2015). The methodology has been applied to extract iron (Agrawal et al., 2018 ; Gu et al., 2017), gallium (Ujaczki et al., 2019), alkalis (Kaußen & Friedrich, 2016 ; Yanxiu Wang et al., 2018), scandium (Anawati & Azimi, 2019, 2020), and other rare earth metals (Borra et al., 2016 ; Chaikin et al., 2020). Attempts have also been made to valorize it as a raw material for sintered ceramics (Pontikes et al., 2009). However, a principal concern in the identification of a suitable end-use for BR is an application that can take advantage of the large volume of BR production and consume the by-product at a scale that is relevant to its production scale.

The cement industry presents one of the strongest opportunities for matching the production of BR because of the scale of global cement consumption (Habert et al., 2020 ; Klauber et al., 2011 ; Pontikes & Angelopoulos, 2013). The feasibility of incorporating BR in cement production has been demonstrated by many studies (X. Liu & Zhang, 2011 ; Rathod, Suryawanshi, & Memade, 2013 ; W. C. Tang, Wang, Donne, Forghani, & Liu, 2019). BR is a viable ingredient in the raw meal used to produce cement when added in controlled doses (Tsakiridis et al., 2004). In this form it acts as a supplemental source of calcium, aluminum, and iron, reducing the required clay and iron corrective that are typically added to the clinker. This offers a cost advantage of using a by-product over virgin raw materials. Moreover, BR has been shown to act as a SCM in cement composites. It exhibits chemical reactivity in cement paste and a filler effect which can strengthen the final binder (Ghalehnovi et al., 2019b ; Nikbin, Aliaghazadeh, Sh Charkhtab, & Fathollahpour, 2018). Some studies have reported a change final hydration of cement blended with BR as an SCM (Romano, Bernardo, Maciel, Pileggi, & Cincotto, 2018). While the compressive strength of these blended cements have been shown to be unchanged (Sapna & Aravindhraj, 2018 ; Venkatesh, Ruben, & Chand, 2020), concerns have been raised about the potential impact of BR SCM on durability (W. C. Tang et al., 2019 ; Venkatesh, Nerella, & Chand, 2020) and the compatibility of superplasticizers (Fujii, dos Reis Torres, de Oliveira Romano, Cincotto, & Pileggi, 2015). These effects may be related to the amount of soluble sodium in BR (Danner & Justnes, 2020). Nevertheless, the use of BR as an SCM presents an avenue for economic and environmental

opportunities. Both avenues of utilization enable the synthesis of cementitious materials with cost and environmental advantages.

The present work is a continuation of a collaboration between aluminum producers and the cement industry to develop a more robust pathway to valorize bauxite residue in the production of ordinary Portland cement (Nattrodt Monteiro, Brial, & Ouellet-Plamondon, 2020). This is a part of a multistep plan, proposed in the International Aluminum Institute in their Technology Roadmap (IAI, 2020), to develop technological and supply line connections between the aluminum and cement industries. The objective of the present work is to quantify the economic incentive to repurpose bauxite residue in the cement industry. However, the value of incorporating BR into cement production is dependent on many factors and constraints which are unique to regions and specific producers. For this reason, the solution to the optimal BR content in cement and its potential value to cement producers cannot be generalized. To remedy this complex situation, the present work has developed a computational tool based in Microsoft Excel, to incorporate the individual requirements of both the cement producers and the alumina suppliers. This will facilitate the future application of BR to cement production and business between the aluminum and cement industrial sectors.

I - 2 Methodology

I - 2.1 Definition of users

To facilitate the collaboration between the alumina and cement industries, this tool was developed to be used equally by users from both sectors. The two categories of users have different terminologies, requirements, and objectives when it comes to the use of BR. As such, the tool is designed to have separate input fields for each type of user, which can be filled in to the extent that the information is available. In the same manner, a separate results page is created for each type of user, to show the parameters and outputs that are relevant to their sector and metrics. The first category of user is a representative of the aluminum sector, labeled in this tool as the “BR Producer.” For this user, the tool compiles an economic evaluation that considers storage and transport costs, potential cost and revenue flow of commercialization of

BR, payback for capital expense expenditure, and local taxation. The tool requires compositional information for the BR for determining the maximal contents which can be valorized in cement.

The second category of user is a representative from the cement sector, labeled in this tool as the "Cement Industry." To satisfy the needs of this industry, the tool calculates the optimal BR content to be used and the impact of this addition on the energy consumption and carbon emissions in the cement plant. In this way, the algorithm presents an environmental and, through consideration of raw material savings, fuel costs, and carbon taxes, economic assessment of the potential value of incorporating BR into cement production. This is conducted on a plant-by-plant basis using user information about their facility's production information, raw materials used, and fuel consumption under normal operating conditions. The tool considers two different avenues for valorizing BR as either a source of alumina, calcium, and iron in the raw meal or as a supplementary cementitious material (SCM). These two computations are completed in parallel to provide a comprehensive assessment of the valorization options for adding BR to the cement production.

I - 2.2 Summary of input parameters

To use the calculator, the user is required to supply certain metrics and information about their products and processes to inform a customized calculation of the economics. The inputs are different for each type of user and a visualization of these input categories is presented in Figure-A I-1. For the BR producers, inputs in the BR composition, physical characteristics, valorization expenses, expected cement production, and transportation costs are required. For the valorization expenses, the user is asked for the quantity which they seek to valorize, their operational costs for the management of conventional BR disposal, and their costs associated with packaging and preparation for transport of BR as a product. The BR composition is defined by the equivalent oxide content, in percentage, for iron oxide, aluminum oxide, silicon oxide, titanium oxide, and alkali oxides, and the loss on ignition. In the calculator, this information is presented alongside a worldwide average and the local national average, for easy comparison. The transportation and cement production inputs refer to the specific cement

plant to which the BR is being sold. The transportation economics of the transportation are calculated from the combination of transport modes required, the cost of shipment, transportation distance, and fuel type, for the calculation of transport emissions. The estimated cement production requires the quantity and type of cement produced at the end-use facility for the BR. Finally, the physical characteristics refer to the physical properties of the BR. This is, namely, the moisture content, particle size distribution, specific surface area, and bulk density. These parameters act as a signature of the BR, for comparison to other potential suppliers.

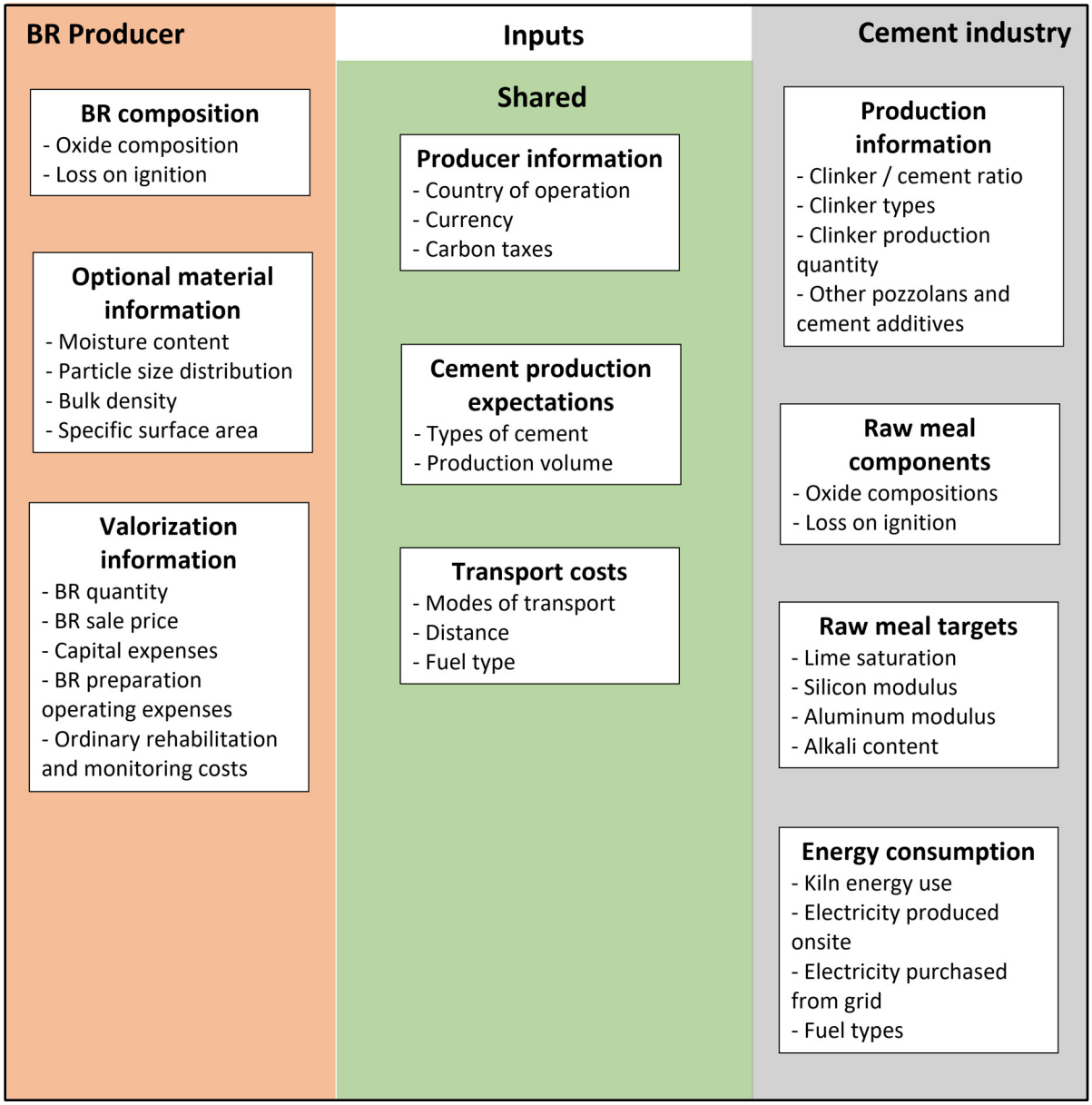

Figure-A I-1: Visualization of input categories for each user with examples of fields required.

For users in the cement industry, a separate input page is provided. In addition to the estimated cement to be produced and transportation costs, which are mirrored from the BR producers input page, this page requires more detailed fields of entry for the chemistry of the cement and clinker produced, onsite energy production, and total energy consumption. Input fields are provided for the chemical composition for up to four raw meal constituents, using the same equivalent oxide contents required of the BR, and targeted raw meal factors of lime saturation,

silica modulus, and alumina modulus, for cement produced with BR in the raw meal. In addition, the tool calculates the economics based on the types of cement being produced and their recipe in terms of limestone, clinker, gypsum, and other pozzolans. The environmental considerations, mainly CO_2 emissions, and energy savings of utilizing BR are calculated based on the amount of onsite fuel consumed and the external electricity purchased. These values are requested from the user to produce an accurate assessment of the value of adding BR to the cement production.

In preparation for the likely scenario that certain quantitative metrics may be unavailable to a specific user, a variety of national averages have been compiled for various BR properties and cement production parameters which are important to the valorization of BR in cement. The database includes national averages from Australia, Brazil, Canada, France, Germany, Greece, India, Ireland, Jamaica, Romania, Spain, and the USA. This enables the tool to progress and make reasonable estimates even in the case of incomplete information. This methodology has been applied for supply and production factors, such as the composition of the BR, the clinker production carbon emissions, and fuel composition by type, and for external market factors such as the purchased electricity carbon emissions and transportation fuel efficiency. To correctly select which national averages to utilize, the tool asks each user to enter geographical information for their aluminum or cement production facility. This information is used to estimate local taxation, relevant carbon taxes, and compose the economic figures in the output in the local currency to facilitate value assessment. With the help of the national average database, the two user input pages can be used separately or concurrently to improve the accuracy of the calculations with more detailed composition information from both the BR and the cement raw meal.

I - 2.3 Calculations employed

I - 2.3.1 Bauxite residue in the raw meal

The calculator takes the inputs and expectations provided by the users and computes options for the valorization of BR within the cement production. An illustration of the way in which

each user input category is utilized to The utilization of BR in the raw meal is evaluated through the calculation of the maximum BR which can be added to clinker. This computation uses the chemical composition of the BR, provided by the producer, the composition of the raw meal under normal operating conditions, and the targeted raw meal factors if desired to be changed with the addition of BR. To calculate the quantity of BR which can be valorized in the raw meal, a Bogue calculation is applied using the lime saturation factor, silica modulus, and alumina modulus. This standard calculation assumes the oxides of calcium, silicon, aluminum, and iron within a cement are distributed stoichiometrically among four phases: alite (tricalcium silicate), belite (dicalcium silicate), tricalcium aluminate, and tetracalcium aluminoferrite (Taylor, 1989). This analysis, in conjunction with the chemical compositions of the raw meal components, enables the calculation of the impact of BR addition into the clinker in terms of the chemistry of the cement. Using the lime saturation, silica modulus, and alumina modulus factors, a maximum allowable BR content can be established, to present the optimal composition for the valorization of BR in the raw meal.

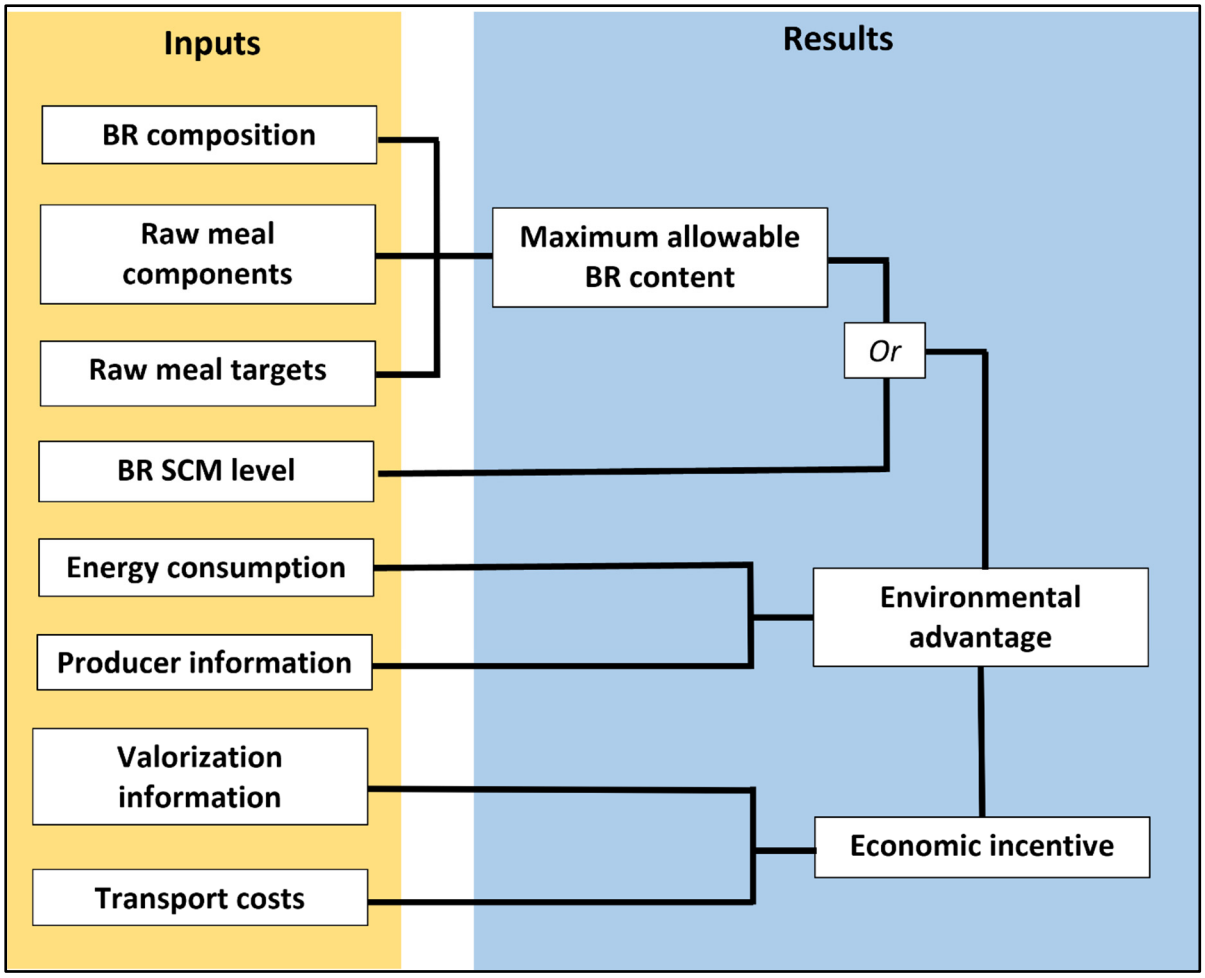

Figure-A I-2: Process flow diagram for computing the calculator results from the categories of user inputs. Refer to Figure-A I-1 for details on each category of input.

Reductions in energy consumption are calculated to quantify the economic value of the addition of BR. Each production step is analyzed separately to enable the independent assessment of savings from each processing stage. The use of BR, as an industrial by-product, in the raw meal can reduce energy consumption related to extraction, homogenization, and grinding of the raw materials. The list of processing equipment and the type and quantity of fuel required to operate it, provided by the cement user as inputs or drawn from the national average database, are used to calculate the energy consumption for each process using standard conversion factors (Canada, 2018 ; US EPA, 2015b). Fuel consumption due to BR

transportation is also accounted for, in the same manner, using the inputs of transportation modes and distances provided by the user.

The calculated reductions in energy consumption are also used to compute the anticipated reductions in greenhouse gas emissions from the use of BR in the raw meal. For BR with high calcium levels, the reduction in limestone required to meet the targeted calcium levels results in a reduced emission from decarbonation. BR also acts as a source of alumina and iron, reducing the quantity of clay and iron corrective required to meet the raw meal specifications and effectively reducing the energy and emissions required for the processing of these raw materials at each processing step. This is converted to a total reduction in carbon dioxide equivalent emissions using standard conversion factors (IPCC, 2006). These carbon reductions are subsequently used with the local carbon taxes supplied by the user or from the national database, to incorporate this factor into the economic analysis.

I – 2.3.2 Bauxite residue as a supplementary cementitious material

In the utilization of BR as a SCM, BR replaces a portion of the clinker. This can reduce the energy costs of cement production by reducing the volume of material requiring heat treatment per ton of product. This effect is directly proportional to the quantity of BR incorporated as an SCM. The cost savings are calculated based on the cost avoidance of the clinker production less the raw material cost and grinding costs of the BR. The energy savings can be computed directly as a proportional reduction in the amount of clinker required per ton of cement products, plus the energy to grind, filter, and dry the BR, as necessary. These energy savings can be translated directly into emissions reductions using the process described in Section 2.3.1 and the user inputs for fuel types and consumption using standard conversion factors. The replacement of clinker with BR as an SCM results in a reduction in the equivalent carbon dioxide emissions which translates to further economic incentives for production facilities in regions with carbon taxes.

I – 3 Results and discussion

The calculation algorithm developed in this work was prepared in Microsoft Excel for ease of use, wide useability, and the capacity to efficiently visualize the results in tables and figures. From the input parameters provided by the user, the tool calculates the results and composes figures to quantify and visualize the options for adding bauxite residue (BR) as a component in cement production. The tool presents the proposed formulations based on the compositional data available, the cost savings, and the reduction in carbon emissions for cement production with BR in comparison to normal operations. These results are presented in a number of subsections dedicated to each topic and subsequently summarized with printer-friendly reports for each type of user. For the BR producers, the tool calculates revenue based on the operational and capital expenses of commercializing BR and the cost avoidance from conventional disposal of the volume of bauxite residue which is being valorized. For cement industry users, the tool presents the options for the use of BR as a component in the raw meal or as a supplementary cementitious material (SCM). For each, there is a numerical display of the proposed recipe and the projected impact of its use on energy consumption and carbon emissions. The raw material, energy, and carbon tax savings are presented separately and in summary to quantify the economic advantage to valorizing BR as a raw meal component and a SCM in cement production. In this section, the results will be explained, and a worked example is shown to display the format and high level of accessibility of the results achieved in this calculation tool. This example calculates the value of BR addition to a hypothetical cement plant in Germany which produces 1 M ton of cement per year, produced in a petroleum coke burning kiln, and assumes national averages for bauxite residue composition and other factors.

I – 3.1 Bauxite residue as a component of the raw meal

The first results which are presented pursue the option of BR as a component of the raw meal in cement clinker. Using the compositional information provided by the user and the targeted clinker moduli, the calculator proposes a maximum content of BR which can be valorized in

the cement production based on the targeted values and inputs provided by the user. In Figure-A I-3, the worked example shows two clinker recipes that have been calculated that include bauxite residue and a comparison to reference cement produced under normal operating conditions. The tool provides a numerical presentation of the proposed BR addition levels and raw meal constituents, as well as a Bogue analysis of the phase composition, as shown below. Finally, the raw material costs of the limestone, clay, sand, iron corrective, and bauxite residue used to form the raw meal are calculated compared to normal operating conditions. This value is used as a part of subsequent calculations of the economics of BR addition in the raw meal.

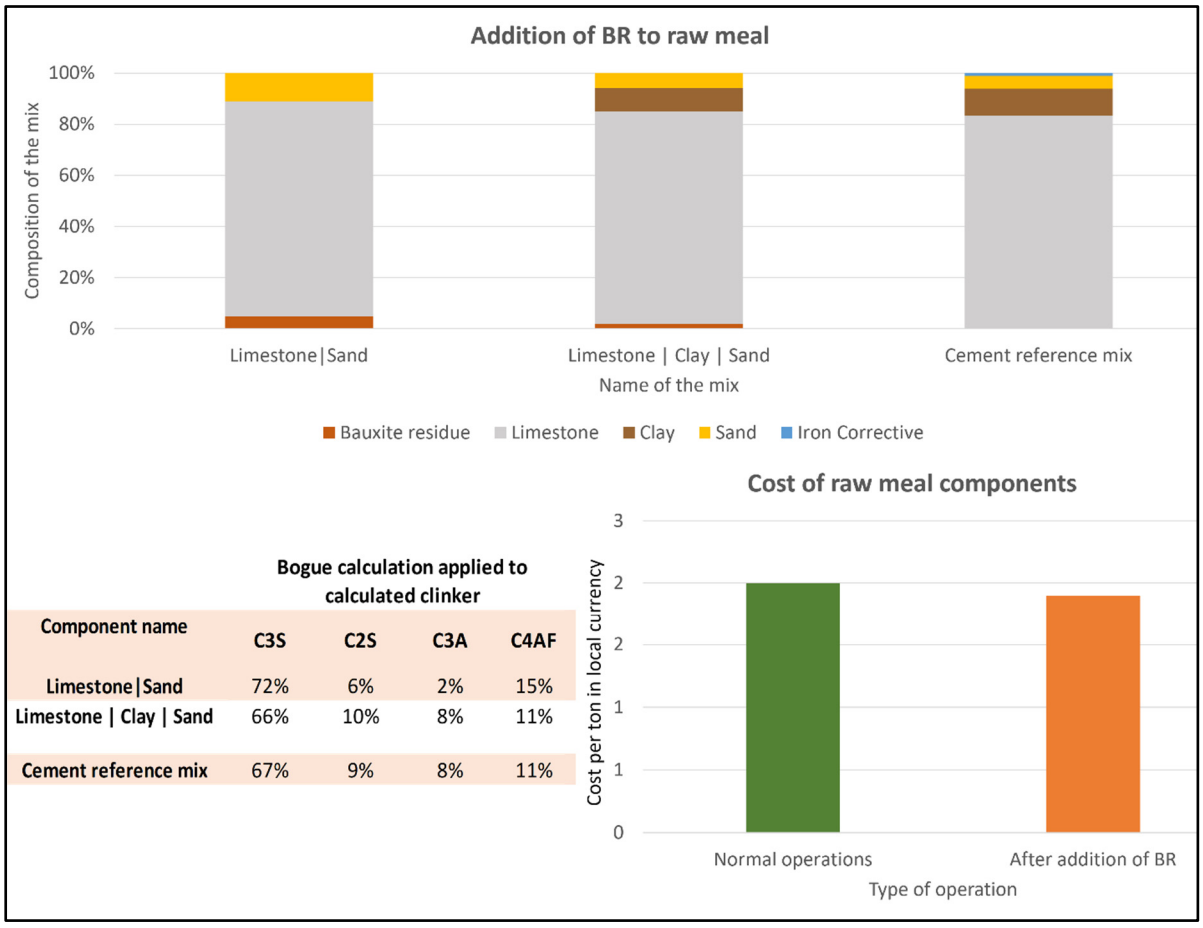

Bogue calculation applied to calculated clinker				
Component name	C3S	C2S	C3A	C4AF
Limestone|Sand	72%	6%	2%	15%
Limestone | Clay | Sand	66%	10%	8%	11%
Cement reference mix	67%	9%	8%	11%

Figure-A I-3: Example of compositions of proposed BR as a component in the raw meal using German national averages. Acronyms in bogue calculation section follow cement chemist notation: (C3S = tricalcium silicate, C2S = dicalcium silicate, C3A = tricalcium aluminate, C4AF = tetracalcium aluminoferrite).

The economics of the proposed raw meal recipe with BR is then calculated in terms of energy savings. This analysis builds upon the user input information as to the energy consumption in each processing stage under normal operating conditions. The addition of BR to the raw meal formulation reduces the required raw material processing which manifests as projected reduced energy consumption in the grinding, homogenization, and blending steps. The energy savings for these processing steps are presented in the results numerically and in a visualization such as in Figure-A I-4. This step-by-step analysis presents a more in-depth rationalization of the total energy savings projected by the tool for the addition of BR to the raw meal. It also enables the breakdown of the energy savings by fuel consumption type, using the input information provided by the user. This allows cost comparison by fuel type consumption, as shown in Figure-A I-4. The total cost savings contribute to the economics of the addition of BR in the raw meal.

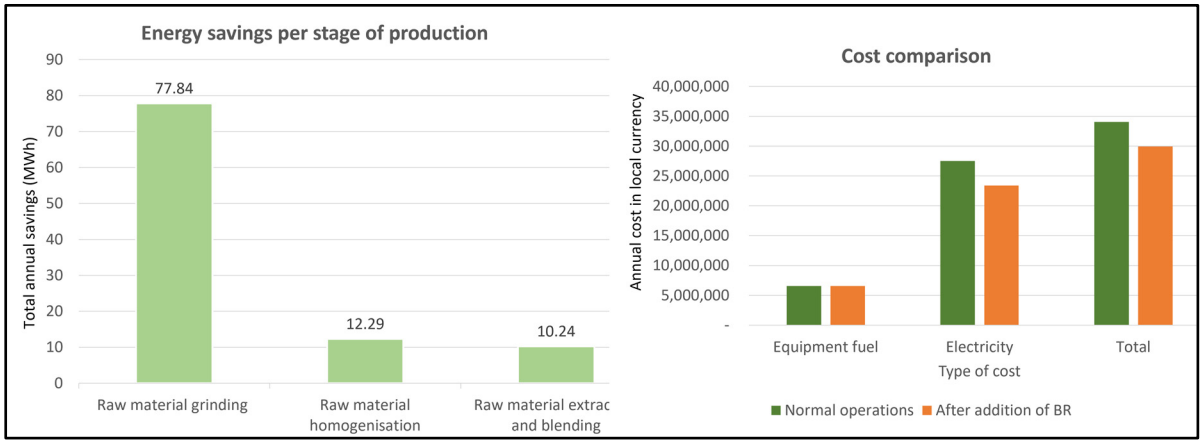

Figure-A I-4: The energy savings with the addition of BR in the raw meal in each production step and the corresponding cost savings due to reduced fuel and electricity consumption for the worked example simulating a 1 M ton annual cement production.

Finally, the reduced energy consumption, analyzed by fuel type, is used to calculate the projected emissions reductions due to the addition of BR in the raw meal. Using standard EPA guidelines for greenhouse gas conversions (US EPA, 2015b) and typical fuel compositions based on established fuel types (Canada, 2018), the carbon dioxide equivalent emissions can be estimated for the proposed BR-modified production and under normal operating conditions

of cement production. A comparison of these values, such as those shown in Figure-A I-5, is presented to the user of the calculation tool to quantify the environmental benefits of incorporating BR into cement production. Based on the local carbon tax information provided by the user, this environmental advantage can be directly translated into the projected cost avoidance by reduced taxation. This value completes the economic analysis of the proposed BR addition to raw meal. All of the results, including numerical descriptions of the proposed raw meal formulation, energy savings, and emission reductions, are presented along with a cumulative analysis of the total economic value of the use of BR in the raw meal. This comprehensive report is structured in a printer-friendly format for the user alongside the same analysis for the use of SCM, which is explained in the following section.

Type of emissions	Total CO2-e (kg/t of clinker) avoided
From cement production	10.9
From electricity	0.1
Total	**11.0**

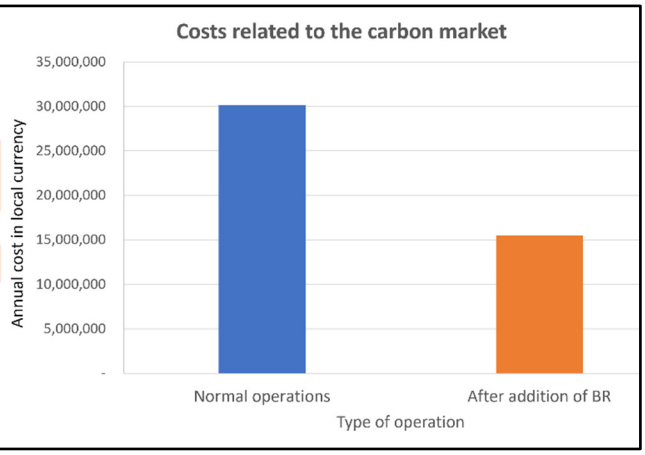

Figure-A I-5: Carbon dioxide equivalent emission reductions caused by the addition of BR to the raw meal and the corresponding reduction in carbon market taxes for the worked example of a 1 M ton per year cement production in a coke-fired kiln, subject to German carbon taxes.

I - 3.2 Bauxite residue as a supplementary cementitious material

The potential use of BR as a SCM is considered as a parallel use-case for the addition of BR to cement production. In this case, BR is being utilized only as a replacement for clinker in the final product. This simplifies the calculation of the economic and environmental impact of BR on cement production because it requires no changes to the clinker formulation or kiln operation. However, the impact of BR as an SCM must be validated with laboratory testing to

confirm that the proposed cementitious material meets local standards. A warning about this is presented in the calculation tool. As mentioned previously, concerns have been raised in the literature about the impact of BR as an SCM on the properties of the cement. Calcination of the BR is a common method for improving the reactivity in the blended cement and minimizing negative impacts on the properties (X. Liu, Zhang, Sun, Zhang, & Li, 2011 ; Wu & Liu, 2012). Since the purpose of this tool is to calculate and compile the economic and environmental advantages of the use of BR, the option of calcination is presented to the user to estimate the impact of this process on the cost and environmental savings of BR addition. Moreover, to facilitate the investigation of BR as an SCM at different potential dosages, the user is provided with the option to select the percentage of BR to be incorporated in the binder as an SCM, in the range of 1% and 30%. For the worked example presented below, 15% BR was selected to generate the figures.

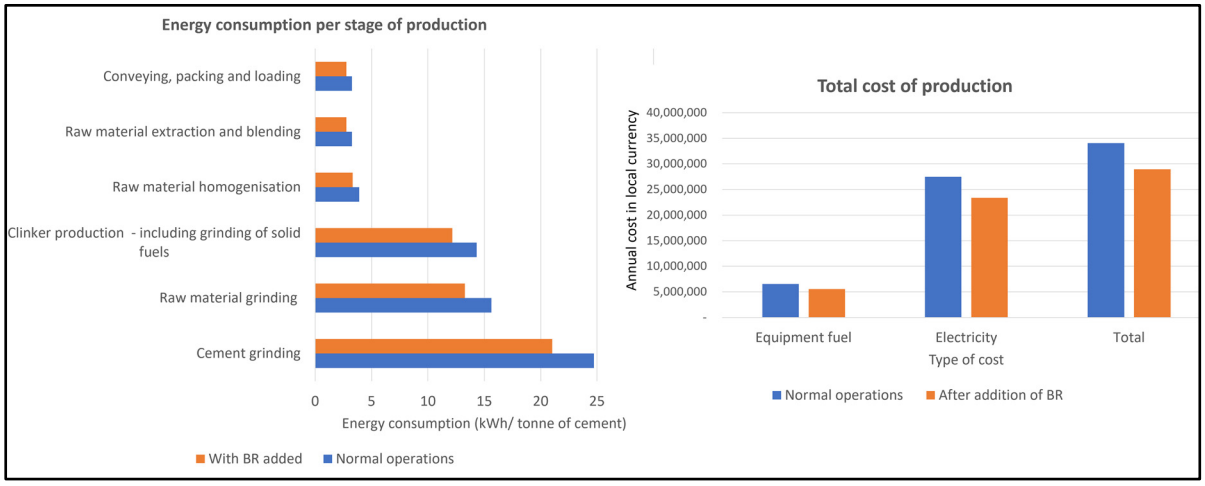

Figure-A I-6: The energy savings, distinguished by stage of production, and the corresponding cost reductions, analyzed by fuel types, for BR as a SCM in the example of a 1 M ton annual production in a coke-fired kiln.

The selected content of BR as an SCM is used to calculate the energy and cost savings in terms of the production volume. This is a proportional reduction for all factors, based on the process information input by the user. A worked example of the figures generated to visualize these results is presented in Figure-A I-6. In the same manner as was calculated for the use of BR in

the raw meal, these energy savings are converted into cost savings, categorized by fuel types. In turn, this analysis is used to calculate the total carbon dioxide equivalent emissions for BR-SCM and normal operations cement production to quantify the emission avoidance enabled by the addition of BR. The tool presents these results to the user and calculates the projected value in terms of cost avoidance due to reduced carbon taxation, based on the provided local carbon market information. Examples of these figures are displayed in Figure-A I-7. The tool compiles the total energy savings, emissions reductions, and economic incentive of apply BR as an SCM in a printer-friendly report presented alongside the options for BR as a raw meal component.

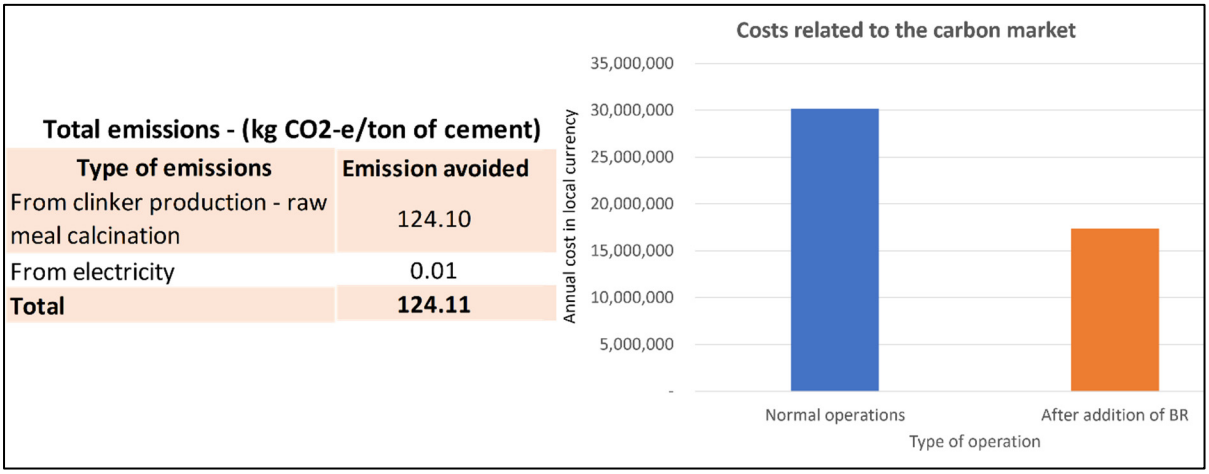

Total emissions - (kg CO2-e/ton of cement)

Type of emissions	Emission avoided
From clinker production - raw meal calcination	124.10
From electricity	0.01
Total	**124.11**

Figure-A I-7: The carbon dioxide equivalent emissions reduction projected for the use of BR as an SCM at a level of 15% and the corresponding reduction in carbon taxes for the worked example of a 1 M ton annual production of cement at a carbon tax of 24€/ton of carbon dioxide equivalent emitted.

I - 4 Conclusion

The present work has developed a new tool to support collaboration between the aluminum and cement industries in the valorization of bauxite residue. The large volume storage of bauxite residue globally creates an opportunity for the use of this material in cement production to the benefit of both industries. The calculation tool is designed to be used by representatives of each industry, separately or jointly, to accurately calculate the value

proposition to both industrial sectors. The tool considers two parallel methods for utilizing bauxite residue in cement production, as a raw meal component or as a supplementary cementitious material. The tool incorporates factors that are unique to each bauxite residue producer and cement production facility, including the bauxite residue composition and equipment-specific energy consumption, improve the accuracy of projections for the energy consumption and carbon emissions reductions on a plant-by-plant basis. In the case of missing data, a database of national averages from countries on four continents has been assembled to provide an avenue for reasonable estimation and allows cement producers to compare their processes to typical productions in their locality. This has created a robust and versatile compositional tool that will be useful for continued collaborations between the aluminum and cement industries to develop economically and environmentally conscious processes for utilizing bauxite residue.

LIST OF BIBLIOGRAPHIC REFERENCES

Acar, C. (2018). A comprehensive evaluation of energy storage options for better sustainability. *International Journal of Energy Research*, *42*(12), 3732-3746. https://doi.org/10.1002/er.4102

Agrawal, S., Rayapudi, V., & Dhawan, N. (2018). Microwave Reduction of Red Mud for Recovery of Iron Values. *Journal of Sustainable Metallurgy*, *4*(4), 427-436. https://doi.org/10.1007/s40831-018-0183-3

Albitar, M., Mohamed Ali, M. S., Visintin, P., & Drechsler, M. (2017). Durability evaluation of geopolymer and conventional concretes. *Construction and Building Materials*, *136*, 374-385. https://doi.org/10.1016/j.conbuildmat.2017.01.056

Alghamdi, H., & Neithalath, N. (2018). Novel synthesis of lightweight geopolymer matrices from fly ash through carbonate-based activation. *Materials Today Communications*, *17*, 266-277.

Alizadeh, V. (2016). Effect of Paste Volume on Performance of Controlled Low Strength Materials. Dans *SCMT4*. Las Vegas, USA.

Alonso, M., Gismera, S., Blanco, M., Lanzón, M., & Puertas, F. (2017). Alkali-activated mortars: Workability and rheological behaviour. *Construction and Building Materials*, *145*, 576-587.

Anawati, J., & Azimi, G. (2019). Recovery of scandium from Canadian bauxite residue utilizing acid baking followed by water leaching. *Waste Management*, *95*, 549-559. https://doi.org/10.1016/j.wasman.2019.06.044

Anawati, J., & Azimi, G. (2020). Recovery of Strategic Materials from Canadian Bauxite Residue by Smelting Followed by Acid Baking–Water Leaching. Dans G. Azimi, K. Forsberg, T. Ouchi, H. Kim, S. Alam, & A. A. Baba (Éds), *Rare Metal Technology 2020* (pp. 139-150). Cham : Springer International Publishing. https://doi.org/10.1007/978-3-030-36758-9_13

Andrew, R. M. (2018). Global CO 2 emissions from cement production. *Earth System Science Data*, *10*(1), 195-217.

Angelopoulos, P. M., Balomenos, E., & Taxiarchou, M. (2016). Thin-Layer Modeling and Determination of Effective Moisture Diffusivity and Activation Energy for Drying of Red Mud from Filter Presses. *Journal of Sustainable Metallurgy*, *2*(4), 344-352. https://doi.org/10.1007/s40831-016-0055-7

Aoki, K., Kusakabe, K., & Morooka, S. (2000). Separation of Gases with an A-Type Zeolite Membrane. *Industrial & Engineering Chemistry Research*, *39*(7), 2245-2251. https://doi.org/10.1021/ie990902c

Arnout, L., Hertel, T., Liard, M., Lootens, D., & Pontikes, Y. (2017). Use of bauxite residue slurry as single activator in a hybrid binder system. Dans *Travaux 46, Proceedings of 35th International ICSOBA Conference* (Vol. 46, pp. 519-527). Repéré à https://lirias.kuleuven.be/retrieve/505982

ASI. (2022). Aluminum Stewardship Initiative. *Aluminium Stewardship Initiative*. Repéré à https://aluminium-stewardship.org/

ASTM International. (2017, 12 octobre). ASTM C62-17 Standard Specification for Building Brick (Solid Masonry Units Made From Clay or Shale). Repéré à https://www.astm.org/c0062-17.html

ASTM International. (2018a, 13 février). ASTM C373-18 Standard Test Methods for Determination of Water Absorption and Associated Properties by Vacuum Method for Pressed Ceramic Tiles and Glass Tiles and Boil Method for Extruded Ceramic Tiles and Non-tile Fired Ceramic Whiteware Products. Repéré à https://www.astm.org/c0373-18.html

ASTM International. (2018b, 25 juillet). ASTM C915-79 Standard Specification for Precast Reinforced Concrete Crib Wall Members. Repéré à https://www.astm.org/c0915-79r18.html

ASTM International. (2019a, 14 mai). ASTM C858-19 Standard Specification for Underground Precast Concrete Utility Structures. Repéré à https://www.astm.org/c0858-19.html

ASTM International. (2019b, 23 décembre). ASTM C825-19 Standard Specification for Precast Concrete Barriers. Repéré à https://www.astm.org/c0825-19.html

ASTM International. (2020a). *ASTM C305-12 Practice for Mechanical Mixing of Hydraulic Cement Pastes and Mortars of Plastic Consistency*. https://doi.org/10.1520/C0305-12

ASTM International. (2020b, 12 mars). ASTM C109/C109M-20B Test Method for Compressive Strength of Hydraulic Cement Mortars (Using 2-in. or [50-mm] Cube Specimens). https://doi.org/10.1520/C0109_C0109M-20B

ASTM International. (2020c, 10 septembre). ASTM C478/C478M-20 Standard Specification for Circular Precast Reinforced Concrete Manhole Sections. Repéré à https://www.astm.org/c0478_c0478m-20.html

ASTM International. (2020d, 7 octobre). ASTM C1504-20 Standard Specification for Manufacture of Precast Reinforced Concrete Three-Sided Structures for Culverts and Storm Drains. Repéré à https://www.astm.org/c1504-20.html

ASTM International. (2021a, 20 mai). ASTM C348-21 Test Method for Flexural Strength of Hydraulic-Cement Mortars. https://doi.org/10.1520/C0348-21

ASTM International. (2021b, 10 août). ASTM C913-21 Standard Specification for Precast Concrete Water and Wastewater Structures. Repéré à https://www.astm.org/c0913-21.html

ASTM International. (2022a, 9 mai). ASTM C129-17 Standard Specification for Nonloadbearing Concrete Masonry Units. Repéré à https://www.astm.org/c0129-17.html

ASTM International. (2022b, 9 mai). ASTM C1776/C1776M-17 Standard Specification for Wet-Cast Precast Modular Retaining Wall Units. Repéré à https://www.astm.org/c1776-c1776m-17r22.html

ASTM International. (2022c, 20 juin). ASTM C1227-20 Standard Specification for Precast Concrete Septic Tanks. Repéré à https://www.astm.org/c1227-20.html

Azhari, F., & Banthia, N. (2012). Cement-based sensors with carbon fibers and carbon nanotubes for piezoresistive sensing. *Cement and Concrete Composites*, *34*(7), 866-873.

Badogiannis, E., Kakali, G., & Tsivilis, S. (2005). Metakaolin as supplementary cementitious material. *Journal of Thermal Analysis and Calorimetry*, *81*(2), 457-462. https://doi.org/10.1007/s10973-005-0806-3

Banfill, P. F. G., Starrs, G., Derruau, G., McCarter, W. J., & Chrisp, T. M. (2006). Rheology of low carbon fibre content reinforced cement mortar. *Cement and Concrete Composites*, *28*(9), 773-780. https://doi.org/10.1016/j.cemconcomp.2006.06.004

Barbosa, T. R., Foletto, E. L., Dotto, G. L., & Jahn, S. L. (2018). Preparation of mesoporous geopolymer using metakaolin and rice husk ash as synthesis precursors and its use as potential adsorbent to remove organic dye from aqueous solutions. *Ceramics International*, *44*(1), 416-423. https://doi.org/10.1016/j.ceramint.2017.09.193

Bear, J. (1988). *Dynamics of Fluids in Porous Media*. (S.l.) : Courier Corporation.

Bell, J. L., Driemeyer, P. E., & Kriven, W. M. (2009a). Formation of Ceramics from Metakaolin-Based Geopolymers: Part I—Cs-Based Geopolymer. *Journal of the American Ceramic Society*, *92*(1), 1-8. https://doi.org/10.1111/j.1551-2916.2008.02790.x

Bell, J. L., Driemeyer, P. E., & Kriven, W. M. (2009b). Formation of Ceramics from Metakaolin-Based Geopolymers. Part II: K-Based Geopolymer. *Journal of the American Ceramic Society*, *92*(3), 607-615. https://doi.org/10.1111/j.1551-2916.2008.02922.x

Belli, A., Mobili, A., Bellezze, T., Tittarelli, F., & Cachim, P. (2018). Evaluating the Self-Sensing Ability of Cement Mortars Manufactured with Graphene Nanoplatelets, Virgin or Recycled Carbon Fibers through Piezoresistivity Tests. *Sustainability*, *10*(11), 4013. https://doi.org/10.3390/su10114013

Bernal, Susan A., Nicolas, R. S., van Deventer, J. S. J., & Provis, J. L. (2015). Alkali-activated slag cements produced with a blended sodium carbonate/sodium silicate activator. *Advances in Cement Research*, *28*(4), 262-273. https://doi.org/10.1680/jadcr.15.00013

Bernal, Susan A, & Provis, J. L. (2014). Durability of alkali-activated materials: progress and perspectives. *Journal of the American Ceramic Society*, *97*(4), 997-1008.

Bernal, Susan A., Provis, J. L., Myers, R. J., San Nicolas, R., & van Deventer, J. S. J. (2015). Role of carbonates in the chemical evolution of sodium carbonate-activated slag binders. *Materials and Structures*, *48*(3), 517-529. https://doi.org/10.1617/s11527-014-0412-6

Bernal, Susan A., San Nicolas, R., Myers, R. J., de Gutiérrez, R. M., Puertas, F., van Deventer, J. S., & Provis, J. L. (2014). MgO content of slag controls phase evolution and structural changes induced by accelerated carbonation in alkali-activated binders. *Cement and Concrete Research*, *57*, 33-43.

Bernal, Susan Andrea. (2016). Advances in near-neutral salts activation of blast furnace slags. *RILEM Technical Letters*, *1*, 39-44. https://doi.org/10.21809/rilemtechlett.2016.8

Bhojaraju, C., Mousavi, S. S., Brial, V., DiMare, M., & Ouellet-Plamondon, C. M. (2021). Fresh and hardened properties of GGBS-contained cementitious composites using graphene and graphene oxide. *Construction and Building Materials*, *300*, 123902. https://doi.org/10.1016/j.conbuildmat.2021.123902

Bi, S., Liu, M., Shen, J., Hu, X. M., & Zhang, L. (2017). Ultrahigh Self-Sensing Performance of Geopolymer Nanocomposites via Unique Interface Engineering. *ACS Applied Materials & Interfaces*, *9*(14), 12851-12858. https://doi.org/10.1021/acsami.7b00419

Blengini, G., Latunussa, C., Eynard, U., Torres de Matos, C., & Wittmer, D. (2020). *Study on the EU's list of Critical Raw Materials – Final Report (2020)*. European Commission.

Bobirică, C., Orbeci, C., Bobirică, L., Palade, P., Deleanu, C., Pantilimon, C. M., … Radu, I. C. (2020). Influence of red mud and waste glass on the microstructure, strength, and leaching behavior of bottom ash-based geopolymer composites. *Scientific Reports*, *10*(1), 19827. https://doi.org/10.1038/s41598-020-76818-4

Borra, C. R., Blanpain, B., Pontikes, Y., Binnemans, K., & Van Gerven, T. (2016). Recovery of Rare Earths and Other Valuable Metals From Bauxite Residue (Red Mud): A Review. *Journal of Sustainable Metallurgy*, *2*(4), 365-386. https://doi.org/10.1007/s40831-016-0068-2

Borra, C. R., Pontikes, Y., Binnemans, K., & Van Gerven, T. (2015). Leaching of rare earths from bauxite residue (red mud). *Minerals Engineering*, *76*, 20-27. https://doi.org/10.1016/j.mineng.2015.01.005

Bulatova, R., Jabbari, M., Kaiser, A., Della Negra, M., Andersen, K. B., Gurauskis, J., & Bahl, C. R. H. (2014). Thickness control and interface quality as functions of slurry formulation and casting speed in side-by-side tape casting. *Journal of the European Ceramic Society*, *34*(16), 4285-4295. https://doi.org/10.1016/j.jeurceramsoc.2014.07.013

Calderín, L., Karasiev, V. V., & Trickey, S. B. (2017). Kubo–Greenwood electrical conductivity formulation and implementation for projector augmented wave datasets. *Computer Physics Communications*, *221*, 118-142. https://doi.org/10.1016/j.cpc.2017.08.008

Canada, N. R. (2018, 30 avril). fuel-consumption-guide. Natural Resources Canada. Repéré à https://www.nrcan.gc.ca/energy-efficiency/energy-efficiency-transportation-alternative-fuels/fuel-consumption-guide/21002

Cândido, V. S., Silva, A. C. R. da, Simonassi, N. T., Lima, E. S., Luz, F. S. da, & Monteiro, S. N. (2018). Mechanical and microstructural characterization of geopolymeric concrete subjected to fatigue. *Journal of Materials Research and Technology*, *7*(4), 566-570. https://doi.org/10.1016/j.jmrt.2018.07.011

Catauro, M., Bollino, F., Cattaneo, A. S., & Mustarelli, P. (2017). Al2O3·2SiO2 powders synthesized via sol–gel as pure raw material in geopolymer preparation. *Journal of the American Ceramic Society*, *100*(5), 1919-1927. https://doi.org/10.1111/jace.14724

CGRi. (2022). Circularity Gap Reporting Initiative. Repéré à https://www.circularity-gap.world/

Chaikin, L., Shoppert, A., Valeev, D., Loginova, I., & Napol'skikh, J. (2020). Concentration of Rare Earth Elements (Sc, Y, La, Ce, Nd, Sm) in Bauxite Residue (Red Mud) Obtained by Water and Alkali Leaching of Bauxite Sintering Dust. *Minerals*, *10*(6), 500. https://doi.org/10.3390/min10060500

Chen, B., Wu, K., & Yao, W. (2004). Conductivity of carbon fiber reinforced cement-based composites. *Cement and Concrete Composites*, *26*(4), 291-297.

Chen, M., Gao, P., Geng, F., Zhang, L., & Liu, H. (2017). Mechanical and smart properties of carbon fiber and graphite conductive concrete for internal damage monitoring of structure. *Construction and Building Materials*, *142*, 320-327.

Chen, P.-W., & Chung, D. D. L. (1993). Carbon fiber reinforced concrete for smart structures capable of non-destructive flaw detection. *Smart Materials and Structures*, *2*(1), 22-30. https://doi.org/10.1088/0964-1726/2/1/004

Chen, X., Guo, Y., Ding, S., Zhang, H., Xia, F., Wang, J., & Zhou, M. (2019). Utilization of red mud in geopolymer-based pervious concrete with function of adsorption of heavy metal ions. *Journal of Cleaner Production*, *207*, 789-800. https://doi.org/10.1016/j.jclepro.2018.09.263

Chindaprasirt, P., Phoo-ngernkham, T., Hanjitsuwan, S., Horpibulsuk, S., Poowancum, A., & Injorhor, B. (2018). Effect of calcium-rich compounds on setting time and strength development of alkali-activated fly ash cured at ambient temperature. *Case Studies in Construction Materials*, *9*, e00198. https://doi.org/10.1016/j.cscm.2018.e00198

Chung, D. (2000). Cement reinforced with short carbon fibers: a multifunctional material. *Composites Part B: Engineering*, *31*(6-7), 511-526.

Collins, F., & Sanjayan, J. G. (2000). Effect of pore size distribution on drying shrinking of alkali-activated slag concrete. *Cement and Concrete Research*, *30*(9), 1401-1406. https://doi.org/10.1016/S0008-8846(00)00327-6

Cui, X., Liu, L., He, Y., Chen, J., & Zhou, J. (2011). A novel aluminosilicate geopolymer material with low dielectric loss. *Materials Chemistry and Physics*, *130*(1), 1-4. https://doi.org/10.1016/j.matchemphys.2011.06.039

Cui, X.-M., Zheng, G.-J., Han, Y.-C., Su, F., & Zhou, J. (2008). A study on electrical conductivity of chemosynthetic Al2O3–2SiO2 geoploymer materials. *Journal of Power Sources*, *184*(2), 652-656. https://doi.org/10.1016/j.jpowsour.2008.03.021

Cui, Y., Chen, J., Zhang, Y., Peng, D., Huang, T., & Sun, C. (2019). pH-Dependent Leaching Characteristics of Major and Toxic Elements from Red Mud. *International Journal of Environmental Research and Public Health*, *16*(11), 2046. https://doi.org/10.3390/ijerph16112046

Dakhane, A., Das, S., Kailas, S., & Neithalath, N. (2016). Elucidating the Crack Resistance of Alkali-Activated Slag Mortars Using Coupled Fracture Tests and Image Correlation. *Journal of the American Ceramic Society*, *99*(1), 273-280. https://doi.org/10.1111/jace.13960

Dakin, T. W. (2006). Conduction and polarization mechanisms and trends in dielectric. *IEEE Electrical Insulation Magazine*, *22*(5), 11-28. https://doi.org/10.1109/MEI.2006.1705854

Damtoft, J. S., Lukasik, J., Herfort, D., Sorrentino, D., & Gartner, E. M. (2008). Sustainable development and climate change initiatives. *Cement and Concrete Research*, *38*(2), 115-127. https://doi.org/10.1016/j.cemconres.2007.09.008

Danner, T., & Justnes, H. (2020). Bauxite Residue as Supplementary Cementitious Material – Efforts to Reduce the Amount of Soluble Sodium. *1-20*. https://doi.org/10.2478/ncr-2020-0001

Daux, V., Guy, C., Advocat, T., Crovisier, J.-L., & Stille, P. (1997). Kinetic aspects of basaltic glass dissolution at 90 C: role of aqueous silicon and aluminium. *Chemical Geology*, *142*(1-2), 109-126.

Davidovits, J. (1991). Geopolymers. *Journal of Thermal Analysis and Calorimetry*, *37*(8), 1633-1656. https://doi.org/10.1007/BF01912193

Davidovits, Joseph. (1982). *Brevet nº US4349386A*. United States. Repéré à https://patents.google.com/patent/US4349386A/en

Davidovits, Joseph. (1994). Properties of geopolymer cements (Vol. 1, pp. 131-149). Communication présentée au First international conference on alkaline cements and concretes, Kiev State Technical University Kiev, Ukraine.

Davidovits, Joseph. (2002a). Environmentally driven geopolymer cement applications. Dans *Proceedings of 2002 Geopolymer Conference. Melbourne. Australia*.

Davidovits, Joseph. (2002b). years of successes and failures in geopolymer applications. Market trends and potential breakthroughs (Vol. 28, p. 29). Communication présentée au Geopolymer 2002 Conference, Geopolymer Institute Saint-Quentin, France; Melbourne, Australia.

Deng, L., Ma, Y., Hu, J., Yin, S., Ouyang, X., Fu, J., … Zhang, Z. (2019). Preparation and piezoresistive properties of carbon fiber-reinforced alkali-activated fly ash/slag mortar. *Construction and Building Materials*, *222*, 738-749. https://doi.org/10.1016/j.conbuildmat.2019.06.134

Deschanvres, A., Raveau, B., & Tollemer, F. (1967). Substitution of copper for a divalent metal in perovskite-type titanates. *Bull. Soc. Chim. Fr*, *11*, 4077-4078.

Di Mare, M., Inumerable, N., Brisebois, P. P., & Ouellet-Plamondon, C. M. (2022). Combined Experimental and Computational Prediction of the Piezoresistivity of Alkali-Activated Inorganic Polymers. *The Journal of Physical Chemistry C*. https://doi.org/10.1021/acs.jpcc.2c03633

Di Mare, M., Nattrodt Monteiro, V., Brial, V., Ouellet-Plamondon, C. M., Fortin, S., Tsesmelis, K., … Rosani, D. (2021). A calculator for valorizing bauxite residue in the cement industry. *Cleaner Materials*, *1*, 100009. https://doi.org/10.1016/j.clema.2021.100009

Di Mare, M., & Ouellet-Plamondon, C. (2022). The effect of composition on the dielectric properties of alkali activated materials: A next generation dielectric ceramic. *Materials Today Communications*, *32*, 104087. https://doi.org/10.1016/j.mtcomm.2022.104087

Dimas, D. D., Giannopoulou, I. P., & Panias, D. (2009). Utilization of alumina red mud for synthesis of inorganic polymeric materials. *Mineral processing & Extractive metallurgy review*, *30*(3), 211-239.

Ding, S., Ruan, Y., Yu, X., Han, B., & Ni, Y.-Q. (2019). Self-monitoring of smart concrete column incorporating CNT/NCB composite fillers modified cementitious sensors. *Construction and Building Materials*, *201*, 127-137.

Ding, Y., Dai, J.-G., & Shi, C.-J. (2016). Mechanical properties of alkali-activated concrete: A state-of-the-art review. *Construction and Building Materials*, *127*, 68-79. https://doi.org/10.1016/j.conbuildmat.2016.09.121

Ding, Y., Dai, J.-G., & Shi, C.-J. (2018). Fracture properties of alkali-activated slag and ordinary Portland cement concrete and mortar. *Construction and Building Materials*, *165*, 310-320. https://doi.org/10.1016/j.conbuildmat.2017.12.202

Dong, W., Li, W., Tao, Z., & Wang, K. (2019). Piezoresistive properties of cement-based sensors: Review and perspective. *Construction and Building Materials*, *203*, 146-163. https://doi.org/10.1016/j.conbuildmat.2019.01.081

Donnini, J., Bellezze, T., & Corinaldesi, V. (2018). Mechanical, electrical and self-sensing properties of cementitious mortars containing short carbon fibers. *Journal of Building Engineering*, *20*, 8-14. https://doi.org/10.1016/j.jobe.2018.06.011

Downey, A., D'Alessandro, A., Ubertini, F., & Laflamme, S. (2018). Automated crack detection in conductive smart-concrete structures using a resistor mesh model. *Measurement Science and Technology*, *29*(3), 035107. https://doi.org/10.1088/1361-6501/aa9fb8

Duan, P., Yan, C., Zhou, W., & Ren, D. (2016). Development of fly ash and iron ore tailing based porous geopolymer for removal of Cu(II) from wastewater. *Ceramics International*, *42*(12), 13507-13518. https://doi.org/10.1016/j.ceramint.2016.05.143

Dufty, J., Wrighton, J., Luo, K., & Trickey, S. b. (2018). On the Kubo-Greenwood model for electron conductivity. *Contributions to Plasma Physics*, *58*(2-3), 150-154. https://doi.org/10.1002/ctpp.201700102

Duxson, P., Fernández-Jiménez, A., Provis, J. L., Lukey, G. C., Palomo, A., & van Deventer, J. S. J. (2007). Geopolymer technology: the current state of the art. *Journal of Materials Science*, *42*(9), 2917-2933. https://doi.org/10.1007/s10853-006-0637-z

Duxson, P., & Provis, J. L. (2008). Designing Precursors for Geopolymer Cements. *Journal of the American Ceramic Society*, *91*(12), 3864-3869. https://doi.org/10.1111/j.1551-2916.2008.02787.x

Dyson, H. M., Richardson, I. G., & Brough, A. R. (2007). A combined 29Si MAS NMR and selective dissolution technique for the quantitative evaluation of hydrated blast furnace slag cement blends. *Journal of the American Ceramic Society*, *90*(2), 598-602.

Ebrahimi, K., Daiezadeh, M. J., Zakertabrizi, M., Zahmatkesh, F., & Habibnejad Korayem, A. (2018). A review of the impact of micro- and nanoparticles on freeze-thaw durability of hardened concrete: Mechanism perspective. *Construction and Building Materials*, *186*, 1105-1113. https://doi.org/10.1016/j.conbuildmat.2018.08.029

El Gass Hamza. (2020). *Formulation d'un mortier géopolymère conducteur à base de résidus de bauxite*. Université du Québec à Chicoutimi.

EPA. (2021). U.S. annual national emission factor, year 2019 data. U.S. Environmental Protection Agency, Washington, DC.

Escalante-García, J. I., Fuentes, A. F., Gorokhovsky, A., Fraire-Luna, P. E., & Mendoza-Suarez, G. (2003). Hydration Products and Reactivity of Blast-Furnace Slag Activated by Various Alkalis. *Journal of the American Ceramic Society*, *86*(12), 2148-2153. https://doi.org/10.1111/j.1151-2916.2003.tb03623.x

Essaidi, N., Nadir, H., Martinod, E., Feix, N., Bertrand, V., Tantot, O., … Rossignol, S. (2017). Comparative study of dielectric properties of geopolymer matrices using different dielectric powders. *Journal of the European Ceramic Society*, *37*(11), 3551-3557. https://doi.org/10.1016/j.jeurceramsoc.2017.04.036

Evans, K. (2016). The History, Challenges, and New Developments in the Management and Use of Bauxite Residue. *Journal of Sustainable Metallurgy*, *2*(4), 316-331. https://doi.org/10.1007/s40831-016-0060-x

Fernández-Jiménez, A., & Palomo, A. (2005). Mid-infrared spectroscopic studies of alkali-activated fly ash structure. *Microporous and Mesoporous Materials*, *86*(1), 207-214. https://doi.org/10.1016/j.micromeso.2005.05.057

Fernández-Jiménez, A., Palomo, A., & Criado, M. (2005). Microstructure development of alkali-activated fly ash cement: a descriptive model. *Cement and Concrete Research*, *35*(6), 1204-1209. https://doi.org/10.1016/j.cemconres.2004.08.021

Fernández-Jiménez, A., & Puertas, F. (2001). Setting of alkali-activated slag cement. Influence of activator nature. *Advances in Cement Research*, *13*(3), 115-121. https://doi.org/10.1680/adcr.2001.13.3.115

Fletcher, R. (2013). *Practical methods of optimization*. (S.l.) : John Wiley & Sons.

Fu, X, Lu, W., & Chung, D. D. L. (1998). Improving the Strain-Sensing Ability of Carbon Fiber-Reinforced Cement by Ozone Treatment of the Fibers 11Communicated by D.M. Roy. *Cement and Concrete Research*, *28*(2), 183-187. https://doi.org/10.1016/S0008-8846(97)00265-2

Fu, Xuli, Ma, E., Chung, D. D. L., & Anderson, W. A. (1997). Self-monitoring in carbon fiber reinforced mortar by reactance measurement. *Cement and Concrete Research*, *27*(6), 845-852. https://doi.org/10.1016/S0008-8846(97)83277-2

Fujii, A. L., dos Reis Torres, D., de Oliveira Romano, R. C., Cincotto, M. A., & Pileggi, R. G. (2015). Impact of superplasticizer on the hardening of slag Portland cement blended with red mud. *Construction and Building Materials*, *101*, 432-439. https://doi.org/10.1016/j.conbuildmat.2015.10.057

Galao, O., Baeza, F. J., Zornoza, E., & Garcés, P. (2014). Strain and damage sensing properties on multifunctional cement composites with CNF admixture. *Cement and Concrete Composites*, *46*, 90-98. https://doi.org/10.1016/j.cemconcomp.2013.11.009

Garcia-Lodeiro, I., Palomo, A., Fernández-Jiménez, A., & Macphee, D. E. (2011). Compatibility studies between N-A-S-H and C-A-S-H gels. Study in the ternary diagram Na2O–CaO–Al2O3–SiO2–H2O. *Cement and Concrete Research*, *41*(9), 923-931. https://doi.org/10.1016/j.cemconres.2011.05.006

García-Macías, E., Castro-Triguero, R., Sáez, A., & Ubertini, F. (2018). 3D mixed micromechanics-FEM modeling of piezoresistive carbon nanotube smart concrete. *Computer Methods in Applied Mechanics and Engineering*, *340*, 396-423.

García-Macías, E., & Ubertini, F. (2019). Earthquake-induced damage detection and localization in masonry structures using smart bricks and Kriging strain reconstruction: A numerical study. *Earthquake Engineering & Structural Dynamics*, *48*(5), 548-569. https://doi.org/10.1002/eqe.3148

Ghalehnovi, M., Roshan, N., Hakak, E., Shamsabadi, E. A., & de Brito, J. (2019a). Effect of red mud (bauxite residue) as cement replacement on the properties of self-compacting concrete incorporating various fillers. *Journal of Cleaner Production*, *240*, 118213. https://doi.org/10.1016/j.jclepro.2019.118213

Ghalehnovi, M., Roshan, N., Hakak, E., Shamsabadi, E. A., & de Brito, J. (2019b). Effect of red mud (bauxite residue) as cement replacement on the properties of self-compacting concrete incorporating various fillers. *Journal of Cleaner Production*, *240*, 118213. https://doi.org/10.1016/j.jclepro.2019.118213

Goracci, G., Monasterio, M., Jansson, H., & Cerveny, S. (2017). Dynamics of nano-confined water in Portland cement-Comparison with synthetic CSH gel and other silicate materials. *Scientific reports*, *7*(1), 1-10.

Gräfe, M., Power, G., & Klauber, C. (2011). Bauxite residue issues: III. Alkalinity and associated chemistry. *Hydrometallurgy*, *108*(1-2), 60-79.

Granizo, M. L., & Blanco, M. T. (1998). Alkaline Activation of Metakaolin An Isothermal Conduction Calorimetry Study. *Journal of Thermal Analysis and Calorimetry*, *52*(3), 957-965. https://doi.org/10.1023/A:1010176321136

Greenwood, D. A. (1958). The Boltzmann Equation in the Theory of Electrical Conduction in Metals. *Proceedings of the Physical Society*, *71*(4), 585-596. https://doi.org/10.1088/0370-1328/71/4/306

Gu, H., Hargreaves, J. S. J., Jiang, J.-Q., & Rico, J. L. (2017). Potential Routes to Obtain Value-Added Iron-Containing Compounds from Red Mud. *Journal of Sustainable Metallurgy*, *3*(3), 561-569. https://doi.org/10.1007/s40831-016-0112-2

Gupta, S., Gonzalez, J. G., & Loh, K. J. (2017). Self-sensing concrete enabled by nano-engineered cement-aggregate interfaces. *Structural Health Monitoring*, *16*(3), 309-323. https://doi.org/10.1177/1475921716643867

Habert, G. (2014). 10 - Assessing the environmental impact of conventional and ‘green’ cement production. Dans F. Pacheco-Torgal, L. F. Cabeza, J. Labrincha, & A. de Magalhães (Éds), *Eco-efficient Construction and Building Materials* (pp. 199-238). (S.l.) : Woodhead Publishing. https://doi.org/10.1533/9780857097729.2.199

Habert, G., Miller, S. A., John, V. M., Provis, J. L., Favier, A., Horvath, A., & Scrivener, K. L. (2020). Environmental impacts and decarbonization strategies in the cement and concrete industries. *Nature Reviews Earth & Environment*, *1*(11), 559-573. https://doi.org/10.1038/s43017-020-0093-3

Habert, G., & Ouellet-Plamondon, C. M. (2016). Recent update on the environmental impact of geopolymers. *RILEM Technical Letters*, *1*, 17-23. https://doi.org/10.21809/rilemtechlett.2016.6

Hairi, S. N. Md., Jameson, G. N. L., Rogers, J. J., & MacKenzie, K. J. D. (2015). Synthesis and properties of inorganic polymers (geopolymers) derived from Bayer process residue (red mud) and bauxite. *Journal of Materials Science*, *50*(23), 7713-7724. https://doi.org/10.1007/s10853-015-9338-9

Hajimohammadi, A., & van Deventer, J. S. J. (2017). Solid Reactant-Based Geopolymers from Rice Hull Ash and Sodium Aluminate. *Waste and Biomass Valorization*, *8*(6), 2131-2140. https://doi.org/10.1007/s12649-016-9735-6

Hajjaji, W., Andrejkovičová, S., Zanelli, C., Alshaaer, M., Dondi, M., Labrincha, J. A., & Rocha, F. (2013). Composition and technological properties of geopolymers based on metakaolin and red mud. *Materials & Design (1980-2015)*, *52*, 648-654. https://doi.org/10.1016/j.matdes.2013.05.058

Han, B., Ding, S., & Yu, X. (2015). Intrinsic self-sensing concrete and structures: A review. *Measurement*, *59*, 110-128. https://doi.org/10.1016/j.measurement.2014.09.048

Han, B., Yu, X., & Kwon, E. (2009). A self-sensing carbon nanotube/cement composite for traffic monitoring. *Nanotechnology*, *20*(44), 445501. https://doi.org/10.1088/0957-4484/20/44/445501

Han, B., Zhang, K., Yu, X., Kwon, E., & Ou, J. (2011). Nickel particle-based self-sensing pavement for vehicle detection. *Measurement*, *44*(9), 1645-1650.

Han, B., Zhang, K., Yu, X., Kwon, E., & Ou, J. (2012). Fabrication of Piezoresistive CNT/CNF Cementitious Composites with Superplasticizer as Dispersant. *Journal of Materials in Civil Engineering*, *24*(6), 658-665. https://doi.org/10.1061/(ASCE)MT.1943-5533.0000435

Hanjitsuwan, S., Chindaprasirt, P., & Pimraksa, K. (2011). Electrical conductivity and dielectric property of fly ash geopolymer pastes. *International Journal of Minerals, Metallurgy, and Materials*, *18*(1), 94-99.

Hanjitsuwan, S., Hunpratub, S., Thongbai, P., Maensiri, S., Sata, V., & Chindaprasirt, P. (2014). Effects of NaOH concentrations on physical and electrical properties of high calcium fly ash geopolymer paste. *Cement and Concrete Composites*, *45*, 9-14. https://doi.org/10.1016/j.cemconcomp.2013.09.012

Hao, X. (2013). A review on the dielectric materials for high energy-storage application. *Journal of Advanced Dielectrics*, *03*(01), 1330001. https://doi.org/10.1142/S2010135X13300016

Hassan, A., Arif, M., & Shariq, M. (2019). Use of geopolymer concrete for a cleaner and sustainable environment – A review of mechanical properties and microstructure. *Journal of Cleaner Production*, *223*, 704-728. https://doi.org/10.1016/j.jclepro.2019.03.051

He, X., Zhu, Y., & Mo, Y. (2017). Origin of fast ion diffusion in super-ionic conductors. *Nature Communications*, *8*(1), 15893. https://doi.org/10.1038/ncomms15893

Hertel, T., Blanpain, B., & Pontikes, Y. (2016). A proposal for a 100% use of bauxite residue towards inorganic polymer mortar. *Journal of Sustainable Metallurgy*, *2*(4), 394-404.

Hertel, T., Iacobescu, R. I., Blanpain, B., & Pontikes, Y. (2016). Large-scale valorization of bauxite residue for inorganic polymers (pp. 199-209). Communication présentée au Proceedings of 34th International ICSOBA Conference.

Hertel, T., Novais, R. M., Murillo Alarcón, R., Labrincha, J. A., & Pontikes, Y. (2019). Use of modified bauxite residue-based porous inorganic polymer monoliths as adsorbents of methylene blue. *Journal of Cleaner Production*, *227*, 877-889. https://doi.org/10.1016/j.jclepro.2019.04.084

Hertel, T., & Pontikes, Y. (2020). Geopolymers, inorganic polymers, alkali-activated materials and hybrid binders from bauxite residue (red mud) – Putting things in perspective. *Journal of Cleaner Production*, *258*, 120610. https://doi.org/10.1016/j.jclepro.2020.120610

Hertel, T., Van den Bulck, A., Blanpain, B., & Pontikes, Y. (2022). Correlating the amorphous phase structure of vitrified bauxite residue (red mud) to the initial reactivity in binder systems. *Cement and Concrete Composites*, *127*, 104410. https://doi.org/10.1016/j.cemconcomp.2022.104410

Hewlett, P., & Liska, M. (2019). *Lea's chemistry of cement and concrete*. (S.l.) : Butterworth-Heinemann.

Hoffmann, K. (1974). *Applying the wheatstone bridge circuit*. (S.l.) : HBM Darmstadt, Germany.

Hosan, A., Haque, S., & Shaikh, F. (2016). Compressive behaviour of sodium and potassium activators synthetized fly ash geopolymer at elevated temperatures: A comparative study. *Journal of Building Engineering*, *8*, 123-130. https://doi.org/10.1016/j.jobe.2016.10.005

Hu, N., Bernsmeier, D., Grathoff, G. H., & Warr, L. N. (2017). The influence of alkali activator type, curing temperature and gibbsite on the geopolymerization of an interstratified illite-smectite rich clay from Friedland. *Applied Clay Science*, *135*, 386-393. https://doi.org/10.1016/j.clay.2016.10.021

Hu, W., Nie, Q., Huang, B., Shu, X., & He, Q. (2018). Mechanical and microstructural characterization of geopolymers derived from red mud and fly ashes. *Journal of cleaner production*, *186*, 799-806.

Hu, Y., Liang, S., Yang, J., Chen, Y., Ye, N., Ke, Y., … Hou, H. (2019). Role of Fe species in geopolymer synthesized from alkali-thermal pretreated Fe-rich Bayer red mud. *Construction and Building Materials*, *200*, 398-407.

Huang, T., & Sun, Z. (2021). Advances in multifunctional graphene-geopolymer composites. *Construction and Building Materials*, *272*, 121619. https://doi.org/10.1016/j.conbuildmat.2020.121619

Humad, A. M., Provis, J. L., & Cwirzen, A. (2017). Alkali activation of a high MgO GGBS – fresh and hardened properties. *Magazine of Concrete Research*, *70*(24), 1256-1264. https://doi.org/10.1680/jmacr.17.00436

Hunpratub, S., Phokha, S., Maensiri, S., & Chindaprasirt, P. (2015). Dielectric Properties of 0–3BCTZO/High Calcium Fly Ash Geopolymer Composites. *Ferroelectrics Letters Section*, *42*(4-6), 115-121. https://doi.org/10.1080/07315171.2015.1068967

IAI. (2020). *IAI Technology Roadmap for maximising the use of BR in cement*. International Aluminum Institute. Repéré à https://www.removal-project.com/iai-technology-roadmap-for-maximising-the-use-of-br-in-cement/

IAI. (2021). *Sustainable Bauxite Residue Management Guidance*. International Aluminum Institute.

Imerys. (2019, juillet). MetaStar 501HP Technical Data Sheet. IMERYS GmbH.

IPCC. (2006). *2006 IPCC Guidelines for National Greenhouse Gas Inventories*. Intergovernmental Panel on Climate Change. Repéré à https://www.ipcc.ch/report/2006-ipcc-guidelines-for-national-greenhouse-gas-inventories/

Jang, J. G., Lee, N., & Lee, H.-K. (2014). Fresh and hardened properties of alkali-activated fly ash/slag pastes with superplasticizers. *Construction and Building Materials*, *50*, 169-176.

Jesurani, S., Kanagesan, S., Velmurugan, R., & Kalaivani, T. (2012). Phase formation and high dielectric constant of calcium copper titanate using sol–gel route. *Journal of Materials Science: Materials in Electronics*, *23*(3), 668-674. https://doi.org/10.1007/s10854-011-0468-9

Jiao, X., Zhang, Y., & Chen, T. (2013). Thermal stability of a silica-rich vanadium tailing based geopolymer. *Construction and Building Materials*, *38*, 43-47. https://doi.org/10.1016/j.conbuildmat.2012.06.076

Jiwei, Z., Xi, Y., Xiaogang, C., Liangying, Z., & Chen, H. (2002). Direct-current field dependence of dielectric properties in B2O3-SiO2 glass doped Ba0. 6Sr0. 4TiO3 ceramics. *Journal of materials science*, *37*(17), 3739-3745.

Jonscher, A. K. (1977). The 'universal' dielectric response. *Nature*, *267*(5613), 673-679. https://doi.org/10.1038/267673a0

Jonscher, A. K. (1981). A new understanding of the dielectric relaxation of solids. *Journal of Materials Science*, *16*(8), 2037-2060. https://doi.org/10.1007/BF00542364

Joyce, P. J., & Björklund, A. (2019). Using Life Cycle Thinking to Assess the Sustainability Benefits of Complex Valorization Pathways for Bauxite Residue. *Journal of Sustainable Metallurgy*, *5*(1), 69-84. https://doi.org/10.1007/s40831-019-00209-x

Joyce, P. J., Hertel, T., Goronovski, A., Tkaczyk, A. H., Pontikes, Y., & Björklund, A. (2018). Identifying hotspots of environmental impact in the development of novel inorganic polymer paving blocks from bauxite residue. *Resources, Conservation and Recycling*, *138*, 87-98. https://doi.org/10.1016/j.resconrec.2018.07.006

Juenger, M. C. G., & Siddique, R. (2015). Recent advances in understanding the role of supplementary cementitious materials in concrete. *Cement and Concrete Research*, *78*, 71-80. https://doi.org/10.1016/j.cemconres.2015.03.018

Kamseu, E., Nait-Ali, B., Bignozzi, M. C., Leonelli, C., Rossignol, S., & Smith, D. S. (2012). Bulk composition and microstructure dependence of effective thermal conductivity of porous inorganic polymer cements. *Journal of the European Ceramic Society*, *32*(8), 1593-1603. https://doi.org/10.1016/j.jeurceramsoc.2011.12.030

Kaußen, F. M., & Friedrich, B. (2016). Methods for Alkaline Recovery of Aluminum from Bauxite Residue. *Journal of Sustainable Metallurgy*, *2*(4), 353-364. https://doi.org/10.1007/s40831-016-0059-3

Ke, X., Bernal, S. A., Hussein, O. H., & Provis, J. L. (2017). Chloride binding and mobility in sodium carbonate-activated slag pastes and mortars. *Materials and Structures*, *50*(6), 252. https://doi.org/10.1617/s11527-017-1121-8

Ke, X., Bernal, S. A., & Provis, J. L. (2016). Controlling the reaction kinetics of sodium carbonate-activated slag cements using calcined layered double hydroxides. *Cement and Concrete Research*, *81*, 24-37. https://doi.org/10.1016/j.cemconres.2015.11.012

Ke, X., Bernal, S. A., & Provis, J. L. (2017). Uptake of chloride and carbonate by Mg-Al and Ca-Al layered double hydroxides in simulated pore solutions of alkali-activated slag cement. *Cement and Concrete Research*, *100*, 1-13. https://doi.org/10.1016/j.cemconres.2017.05.015

Ke, X., Bernal, S. A., Ye, N., Provis, J. L., & Yang, J. (2015). One-Part Geopolymers Based on Thermally Treated Red Mud/NaOH Blends. *Journal of the American Ceramic Society*, *98*(1), 5-11. https://doi.org/10.1111/jace.13231

Keyte, L. M., Lukey, G. C., & van Deventer, J. S. (2005). The effect of coal ash glass chemistry on the tailored design of waste-based geopolymeric products (pp. 17-20). Communication présentée au CD-ROM Proceedings of WasteEng2005 International Conference, Albi, France.

Khalid, H. R., Lee, N. K., Park, S. M., Abbas, N., & Lee, H. K. (2018). Synthesis of geopolymer-supported zeolites via robust one-step method and their adsorption potential. *Journal of Hazardous Materials*, *353*, 522-533. https://doi.org/10.1016/j.jhazmat.2018.04.049

Kiesow, I., Marczewski, D., Reinhardt, L., Mühlmann, M., Possiwan, M., & Goedel, W. A. (2013). Bicontinuous Zeolite Polymer Composite Membranes Prepared via Float Casting. *Journal of the American Chemical Society*, *135*(11), 4380-4388. https://doi.org/10.1021/ja311785f

Kim, J., Kim, S., Yang, Y., & Ohshima, K. (2005). Crystallization and dielectric properties of 2SrTiO 3-SiO 2 glass. *Journal of the Korean Physical Society*, *46*(1), 163-166.

Klauber, C., Gräfe, M., & Power, G. (2011). Bauxite residue issues: II. options for residue utilization. *Hydrometallurgy*, *108*(1), 11-32. https://doi.org/10.1016/j.hydromet.2011.02.007

Kokubo, T. (1970). Crystallization of BaO• TiO-Si0_2-Al_2 0_3 Glasses and Dielectric Properties of their Crystallized Products. *Bulletin of the Institute for Chemical Research, Kyoto University*, *47*(6), 572-583.

Kokubo, T., Kung, C., & Tashiro, M. (1968). 14. Preparation of Thin Films of BaTiO3 Glass Ceramics and Their Dielectric Properties.

Kovtun, M., Kearsley, E. P., & Shekhovtsova, J. (2015). Chemical acceleration of a neutral granulated blast-furnace slag activated by sodium carbonate. *Cement and Concrete Research*, *72*, 1-9. https://doi.org/10.1016/j.cemconres.2015.02.014

Kriven, W. M., Bell, J. L., & Gordon, M. (2003). Microstructure and microchemistry of fully-reacted geopolymers and geopolymer matrix composites. *Ceramic Transactions*, *153*(1994).

Kubo, R. (1957). Statistical-Mechanical Theory of Irreversible Processes. I. General Theory and Simple Applications to Magnetic and Conduction Problems. *Journal of the Physical Society of Japan*, *12*(6), 570-586. https://doi.org/10.1143/JPSJ.12.570

Kumar, A., & Kumar, S. (2013). Development of paving blocks from synergistic use of red mud and fly ash using geopolymerization. *Construction and Building Materials*, *38*, 865-871. https://doi.org/10.1016/j.conbuildmat.2012.09.013

Kumar, S., García-Triñanes, P., Teixeira-Pinto, A., & Bao, M. (2013). Development of alkali activated cement from mechanically activated silico-manganese (SiMn) slag. *Cement and Concrete Composites*, *40*, 7-13. https://doi.org/10.1016/j.cemconcomp.2013.03.026

Lamuta, C., Bruno, L., Candamano, S., & Pagnotta, L. (2017). Piezoresistive characterization of graphene/metakaolin based geopolymeric mortar composites. *MRS Advances*, *2*(61), 3773-3779. https://doi.org/10.1557/adv.2017.595

Lamuta, Caterina, Candamano, S., Crea, F., & Pagnotta, L. (2016). Direct piezoelectric effect in geopolymeric mortars. *Materials & Design*, *107*, 57-64.

Lassinantti Gualtieri, M., Cavallini, A., & Romagnoli, M. (2016). Interactive powder mixture concept for the preparation of geopolymers with fine porosity. *Journal of the European Ceramic Society*, *36*(10), 2641-2646. https://doi.org/10.1016/j.jeurceramsoc.2016.03.030

Lee, K.-M., Choi, S., Choo, J. F., Choi, Y.-C., & Yoo, S.-W. (2017, 20 juillet). Flexural and Shear Behaviors of Reinforced Alkali-Activated Slag Concrete Beams. *Advances in Materials Science and Engineering*. [Research Article], Hindawi. https://doi.org/10.1155/2017/5294290

Lee, W. K. W., & van Deventer, J. S. J. (2002). The effect of ionic contaminants on the early-age properties of alkali-activated fly ash-based cements. *Cement and Concrete Research*, *32*(4), 577-584. https://doi.org/10.1016/S0008-8846(01)00724-4

Lee, W. K. W., & van Deventer, J. S. J. (2003). Use of Infrared Spectroscopy to Study Geopolymerization of Heterogeneous Amorphous Aluminosilicates. *Langmuir*, *19*(21), 8726-8734. https://doi.org/10.1021/la026127e

Lemougna, P. N., Wang, K., Tang, Q., & Cui, X. (2017). Synthesis and characterization of low temperature (<800°C) ceramics from red mud geopolymer precursor. *Construction and Building Materials*, *131*, 564-573. https://doi.org/10.1016/j.conbuildmat.2016.11.108

Li, G. Y., Wang, P. M., & Zhao, X. (2007). Pressure-sensitive properties and microstructure of carbon nanotube reinforced cement composites. *Cement and Concrete Composites*, *29*(5), 377-382.

Li, H., Xiao, H., & Ou, J. (2008). Electrical property of cement-based composites filled with carbon black under long-term wet and loading condition. *Composites Science and Technology*, *68*(9), 2114-2119. https://doi.org/10.1016/j.compscitech.2008.03.007

Li, N., Shi, C., & Zhang, Z. (2019). Understanding the roles of activators towards setting and hardening control of alkali-activated slag cement. *Composites Part B: Engineering*, *171*, 34-45. https://doi.org/10.1016/j.compositesb.2019.04.024

Li, W., Dong, W., Guo, Y., Wang, K., & Shah, S. P. (2022). Advances in multifunctional cementitious composites with conductive carbon nanomaterials for smart infrastructure. *Cement and Concrete Composites*, *128*, 104454. https://doi.org/10.1016/j.cemconcomp.2022.104454

Li, W., Qu, F., Dong, W., Mishra, G., & Shah, S. P. (2022). A comprehensive review on self-sensing graphene/cementitious composites: A pathway toward next-generation smart concrete. *Construction and Building Materials*, *331*, 127284. https://doi.org/10.1016/j.conbuildmat.2022.127284

Li, Yongchao, Huang, H., Xu, Z., Ma, H., & Guo, Y. (2020). Mechanism study on manganese(II) removal from acid mine wastewater using red mud and its application to a lab-scale column. *Journal of Cleaner Production*, *253*, 119955. https://doi.org/10.1016/j.jclepro.2020.119955

Li, Yuancheng, Min, X., Ke, Y., Liu, D., & Tang, C. (2019). Preparation of red mud-based geopolymer materials from MSWI fly ash and red mud by mechanical activation. *Waste Management*, *83*, 202-208. https://doi.org/10.1016/j.wasman.2018.11.019

Liguori, B., Aprea, P., Roviello, G., & Ferone, C. (2019). Self-supporting zeolites by Geopolymer Gel Conversion (GGC). *Microporous and Mesoporous Materials*, *286*, 125-132. https://doi.org/10.1016/j.micromeso.2019.05.045

Liu, C., Liu, G., Ge, Z., Guan, Y., Cui, Z., & Zhou, J. (2019). Mechanical and Self-Sensing Properties of Multiwalled Carbon Nanotube-Reinforced ECCs. *Advances in Materials Science and Engineering*, *2019*.

Liu, J., Fu, J., Yang, Y., & Gu, C. (2019). Study on dispersion, mechanical and microstructure properties of cement paste incorporating graphene sheets. *Construction and Building Materials*, *199*, 1-11. https://doi.org/10.1016/j.conbuildmat.2018.12.006

Liu, R.-X., & Poon, C.-S. (2016). Utilization of red mud derived from bauxite in self-compacting concrete. *Journal of Cleaner Production*, *112*, 384-391. https://doi.org/10.1016/j.jclepro.2015.09.049

Liu, S., Shen, B., Hao, H., & Zhai, J. (2019). Glass–ceramic dielectric materials with high energy density and ultra-fast discharge speed for high power energy storage applications. *Journal of Materials Chemistry C*, *7*(48), 15118-15135. https://doi.org/10.1039/C9TC05253D

Liu, X., & Zhang, N. (2011). Utilization of red mud in cement production: a review. *Waste Management & Research*, *29*(10), 1053-1063. https://doi.org/10.1177/0734242X11407653

Liu, X., Zhang, N., Sun, H., Zhang, J., & Li, L. (2011). Structural investigation relating to the cementitious activity of bauxite residue — Red mud. *Cement and Concrete Research*, *41*(8), 847-853. https://doi.org/10.1016/j.cemconres.2011.04.004

Liu, Y., Lin, C., & Wu, Y. (2007). Characterization of red mud derived from a combined Bayer Process and bauxite calcination method. *Journal of Hazardous Materials*, *146*(1), 255-261. https://doi.org/10.1016/j.jhazmat.2006.12.015

Lothenbach, B., Scrivener, K., & Hooton, R. D. (2011). Supplementary cementitious materials. *Cement and Concrete Research*, *41*(12), 1244-1256. https://doi.org/10.1016/j.cemconres.2010.12.001

Lu, Y., & Li, Z. (2011). Frequency characteristic analysis on acoustic emission of mortar using cement-based piezoelectric sensors. *Smart Structures and Systems*, *8*(3), 321-341. https://doi.org/10.12989/SSS.2011.8.3.321

Lu, Y., Zhang, J., Li, Z., & Dong, B. (2013). Corrosion monitoring of reinforced concrete beam using embedded cement-based piezoelectric sensor. *Magazine of Concrete Research*, *65*(21), 1265-1276. https://doi.org/10.1680/macr.13.00071

Luukkonen, T., Abdollahnejad, Z., Yliniemi, J., Kinnunen, P., & Illikainen, M. (2018). One-part alkali-activated materials: A review. *Cement and Concrete Research*, *103*, 21-34. https://doi.org/10.1016/j.cemconres.2017.10.001

Ma, Y., Liu, W., Hu, J., Fu, J., Zhang, Z., & Wang, H. (2020). Optimization on the piezoresistivity of alkali-activated fly ash/slag mortar by using conductive aggregates and carbon fibers. *Cement and Concrete Composites*, *114*, 103735. https://doi.org/10.1016/j.cemconcomp.2020.103735

Malkawi, A. B., Al-Mattarneh, H., Achara, B. E., Mohammed, B. S., & Nuruddin, M. F. (2018). Dielectric properties for characterization of fly ash-based geopolymer binders. *Construction and Building Materials*, *189*, 19-32. https://doi.org/10.1016/j.conbuildmat.2018.08.180

Marsh, A., Heath, A., Patureau, P., Evernden, M., & Walker, P. (2018). Alkali activation behaviour of un-calcined montmorillonite and illite clay minerals. *Applied Clay Science*, *166*, 250-261.

Mehta, A., & Siddique, R. (2016). An overview of geopolymers derived from industrial by-products. *Construction and Building Materials*, *127*, 183-198. https://doi.org/10.1016/j.conbuildmat.2016.09.136

Meng, Q., & Chung, D. D. L. (2010). Battery in the form of a cement-matrix composite. *Cement and Concrete Composites*, *32*(10), 829-839. https://doi.org/10.1016/j.cemconcomp.2010.08.009

Meral, C., Benmore, C. J., & Monteiro, P. J. M. (2011). The study of disorder and nanocrystallinity in C–S–H, supplementary cementitious materials and geopolymers using pair distribution function analysis. *Cement and Concrete Research*, *41*(7), 696-710. https://doi.org/10.1016/j.cemconres.2011.03.027

Mizerová, C., Rovnaník, P., Kusák, I., & Schmid, P. (2021). Self-sensing performance of metakaolin geopolymer with carbon nanotubes subjected to repeated compressive loading. *IOP Conference Series: Materials Science and Engineering*, *1209*(1), 012043. https://doi.org/10.1088/1757-899X/1209/1/012043

Mizerová, Cecílie, Kusák, I., Topolář, L., Schmid, P., & Rovnaník, P. (2021). Self-Sensing Properties of Fly Ash Geopolymer Doped with Carbon Black under Compression. *Materials*, *14*(16), 4350. https://doi.org/10.3390/ma14164350

Mobasher, N., Bernal, S. A., & Provis, J. L. (2016). Structural evolution of an alkali sulfate activated slag cement. *Journal of Nuclear Materials*, *468*, 97-104. https://doi.org/10.1016/j.jnucmat.2015.11.016

Mun Jae-Sung, Yang Keun-Hyeok, & Kim Si-Jun. (2016). Tests on the Compressive Fatigue Performance of Various Concretes. *Journal of Materials in Civil Engineering*, *28*(10), 04016099. https://doi.org/10.1061/(ASCE)MT.1943-5533.0001612

Myers, R. J., Bernal, S. A., San Nicolas, R., & Provis, J. L. (2013). Generalized Structural Description of Calcium–Sodium Aluminosilicate Hydrate Gels: The Cross-Linked Substituted Tobermorite Model. *Langmuir*, *29*(17), 5294-5306. https://doi.org/10.1021/la4000473

Nalon, G. H., Santos, R. F., Lima, G. E. S. de, Andrade, I. K. R., Pedroti, L. G., Ribeiro, J. C. L., & Franco de Carvalho, J. M. (2022). Recycling waste materials to produce self-sensing concretes for smart and sustainable structures: A review. *Construction and Building Materials*, *325*, 126658. https://doi.org/10.1016/j.conbuildmat.2022.126658

Nath, P., & Sarker, P. K. (2016). Fracture properties of GGBFS-blended fly ash geopolymer concrete cured in ambient temperature. *Materials and Structures*, *50*(1), 32. https://doi.org/10.1617/s11527-016-0893-6

Nattrodt Monteiro, V., Brial, V., & Ouellet-Plamondon, C. (2020). Bauxite residue in the cement industry: a calculation tool. Dans *Proceedings of the 3rd International Bauxite Residue Valorisation and Best Practices Conference, BR2020, October 2020*.

Nava Quintero, R. J., Guillemet, S., Aguilar-Garib, J. A., Reyes Melo, M. E., & Durand, B. (2012). The thickness of BaTiO3 tape castings as function of the slip system. *Journal of Ceramic Processing Research*, *13*(2), 101-104.

Nguyen, H. T., Bui, T. H., Pham, V. T. H. Q., Do, M. Q., Hoang, M. D., & Le, V. Q. (2018). Leaching Behavior and Immobilization of Heavy Metals in Geopolymer Synthesized from Red Mud and Fly Ash. *Key Engineering Materials*, *777*, 518-522. https://doi.org/10.4028/www.scientific.net/KEM.777.518

Nikbin, I. M., Aliaghazadeh, M., Sh Charkhtab, & Fathollahpour, A. (2018). Environmental impacts and mechanical properties of lightweight concrete containing bauxite residue (red mud). *Journal of Cleaner Production*, *172*, 2683-2694. https://doi.org/10.1016/j.jclepro.2017.11.143

Noushini, A., Aslani, F., Castel, A., Gilbert, R. I., Uy, B., & Foster, S. (2016). Compressive stress-strain model for low-calcium fly ash-based geopolymer and heat-cured Portland cement concrete. *Cement and Concrete Composites*, *73*, 136-146. https://doi.org/10.1016/j.cemconcomp.2016.07.004

Ouellet-Plamondon, C., & Habert, G. (2015). 25 - Life cycle assessment (LCA) of alkali-activated cements and concretes. Dans F. Pacheco-Torgal, J. A. Labrincha, C.

Leonelli, A. Palomo, & P. Chindaprasirt (Éds), *Handbook of Alkali-Activated Cements, Mortars and Concretes* (pp. 663-686). Oxford : Woodhead Publishing. https://doi.org/10.1533/9781782422884.5.663

Papanikolaou, I., Arena, N., & Al-Tabbaa, A. (2019). Graphene nanoplatelet reinforced concrete for self-sensing structures – A lifecycle assessment perspective. *Journal of Cleaner Production*, *240*, 118202. https://doi.org/10.1016/j.jclepro.2019.118202

Part, W. K., Ramli, M., & Cheah, C. B. (2015). An overview on the influence of various factors on the properties of geopolymer concrete derived from industrial by-products. *Construction and Building Materials*, *77*, 370-395. https://doi.org/10.1016/j.conbuildmat.2014.12.065

Pascual, A. B., Tognonvi, M. T., & Tagnit-Hamou, A. (2014). Waste glass powder-based alkali-activated mortar. *International journal of Research in Engineering and Technology*, *3*(13), 15-19.

Perera, D. S., Nicholson, C. L., Blackford, M. G., Fletcher, R. A., & Trautman, R. L. (2004). Geopolymers Made Using New Zealand Flyash. *Journal of the Ceramic Society of Japan, Supplement*, *112*, S108-S111. https://doi.org/10.14852/jcersjsuppl.112.0.S108.0

Perry, M., Saafi, M., Fusiek, G., & Niewczas, P. (2015). Hybrid optical-fibre/geopolymer sensors for structural health monitoring of concrete structures. *Smart Materials and Structures*, *24*(4), 045011. https://doi.org/10.1088/0964-1726/24/4/045011

Pontikes, Y., & Angelopoulos, G. N. (2013). Bauxite residue in cement and cementitious applications: Current status and a possible way forward. *Resources, Conservation and Recycling*, *73*, 53-63. https://doi.org/10.1016/j.resconrec.2013.01.005

Pontikes, Y., Rathossi, C., Nikolopoulos, P., Angelopoulos, G. N., Jayaseelan, D. D., & Lee, W. E. (2009). Effect of firing temperature and atmosphere on sintering of ceramics made from Bayer process bauxite residue. *Ceramics International*, *35*(1), 401-407. https://doi.org/10.1016/j.ceramint.2007.11.013

Poraver. (2019, novembre). Metapor Specifications and Technical Information. Poraver North America.

Power, G., Gräfe, M., & Klauber, C. (2011). Bauxite residue issues: I. Current management, disposal and storage practices. *Hydrometallurgy*, *108*(1), 33-45. https://doi.org/10.1016/j.hydromet.2011.02.006

Provis, J. L., Arbi, K., Bernal, S. A., Bondar, D., Buchwald, A., Castel, A., … Zuo, Y. (2019). RILEM TC 247-DTA round robin test: mix design and reproducibility of compressive strength of alkali-activated concretes. *Materials and Structures*, *52*(5), 99. https://doi.org/10.1617/s11527-019-1396-z

Provis, J. L., Palomo, A., & Shi, C. (2015). Advances in understanding alkali-activated materials. *Cement and Concrete Research*, *78*, 110-125. https://doi.org/10.1016/j.cemconres.2015.04.013

Provis, J. L., & Van Deventer, J. S. J. (2009). *Geopolymers: structures, processing, properties and industrial applications*. (S.l.) : Elsevier.

Puertas, F., Palacios, M., Manzano, H., Dolado, J. S., Rico, A., & Rodríguez, J. (2011). A model for the C-A-S-H gel formed in alkali-activated slag cements. *Journal of the European Ceramic Society*, *31*(12), 2043-2056. https://doi.org/10.1016/j.jeurceramsoc.2011.04.036

QC MELCC. (2012, 7 décembre). Protocole de lixiviation pour les espèces inorganiques CTEU-9. Ministère de l'Environnement et de la Lutte contre les changements climatiques. Repéré à https://www.ceaeq.gouv.qc.ca/methodes/pdf/MA100Lixcom11.pdf

Qi, X., Wang, H., Huang, C., Zhang, L., Zhang, J., Xu, B., … Araruna, J. T. (2018). Analysis of bauxite residue components responsible for copper removal and related reaction products. *Chemosphere*, *207*, 209-217. https://doi.org/10.1016/j.chemosphere.2018.05.041

Quebec. (2021, mai). Guide d'intervention - Protection des sols et réhabilitation des terrains contaminés, Annexe 7 : Grille des critères de qualité des eaux souterraines. Ministère de l'Environnement et de la Lutte contre les changements climatiques. Repéré à https://www.environnement.gouv.qc.ca/sol/terrains/guide-intervention/

Rahaman, M. N. (2017). *Ceramic Processing and Sintering* (2e éd.). Boca Raton : CRC Press. https://doi.org/10.1201/9781315274126

Rai, S., Bahadure, S., Chaddha, M. J., & Agnihotri, A. (2020). Disposal Practices and Utilization of Red Mud (Bauxite Residue): A Review in Indian Context and Abroad. *Journal of Sustainable Metallurgy*, *6*(1), 1-8. https://doi.org/10.1007/s40831-019-00247-5

Rai, U. S., Singh, L., Mandal, K. D., & Singh, N. B. (2014). An Overview on Recent Developments in the Synthesis, Characterization and Properties of High Dielectric Constant Calcium Copper Titanate Nano-Particles, 18.

Rathod, R. R., Suryawanshi, N. T., & Memade, P. D. (2013). Evaluation of the properties of red mud concrete. *IOSR Journal of Mechanical and Civil Engineering*, 2278-1684.

Reddy, P. N., Kavyateja, B. V., & Jindal, B. B. (2021). Structural health monitoring methods, dispersion of fibers, micro and macro structural properties, sensing, and mechanical properties of self-sensing concrete—A review. *Structural Concrete*, *22*(2), 793-805. https://doi.org/10.1002/suco.202000337

Rees, C. A., Provis, J. L., Lukey, G. C., & van Deventer, J. S. J. (2007). In Situ ATR-FTIR Study of the Early Stages of Fly Ash Geopolymer Gel Formation. *Langmuir*, *23*(17), 9076-9082. https://doi.org/10.1021/la701185g

Rehman, S. K. U., Ibrahim, Z., Memon, S. A., Javed, M. F., & Khushnood, R. A. (2017). A sustainable graphene based cement composite. *Sustainability*, *9*(7), 1229.

Reza, F., Batson, G. B., Yamamuro, J. A., & Lee, J. S. (2003). Resistance changes during compression of carbon fiber cement composites. *Journal of materials in civil engineering*, *15*(5), 476-483.

Reza, F., Yamamuro, J. A., & Batson, G. B. (2004). Electrical resistance change in compact tension specimens of carbon fiber cement composites. *Cement and Concrete Composites*, *26*(7), 873-881.

Rhim, S. M., Hong, S., Bak, H., & Kim, O. K. (2000). Effects of B2O3 addition on the dielectric and ferroelectric properties of Ba0. 7Sr0. 3TiO3 ceramics. *Journal of the American Ceramic Society*, *83*(5), 1145-1148.

Romano, R. C. O., Bernardo, H. M., Maciel, M. H., Pileggi, R. G., & Cincotto, M. A. (2018). Hydration of Portland cement with red mud as mineral addition. *Journal of Thermal*

Analysis and Calorimetry, *131*(3), 2477-2490. https://doi.org/10.1007/s10973-017-6794-2

Rovnaník, P., Kusák, I., Bayer, P., Schmid, P., & Fiala, L. (2019). Comparison of electrical and self-sensing properties of Portland cement and alkali-activated slag mortars. *Cement and Concrete Research*, *118*, 84-91. https://doi.org/10.1016/j.cemconres.2019.02.009

Rowles, M., & O'connor, B. (2003). Chemical optimisation of the compressive strength of aluminosilicate geopolymers synthesised by sodium silicate activation of metakaolinite. *Journal of materials chemistry*, *13*(5), 1161-1165.

Saafi, M., Gullane, A., Huang, B., Sadeghi, H., Ye, J., & Sadeghi, F. (2018). Inherently multifunctional geopolymeric cementitious composite as electrical energy storage and self-sensing structural material. *Composite Structures*, *201*, 766-778. https://doi.org/10.1016/j.compstruct.2018.06.101

Saafi, Mohamed, Tang, L., Fung, J., Rahman, M., Sillars, F., Liggat, J., & Zhou, X. (2014). Graphene/fly ash geopolymeric composites as self-sensing structural materials. *Smart Materials and Structures*, *23*(6), 065006. https://doi.org/10.1088/0964-1726/23/6/065006

Sadat, M. R., Bringuier, S., Asaduzzaman, A., Muralidharan, K., & Zhang, L. (2016). A molecular dynamics study of the role of molecular water on the structure and mechanics of amorphous geopolymer binders. *The Journal of Chemical Physics*, *145*(13), 134706. https://doi.org/10.1063/1.4964301

San Nicolas, R., & Provis, J. L. (2015). The Interfacial Transition Zone in Alkali-Activated Slag Mortars. *Frontiers in Materials*, *2*. https://doi.org/10.3389/fmats.2015.00070

Sapna, B. T., & Aravindhraj, M. (2018). INFLUENCE OF RED MUD AS A PARTIAL REPLACEMENT OF CEMENT WITH HYDRATED LIME, *05*(08), 8.

Sarkar, C., Basu, J. K., & Samanta, A. N. (2017). Removal of Ni2+ ion from waste water by Geopolymeric Adsorbent derived from LD Slag. *Journal of Water Process Engineering*, *17*, 237-244. https://doi.org/10.1016/j.jwpe.2017.04.012

Sathonsaowaphak, A., Chindaprasirt, P., & Pimraksa, K. (2009). Workability and strength of lignite bottom ash geopolymer mortar. *Journal of Hazardous Materials*, *168*(1), 44-50. https://doi.org/10.1016/j.jhazmat.2009.01.120

Sazama, P., Bortnovsky, O., Dědeček, J., Tvarůžková, Z., & Sobalík, Z. (2011). Geopolymer based catalysts—New group of catalytic materials. *Catalysis Today*, *164*(1), 92-99. https://doi.org/10.1016/j.cattod.2010.09.008

Shankar, J., & Deshpande, V. (2011). Electrical and thermal properties of lead titanate glass ceramics. *Physica B: Condensed Matter*, *406*(3), 588-592.

Shi, C., & Day, R. L. (1995). A calorimetric study of early hydration of alkali-slag cements. *Cement and Concrete Research*, *25*(6), 1333-1346. https://doi.org/10.1016/0008-8846(95)00126-W

Shi, C., Qu, B., & Provis, J. L. (2019). Recent progress in low-carbon binders. *Cement and Concrete Research*, *122*, 227-250. https://doi.org/10.1016/j.cemconres.2019.05.009

Sooksaen, P., Reaney, I. M., & Sinclair, D. C. (2007). Crystallization and dielectric properties of borate-based ferroelectric PbTiO3 glass-ceramics. *Journal of electroceramics*, *19*(2), 221-228.

Stallard, R. D., & Amis, E. S. (1952). Heat of vaporization and other properties of dioxane, water and their mixtures. *Journal of the American Chemical Society*, *74*(7), 1781-1790.

Sturm, P., Greiser, S., Gluth, G. J. G., Jäger, C., & Brouwers, H. J. H. (2015). Degree of reaction and phase content of silica-based one-part geopolymers investigated using chemical and NMR spectroscopic methods. *Journal of Materials Science*, *50*(20), 6768-6778. https://doi.org/10.1007/s10853-015-9232-5

Sun, M., Liu, Q., Li, Z., & Hu, Y. (2000). A study of piezoelectric properties of carbon fiber reinforced concrete and plain cement paste during dynamic loading. *Cement and Concrete Research*, *30*(10), 1593-1595.

Suwan, T., & Fan, M. (2017). Effect of manufacturing process on the mechanisms and mechanical properties of fly ash-based geopolymer in ambient curing temperature. *Materials and Manufacturing Processes*, *32*(5), 461-467.

Tang, Q., Ge, Y., Wang, K., He, Y., & Cui, X. (2015). Preparation and characterization of porous metakaolin-based inorganic polymer spheres as an adsorbent. *Materials & Design*, *88*, 1244-1249. https://doi.org/10.1016/j.matdes.2015.09.126

Tang, W. C., Wang, Z., Donne, S. W., Forghani, M., & Liu, Y. (2019). Influence of red mud on mechanical and durability performance of self-compacting concrete. *Journal of Hazardous Materials*, *379*, 120802. https://doi.org/10.1016/j.jhazmat.2019.120802

Tang, Z., Li, W., Hu, Y., Zhou, J. L., & Tam, V. W. Y. (2019). Review on designs and properties of multifunctional alkali-activated materials (AAMs). *Construction and Building Materials*, *200*, 474-489. https://doi.org/10.1016/j.conbuildmat.2018.12.157

Taylor, H. F. W. (1989). Modification of the Bogue calculation. *Advances in Cement Research*, *2*(6), 73-77. https://doi.org/10.1680/adcr.1989.2.6.73

Tchakouté, H. K., Rüscher, C. H., Kong, S., Kamseu, E., & Leonelli, C. (2016). Geopolymer binders from metakaolin using sodium waterglass from waste glass and rice husk ash as alternative activators: A comparative study. *Construction and Building Materials*, *114*, 276-289. https://doi.org/10.1016/j.conbuildmat.2016.03.184

Thomas, R. J., & Peethamparan, S. (2015). Alkali-activated concrete: Engineering properties and stress–strain behavior. *Construction and Building Materials*, *93*, 49-56. https://doi.org/10.1016/j.conbuildmat.2015.04.039

Tian, Z., Li, Y., Zheng, J., & Wang, S. (2019). A state-of-the-art on self-sensing concrete: Materials, fabrication and properties. *Composites Part B: Engineering*, *177*, 107437. https://doi.org/10.1016/j.compositesb.2019.107437

Tok, A. I. Y., Boey, F. Y. C., & Lam, Y. C. (2000). Non-Newtonian fluid flow model for ceramic tape casting. *Materials Science and Engineering: A*, *280*(2), 282-288. https://doi.org/10.1016/S0921-5093(99)00691-7

Topçu, İ. B., & Toprak, M. U. (2011). Properties of geopolymer from circulating fluidized bed combustion coal bottom ash. *Materials Science and Engineering: A*, *528*(3), 1472-1477. https://doi.org/10.1016/j.msea.2010.10.062

Tsakiridis, P. E., Agatzini-Leonardou, S., & Oustadakis, P. (2004). Red mud addition in the raw meal for the production of Portland cement clinker. *Journal of Hazardous Materials*, *116*(1), 103-110. https://doi.org/10.1016/j.jhazmat.2004.08.002

Ujaczki, É., Courtney, R., Cusack, P., Krishna Chinnam, R., Clifford, S., Curtin, T., & O'Donoghue, L. (2019). Recovery of Gallium from Bauxite Residue Using Combined Oxalic Acid Leaching with Adsorption onto Zeolite HY. *Journal of Sustainable Metallurgy*, *5*(2), 262-274. https://doi.org/10.1007/s40831-019-00226-w

US EPA. (2015a, 8 décembre). SW-846 Test Method 1311: Toxicity Characteristic Leaching Procedure. U.S. Environmental Protection Agency, Washington, DC. Repéré à https://www.epa.gov/hw-sw846/sw-846-test-method-1311-toxicity-characteristic-leaching-procedure

US EPA, O. (2015b). *Green House Gas Emission Factors Hub*. United States EnvironmentalProtection Agency. Repéré à https://www.epa.gov/climateleadership/ghg-emission-factors-hub

Vaidya, S., & Allouche, E. (2011). Experimental evaluation of electrical conductivity of carbon fiber reinforced fly-ash based geopolymer. *Smart Structures and Systems*, *7*, 27-40.

Valencia Saavedra, W. G., & Mejía de Gutiérrez, R. (2017). Performance of geopolymer concrete composed of fly ash after exposure to elevated temperatures. *Construction and Building Materials*, *154*, 229-235. https://doi.org/10.1016/j.conbuildmat.2017.07.208

Vance, E. R., & Perera, D. S. (2009). 18 - Geopolymers for nuclear waste immobilisation. Dans J. L. Provis & J. S. J. van Deventer (Éds), *Geopolymers* (pp. 401-420). (S.l.) : Woodhead Publishing. https://doi.org/10.1533/9781845696382.3.401

van Deventer, J. S. J., Provis, J. L., Duxson, P., & Lukey, G. C. (2007). Reaction mechanisms in the geopolymeric conversion of inorganic waste to useful products. *Journal of Hazardous Materials*, *139*(3), 506-513. https://doi.org/10.1016/j.jhazmat.2006.02.044

Venkatesh, C., Chand, M. S. R., & Nerella, R. (2019). A state of the art on red mud as a substitutional cementitious material. *Ann. de Chimie: Sci. des Materiaux*, *43*(2), 99-106.

Venkatesh, C., Nerella, R., & Chand, M. S. R. (2020). Role of red mud as a cementing material in concrete: a comprehensive study on durability behavior. *Innovative Infrastructure Solutions*, *6*(1), 13. https://doi.org/10.1007/s41062-020-00371-2

Venkatesh, C., Ruben, N., & Chand, M. S. R. (2020). Red mud as an additive in concrete: comprehensive characterization. *Journal of the Korean Ceramic Society*, *57*(3), 281-289. https://doi.org/10.1007/s43207-020-00030-3

Vilaplana, J. L., Baeza, F. J., Galao, O., Zornoza, E., & Garcés, P. (2013). Self-Sensing Properties of Alkali Activated Blast Furnace Slag (BFS) Composites Reinforced with Carbon Fibers. *Materials*, *6*(10), 4776-4786. https://doi.org/10.3390/ma6104776

Vlachakis, C., Perry, M., & Biondi, L. (2020). Self-Sensing Alkali-Activated Materials: A Review. *Minerals*, *10*(10), 885. https://doi.org/10.3390/min10100885

Wadsö, L., Karlsson, J., & Tammo, K. (2012). Thermal properties of concrete with various aggregates. *Cement and Concrete Research*.

Wagh, A. S., & Douse, V. E. (1991). Silicate bonded unsintered ceramics of Bayer process waste. *Journal of materials research*, *6*(5), 1094-1102.

Walther, B., Feichtenschlager, B., & Zhou, S. (2017). *Brevet nº US9580356B2*. United States. Repéré à https://patents.google.com/patent/US9580356B2/en

Wang, H., Gao, X., & Liu, J. (2018). Effects of salt freeze-thaw cycles and cyclic loading on the piezoresistive properties of carbon nanofibers mortar. *Construction and Building Materials*, *177*, 192-201. https://doi.org/10.1016/j.conbuildmat.2018.05.103

Wang, H., Gao, X., & Wang, R. (2017). The influence of rheological parameters of cement paste on the dispersion of carbon nanofibers and self-sensing performance. *Construction and Building Materials*, *134*, 673-683. https://doi.org/10.1016/j.conbuildmat.2016.12.176

Wang, R., Gu, H., Mo, Y., & Song, G. (2013). Proof-of-concept experimental study of damage detection of concrete piles using embedded piezoceramic transducers. *Smart Materials and Structures*, *22*(4), 042001.

Wang, S., Jin, H., Deng, Y., & Xiao, Y. (2021). Comprehensive utilization status of red mud in China: A critical review. *Journal of Cleaner Production*, *289*, 125136. https://doi.org/10.1016/j.jclepro.2020.125136

Wang, Yanxiu, Zhang, T., Lyu, G., Guo, F., Zhang, W., & Zhang, Y. (2018). Recovery of alkali and alumina from bauxite residue (red mud) and complete reuse of the treated residue. *Journal of Cleaner Production*, *188*, 456-465. https://doi.org/10.1016/j.jclepro.2018.04.009

Wang, Yongfeng, Nie, Q., Huang, B., Cheng, H., Wang, L., & He, Q. (2020). Removal of ciprofloxacin as an emerging pollutant: A novel application for bauxite residue reuse. *Journal of Cleaner Production*, *253*, 120049. https://doi.org/10.1016/j.jclepro.2020.120049

White, C. E., Provis, J. L., Bloomer, B., Henson, N. J., & Page, K. (2013). In situ X-ray pair distribution function analysis of geopolymer gel nanostructure formation kinetics. *Physical Chemistry Chemical Physics*, *15*(22), 8573-8582. https://doi.org/10.1039/C3CP44342F

White, C. E., Provis, J. L., Llobet, A., Proffen, T., & Deventer, J. S. J. van. (2011). Evolution of Local Structure in Geopolymer Gels: An In Situ Neutron Pair Distribution Function Analysis. *Journal of the American Ceramic Society*, *94*(10), 3532-3539. https://doi.org/10.1111/j.1551-2916.2011.04515.x

Wu, C., & Liu, D. (2012). Mineral Phase and Physical Properties of Red Mud Calcined at Different Temperatures. *Journal of Nanomaterials*, *2012*, e628592. https://doi.org/10.1155/2012/628592

Yadav, A. K., & Gautam, C. (2014). Dielectric behavior of perovskite glass ceramics. *Journal of Materials Science: Materials in Electronics*, *25*(12), 5165-5187. https://doi.org/10.1007/s10854-014-2311-6

Yao, K., Zhang, L., Yao, X., & Zhu, W. (1997). Preparation and properties of barium titanate glass-ceramics sintered from sol–gel-derived powders. *Journal of materials science*, *32*(14), 3659-3665.

Ye, N., Chen, Y., Yang, J., Liang, S., Hu, Y., Hu, J., … Xiao, B. (2017). Transformations of Na, Al, Si and Fe species in red mud during synthesis of one-part geopolymers. *Cement and Concrete Research*, *101*, 123-130. https://doi.org/10.1016/j.cemconres.2017.08.027

Ye, N., Yang, J., Ke, X., Zhu, J., Li, Y., Xiang, C., … Xiao, B. (2014). Synthesis and Characterization of Geopolymer from Bayer Red Mud with Thermal Pretreatment.

Journal of the American Ceramic Society, *97*(5), 1652-1660. https://doi.org/10.1111/jace.12840

Ye, N., Yang, J., Liang, S., Hu, Y., Hu, J., Xiao, B., & Huang, Q. (2016). Synthesis and strength optimization of one-part geopolymer based on red mud. *Construction and Building Materials*, *111*, 317-325. https://doi.org/10.1016/j.conbuildmat.2016.02.099

Yoo, D.-Y., Kim, S., & Lee, S. H. (2018). Self-sensing capability of ultra-high-performance concrete containing steel fibers and carbon nanotubes under tension. *Sensors and Actuators A: Physical*, *276*, 125-136.

Yoo, D.-Y., You, I., Youn, H., & Lee, S.-J. (2018). Electrical and piezoresistive properties of cement composites with carbon nanomaterials. *Journal of Composite Materials*, *52*(24), 3325-3340.

Yunsheng, Z., Wei, S., & Zongjin, L. (2007). Preparation and microstructure of K-PSDS geopolymeric binder. *Colloids and Surfaces A: Physicochemical and Engineering Aspects*, *302*(1), 473-482. https://doi.org/10.1016/j.colsurfa.2007.03.031

Zaharaki, D., Galetakis, M., & Komnitsas, K. (2016). Valorization of construction and demolition (C&D) and industrial wastes through alkali activation. *Construction and building Materials*, *121*, 686-693.

Zhang, G., He, J., & Gambrell, R. P. (2010). Synthesis, Characterization, and Mechanical Properties of Red Mud–Based Geopolymers. *Transportation Research Record*, *2167*(1), 1-9. https://doi.org/10.3141/2167-01

Zhang, Jian, Shi, C., Zhang, Z., & Ou, Z. (2017). Durability of alkali-activated materials in aggressive environments: A review on recent studies. *Construction and Building Materials*, *152*, 598-613. https://doi.org/10.1016/j.conbuildmat.2017.07.027

Zhang, Jinrui, Lu, Y., Lu, Z., Liu, C., Sun, G., & Li, Z. (2015). A new smart traffic monitoring method using embedded cement-based piezoelectric sensors. *Smart Materials and Structures*, *24*(2), 025023. https://doi.org/10.1088/0964-1726/24/2/025023

Zhang, Junjun, Xu, J., & Zhang, D. (2016). A Structural Supercapacitor Based on Graphene and Hardened Cement Paste. *Journal of The Electrochemical Society*, *163*(3), E83-E87. https://doi.org/10.1149/2.0801603jes

Zhang, L., Ahmari, S., & Zhang, J. (2011). Synthesis and characterization of fly ash modified mine tailings-based geopolymers. *Construction and Building Materials*, *25*(9), 3773-3781. https://doi.org/10.1016/j.conbuildmat.2011.04.005

Zhang, M., Deskins, N. A., Zhang, G., Cygan, R. T., & Tao, M. (2018). Modeling the polymerization process for geopolymer synthesis through reactive molecular dynamics simulations. *The Journal of Physical Chemistry C*, *122*(12), 6760-6773.

Zhang, M., Zhao, M., Zhang, G., Mann, D., Lumsden, K., & Tao, M. (2016). Durability of red mud-fly ash based geopolymer and leaching behavior of heavy metals in sulfuric acid solutions and deionized water. *Construction and Building Materials*, *124*, 373-382. https://doi.org/10.1016/j.conbuildmat.2016.07.108

Zhang, Q., Cui, J., Dong, G., & Du, J. (2009). The effect of lead-glass additives on densification and dielectric properties of Ba0. 4Sr0. 6TiO3 ceramics (Vol. 152, p. 012066). Communication présentée au Journal of Physics: Conference Series, IOP Publishing.

Zhang, Y., Ma, T., Wang, X., Yuan, Z., & Zhang, Q. (2011). Two dielectric relaxation mechanisms observed in lanthanum doped barium strontium titanate glass ceramics. *Journal of Applied Physics*, *109*(8), 084115.

Zhang, Z., Huang, Y., Bridgelall, R., Palek, L., & Strommen, R. (2015). Sampling optimization for high-speed weigh-in-motion measurements using in-pavement strain-based sensors. *Measurement Science and Technology*, *26*(6), 065003. https://doi.org/10.1088/0957-0233/26/6/065003

Zhao, J., Bao, T., Chen, S., & Kundu, T. (2016). Smart aggregate-piezoceramic patch combination for health monitoring of concrete structures. *Journal of Sensors*, *2016*.

Zhao, X., Li, H., Du, D., & Wang, J. (2008). Concrete structure monitoring based on built-in piezoelectric ceramic transducers (Vol. 6932, p. 693208). Communication présentée au Sensors and Smart Structures Technologies for Civil, Mechanical, and Aerospace Systems 2008, International Society for Optics and Photonics.

Zheng, Z., Ma, X., Zhang, Z., & Li, Y. (2019). In-situ transition of amorphous gels to Na-P1 zeolite in geopolymer: Mechanical and adsorption properties. *Construction and Building Materials*, *202*, 851-860. https://doi.org/10.1016/j.conbuildmat.2019.01.067

Zhou, X., Chu, B., Neese, B., Lin, M., & Zhang, Q. (2007). Electrical energy density and discharge characteristics of a poly (vinylidene fluoride-chlorotrifluoroethylene) copolymer. *IEEE transactions on dielectrics and electrical insulation*, *14*(5), 1133-1138.